COMPUTER MODELLING AND ANALYSIS
OF PARTICULATE LADEN GAS FLOWS

BY

PHOTIS ｌKOSTAMIS

BSc, MSc, AFIMA

Thesis submitted to the Council for National Academic Awards in partial fulfilment of the requirements for the Degree of Doctor of Philosophy

Centre for Numerical Modelling and Process Analysis
School of Mathematics, Statistics and Computing
Thames Polytechnic, London

CRA (Australia)

Klockner Stahlforschung GmbH (FRG)

MARCH 1987

COMPUTER MODELLING AND ANALYSIS
OF PARTICULATE LADEN GAS FLOWS

BY

PHOTIS KOSTAMIS
Centre for Numerical Modelling and Process Analysis
School of Mathematics, Statistics and Computing
Thames Polytechnic, London

March 1987

ABSTRACT

This study is concerned with the prediction of the fluid-flow, chemical reactions and heat transfer processes in an industrial off-gas ducting system.

A mathematical model is developed and then applied to predict the processes occurring in the off-gas ducting system. Particular attention is focussed on the two-phase thermal behaviour and the chemical reactions. A three-dimensional, two-phase numerical solution technique is used to solve the governing time-averaged partial differential equations. The model includes equations for turbulence, chemical reactions and two-phase thermal radiation. The calculations are performed for a particulate phase comprising non-reacting particles and a gaseous phase comprising chemically reacting gases. Both exothermic and endothermic reactions are considered.

The effects of thermal radiation, particle solidification, chemical reactions and heat transfer on the two-phase flow are introduced and examined in detail.

Predictions are made for an extensive range of parameters. The effects of these parameters on the off-gas ducting system are quantified. Comparisons are made between predicted results and experimental data when available and agreement is reasonable.

The models developed can be easily incorporated into general-purpose fluid-flow packages. The procedure is general, and allows two-phase, two- or three-dimensional computations. Industrial plant can be modelled realistically on minicomputers at moderate costs. Convergence can normally be obtained with ease.

It is concluded that for the cases studied, thermal radiation is a dominant factor in the calculation of the heat losses and that the particle contribution to these losses is small compared with that of the gases. The model indicates that the strongly temperature dependent reaction rates have a dominant influence in determining optimal operating conditions.

ABSTRACT

This study is concerned with the prediction of the fluid-flow, chemical reactions and heat transfer processes in an industrial off-gas ducting system.

A mathematical model is developed and then applied to predict the processes occurring in the off-gas ducting system. Particular attention is focussed on the two-phase thermal behaviour and the chemical reactions. A three-dimensional, two-phase numerical solution technique is used to solve the governing time-averaged partial differential equations. The model includes equations for turbulence, chemical reactions and two-phase thermal radiation. The calculations are performed for a particulate phase comprising non-reacting particles and a gaseous phase comprising chemically reacting gases. Both exothermic and endothermic reactions are considered.

The effects of thermal radiation, particle solidification, chemical reactions and heat transfer on the two-phase flow are introduced and examined in detail.

Predictions are made for an extensive range of parameters. The effects of these parameters on the off-gas ducting system are quantified. Comparisons are made between predicted results and experimental data when available and agreement is reasonable.

The models developed can be easily incorporated into general-purpose fluid-flow packages. The procedure is general, and allows two-phase, two- or three-dimensional computations. Industrial plant can be modelled realistically on minicomputers at moderate costs. Convergence can normally be obtained with ease.

It is concluded that for the cases studied, thermal radiation is a dominant factor in the calculation of the heat losses and that the particle contribution to these losses is small compared with that of the gases. The model indicates that the strongly temperature dependent reaction rates have a dominant influence in determining optimal operating conditions.

ACKNOWLEDGEMENTS

TABLE OF CONTENTS PAGE NO.

CHAPTER 3 - MODELLING OF RADIANT HEAT TRANSFER

CHAPTER 4 - THE COMBUSTION MODEL

CHAPTER 6 - THE INDUSTRIAL FURNACE MODELLED WITH COMBUSTION

CHAPTER 1 - INTRODUCTION

1.1   The Problem Considered

This work is concerned with numerical prediction of the flow characteristics in the 'off-gas ducting system' of a modern industrial steel making plant.   The flow is turbulent and two-phase with a particulate phase which solidifies within the region and a gaseous phase in which chemical reactions occur.

A model is developed which consists of a set of coupled non-linear partial differential equations describing the flow, heat-transfer, composition of the reacting chemical species and volume fractions of the two phases.   These equations are converted to finite-difference schemes by means of a control volume approach and are solved using the widely used fluid-flow package PHOENICS (Spalding (1981)).

The main objectives of this research are to develop a comprehensive computer model of off-gas ducting systems.   This provides both insight into the interaction between the major physicochemical factors and a tool for design assessment and optimisation.

Section 1.2 consists of a description of a modern steelmaking furnace. In Section 1.3 a general review of recent work on similar industrial plant is presented which provided the background for the present work. Sections 1.4 and 1.5 state the objectives of the present work, the novel features it contains and the subject and method of investigation. Section 1.6 provides an outline of the structure of the rest of the thesis.

1.2   Description of a Steelmaking Converter and Off-Gas System

In oxygen steelmaking, the converter is used to process blast furnace metal and ferrous scrap into steel. This involves reacting oxygen with the bath of molten iron to decarburize the metal and to remove other impure elements such as silicon, manganese and phosphorus. In addition lime and other fluxes are added to the vessel to form a slag which allows further removal of impure elements. All these reactions lead to the formation of an off-gas which leaves the converter vessel at high temperature. The off-gas also contains particulate matter such as iron dust and slag droplets. The off-gas is drawn off through a ducting system. Figure 1 shows a typical steelmaking converter and off-gas system.

There is quite a range of oxygen and steelmaking processes and many variations and improvements have been made over the last 30 years. These involve, in varying degrees, injection of oxygen from the top and/or bottom of the bath, with the co-injection of nitrogen, argon or natural gas from the bottom. In addition, coal, iron ore, lime and other fluxes can be added by either top charging or injection, or bottom injection. A particularly interesting development has been the injection of coal into the molten iron bath, which results in an increased energy input into the converter. This means that the process is made more flexible so that greater amounts of scrap or iron ore can be melted.

The off-gas produced is derived from the reaction of oxygen with the bath carbon, from the decomposition and reaction of injected coal and from other injectants such as hydrocarbons and flushing or stirring gas. By

applying combinations of top and bottom oxygen injection together with coal and hydrocarbon injection, it is possible to obtain a wide range of off-gases containing CO, CO_2, H_2, H_2O and N_2.

Particulate matter is also formed as a consequence of the gas/liquid reactions and the gas/liquid disengagement. This is largely in the form of iron particles but can also contain amounts of slag or ash.

In normal steelmaking operations, the off-gas leaves the converter between 1500 and 1700°C. It enters a water-cooled off-gas duct or vessel where it is cooled to 1000°C or lower. Often air is drawn in at the seal between the converter and the duct and combusts in this section of the off-gas system.

Following this, the off-gas is further cooled and is cleaned in a wet scrubbing or a dry electrofilter off-gas cleaning system. The gas is then either flared or used in the steelworks fuel gas network.

Under some process situations it may be desired to modify the composition of this gas in order to make it more suitable for a subsequent reaction. One such example is to inject hydrocarbons into the off-gas duct to increase the fuel content of the gas, that is, to reduce the oxidation potential of the gas.

The research described in this thesis was carried out in order to provide a greater understanding of the processes which can be carried out in off-gas systems.

1.3 General Review of Previous Modelling Work on Similar Plant

In this section a general review is presented for work on modelling of flow and calculations for furnaces and ducted flow. Attention is focussed on complex three-dimensional modelling work that includes thermal radiation and chemical reactions and resemble the present application. More detailed reviews on thermal radiation and chemical reactions modelling work are given in Chapters 3 and 4, respectively.

Patankar and Spalding (1972) presented the basis of a computer model for the prediction of a two-phase flow, heat-transfer and combustion processes in a three-dimensional furnace. The main physical features was the assumption of a simple chemically reacting system (ie. species mix in unique proportions and produce a unique single product). The effective diffusivities of all species were assumed equal, fuel and oxidant could not co-exist and the effective viscosities were computed from a pre-specified algebraic formula, in the absence of any advance turbulence model.

Patankar and Spalding (1974) subsequently developed this model and demonstrated its application for a three-dimensional turbulent flow in a gas-turbine combustion chamber. The geometry considered involved the mixing of the streams of fuel and air in a confined space with additional air streams being used for film-cooling and dilution purposes. Differential equations were solved for two turbulence quantities, for the concentration of the species, and for the radiation fluxes. A cartesian coordinate system was adopted and the integration domain covered only a small section of the annular combustor, which was treated as a perfectly rectangular geometry. The results reported were plausible but actual

comparison with measurements was not made.

Serag-El-Din (1977) applied a polar coordinate version of Patankar and Spalding (1974), to a three-dimensional can combustor geometry. Thermal radiation was neglected and so was the influence of chemical kinetics on the predicted reaction rates. Overall, the predicted results displayed generally good agreement with cold-flow measurements, but when combustion was introduced the agreement was very poor. This was attributed to the neglect of the chemical kinetics in the predicted reaction rates. Nevertheless, the same combustion model has been used in other flow configurations with good results. For example, Pai et al (1978), applied the Patankar and Spalding (1974) procedure for the case of an experimental rectangular furnace of the International Flame Research Foundation in Holland, and quite realistic predictions were obtained.

Abou Ellail et al (1977) described a prediction method for three-dimensional reacting flows. It comprised of a numerical solution technique for the time-averaged governing partial-differential equations and physical modelling for turbulence, combustion and thermal radiation. The combustion model was based on a 'fast kinetics' statistical approach and the radiation model was based on a flux method. Comparisons of predictions and data was presented for an industrial furnace. The TEACH-3E computer program was employed.

Megahed (1979) used a similar mathematical model to the ones described above with a curvilinear coordinate system. In the first part of the work he used a flux model for the thermal radiation and then a more

-5-

flexible method, the 'discrete transfer' method of Shah (1979). The model was applied to a real-life industrial glass furnace and validation of the results was made with experimental results.

Khalil et al (1975) performed calculations with three combustion models, characterised by instant reaction, with scalar fluctuations and Arrhenius or eddy-breakup reaction rate with scalar fluctuations. Comparison with furnace measurements indicated that the last two models lead to reasonably correct results. Radiation was accounted for with a four-flux model.

Gosman et al (1978) described a general-computer based procedure for the prediction of gaseous-fired cylindrical combustion chambers. Combustion modelling has been developed to handle diffusion, partially-premixed and premixed combustion. A flux method was employed for the radiation heat transfer, producing qualitatively good results. The TEACH-T code was employed for the numerical solution of the equations.

Khalil (1979) developed a general computer programme to calculate the local flow properties in turbulent reactive and non-reactive flows with recirculation. He employed a four flux representation for the thermal radiation modelling. The combustion models employed were characterised by instant reaction, with clipped Gaussian probability distribution of concentration, finite-reaction rate with an eddy-breakup formulation, and a finite-reaction rate which accounts for temperature and concentration fluctuations. The model was assessed with comparison with experimental results and indicated satisfactory agreement. The

model was further extended and refined by Khalil et al (1981) and was applied to more complex furnace geometries with reasonable success.

Carvalho (1983) applied a new mathematical model to predict the processes occurring in a combustion chamber. A three-dimensional numerical solution technique was used to solve the governing differential equations and the physical modelling for the turbulence, combustion and thermal radiation. The radiation model was based on the 'discrete transfer' method and reaction model employed a clipped Gaussian distribution function. The model was applied in a glass-furnace (Carvalho and Lockwood (1985)) but predictions were not fully validated because of the lack of experimental results.

Lixing et al (1986) studied a three-dimensional flow field and two-dimensional coal combustion in a cylindrical combustor of co-flow jets with large velocity difference. Their solution procedure was based on the Patankar and Spalding procedure and thermal radiation was not accounted for. The reaction model was based on the eddy-breakup and Arrhenius rates and $k-\epsilon$ turbulence model was employed. The predicted results were not validated against experimental ones.

Boyd and Kent (1986) presented a fully three-dimensional computer model of a pulverised fuel, tangentially fired furnace. The models predicts gas flows species concentrations and temperature, particle trajectories and combustion and radiation heat fluxes. Radiation was based on the 'discrete transfer' method and chemical reaction of a very simple model. Overall agreement of the results was pleasing, except in the case of the temperatures around the burners where temperatures were

overpredicted. This is attributed to the simplistic nature of the combustion model.

Summary

The work described in this short review, highlights the problems associated with modelling the complexity of typical furnaces and similar plants. The geometry is complex and the chemical reactions not fully understood. Heat transfer processes are also complex. The models place a severe strain on even the most powerful modern computers.

Another feature is the lack of detailed experimental results to validate the models. Authors resort to statements such as 'the results seemed plausible' or vague statements like 'agreement with experimental measurements was reasonable', without actually quoting figures. The reason for this is not hard to see. The conditions within the plant are so hostile that experimental measurements are very difficult to obtain. Furthermore, industrial plant is expensive and must be kept in full production to recover costs. Few industrialists would be prepared to hold up production in order to carry out detailed experimental measurements.

Unfortunately experimental measurements for off-gas ducting systems have also been difficult to obtain. It has been necessary to rely on the judgement of engineers at the collaborating establishment to assess results. However, in some cases temperature and gas composition measurements were available and enabled the models to be validated.

1.4   Objectives and Contributions of the Present Study

The development of the converter processes in the metallurgical industry to their present standard or efficiency has been brought about largely by trial and error and by experience gained under production conditions. Present status of design and operating conditions are to a great extent the product of many years of engineering evolution. They perform their functions reasonably well and thus attention is becoming focussed upon the behaviour of the gases and particulate matter in the off-gas ducting. This is because, in reality, the behaviour of the gaseous species in the ducting and their interaction with the particulates is not well understood. Disasters can occur when particulate accumulates and blocks the off-gas duct.

It would be useful to know how ducting dimensions and geometry influence:

\#   the global and relative movement of the gas and particulate phases;

\#   the rates of heat loss of both phases and radiation heat transfer impact on them for different particle sizes and particle loading;

\#   the chemical reactions between the gaseous species; and

\#   the influence on gas and particle chemical composition of temperature, etc, on entry to the ducting.

In particular, it would be useful to identify the means to control the amount of combustion in the hood and the distribution of the particulate phase.

Increasing pressure is being placed on engineers and plant designers to have recourse to every available modern theoretical and analytical means to quantify and enhance the off-gas duct performance. Much could be learned from the careful instrumentation and monitoring of the daily operating of existing systems. Any attempt to do more than this is however filled with problems. Converters and off-duct systems are very expensive and there is no reassurance that a new radical design will offer improved performance. Even the cost of experimenting with modifications on existing designs is prohibitive.

Over the last decade some work has been done in this subject area, but it has tended to concentrate on one or two at the most of the above aspects. Also the nature of the physical system, renders laboratory experimental work very difficult since the problems of scale-up yield inherent constraints, thus frequently making the scaled-down models results not valid for the full-scale system. At the same time, as mentioned before, the 'hostile' plant environment makes full-scale measurements difficult.

The short literature survey in Section 1.3 reveals deficiencies in many of the chemical reaction models and the exclusion of radiation from some of the heat transfer models, is clearly unacceptable for the temperatures found in the off-gas ducts. New models have been developed which make fewer simplifying assumptions concerning the chemical reactions. Also a new radiation model has been developed which takes account of both the gaseous and particulate phases.

The code for both the radiation and combustion models is lengthy and

complex.   However, it was modularised in the form of convenient subroutines designed to be easily added to a general fluid-flow solver, such as PHOENICS.   This provides a powerful framework for the modelling and analysis of ducting systems, accounting for:

three-dimensional turbulent fluid flow;

gaseous and particulate phase; and

heat transfer.

The implementation of the newly developed models into PHOENICS enhanced its capabilities and overcame previous difficulties in modelling of furnaces.

The present work is developed with reference to a real industrial problem of paramount importance, namely the flow of a mixture of reacting gases and pure iron particles, through off-gas ducts, encountered in metallurgical applications.

In summary, items that have been studied and models that have been developed are:

multiphase radiative heat transfer between the particles, gases and walls, factors that are of prime importance in evaluating heat losses;

chemical reactions in the gaseous phase;

interphase processes (momentum, heat and mass transfer);

solidification of iron particles;

the influence of turbulence; and

\#   the influence of geometric configuration.

To the authors knowledge, no previous published model makes a detailed examination of all these phenomena in off-gas ducts. For the case of radiation heat transfer, no previous model accounts for emission and absorption from both phases and scattering by the particulate phase, in such a way as to be easily incorporated into a general fluid-flow solver. For the chemical reaction model, important ideas have been developed, taking into account a combined turbulence influenced and Arrhenius type reaction rate, suitable for both exothermic and endothermic reactions and coping with non-premixed gases of arbitrary composition. This involves far fewer simplifying assumptions than previous models.

This thesis examines all the important aspects of the off-gas phenomena and important conclusions are drawn about efficiency and operating conditions.

1.5   Subject and Method of Investigation

This thesis can be divided into two main parts.

The first part deals with the general phenomena occurring in the duct, including turbulence and two-phase radiation heat transfer. Predictions are made for different operating conditions, different geometric configurations, particle sizes and loadings. Where possible the predictions are compared with available experimental results.

In the second part of the work, predictions are made for systems that also include chemical reactions in the gaseous phase. Air and natural

gas are also injected into the system, through various injection points and results are presented for a variety of cases in two- and three-dimensions with various gas compositions. Reaction models for one, two-reactions, with Arrhenius and kinetically influenced rates are considered and again where possible predictions are compared with experimental results.

In summary, the ultimate object to the present study is the development and application of a complete mathematical model and of a computer simulation methods for off-gas ducting systems which provide both insight into the interaction between the major physicochemical factors and a tool for design assessment and optimisation.

1.6 Outline of the Thesis

This thesis contains seven chapters.

Chapter 1, the present chapter, forms the introduction. Chapter 2 gives an outline of the physical and mathematical modelling of the problem. It contains descriptions of the governing two-phase equations, turbulence and auxiliary relations, such as interphase heat transfer, interphase friction, particle solidification and boundary conditions. It also contains an outline of the solution procedure embodied in the employed software package PHOENICS.

Chapter 3 is devoted to the modelling of thermal radiation. The newly developed two-phase radiation model is discussed in detail and existing models are presented.

Chapter 4 is concerned with the novel chemical reaction models.

Chapter 5 presents results with and without radiation, for a variety of geometries and operating conditions. Comparison with experiments are presented where possible.

Chapter 6 contains results with radiation and chemical reactions for a variety of two- and three-dimensional geometries for one and two-phase problems.

The last chapter in the thesis, Chapter 7, assesses the extent to which the objectives of the present investigation are fulfilled and makes suggestions for future work.

T=1000°C

CONVERTER
OFF-TAKE DUCT

Rest of plant

CO_2,CO

H_2,H_2O

etc

Fe +
oxides

Possible injection points
natural gas or air

Water-cooled lance
O_2-injection tuyere

T=1600°C

side jets

O_2

O_2 or coal, natural gas etc
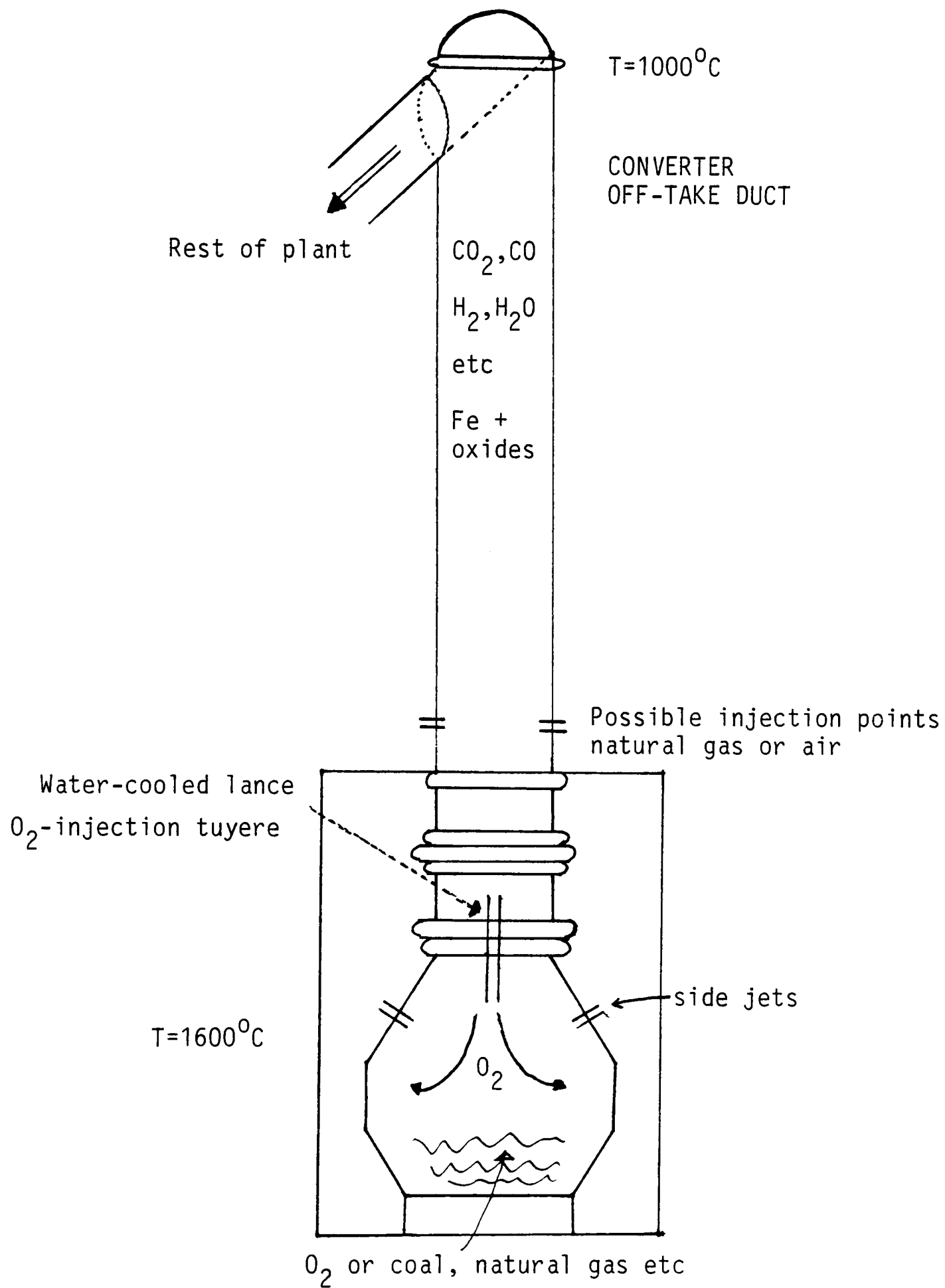
FIGURE 1.1: TYPICAL OFF-GAS DUCTING SYSTEM

CHAPTER 2 – THE BASIC MATHEMATICAL MODEL

2.1 Introduction

The problems of flow and heat transfer in combustors and furnaces are of a multidisciplinary nature because of the multitude of physical and chemical phenomena involved. For this reason, attention must be focussed on the general principles which govern the behaviour of the flow in such complex configurations as well as on the validity of assumptions made to reduce the complexity of the problem.

One type of assumption concerns the simplification of the furnace geometry, which in its full complexity would be prohibitively expensive to model, in terms of storage and computational time. A second type of assumption is needed since the physical and chemical processes cannot at present be calculated by an exact method (Bradshaw et al (1981)). The validity of these assumptions may be demonstrated only by comparison with experimental data.

The conservation equations of mass, momentum, chemical species and energy are well established and, when expressed in partial-differential forms, can be coupled with the above assumptions, to provide the foundations upon which the prediction procedures will be based. Empirical correlations for interphase-friction factors, interphase heat-transfer factors, latent heat, reaction-rate laws and others are also needed to provide a quantitative formulation of such complex two-phase flows.

The equations which describe such processes are known and numerical procedures are available to solve them, but the storage capacity and

speed of present day computers are not sufficient to allow a practical solution. Hence the need to develop physical and mathematical models that can be applied to such complex situations within practical resources.

For laminar flow the equations can be solved numerically using existing numerical techniques, without major problems. However, in the case of turbulence, numerical solution of the equations requires a fine computational mesh, which is vastly in excess of what current computer hardware and software can accommodate (Spalding (1983(a)); Anderson et al (1984)). This is due to the fine scales of the energy-containing eddies. However, for most practical purposes, details of the fine-scale fluctuations are seldom required, since the knowledge of time-averaged values of the dependent variables is usually sufficient for engineering purposes.

In the present chapter the differential equations governing the fluid dynamics and heat-transfer for three-dimensional flows are presented, in polar coordinates, together with the required auxiliary relations.

2.2   The Dependent and Independent Variables

The following are the dependent variables of the problem: velocities of the gas and particles in the radial, azimuthal and axial directions, v_1, v_2, u_1, u_2, w_1 and w_2; pressure p, assumed to be the same for both phases; gas and particle volumetric concentrations, R_1, R_2; enthalpies of gas and particles, h_1, h_2; turbulence kinetic energy and dissipation rate of the gaseous phase, k, ϵ; composite radiation fluxes in the radial, azimuthal and axial direction, RY, RX and RZ; and, the chemical species concentrations, c_1, c_2, c_3 and c_4.

The independent variables are: the radial, circumferential and axial distances, r, θ, z of a polar-cylindrical coordinate system.

2.3   The Partial-Differential Equations

The mathematical model used in this work is based on the finite-difference analogues of the partial-differential equations that govern the three-dimensional, transient or steady flow of two distinct fluid phases. The terms in the following differential equations denote influence on a 'unit-volume' basis.

2.3.1   The mass-conservation equations

The volume fractions, densities and velocities of each of the two phases, in order to satisfy the mass-conservation principle, obey the following equations.

(i)   Gas-phase equation:

$$\frac{\partial}{\partial t}(\rho_1 R_1) + \frac{\partial}{\partial z}(\rho_1 R_1 w_1) + \frac{1}{r}\frac{\partial}{\partial r}(\rho_1 R_1 r v_1)$$

$$+ \frac{1}{r}\frac{\partial}{\partial \theta}(\rho_1 R_1 u_1) = 0 \qquad\qquad (2.1).$$

(ii)   Particle-phase equation:

$$\frac{\partial}{\partial t}(\rho_2 R_2) + \frac{\partial}{\partial z}(\rho_2 R_2 w_2) + \frac{1}{r}\frac{\partial}{\partial r}(\rho_2 R_2 r v_2)$$

$$+ \frac{1}{r}\frac{\partial}{\partial \theta}(\rho_2 R_2 u_2) = 0 \qquad\qquad (2.2).$$

The volumetric fractions R_1 and R_2 are related by the 'space-sharing' equation:

$$R_1 + R_2 = 1 \qquad\qquad (2.3).$$

2.3.2 The conservation of momentum equations

$$\frac{\partial}{\partial t}(\rho_i R_i \phi) + \frac{1}{r}\frac{\partial}{\partial r}(r R_i \rho_i v_i \phi) + \frac{1}{r}\frac{\partial}{\partial \theta}(R_i \rho_i u_i \phi)$$

$$+ \frac{\partial}{\partial z}(R_i \rho_i w_i \phi) = \frac{1}{r}\frac{\partial}{\partial r}\left(r R_i \Gamma_\phi \frac{\partial \phi}{\partial r}\right)$$

$$+ \frac{1}{r}\frac{\partial}{\partial \theta}\left(R_i \Gamma_\phi \frac{\partial \phi}{\partial \theta}\right) + \frac{\partial}{\partial z}\left(R_i \Gamma_\phi \frac{\partial \phi}{\partial z}\right) + S_\phi \qquad (2.4);$$

where ϕ stands for u_1, u_2, v_1, v_2, w_1 and w_2; Γ_ϕ and S_ϕ are diffusion coefficients and source terms; and subscript i refers to the phase in question (gaseous or particulate). For the applications considered, Γ_ϕ for the gaseous phase is equal to $\mu_{eff}/\sigma_{\phi, 1}$, where μ_{eff} is the effective viscosity and $\sigma_{\phi, 1}$ the Prandtl/Schmidt number for variable ϕ. For the particulate phase Γ_ϕ is assumed to be zero (eg. no diffusion) in the absence of other reliable physical information.

The effective viscosity, μ_{eff}, of the gaseous phase is defined and calculated from the (k-ϵ) two-equation model of turbulence (Launder and Spalding (1974)):

$$\mu_{eff} = \frac{C_\mu \rho_1 k^2}{\epsilon} + \mu_\ell \qquad\qquad (2.5);$$

where the empirical constant C_μ is equal to 0.09 and k, ϵ and μ_ℓ are the turbulence energy, its dissipation rate and the laminar viscosity coefficient, respectively.

The source terms, S_ϕ, for the momentum equations, are given in Table

2.1 below in the form in which they occur in the finite-difference equations, eg. as the integral over the finite-difference cells. They contain contributions such as: the pressure gradient in the relevant direction, the gravitational force, the interphase-friction term, viscous stress terms (involving gradients of velocities) as defined by the Navier-Stokes equations, etc.

ϕ	$\int S_\phi dvol$ (Integral source term for finite-difference cell)
w_1	$VR_1(\rho_1 g - \partial p/\partial z) + C_f(w_2-w_1)$
w_2	$VR_2(\rho_2 g - \partial p/\partial z) + C_f(w_1-w_2)$ V is cell volume; C_f is interphase friction coefficient.
v_1	$VR_1 \left(\dfrac{\rho_1 u_1^2}{r} - \dfrac{\partial p}{\partial r} \right) + C_f(v_2-v_1)$
v_2	$VR_2 \left(\dfrac{\rho_2 u_2^2}{r} - \dfrac{\partial p}{\partial r} \right) + C_f(v_1-v_2)$
$u_1 r$	$-VR_1 \dfrac{\partial p}{\partial \theta} + C_f r(u_2-u_1)$
$u_2 r$	$-VR_2 \dfrac{\partial p}{\partial \theta} + C_f r(u_1-u_2)$ The equations for the angular momentum, ur, is solved in preference to that for u.

TABLE 2.1:   SOURCE TERMS IN MOMENTUM EQUATIONS

2.3.3   The conservation of energy equation

Let h_1, h_2 stand for the stagnation enthalpy of the gas and solid phases per unit mass, respectively, by which is meant the thermodynamic enthalpy plus the kinetic energy of the phase plus any potential energy associated with the position of the fluid in a force field, plus heat of combustion (see Chapter 4). Then the first law of thermodynamics leads to the following equations.

(i)   **Gas-phase energy equation**

$$\frac{\partial}{\partial t}\left[(\rho_1 h_1 - p)R_1\right] + \frac{1}{r}\frac{\partial}{\partial r}(rR_1\rho_1 v_1 h_1)$$

$$+ \frac{1}{r}\frac{\partial}{\partial \theta}(R_1\rho_1 u_1 h_1) + \frac{\partial}{\partial z}(\rho_1 R_1 w_1 h_1)$$

$$= C_f(v_2 - v_1)v_2 + C_f(w_2 - w_1)w_2 + C_f(u_2 - u_1)u_2$$

$$- \dot{q}_{12} - p\frac{\partial R_1}{\partial t} + S_h \qquad\qquad (2.6).$$

(ii)   **Particle-phase energy equation**

$$\frac{\partial}{\partial t}\left[(\rho_2 h_2 - p)R_2\right] + \frac{1}{r}\frac{\partial}{\partial r}(rR_2\rho_2 v_2 h_2)$$

$$+ \frac{1}{r}\frac{\partial}{\partial \theta}(R_2\rho_2 u_2 h_2) + \frac{\partial}{\partial z}(\rho_2 R_2 w_2 h_2)$$

$$= C_f(v_1 - v_2)v_1 + C_f(w_1 - w_2)w_1 + C_f(u_1 - u_2)u_1$$

$$- \dot{q}_{12} - p\frac{\partial R_2}{\partial t} + S_h \qquad\qquad (2.7).$$

where $\dot{q}_{12}$ is the rate of heat transfer from gas to particles; and p is the pressure which is assumed to be shared by both phases. S_h includes the terms accounting for radiation heat transfer (see Chapter 3).

2.3.4   The conservation of chemical species equation

If we denote the mass fraction of a chemical species ℓ by m_ℓ, then the conservation of chemical species equation is given by:

$$\frac{\partial}{\partial t}(\rho_L m_\ell) + \frac{1}{r}\frac{\partial}{\partial r}(rm_\ell \rho_L v_L) + \frac{1}{r}\frac{\partial}{\partial \theta}(m_\ell \rho_L u_L)$$

$$+ \frac{\partial}{\partial z}(m_\ell \rho_L w_L) = \frac{1}{r}\frac{\partial}{\partial r}\left(rm_\ell \Gamma_\ell \frac{\partial \phi}{\partial r}\right)$$

$$+ \frac{1}{r} \frac{\partial}{\partial \theta} (m_\ell \Gamma_\ell \frac{\partial \phi}{\partial \theta}) + \frac{\partial}{\partial z} (m_\ell \Gamma_\ell \frac{\partial \phi}{\partial z}) + S_\phi \qquad (2.8);$$

where S_ϕ is the rate of generation/destruction of species ℓ, by chemical reaction, per unit volume. The term S_ϕ is discussed in Chapter 4, and Γ_ℓ is the exchange coefficient of ℓ.

2.3.5   The general differential equation

The above conservation equations (2.6), (2.7) and (2.8) can be cast into a generalised conservation equation of the form:

$$\frac{\partial}{\partial t} (r \rho \phi) + \text{div} (r \rho \bar{v} \phi - r \Gamma_\phi \text{grad} \phi) = S_\phi$$

$$\uparrow \qquad \qquad \uparrow \qquad \qquad \uparrow \qquad \qquad \uparrow$$
transient   convection   diffusion   source $\qquad (2.9)$.

The pressure variable is associated with the continuity equation:

$$\frac{\partial \rho}{\partial t} + \text{div} (\rho \bar{v}) = 0 \qquad (2.10).$$

2.4   Auxiliary Relations

The above set of equations has to be solved in conjunction with observance of constraints on the values of the variables, represented by algebraic relations. The constitutive relations used for the present application are given below. It should be mentioned that, although little emphasis is placed on these relations, their proper form and function are essential to realistic predictions for the two-phase flows under consideration.

2.4.1   The interphase-friction coefficient

The ability to predict the interphase drag or the relative velocity between

phases is of considerable importance for modelling a two-phase system, as the use of a reliable interphase drag correlation can affect significantly the results. In this work, prescribed functions for the coefficient in the drag terms of equations (2.4), (2.6) and (2.7), are used.

The expression for the interphase-friction force for the finite-difference cell is given by:

$$F = 0.5 * C_D * A_P * \rho_g * V_{s\ell p}^2 \qquad (2.11);$$

where:

A_p = Total projected area of particles/cell

       = $1.5 * R2 * Vol/2r_p$ (2.12).

r_p = Radius of particles.

$R2$ = Volume fraction of phase-2 (particles).

Vol = Volume of the cell.

ρ_g = Density of phase-1 (gases).

$V_{s\ell p}$ = Slip velocity.

        $= \sqrt{u_{s\ell}^2 + v_{s\ell}^2 + w_{s\ell}^2}$ (2.13).

$u_{s\ell}$ = $(u_g - u_p)$, etc.

u_g = u-velocity component of gases.

u_p = u-velocity of particles, etc.

The drag coefficient C_D is given by Clift et al (1971) as:

$$C_D = \max[0.42, \frac{24}{Re}(1+0.15Re^{0.687})+0.42/(1+4.25*10^4*Re^{-1.16})]$$

$$(2.14);$$

where Re is the particle Reynolds number given by:

$$Re = \rho_g 2r_p \, V_{slip}/\mu_\ell \qquad\qquad (2.15);$$

Although the drag experienced by a solid particle moving through a fluid is also dependent upon a number of other factors including fluid turbulence, acceleration, particle shape etc, equation (2.14) can be used with reasonable confidence in most problems of practical interest (Clift et al (1971)).

2.4.2   The interphase heat-transfer coefficient

Although the equations solved for the transport of heat between the gaseous and particulate phases are those of the phase enthalpies, equations (2.6) and (2.7), it is convenient to think in terms of temperatures, T_1 and T_2, by introducing the specific heat capacities, c_1 and c_2, of the two phases, respectively.   Then, assuming T_s to be the particle surface temperature (ie the temperature of the interface between the two phases), we can calculate the rates of heat transfer from gas to the particle surface, $\dot{q}_{1s}$, and from particle surface to the particle interior, $\dot{q}_{s2}$.   These are given by:

$$\dot{q}_{1s} = a_1 \, (T_1 - T_s) \qquad\qquad (2.16);$$

$$\dot{q}_{s2} = a_2 \, (T_s - T_2) \qquad\qquad (2.17);$$

where a_1 and a_2 are heat-transfer coefficients for the gas and solid, respectively, multiplied by the interface area through which the transfer occurs. a_1 is calculated by assuming Nusselt numbers for the gas is 2, valid for spherical particles, in the absence of any other reliable experimental evidence.   The heat-transfer coefficient a_2 is computed assuming a cubic temperature distribution within the particle (Markatos and Kirkcaldy (1983)), which leads to:

$$a_2 = \frac{3\lambda}{r_p} A_s \qquad\qquad (2.18);$$

where A_s is the interface area, λ is the particle thermoconductivity and r_p is the particle radius.

An energy balance over a control volume enclosing the interface yields:

$$\dot{q}_{s2} - \dot{q}_{1s} = 0 \qquad\qquad (2.19).$$

Combination of equations (2.16), (2.17) and (2.19) yields:

$$T_s = \frac{a_1 T_1 + a_2 T_2}{(a_1 + a_2)} \qquad\qquad (2.20);$$

and

$$\dot{q}_{1s} = \frac{a_1 a_2 (T_1 - T_2)}{(a_1 + a_2)} = \dot{q}_{s2} \qquad\qquad (2.21).$$

2.4.3 Latent heat – particle solidification

In many practical applications, particles enter a domain at high temperature, in a molten state. As the flow progresses, the temperature drops, due to radiation and convective heat losses. The particles solidify at a temperature which is constant for a given pure substance. Therefore, given that T_m is the particle melting temperature, and L is the heat of solidification, the particle surface temperature, T_s, is now defined as:

$$T_s = \begin{cases} \dfrac{h_2}{c_2} & \text{for } h_2 \leqslant T_m\, c_2 \\[2ex] \dfrac{h_2 - L}{c_2} & \text{for } h_2 \geqslant (T_m c_2 + L) \\[2ex] T_m & \text{for } T_m c_2 < h_2 < T_m\, c_2 + L \end{cases} \qquad (2.22).$$

2.4.4　Wall heat transfer

In many practical applications, as in a furnace for example, the walls are either water-cooled or sustained at a constant temperature, T_w.

To calculate the wall heat-transfer rate for turbulent flow, the Chilton-Colburn form of the Reynolds analogy is used (Gunton et al (1983); Cebeci and Bradshaw (1984)), in which the Stanton number, St, is related to the friction coefficient, C_f, as follows:

$$St = C_f \; Pr^{-2/3} \qquad\qquad (2.23);$$

where Pr is the Prandtl number and the friction coefficient, C_f, is related to the wall shear-stress, τ_w.

For points near the wall the generation of turbulence energy is balanced by the dissipation and it can be assumed to be in local equilibrium; therefore we can write (Ng and Spalding (1972)):

$$\tau_w = 0.09 \; k\rho \qquad\qquad (2.24).$$

The friction coefficient, C_f, can now be calculated using the 'wall-friction' approach, (Spalding (1982(a)); Launder and Spalding (1974); Gupta and Lilley (1985)), and is given in terms of the P_j-function, where now:

$$C_f = \frac{(\frac{\tau}{u^2\rho})}{(1+P_j \; \sqrt{\frac{\tau}{u^2\rho}})} \qquad\qquad (2.25);$$

and

$$P_j = 9.24 \; (\frac{\sigma_\phi}{\sigma_{t,\phi}} - 1) \; (\frac{\sigma_\phi}{\sigma_{t,\phi}})^{-1/4} \qquad\qquad (2.26);$$

where σ_ϕ and $\sigma_{t,\phi}$ denote the laminar and turbulent values of the Prandtl/Schmidt number appropriate to the transport of ϕ (ie. the enthalpy in this case), and u is the velocity component parallel to the wall.

The heat transfer rate per unit area at the wall, $\dot{q}_w''$, is then deduced from:

$$\dot{q}_w'' = St \; \rho|u| \; (h_p - h_w) \qquad (2.27);$$

where h_p is the enthalpy at the grid node near the wall and h_w is the enthalpy corresponding to the prescribed wall temperature; T_w.

2.4.5   Turbulence model

Turbulence motion is very important in most practical simulations, including the present one.   Ideally, to predict a turbulent flow, the exact time-dependent Navier-Stokes equations should be solved.   In practice this is not feasible because turbulence is fully three-dimensional with some of the important processes taking place in very small time- and space-scales.   The numerical solution of the exact time-dependent equations would require prohibitive computational time and storage (Spalding (1983(a)) and (b)).

Fortunately, we are usually interested in only time-averaged effects and therefore can approximate these equations by statistical correlations in terms of quantities that can be measured or deduced.

Many turbulence models have been proposed and their validity varies

according to their application (Launder and Spalding (1974)). A survey and classification of turbulence models (zero-, one-, two-equation, stress equation models, large eddy simulations, etc), can be found in Markatos (1986); Carvalho (1983); Lumley (1983); and Rodi (1980).

In the present work, the two-equation $k-\epsilon$ (energy-dissipation rate) turbulence model is used for the gaseous phase. The $k-\epsilon$ model has been tested in inert as well as in reacting flows (Khalil (1981, 1982); Markatos (1986); and Bradshaw et al (1981)). It was the obvious choice because of its simplicity, economy and because its abilities and limitations are known.

2.5   The Solution Procedure

The solution of the above conservation equations has been obtained by application of the finite-domain solution procedure embodied in the general purpose PHOENICS computer program (Spalding (1981); Gunton et al (1983)).

The finite-domain equations are solved using the SIMPLEST and IPSA algorithms (Spalding (1979(a),1980(b)). The integration proceeds along the axis of the off-gas duct from bottom to the top and it is repeated, sweeping the domain until convergence is achieved.

2.5.1   The finite-difference grid

For the finite-domain equations a conventional staggered grid that overlays the physical domain is used. For a general, three-dimensional grid, each cell (control-volume) has 6 faces, e, w, s, n, h and ℓ, and 6 neighbours E, W, S, N, H and L, as shown in Figure 2.1.

Cell-centre points P are defined within each cell and are located at its geometrical centre. Its neighbour-nodal points are referred to as points N, S, E, W, H and L (north, south, east, west, high and low). The lines joining P to its neighbours cut the cell-faces at points n, s, e, w, h and ℓ. The velocities are stored at the centre of the cell faces, to which they are normal (denoted by (→)), ie. at points n, s, e, w, h and ℓ. All other variables φ are stored at the centres of the cell themselves, see Figure 2.1.

The advantages of the staggered arrangement for the location of the velocities are:

\#   It places the velocities between the pressures which drive them. This is an advantage for the solution procedure adopted for the continuity equation.

\#   These velocities are directly available for the calculation of the convective fluxes across the boundaries of the node containing control volumes.

The only disadvantage is that the control volumes used to calculate velocities are displaced from those used to calculate the other variables and therefore need special consideration.

2.5.2   The finite-difference equations

The finite-diference equivalent of the differential equation (2.9) for a general variable φ, is obtained by integration over the entire volume of the domain. Thus assuming steady-state:

$$\iiint_V \operatorname{div}[r\rho \bar{v}\phi - r\Gamma_\phi \operatorname{grad}\phi]\,dV = \iiint_V S_\phi\,dV \qquad (2.28);$$

where V denotes volume of the integration domain.

Application of the Gauss divergence theorem on (2.28), yields:

$$\iint\limits_A (r\rho\bar{v}\phi - r\Gamma_\phi \,\text{grad}\phi).\,d\underline{A} = \iiint\limits_V S_\phi \,dV \qquad (2.29);$$

where A denotes surface area.

For the source term, ϕ is assumed uniform throughout the control cell and therefore:

$$\iiint\limits_V S_\phi \,dV \simeq VS_\phi \qquad (2.30).$$

In the surface integral of (2.29), variables are assumed constant over each cell face and thus:

$$\iint\limits_A (r\rho\bar{v}\phi - r\Gamma_\phi \,\text{grad}\phi).\,d\underline{A} = \sum_{\substack{e,w,n,s, \\ h,\ell}} (r\rho\bar{v}\phi - r\Gamma_\phi \,\text{grad}\phi).\,\underline{A}$$

$$(2.31).$$

In the RHS of (2.31) the partial derivatives contained in the term $r\Gamma_\phi \text{grad}\phi.\underline{A}$ is represented from a piecewise-linear profile for ϕ (Patankar (1980)). For example for the s-face we have:

$$\left(r\Gamma_\phi \frac{\partial\phi}{\partial s}\right)_s A_s = (r\Gamma_\phi)_s \left(\frac{\phi_p - \phi_s}{(dz)_s}\right) A_s \qquad (2.32);$$

where ϕ_p is the value of ϕ at the nodal point P, ϕ_s is the unknown value of ϕ at the face s.

It is convenient to introduce F_i and D_i where:

$$F_i = r\rho v_i A_i \qquad\qquad D_i = \frac{(r\Gamma_\phi A_i)_i}{\delta_i} \qquad\qquad (2.33);$$

where i stands for the cell-faces s, n, ℓ, h, w, e and δ_i for the distances δx, δy, δx at the different cell faces i.   Both F and D have the same dimensions, with F indicating the strength of the convection and D is the diffusion conductance.   D always remains positive and F can take both positive and negative values, depending on the direction of the flow (Patankar (1980)).

The discretised equation can now be written as:

$$\sum_{i=e,n,h} (\Gamma_i \phi_i) - \sum_{i=w,s,\ell} (\Gamma_i \phi_i) + \sum_{i=w,s,\ell} D_i (\phi_p - \phi_i)$$

$$- \sum_{i=e,n,h} D_i (\phi_i - \phi_p) = VS_\phi \qquad\qquad (2.34);$$

where ϕ_p, ϕ_i, Γ_i and D_i as above.

The values of the ϕ_i at the control volume faces are obtained by an upwind-difference scheme, which states that the value of ϕ_i at an interface i, is equal to the value of ϕ at the grid point on the upwind side of the face.   For example:

$$\left.\begin{array}{ll} \phi_e = \phi_p & \text{if } F_e > 0 \\[2mm] \phi_e = \phi_E & \text{if } F_e < 0 \end{array}\right\} \qquad\qquad (2.35).$$

The values of the other ϕ_i can be defined similarly.

Equation (2.30) for the source-term at a nodal point P is expressed in a 'linearised' form (Patankar (1980)), such as:

$$(S_\phi)_p = S_c + S_p \phi_p \qquad (2.36);$$

where:

$$S_c = (S_\phi)^* - \left(\frac{\partial S}{\partial \phi}\right)^* \phi_p^* \quad \text{and} \quad S_p = \left(\frac{\partial S}{\partial \phi}\right)^*;$$

with the '*' values denoting the guess value or the previous-iteration value of ϕ_p.

Substitution of the linearised form (2.36) of the source term and the upwind-difference forms of ϕ_i into equation (2.34) we now obtain:

$$(A_p - S_p V)\phi_p = \left(\sum_{j=E,W,S,N,H,L} A_j \phi_j\right) + S_c V \qquad (2.37);$$

where:

$$\left.\begin{array}{l} A_j = D_j + [[-F_j, 0]] \text{ for } j=E,N,H \\ A_j = D_j + [[F_j, 0]] \text{ for } j=W,S,L \end{array}\right\} \qquad (2.38);$$

where the symbol [[A,B]] denotes the greater of A and B, j are the neighbour nodal points of P, ie. W, E, S, N, H and L and V is the cell volume.

Also the A_p coefficient expresses the combined effects of convection, and diffusion, linking the property at the point P with its E, W, S, N, H and L nodal neighbours, and is given by:

$$A_p = \sum_{i=E,W,S,N,H,L} A_i \qquad\qquad (2.39);$$

in the absence of sources and boundary conditions.

To obtain the volume fractions $(r)_i$ and densities $(\rho)_i$, used in equations (2.33), at the cell faces i=e,w,n,s,h and ℓ, linear interpolation is employed between the nodal points j=E,W,N,S,H and L, one either side of these i-faces. The values of Γ_i coefficients at the i-faces are obtained as the harmonic mean of the nodal points j, on either side of these i-faces (Patankar (1980)). For the velocities no interpolation is needed since they are stored at the cell faces.

2.5.3 Solving the sets of finite-domain equations

The means by which PHOENICS solves these coupled system of finite-difference equations is complex and a full description of algorithms would be extremely lengthy. Details are given in Patankar and Spalding (1972), Patankar (1980), Spalding (1980(b)),(1981) and Markatos and Spalding (1983). However, in order to use the package effectively the user has control over a number of numerical parameters which greatly influence the convergence properties of the algorithm. These will now be described.

The solution of the sets of equations for all ϕ are obtained by an iterative scheme, which is called 'repeated z-direction sweeps' (Spalding (1981)), through the integration domain. The whole set of cells is regarded as consisting of one-cell-thick 'slabs', extending in the x- and y-directions, and piled one on top of the other in the z-direction. A single 'sweep' therefore starts with attention being paid to the bottom slab

of cells and solves for all variable φ, with the values of φ at the next higher slab regarded as known. Attention is then focussed on the next slab up with the φ-value being adjusted by reference to those in the slabs both above and below. The procedure continues until the top-most slab is reached. The user specifies the number of sweeps to be performed in a run.

Velocities u and v are solved by a Jacobi point-by-point procedure and this means that any φp is updated for all nodes of the grid form:

$$\phi_p = \frac{\sum\limits_{i} A_i \, \phi_i + S_c}{A_p - S_p} \qquad (2.40).$$

At the next sweep, the φ's on the RHS have the values created in the previous one.

The user has a choice of two ways in which the pressure values are updated. Either the values are updated at each slab with the other φ flow variables or the pressure values are updated at the end of each complete sweep (called a 'whole-field solution').

Convergence is monitored by calculating the change in each flow variable value between iterations. Printouts of variable values can be obtained at special monitor points defined by the user. Residuals in mass conservations can also be printed.

DTFALS(φ) is a 'false-time step', used to slow down the variation of any solved-for variable φ, other than pressure. It is not always necessary to use these values, but if divergence occurs without them, the user can

slow down the variation by employing them. DTFALS operates by adding to the balance equation for variable ϕ, the term: $(\phi-\phi^*) r\rho . vol/\delta t_f$ where r is the volume fraction of the phase in question, ρ is its density, vol stands for cell volume, and δt_f is the chosen value of false timestep. The above term is added to both sides of the equation, (using new and old values) so it makes no difference to the ultimate solution.

2.5.4 Boundary conditions – sources/sinks

All boundary conditions are inserted in PHOENICS as source or sinks of one or more variables. These are represented by linear expressions of the form:

$$S_\phi = (C_\phi + [[S_m]]) \, (V_\phi - \phi_p) \qquad\qquad (2.41);$$

where the mass source S_m is given by:

$$S_m = C_m \, (V_m - \rho_p) \qquad\qquad (2.42).$$

The symbol $[[\ ]]$ refers to the use of the upwind practice, the subscript P refers to the centre of the finite-domain cell in question and C_ϕ, V_ϕ are referred to as the 'coefficient' and the 'value' of the variable ϕ.

The finite-domain equation for a boundary cell is the same as Equation (2.40), where one of the neighbours is missing (the one corresponding to the boundary cell face) and where the linearised source $S_c + S_p \phi_p$ contains the additional source/sink due to the boundary conditions. Thus the equation becomes:

$$\phi_p = \frac{\sum_{\substack{i \ (\text{except boundary})}} A_i \phi_i + S_c + C_\phi S_\phi}{(A_p - S_p - C_\phi)} \qquad (2.43).$$

2.5.5 The steady-state solution sequence in PHOENICS

The solution sequence for the complete model discussed above is summarised in the following flow chart, Figure 2.2.

```
                        ┌─────────┐
                        │  START  │
                        └─────────┘
                             │
                             ▼
                     ┌──────────────────┐
                     │ Read       Data  │
                     └──────────────────┘
                             │
                             ▼
                     ┌──────────────────┐
         ┌──────────▶│  Start of sweep  │
         │           └──────────────────┘
         │                   │
         │                   ▼
         │           ┌──────────────────────┐
         │           │ Start of slab solution│◀──────┐
         │           └──────────────────────┘        │
         │                   │                        │
         │                   ▼                        │
         │           ┌──────────────────────┐        │
         │           │ Correct p and velocities│      │
         │           └──────────────────────┘        │
         │                   │                        │
         │                   ▼                        │
         │   ┌──────────────────────────────────┐    │
         │   │ Slab solution for R's,c's, h's, k-ε│   │
         │   │ velocities and radiation fluxes    │   │
         │   └──────────────────────────────────┘    │
         │                   │                        │
         │                   ▼                        │
         │   ┌──────────────────────────────────┐    │
         │   │ Calculate continuity errors and store│ │
         │   └──────────────────────────────────┘    │
         │                   │                        │
   ┌──────────────┐         ▼              ┌─────────────┐
   │ Repeat until │  ┌──────────────┐      │ Repeat for  │
   │ ISWEEP=LSWEEP│  │ End of slab  │─────▶│ IZ=1,NZ     │
   │ then STOP    │  └──────────────┘      └─────────────┘
   └──────────────┘         │
         ▲                  ▼
         │          ┌──────────────────────┐
         │          │ Solve p' for whole field│
         │          └──────────────────────┘
         │                  │
         │                  ▼
         │          ┌──────────────┐
         └──────────│ End of sweep │
                    └──────────────┘
```
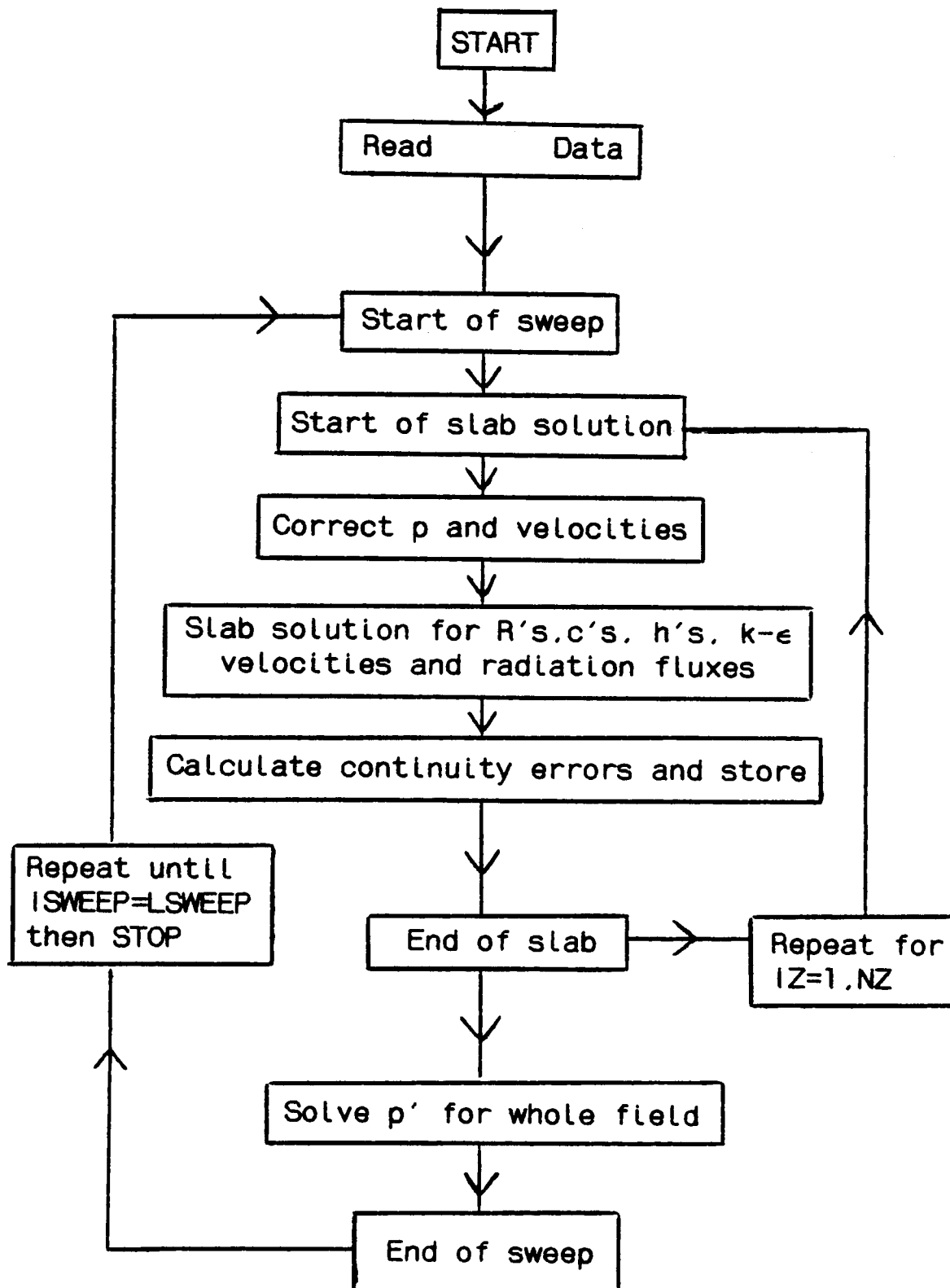
FIGURE 2.2: SOLUTION SEQUENCE FLOW CHART FLOW

2.5.6   Short description of PHOENICS

The computer package PHOENICS is a general computer code system capable of simulating a large variety of fluid flow, heat transfer and chemical processes.   It is divided into three main parts, each with its own individual function to perform: EARTH, SATELLITE and GROUND. EARTH is the general equation solver and it is supplied with data from the SATELLITE in a once-for-all manner.   The SATELLITE is used for setting up the problem, input data such as domain dimensions, finite-difference grid spacing, initial values and boundary conditions in linear form only. The GROUND routine is, in contrast, in constant communication with EARTH.   Therefore, it is generally used to provide EARTH with any additional information, such as fluid property functions, non-linear boundary conditions, reaction rates, solution of radiation fluxes and others not available in EARTH.   In short, it is used to provide EARTH with information that has to be updated as the calculation proceeds. GROUND is the means by which an advanced user can greatly extend the capabilities of PHOENICS.
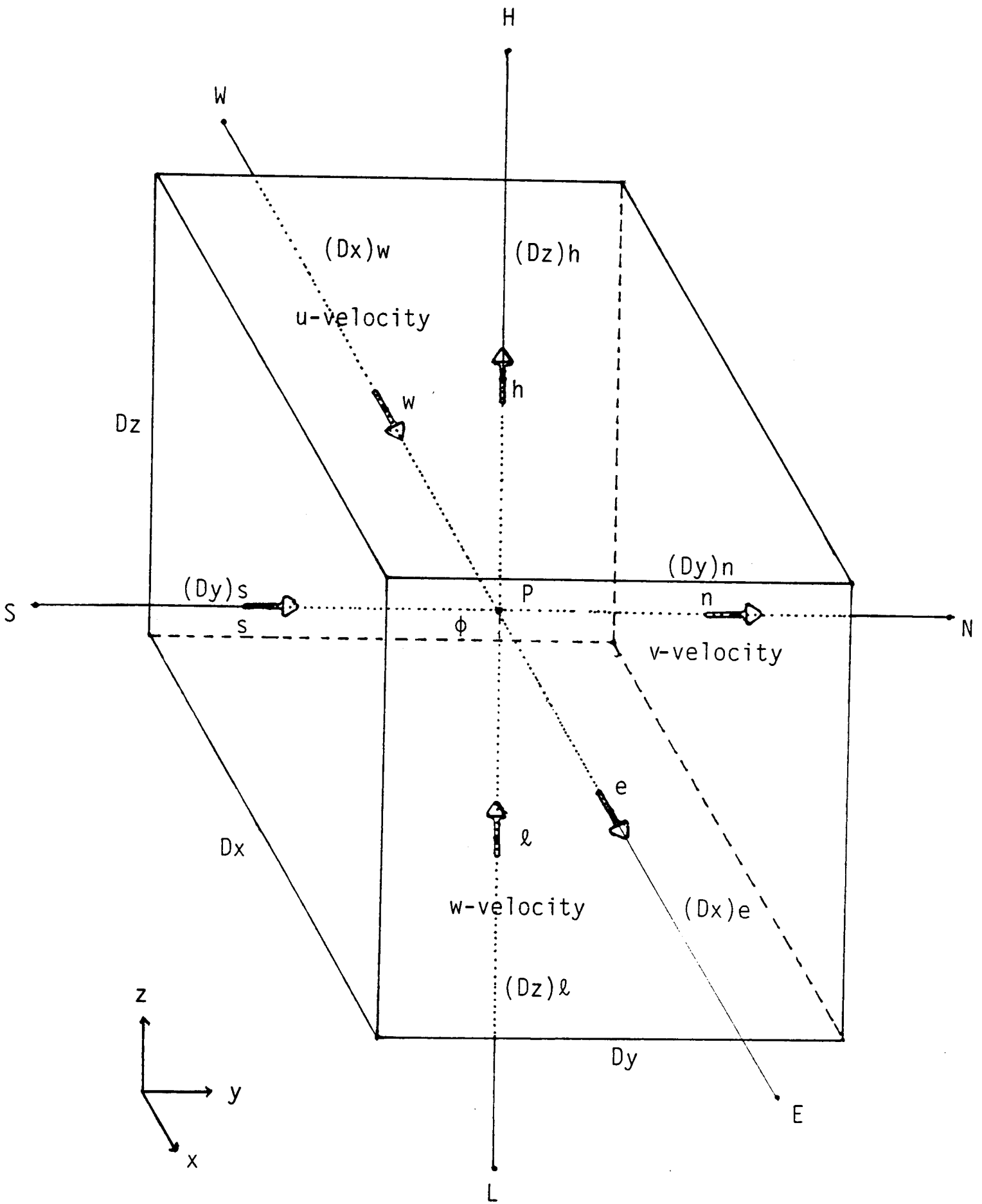
FIGURE 2.1: THE STAGGERED GRID

CHAPTER 3 - MODELLING OF RADIANT HEAT TRANSFER

3.1   Introduction

In mathematical modelling of flow and reaction processes in furnaces and combustors, it is most essential to represent adequately the characteristics of heat and mass transfer. The model should be able to determine, among other things, the actual heat flux distribution to the furnace walls, and to predict the local temperature distribution of the participating phases. Since chemical reactions involved in the combustion process are strongly temperature dependent, accurate calculation of the local temperatures is needed if the evaluation of the reaction rates and species concentrations are to be meaningful.

In real furnaces and combustors of industrial size, two main modes of heat transfer exist, namely radiation and convection, with the former being often the dominant one. The problem of determining the radiation heat transfer at a point located either on a wall or within the gas in a furnace is a very complex one, especially if there is more than one phase present (eg. gases and particles).

Consider a small volume of gas and particles within the furnace. Energy will be emitted by this volume. The emission depends on the gas composition, the particle sizes and the local temperature, and it is not difficult to calculate. The amount of energy arriving at this volume is, however, difficult to determine. The reason is that the intensity of radiation at a given small volume is influenced by the geometry and the properties of the absorbing and scattering medium filling the furnace.

When the mean path of radiation is very large, and the wall temperature

is uniform, it is possible to express the influence of radiative heat transfer by way of sinks, proportional to the fourth power of the local temperatures. The calculation of these sinks is based on the assumption that there is a negligible amount of absorption and scattering of radiation within the medium. Their effect on the temperature distribution through the medium is then deducted by direct solution of the regular differential equations for the stagnation enthalpy.

Another simple way of accounting for radiation when the mean-free-path of radiation is small compared with the furnace dimensions, is the 'conduction approximation', in which the effect of radiation is accounted for via an additional thermal conductivity coefficient, proportional to the third power of the local temperature.

Unfortunately, in most practical cases, the value of the mean-free-path of radiation varies with position within the furnace and is neither large nor small enough for either of the above methods to be used.

3.1.1. Equation of radiant energy transfer

The basis of all commonly used methods of solving the radiation problems, is the equations of radiant energy transfer. It is derived by writing a balance equation for monochromatic radiant energy, passing in a specified direction, through a small volume of an emitting-absorbing-scattering medium. For steady-state conditions, and for coherent isotropic scattering, the equation is expressed (see for example, Khalil (1982)) as:

$$(\Omega.\nabla) \ I_\lambda(r,\Omega) = - (K_{a,\lambda} + K_{s,\lambda}) \ I_\lambda(r,\Omega) + K_{a,\lambda} \ I_{b,\lambda}(r)$$

$$+ \frac{K_{s,\lambda}}{4\pi} \int_{\Omega=4\pi} I_\lambda (r,\Omega) \, d\Omega \qquad\qquad (3.1);$$

where: $I_\lambda (r,\Omega)$ is the radiation intensity; which is a function of the wavelength, position and direction; $I_{b,\lambda}$ is the monochromatic intensity of black body radiation at the temperature of the medium; Ω is the solid angle; and $K_{a,\lambda}$ and $K_{s,\lambda}$ are the spectral absorption and scattering coefficients of the medium, respectively, for a wavelength λ.

3.2 Existing Methods for Radiation Heat Transfer

The difficulty of solving equation (3.1) has given rise to various approaches and solution procedures. These approaches are termed to be either of the differential type or the integral one. For a sufficiently fine discretisation they all yield accurate solutions and to this extent they are all satisfactory. However, for real engineering combustors, there are some additional requirements to be satisfied. The two most important of these are the geometric flexibility and computing economy of the radiation solution calculations.

All existing radiation models are normally divided into three groups, commonly referred to as: 'zone method', 'Monte Carlo method' and 'flux method'.

In the zone method (Hottel and Cohen (1958); Hottel and Sarofim (1967) and Smith et al (1985)), the walls and the interior of the enclosure are divided into zones (surfaces and volumes) of finite sizes; these are sufficiently small for the local temperature and other physical properties to be considered uniform within each of the zones. The radiative interchange in the enclosure, is first obtained by determining radiative

exchange factors for each zone pair combination in the furnace, taking account of attenuation by intervening gases, and including the effects of reflection within the enclosure. These exchange factors, the 'total exchange areas', are the constants of proportionality in equations relating the exchange of radiative energy to the difference in the fourth power and temperature of each respective zone pair, and give a solution for the radiation exchange within the furnace.

The evaluation of the total exchange areas forms an essential part of the zone method of analysis. They are constructed according to the laws of radiation geometry, taking account of the physical-chemical properties (emissivity and absorptivity) of the radiation media, and describe the way in which radiation is exchanged between the various combinations of emitting-absorbing volumes and emitting-absorbing-reflecting surfaces. For simple geometries these volumes have been tabulated (see Hottel and Sarofin (1967) and Hottel (1975)). This technique gives the complete solution of grey gas system, ie one in which the gas absorption coefficient, K_g, is independent of the gas temperature and the wavelength of the incident radiation. The model can also be applied to real gases, such as water vapour and carbon dioxide, which do not behave as grey gases, because of the discrete nature of their absorption bounds. This is done, representing the emissivity of the real grey gas as a weighted sum of the emissivities of a number of grey gases, as given by (see Beer (1974) and Smith et al (1985)):

$$\epsilon_g = \sum_n a_{g,n} \left(1 - e^{-K_n n^{pL}}\right) \qquad (3.2);$$

where: $a_{g,n}$ is the fractional amount of energy in the spectral region

where grey gas of absorption coefficient Kn exists; L is the path length for radiation; p is the partial pressure of the absorbing gas; and n is the number of gases. The exchange between each zone pair is then calculated using the integrated form of the transport equation (see Shah (1979)):

$$\frac{dI}{ds} = - \underset{\underset{\text{absorption}}{\uparrow}}{KI} + \underset{\underset{\text{emission}}{\uparrow}}{\frac{K \sigma T^4}{\pi}} \qquad (3.3);$$

where: I is the intensity of radiant energy; K is the absorption coefficient; and σ is the Stefan-Boltzman constant.

This method has been extensively and successfully used to predict radiant heat transfer in furnaces (Hottel (1975) and Steward et al (1974)). However, the zone method is based on the integral form of the radiation transport equation and for this reason does not couple easily to the simultaneous solution of the differential equations for flow and chemical reactions. Furthermore, it is too demanding in both computer time and storage capacity to be incorporated economically into a complete prediction code for general three-dimensional problems (see Khalil (1982)).

The Monte Carlo method (see Xu (1981) and Wall et al (1982)), uses a random number generator to establish directions and the process of radiative emission, absorption, scattering and reflections are expressed as probabilistic events. Representative rays, typically no more than 9 for reasons of economy, are fired in random directions. The required quantities are then evaluated as each ray crosses the enclosure. A

-43-

high degree of accuracy can be achieved provided we take enough rays, but these will always be a statistical error in the generation of numbers and a significant amount of computer time is needed.

The flux methods (see Siddall (1973) and Beer (1974)) provide an easier alternative to the calculation of the radiant heat transfer, without too great a loss of accuracy in many cases. The flux methods employ diffusion-type differential equations for radiation-flux parameters and are therefore compatible with the flow equations and associated solution procedures.

The basis of most flux methods analysis is a balance for the flux of radiant energy in a specified direction through an elementary volume, derived on the assumption that the material within the element is optically grey (greater accuracy can be achieved by relaxing this restriction). The main physical generalisation associated with the flux methods is the division of the solid angle surrounding a point into a number (2N) of solid angles, in which the intensity is assumed to be a specific function. The 2N simultaneous differential equations, thus derived, can be solved with relative ease by standard finite-difference techniques.

Very simplified assumptions for the intensity distribution lead to methods for one-dimensional radiation transfer of the Schuster-Hamaker, Milne-Eddington etc types used in astrophysics (see Siddall (1973) and Truelove (1976a).

In the approximation by Hamakar (1947), for a one-dimensional case in light-scattering material, the following flux distributions are used:

$$\frac{dI}{dx} = -(a+s)I + sJ + aE \qquad \text{(a)}$$

$$\frac{dJ}{dx} = (a+s)J - sI - aE \qquad \text{(b)}$$

(3.4);

where: I and J are fluxes in the positive and negative x-direction and a and s are the absorptivity and scattering coefficients, respectively.

Lockwood and Spalding (1971) have extended the above model to axisymmetric geometries, thus accounting for the radiation fluxes in both axial and radial directions, in an absorbing and scattering medium. They also assumed that the angular distribution of both incident and scattered radiation is isotropic.

The model was further extended to cover three-dimensional geometries while preserving the nature of the ordinary differential equations (Patankar and Spalding (1972) and Spalding (1980(a)) and it is known as the 'six-flux' model. Several applications of this model in two- and three-dimensional combustion chambers and furnaces (Gosman and Lockwood (1973); Khalil et al (1975); Whitacre et al (1975); and Khalil (1979)) and in fires in enclosures (Markatos and Pericleous (1984)) have been reported, often with satisfactory results.

De Marco and Lockwood (1975) and Lockwood and Shah (1978), developed and evaluated a variant of the above flux model, based originally on a six-term Taylor series approximation for the angular distribution of intensity in a grey scattering and absorbing medium. The model also combines features of the spherical-harmonics and discrete-ordinate methods. It was tested for a number of cases, but it

has the disadvantage that it is not easily adapted to new-coordinate systems. Also by increasing the number of terms retained in the Taylor series to improve accuracy, it has proved to be expensive with respect to computer time.

Shah (1979) and Lockwood and Shah (1980) discuss the merits of the zone, Monte-Carlo and flux methods, and propose a new 'discrete transfer' model which is essentially a mixture of all three methods. It is based on solving for representatively directed beams of radiation within the enclosure between the known wall boundary conditions and on the subsequent computing of the radiation sources, which arise within the finite-difference control volumes of the flow domain, due to the passage of the beams. This method presents the advantage of being easily adaptable to complex geometries and yielding solutions of good accuracy (Carvalho (1983, 1985); Jeng et al (1984); and Boyd and Kent (1986)). However, computer time economy is its critical point especially in the case of complex geometries, where fine discretisation is needed, coupled with careful shaping of the control volumes and positioning of the rays.

Other methods are the Spherical Harmonics model, the discrete ordinary model and others, but these are not widely used. More details may be found in Khalil (1982).

In parallel with the development of the above models and increased emphasis on burning fuel more efficiently, researchers started paying attention to the radiative properties of the emitting species (Truelove (1976b)). The principal radiating species in conventional fuel flames are CO_2 and H_2O and suspended particulates. Studies were performed

on the spectral distribution of the radiative transfer for various compositions of gases and particle sizes in simple geometries (Beer et al (1973), Karman et al (1984), Steward et al (1974) and Grosshandler et al (1985)), and although the results were encouraging, the models were too demanding in both computer time and storage capacity. Other 'simple' models, (Truelove (1984)), combined the Mie theory of electromagnetic scattering with optical properties predicted by the classical electron theory of metals, to predict radiant heat transfer through the cover-gas in a sodium-cooled fast reactor.

The present work is based on the single-phase six-flux radiation model of Spalding (1980(a)), which was developed to account for two-phase problems (ie radiating gases and particles). Both models are described in detail below, in polar coordinates.

3.3   The Single-Phase Six-Flux Model in Polars

Patankar and Spalding (1972) and Spalding (1980(a)) developed a radiation model for single-phase applications by extending and modelling the original ideas of Hamaker (1947). The model involves the solution of three second order differential equations, for the 'six-fluxes' of radiation, in a semi-transparent medium. In this model attention is focussed on the quantities, I+J, K+L, M+N, (Figure 3.1), where I and J are, respectively, the forward and backward radiation fluxes in the radial direction, and K and L, and M and N, are the corresponding fluxes in the axial z-direction and θ-direction in units of W/m^2.

3.3.1   The differential equations

In polar coordinate, the single-phase, six-flux model is:

$$\frac{1}{r}\frac{d}{dr}(rI) = -(a+s)I + aE + \frac{s}{6}(I+J+K+L+M+N) + J/r \qquad (a)$$

$$\frac{1}{r}\frac{d}{dr}(rJ) = (a+s)J - aE - \frac{s}{6}(I+J+K+L+M+N) + J/r \qquad (b)$$

$$\frac{dK}{dz} = -(a+s)K + aE + \frac{s}{6}(I+J+K+L+M+N) \qquad (c)$$

$$\frac{dL}{dz} = (a+s)L - aE - \frac{s}{6}(I+J+K+L+M+N) \qquad (d)$$

$$\frac{1}{r}\frac{dM}{d\theta} = -(a+s)M + aE + \frac{s}{6}(I+J+K+L+M+N) \qquad (e)$$

$$\frac{1}{r}\frac{dN}{d\theta} = (a+s)N - aE - \frac{s}{6}(I+J+K+L+M+N) \qquad (f)$$

$$(3.5);$$

where:

r   = radial distance (m);

z   = axial distance (m);

θ = angular distance (rad);

a   = absorptivity coefficient (m^{-1});

s   = scattering coefficient (m^{-1});

E   = σT^4: black body emissive power (W/m^2); and

σ = Stefan-Boltzmann constant $(W/m^2/K^4)$.

Algebraic manipulation of equations (3.5) gives the second-order differential equations, which are:

$$\frac{1}{r}\frac{d}{dr}\left[\frac{r}{a+s+\frac{1}{r}}\frac{d}{dr}(I+J)\right] = -2Ea + (a + \frac{2s}{3})(I+J) - \frac{s}{3}(K+L+M+N)$$

$$(a)$$

$$\frac{d}{dz}\left[\frac{1}{a+s}\frac{d}{dz}(K+L)\right] = -2Ea + (a + \frac{2s}{3})(K+L) - \frac{s}{3}(I+J+M+N)$$

(b)

$$\frac{1}{r}\frac{d}{d\theta}\left[\frac{1}{(a+s)r}\frac{d}{d\theta}\right](M+N) = -2Ea + (a + \frac{2s}{3})(M+N) - \frac{s}{3}(I+J+K+L)$$

(c)

(3.6).

The above equations (3.5) and (3.6) can only be applied to one-phase problems, eg only gases or only particles with small modifications; and the absorption coefficient, a, in some early work by Gosman and Lockwood (1972) was taken to be:

$$a = 0.21 \, m_{fu} + 0.12 \, m_{pr}$$

(3.7);

to account for the emitting properties of the gas-fuel m_{fu}, and the gas-product m_{pr} in a reacting system.

3.4   The Two-Phase Six-Flux Model in Polars

The present contribution is concerned with the prediction of the radiant heat transfer in two-phase flows of gases and particles in polar coordinates, with direct industrial applications in the metallurgical industry.   The new two-phase model developed in this work attempts to overcome the limitations and problems of the single-phase model in predicting accurately the radiant heat transfer distribution inside an industrial system.

3.4.1   Assumptions

The following formulation is based on the assumptions that:

(i)   Gaseous radiation is a volumetric phenomenon.

-49-

(ii)   Particle radiation is a surface phenomenon.

(iii)   No radiation is transferred by scattering of the gases; this is not a limitation of the model, but a justified simplification for the present application, described below where scattering from the gases is negligible.

(iv)   The surfaces of the particles are assumed to be diffuse. In other words, diffuse reflection occurs if, regardless of the direction of the incident radiation, the intensity of the reflected radiation is independent of the reflection angle. Thus reflected radiation is of uniform intensity in all directions.

3.4.2   **Formulation of the equations**

Define:

a_p particles absorptivity coefficient (dimensionless);

s_p particles scattering coefficient (dimensionless);

a_g in-depth gas-absorptivity coefficient (m^{-1});

E_p black-body emissive power for particles (W/m^2);

E_g black-body emissive power for gases (W/m^2).

Consider N number of particles in a volume, V, and let R_p be the particle volume-fraction present in V.   Then:

$$R_p = N*(particle\ volume)/V \qquad (3.8).$$

Assuming that the particles are spherical and of the same size, say radius r, the number of particles, N, in volume V, is given by:

$$N = \frac{3\ R_p\ V}{4\ \pi\ r^3} \qquad (3.9).$$

It follows that the total surface area, A_t, of particles in volume V, is:

$$A_t = (4\pi r^2)N \qquad (3.10);$$

or using (3.9):

$$A_t = \frac{3\ R_p\ V}{r} \qquad (3.11).$$

In reality, radiation is distributed through all 4π radius of solid angle, but is resolved into the six-coordinate directions, shown in Figure 3.1, in the present model. Therefore, considering a unit volume containing a number of radiating particles, the particle radiation from their surface is divided equally amoung the six-directions of Figure 3.1.

In order to comply with Spalding's single-phase six-flux model the dimensionless particle absorption, and scattering coefficients, a_p and s_p, respectively, must be converted to 'in-depth' coefficients having units of m^{-1}. This leads to the definition of the 'effective in-depth absorption coefficient', a_p', (m^{-1}), and 'effective in-depth scattering coefficient', s_p', (m^{-1}) given by:

$$a_p' = a_p\ A_p \qquad (3.12);$$

and

$$s_p' = s_p\ A_p \qquad (3.13);$$

where:

$$A_p = \frac{A_t}{6} \qquad (3.14);$$

where V is now taken to be unity and A_p is the total effective surface of particles per unit volume for each of the six-directions.

The above modifications are incorporated into the new, two-phase, six-flux model described below.

3.4.3 The differential equations

The six first-order differential equations for the radiation fluxes, I, J, K, L, M and N, and in the presence of two-phase, using the notation defined above are given by:

$$\frac{1}{r}\frac{d}{dr}(rI) = a_gE_g + a_pA_pE_p - [a_g + (a_p + s_p)A_p]I + \frac{s_p}{6}A_p\ (I+J+K+L+M+N) + \frac{J}{r}$$

$$(a)$$

$$\frac{1}{r}\frac{d}{dr}(rJ) = -a_gE_g - a_pA_pE_p - [a_g + (a_p + s_p)A_p]J - \frac{s_p}{6}A_p\ (I+J+K+L+M+N) + \frac{J}{r}$$

$$(b)$$

$$\frac{dK}{dz} = a_gE_g + a_pA_pE_p - [a_g + (a_p + s_p)A_p]K + \frac{s_p}{6}A_p\ (I+J+K+L+M+N)$$

$$(c)$$

$$\frac{dL}{dz} = -a_gE_g - a_pA_pE_p + [a_g + (a_p + s_p)A_p]L + \frac{s_p}{6}A_p\ (I+J+K+L+M+N)$$

$$(d)$$

$$\frac{1}{r}\frac{dM}{d\theta} = a_gE_g + a_pA_pE_p - [a_g + (a_p + s_p)A_p]M + \frac{s_p}{6}A_p\ (I+J+K+L+M+N)$$

$$(e)$$

$$\frac{1}{r}\frac{dN}{d\theta} = -a_gE_g - a_pA_pE_p + [a_g + (a_p + s_p)A_p]N + \frac{s_p}{6}A_p\ (I+J+K+L+M+N)$$

$$(f)$$

$$(3.15).$$

The result of further manipulation of equations (3.15) gives the second-order equations:

$$\frac{1}{r}\frac{d}{dr}\left[\left(\frac{r}{a_g+(a_p+s_p)A_p+\frac{1}{r}}\right)\frac{d}{dr}(I+J)\right] = -2a_pA_pE_p - 2a_gE_g$$

$$- \frac{S_p}{3}A_p\ (K+L+M+N) + (a_pA_p+a_g + \frac{2s_pA_p}{3})\ (I+J) \qquad\qquad (a)$$

$$\frac{d}{dz}\left[\left(\frac{1}{a_g+(a_p+s_p)A_p}\right)\frac{d}{dz}(K+L)\right] = - \frac{S_p}{3}\ (I+J+M+N)A_p$$

$$+ (a_pA_p+a_g + \frac{2s_pA_p}{3})\ (K+L) - 2a_pA_pE_p - 2a_gE_g \qquad\qquad (b)$$

$$\frac{1}{r}\frac{d}{d\theta}\left[\left(\frac{1}{(a_g+(a_p+s_p)A_p)r}\right)\frac{d}{d\theta}(M+N)\right] = - 2a_pA_pE_p - 2a_gE_g$$

$$- \frac{S_p}{3}A_p\ (I+J+K+L) + (a_pA_p+a_g + \frac{2s_pA_p}{3})\ (M+N) \qquad\qquad (c)$$

$$(3.16).$$

The finite-difference equivalent of equations (3.16) are easy to derive and they are given in Section 3.5.

The variables solved for in the developed program are the combined radiation fluxes RX, RY and RZ of both phases, given by:

$$
\left.
\begin{array}{lll}
RX=M+N & (a) & \theta\text{-combined flux} \\
RY=I+J & (b) & \text{radial-combined flux} \\
RZ=K+L & (c) & \text{axial-combined flux}
\end{array}
\right\} \qquad (3.17).
$$

3.4.4   Further notes on the six-flux model

The six-flux model, as well as the four- and two-flux models, is applicable only when the medium (eg gases, particles, etc) is not transparent.   In the absence of scattering and absorption, radiation will be transmitted, say from z_1 to z_2 etc, but not from z_1 to y_1 (Figure 3.2), because equations (3.15) are one-dimensional.

The only way that radiation from the y-wall can be 'felt' on the z-wall is

via absorption and scattering within the present medium.

3.4.5 Enthalpy-source terms

The influence of the radiative heat transfer is expressed by way of sources and sinks, as functions of the fourth order power of the local temperatures, distributed throughout the domain.

Then the contribution of the radiation fluxes to the stagnation-enthalpy source/sink term is given by:

(i)   For the gaseous phase:

$$S^{(1)}_{rad} = a_g \, (RX+RY+RZ) - 6a_g E_g \qquad (3.18).$$

(ii)   For the particulate phase:

$$S^{(2)}_{rad} = a'_p \, (RX+RY+RZ) - 6a'_p E_p \qquad (3.19).$$

A linearisation procedure was applied to equations (3.18) and (3.19), (Patankar (1980)) to help convergence.

3.4.6 Derivation of the radiation boundary conditions

There are six boundary conditions to be considered, one for every direction. These are:

$$\left.\frac{dRX}{d\theta}\right|_{\theta=0}, \quad \left.\frac{dRX}{d\theta}\right|_{\theta=\theta'}, \quad \left.\frac{dRY}{dr}\right|_{r=0}, \quad \left.\frac{dRY}{dr}\right|_{r=R'}, \quad \left.\frac{dRZ}{dz}\right|_{z=0}, \quad \left.\frac{dRZ}{dz}\right|_{z=h}$$

$$\text{(a)} \qquad \text{(b)} \qquad \text{(c)} \qquad \text{(d)} \qquad \text{(e)} \qquad \text{(f)} \qquad (3.20);$$

where conditions (3.20) refer to either walls, inlets or outlets.

In general, the walls of a furnace or combustion chamber are either

-54-

water-cooled, or refractory surfaces, or composites of both with which
the computational cells used in a finite-diference procedure are in
contact, and it is possible to derive boundary conditions for a quite
general wall. In this work, the walls are assumed opaque; that is if the
transmitted component of wall radiation is assumed to be zero.

Some of the flux arriving at the wall, Figure 3.3, is reflected back into
the chamber and this is augmented by the emission due to the
temperature of the wall.

For a general case, equating the wall fluxes, the flux, F_W, leaving the
wall is given by:

$$F_W^- = (1 - \epsilon_W)\ F_W^+ + \epsilon_W\ \sigma\ T_W^4$$

$$\underset{\text{reflected}}{\uparrow} \qquad \underset{\text{emitted}}{\uparrow}$$

(3.21);

where ϵ_W is the emissivity of the wall and T_W is the temperature of the
wall. This relationship (ie equation 3.21), is commonly found in the
literature (see for example, Shah (1979)).

Boundary conditions (equation 3.20(a), (b) and (c)), are assumed to
be the zero gradient conditions in an axisymmetric coordinate system, and
in the absence of walls in the θ-direction, to comply with the symmetry
requirement that the net flux (ie $F_W^+ + F_W^-$) is equal to zero.

The rest of the boundary conditions are described below.

3.4.6.1 Radial direction boundary condition

There are two cases to be considered, one with the boundary wall and the second one, when there is a blocked region inside the domain, as shown in Figure 3.4.

For the wall case, at point P_W, using equation (3.21), flux J_W, leaving the wall is:

$$J_W = \epsilon_W \, \sigma \, T_W^4 + (1-\epsilon_W) \, I_W \qquad (3.22).$$

Using equation (3.17(b)) and back-substituting in (3.22), we get:

$$I_W = \frac{RY_W - \epsilon_W \, \sigma \, T_W^4}{2-\epsilon_W} \qquad (3.23);$$

and

$$J_W = \frac{(1-\epsilon_W) \, RY_W + \epsilon_W \, \sigma \, T_W^4}{2-\epsilon_W} \qquad (3.24).$$

Algebraic manipulation of equations (3.15), (3.23) and (3.24) gives:

$$\left.\frac{dRY}{dr}\right|_{\substack{r=R\\ \text{wall}}} = (2\sigma T_W^4 - RY_W) \, \frac{\epsilon_W [R(a_g + (a_p + s_p)A_p) + 1]}{R(2-\epsilon_W)} \qquad (3.25).$$

Similarly, for the blocked region boundary condition, we have:

$$\left.\frac{dRY}{dr}\right|_{\substack{r=r\\ \text{blocked}\\ \text{region}}} = (RY_B - 2\sigma T_B^4) \, \frac{\epsilon_B (\bar{r}(a_g + (a_p + s_p)A_p + 1]}{\bar{r}(2-\epsilon_B)} \qquad (3.26).$$

In the case of an outlet or inlet in the radial-direction, we assume:

$$\frac{dRY}{dr}\bigg| = 0 \; .$$

3.4.6.2 Axial direction boundary conditions

There are four cases to be considered. Two for walls, one for inlet and one for outlet, as shown in Figure 3.5.

As before, at point P_H, flux L_H, leaving the top wall is:

$$L_H = \epsilon_w \; \sigma \; T_w^4 + (1-\epsilon_w) \; K_H \qquad (3.27).$$

Algebraic manipulation of equations (3.27), (3.15(c),(d)) and (3.17(c)) gives:

$$\frac{dRZ}{dz}\bigg|_{\substack{z=H \\ top \\ wall}} = (2\sigma T_w^4 - RZ_H) \; \frac{[a_g + (a_p + s_p)A_p]\epsilon_w}{2-\epsilon_w} \qquad (3.28).$$

Similarly for the lower wall, at point P_L:

$$\frac{dRZ}{dz}\bigg|_{\substack{z=h \\ lower \\ wall}} = (RZ_L - 2\sigma T_w^4) \; \frac{[a_g + (a_p + s_p)A_p]\epsilon_w}{2-\epsilon_w} \qquad (3.29).$$

For the inlet, at point P_I, if we assume that there is no radiation in the negative z-direction (ie flux $L_I=0$), leaving the domain at z=0, but a percentage, α, of radiation is crossing the plane z=0 into the domain, then the inlet radiation flux K_I, at point P_I, is given by:

$$K_I = \alpha \; \epsilon_g \; \sigma \; T_{in}^4 \qquad (3.30);$$

where ϵ_g is the absorptivity of the gas at inlet and T_{in} is the gas inlet temperature.

Algebraic manipulation of equations (3.30), (3.15(c), (d)) and (3.17(c)) gives:

$$\frac{dRZ}{dz}\bigg|_{\substack{z=0 \\ \text{inlet}}} = (a_g + a_p' + s_p') K \qquad (3.31).$$

The outlet boundary condition, at point P_o, $dRZ/dz|_{z=L}$ is assumed to be the zero gradient condition.

In the case of an inlet in the y-direction a similar equation to (3.30) can be used ie:

$$J_w = \alpha\epsilon_g \, \sigma \, T_{in}^4 \qquad (3.32).$$

3.5   Discretisation of the Two-Phase Six-Flux Radiation Equations

3.5.1   The control-volume approach

To solve the second-order differential equations (3.16), the control-volume approach is used (see Patankar (1980), Anderson et al (1984), which is also used in PHOENICS.

The calculation domain is divided into a number of non-overlapping control volumes (sub-domains), such that there is one control-volume surrounding each grid point.   It is most convenient to establish the control volumes in such a way that the grid point lies halfway between the boundaries of the two-dimensional control volume, for example, as in Figure 3.6.   The differential equations (3.16) are integrated over each control volume.   Piecewise profiles expressing the variation of the fluxes R_i between the grid points are used to evaluate the required integrals. The result is the discretisation equation containing the values of R_i for a group of grid points.

The discretisation equation obtained in this manner expresses the conservation principle of all fluxes R_i, for the finite-control volume, just as the differential equation expresses it for an infinitesimal control volume.

In reality the control volumes are three-dimensional cells, having six sides and eight corners, as in Figure 3.7 where points:

P refers to the node point within the cell;

N north neighbour node (+ve y-direction);

S south neighbour node (-ve y-direction);

E east neighbour node (+ve x-direction);

W west neighbour node (-ve x-direction);

H high heighbour node (+ve z-direction); and

L low neighbour node (-ve z-direction).

3.5.2 Discretising the z-direction fluxes

Using equations (3.16(b)) and (3.17(c)), the second order differential equation for the z-direction can be rewritten as:

$$\frac{d}{dz}\left[\left(\frac{1}{a_g+(a_p+s_p)A_p}\right)\frac{d}{dz}(RZ)\right] = -\frac{S_p}{3}(RX+RY)A_p$$

$$+ RZ(a_pA_p+a_g+\frac{2s_pA_p}{3}) - 2a_pA_pE_p - 2a_gE_g \qquad (3.33).$$

Let

$$\Gamma = \frac{1}{a_g+(a_p+s_p)A_p} \qquad (3.34);$$

then, there are three cases to be considered, one for a general cell away from the boundaries and one for each boundary (ie high and low).

3.5.2.1 General case away from boundaries

Consider the node point P and its high and low neighbours, H and L, respectively, and the distances between them as shown in Figure 3.8. Points ℓ and h refer to the locations of the low and high boundaries, respectively.

The LHS of equation (3.33) using (3.34) can now be written as:

$$\text{LHS (3.33)} = \frac{\Gamma_h \left.\frac{dRZ}{dz}\right|_h - \Gamma_\ell \left.\frac{dRZ}{dz}\right|_\ell}{2D_p} \tag{3.35};$$

$$= \frac{1}{2D_p} \left[\Gamma_h \left(\frac{RZ_H - RZ_p}{D_p + D_H}\right) - \Gamma_\ell \left(\frac{RZ_p - RZ_L}{D_L + D_p}\right) \right]$$

$$= \frac{1}{2D_p} \left[\frac{\Gamma_h}{D_p + D_H} RZ_H + \frac{\Gamma_\ell}{D_L + D_p} RZ_L - \left(\frac{\Gamma_h}{D_p + D_H} + \frac{\Gamma_\ell}{D_L + D_p}\right) RZ_p \right] \tag{3.36}.$$

Equating (3.36) with the RHS of (3.33) we now get:

$$RZ_p = \frac{\frac{\Gamma_h}{D_p + D_H} RZ_H + \frac{\Gamma_\ell}{D_L + D_p} RZ_L + 2D_p \left[\frac{S_p}{3} (RX_p + RY_p)A_p + 2A_p a_p E_p + 2a_g E_g\right]}{\frac{\Gamma_h}{D_p + D_H} + \frac{\Gamma_\ell}{D_L + D_p} + 2D_p \left[a_g + (a_p + \frac{2s_p}{3}) A_p\right]}$$

$$\tag{3.37}.$$

3.5.2.2 High boundary

In the case of a high boundary such as in Figure 3.9 we define: $dRZ/dz|_{z=h}$ as a linear combination of such that:

$$\left.\frac{dRZ}{dz}\right|_{z=h} = \alpha RZ_p + \beta \tag{3.38}.$$

Then from equation (3.35) and using (3.33) we obtain:

$$\text{LHS } (3.33) = \frac{1}{2D_p} \left[\Gamma_h \ (\alpha RZ_p + \beta) - \Gamma_\ell \ (\frac{RZ_p - RZ_L}{D_L + D_p}) \right] \qquad (3.39$$

Equating (3.39) with the RHS of (3.33) we now obtain RZ_p obtain F boundary given by:

$$RZ_p = \frac{\Gamma_h \ \beta + \frac{\Gamma_\ell}{D_L + D_p} \ RZ_L + 2D_p \left[2a_p A_p E_p + 2a_g E_g + \frac{S_p}{3} \ A_p \ (RX + RY) \right]}{(\frac{\Gamma_\ell}{D_p + D_L} - \Gamma_h \ \alpha) + 2D_p \left[a_g + (a_p + \frac{2s_p}{3}) \ A_p \right]} \qquad (3.40$$

The coefficients α and β for equation (3.38) are obtained from eqed fron (3.28), where:

$$\alpha = - \ \frac{[a_g + (a_p + s_p) A_p] \ \epsilon_w}{2 - \epsilon_w} \qquad (3.41)$$

and

$$\beta = (-\alpha) \ (2\sigma T_w^4) \qquad (3.42)$$

3.5.2.3 Low boundary

As before, for the case of a low boundary, Figure 3.10, we de. 10, wi $dRZ/dz|_{z=\ell}$ as a linear combination of RZ_p, using equation (3.38), on (3.3 that:

$$\frac{dRZ}{dz}\bigg|_{z=\ell} = \alpha RZ_p + \beta \qquad (3.43).$$

Again using equations (3.43), (3.33) and (3.35) with alge with manipulation we obtain:

$$RZ_p = \frac{\frac{\Gamma_h}{D_p + D_H} RZ_H - \Gamma_\ell \beta + 2D_p \left[\frac{S_p}{3} A_p (RX+RY) + 2a_pA_pE_p + 2a_gE_g\right]}{\frac{\Gamma_h}{D_p + D_H} + \Gamma_\ell \alpha + 2D_p \left[a_g + (a_p + \frac{2s_p}{3}) A_p\right]}$$

<div align="right">(3.44).</div>

Equation (3.44) gives the value of flux at point P at the low boundary and the coefficients α and β of equation (3.43) are obtained from equation (3.29), where:

$$\alpha = \frac{(a_g + (a_p + s_p)A_p) \; \epsilon_w}{2 - \epsilon_w} \qquad\qquad (3.45);$$

and

$$\beta = (-\alpha) \; (2\sigma T_w^4) \qquad\qquad (3.46).$$

In the case of an inlet at low-z the low boundary condition is given by equation (3.30) and therefore appropriate values should be given to the coefficients α and β of equation (3.43).

3.5.3 Discretising the radial-direction fluxes

Using equations (3.16(a)) and (3.17(b)), the second-order differential equation of the y-direction can be rewritten as:

$$\frac{1}{r} \frac{d}{dr} \left[\frac{r}{a_g + (a_p + s_p)A_p + \frac{1}{r}} \frac{d}{dr} (RY)\right] = -\frac{s_p}{3} A_p \; (RX+RZ)$$

$$+ (a_pA_p + a_g + \frac{2s_pA_p}{3}) \; RY - 2a_pA_pE_p - 2a_gE_g \qquad (3.47).$$

Let:

$$\Gamma = \frac{r}{a_g + (a_p + s_p)A_p + \frac{1}{r}} \qquad (3.48).$$

Then, there are three cases to be considered, one for a general cell away from the boundaries, and one for each boundary (ie north and south).

3.5.3.1 General case away from boundaries

Consider the node joint P and its north and south neighbours, N and S, respectively, and the distances between them, as shown in Figure 3.11. Points n and s, refer to the locations of the north and south boundaries respectively.

The LHS of equation (3.47), using (3.48) can now be written as:

$$\text{LHS } (3.47) = \frac{1}{r}\left[\frac{\Gamma_n \left.\frac{dRY}{dr}\right|_n - \Gamma_s \left.\frac{dRY}{dr}\right|_s}{2D_p}\right] \qquad (3.49);$$

$$= \frac{1}{r2D_p}\left[\Gamma_n \frac{RY_N - RY_p}{D_p + D_N} - \Gamma_s \frac{RY_p - RY_S}{D_S + D_p}\right]$$

$$= \frac{1}{r2D_p}\left[\frac{\Gamma_n}{D_p + D_N} RY_N + \frac{\Gamma_s}{D_S + D_p} RY_S\right] - \frac{1}{r2D_p}\left[\frac{\Gamma_n}{D_p + D_N} + \frac{\Gamma_s}{D_S + D_p}\right] RY_p$$

$$(3.50).$$

Equating (3.50) with the RHS of equation (3.47), we now obtain:

$$RY_p = \frac{\frac{\Gamma_n}{D_p + D_N} RY_N + \frac{\Gamma_s}{D_S + D_p} RY_S + 2D_p r\left[2a_g E_g + 2a_p A_p E_p + \frac{s_p}{3}(RX_p + RX_p)\right]}{\frac{\Gamma_n}{D_p + D_N} + \frac{\Gamma_s}{D_S + D_p} + 2rD_p\left[a_g + (a_p + \frac{2s_p}{3})A_p\right]}$$

$$(3.51).$$

3.5.3.2 North boundary

In the case of a north boundary, such as in Figure 3.12, we define

$dRY/dr|_{r=n}$, as a linear combination of RY_p, such that:

$$\frac{dRY}{dr}\bigg|_{r=n} = \alpha RY_p + \beta \qquad (3.52).$$

Then, from equation (3.49) and using (3.52), we obtain:

$$LHS \ (3.47) = \frac{1}{2rD_p} \left[\Gamma_n \ (\alpha RY_p + \beta) - \Gamma_s \ (\frac{RY_p - RY_s}{D_p + D_s}) \right] \qquad (3.53).$$

Equating (3.53) with RHS of (3.47), we now obtain the RY-flux value at the north boundary, given by:

$$RY_p = \frac{\frac{\Gamma_s}{D_p + D_s} RY_s + \Gamma_n \ \beta + 2rD_p \left[2a_p A_p E_p + 2a_g E_g + \frac{s_p}{3} A_p \ (RX_p + RZ_p) \right]}{\frac{\Gamma_s}{D_p + D_s} - \Gamma_n \alpha + 2rD_p \left[a_g + A_p \ (a_p + \frac{2s_p}{3}) \right]}$$

$$(3.54).$$

The coefficients α and β for equation (3.52) are obtained from equation (3.30), where:

$$\alpha = - \frac{\epsilon_w [1 + \bar{R}(a_g + (a_p + s_p)A_p)]}{\bar{R}(2 - \epsilon_w)} \qquad (3.55);$$

and

$$\beta = (-\alpha) \ (2\sigma T_w^4) \qquad (3.56).$$

3.5.3.3 South boundary

As before, for the case of a south boundary, Figure 3.13, we define $dRY/dr|_{r=s}$, as a linear combination of RY_p, using equation (3.52), such that:

$$\frac{dRY}{dr}\bigg|_{r=s} = \alpha RY_p + \beta \qquad (3.57).$$

Again using equations (3.57), (3.48) and (3.49), with algebraic manipulation, we obtain:

$$RZ_p = \frac{\frac{\Gamma_n}{D_p+D_N} RY_N - \Gamma_s\,\beta + 2D_pr\left[\frac{s_p}{3}A_p(RX_p+RZ_p)+2a_pE_pD_p+2a_gE_g\right]}{\frac{\Gamma_n}{D_p+D_N} + \Gamma_s\,\alpha + 2rD_p\left[a_g + (a_p+\frac{2s_p}{3})A_p\right]}$$

$$(3.58).$$

Equation (3.58) gives the value of the radial flux at the south boundary and the coefficients of α and β of equation (3.57) are obtained from equation (3.26), where:

$$\alpha = \frac{\epsilon_B[\bar{r}(a_g+(a_p+s_p)A_p)+1]}{\bar{r}\,(2-\epsilon_B)} \qquad (3.59);$$

and

$$\beta = (-\alpha)\,(2\sigma T_B{}^4) \qquad (3.60).$$

In the case where the south boundary is the symmetry axis, α and β are taken to be equal to zero (ie equation (3.20(c)).

3.5.4   Discretising the θ-direction fluxes

Using equations (3.16(c)) and (3.17(a)), the second-order differential equation for the θ-direction can be rewritten as:

$$\frac{1}{r}\frac{d}{d\theta}\left[\frac{1}{(a_g+(a_p+s_p)A_p)r}\frac{d}{d\theta}RX\right] = -\frac{s_p}{3}A_p(RZ_p+RY_p)$$

$$+ (a_pA_p+a_g + \frac{2s_pA_p}{3})\,RX - 2a_pE_pA_p - 2a_gE_g \qquad (3.61).$$

Let:

$$\Gamma = \frac{1}{[a_g + (a_p + s_p)A_p] \, r} \qquad (3.62).$$

Then, there are again three cases to be considered: one for a general cell away from the boundaries, and one for each boundary (ie east and west).

3.5.4.1 General case away from boundaries

Consider the node point P, and its west and east neighbours, W and E, respectively, and the distances between then as shown in Figure 3.14. Points w and e, refer to the locations of the west and east boundaries, respectively.

The LHS of equation (3.61) using (3.62) can now be written as:

$$\text{LHS} \ (3.61) = \frac{1}{2rD_p} \left[\Gamma_e \left. \frac{dRX}{d\theta} \right|_e - \Gamma_w \left. \frac{dRX}{d\theta} \right|_w \right] \qquad (3.63).$$

$$= \frac{1}{2rD_p} \left[\Gamma_e \left(\frac{RX_E - RX_p}{D_p + D_E} \right) - \Gamma_w \left(\frac{RX_p - RX_w}{D_p + D_W} \right) \right]$$

$$= \frac{1}{2rD_p} \left[\frac{\Gamma_e}{D_p + D_E} RX_E + \frac{\Gamma_w}{D_p + D_W} RX_W \right] - \frac{1}{2rD_p} \left[\frac{\Gamma_e}{D_p + D_E} + \frac{\Gamma_w}{D_p + D_W} \right] RX_p$$

$$(3.64).$$

Equations (3.64) with the RHS of equation (3.61), we now obtain:

$$RX_p = \frac{\dfrac{\Gamma_e}{D_p + D_E} RX_E + \dfrac{\Gamma_w}{D_p + D_W} RX_W + 2rD_p \left[2a_g E_g + 2a_p A_p E_p + \dfrac{s_p}{3} A_p (RY_p + RZ_p) \right]}{\dfrac{\Gamma_e}{D_p + D_E} + \dfrac{\Gamma_w}{D_p + D_W} + 2rD_p \left[a_g + (a_p + \dfrac{2s_p}{3}) A_p \right]}$$

$$(3.65).$$

3.5.4.2 West boundary

For the case of a west boundary, as in Figure 3.15, we define $dRX/d\theta|_{\theta=w}$, as a linear combination of RX_p, such that:

$$\frac{dRX}{d\theta}\bigg|_{\theta=w} = \alpha\,RX_p + \beta \qquad (3.66).$$

Substituting (3.66) in (3.63) and equating LHS and RHS of equation (3.61), we obtain:

$$RX_p = \frac{\dfrac{\Gamma_e}{D_p+D_E}\,RX_E - \Gamma_w\,\beta + 2rD_p\left[2a_gE_g+2a_pA_pE_p + \dfrac{S_p}{3}\,A_p(RY_p+RZ_p)\right]}{\dfrac{\Gamma_e}{D_p+D_E} + \alpha\Gamma_w + 2rD_p\left[a_g+(a_p + \dfrac{2S_p}{3})\,A_p\right]}$$

$$(3.67).$$

Equation (3.67) gives the value of the RX-flux at the west boundary, and values of the coefficients α and β are obtained from equation (3.20(a)) and they are equal to zero, for reasons explained in Section 3.4.6.

3.5.4.3 East boundary

As in the case of the west boundary, $dRX/d\theta|_{\theta=e}$, is defined by equation (3.66), where:

$$\frac{dRX}{d\theta}\bigg|_{\theta=e} = \alpha\,RX_p + \beta \qquad (3.68).$$

Algebraic manipulation of (3.68), (3.66), (3.63) and (3.61), gives:

$$RX_p = \frac{\Gamma_e\,\beta + \dfrac{\Gamma_w}{D_p+D_W}\,RX_W + 2rD_p\left[2a_gE_g+2a_pA_pE_p + \dfrac{S_p}{3}\,A_p\,(RY_p+RZ_p)\right]}{\dfrac{\Gamma_w}{D_p+D_W} - \Gamma_e\,\alpha + 2rD_p\left[a_g+(a_p + \dfrac{2S_p}{3})\,A_p\right]}$$

$$(3.69).$$

The coefficients α and β in (3.68) can be obtained from equation (3.20(b)) and these equal to zero, for the reasons explained in Section 3.4.6.
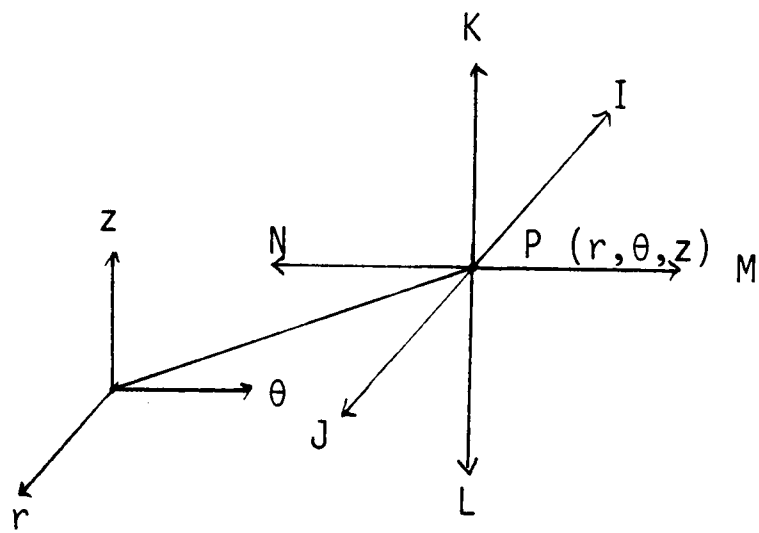
FIGURE 3.1: RADIATION FLUXES IN POLARS
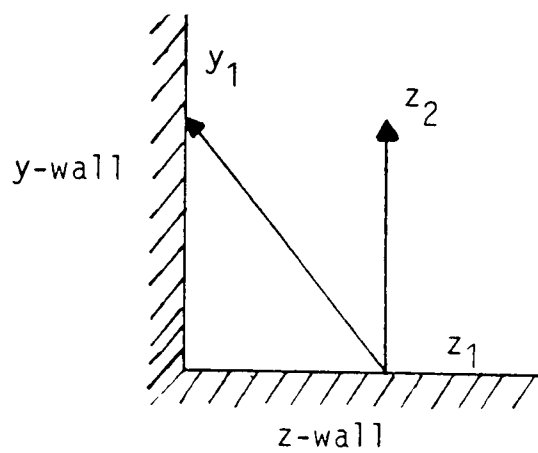

FIGURE 3.2:
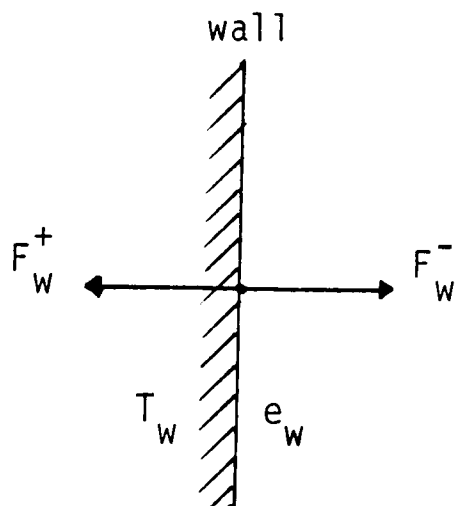

FIGURE 3.3: WALL RADIATION FLUXES
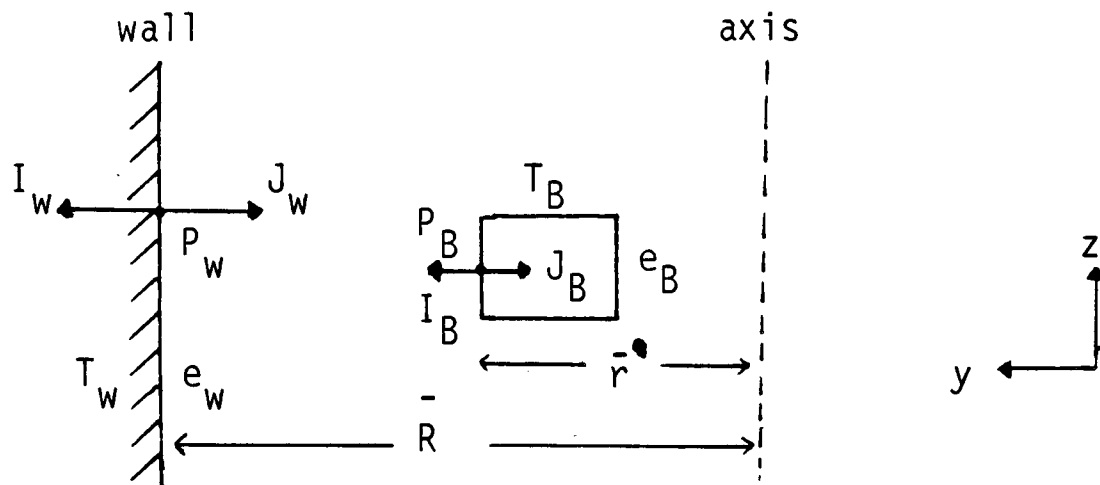
FIGURE 3.4: RADIAL DIRECTION BOUNDARY CONDITIONS
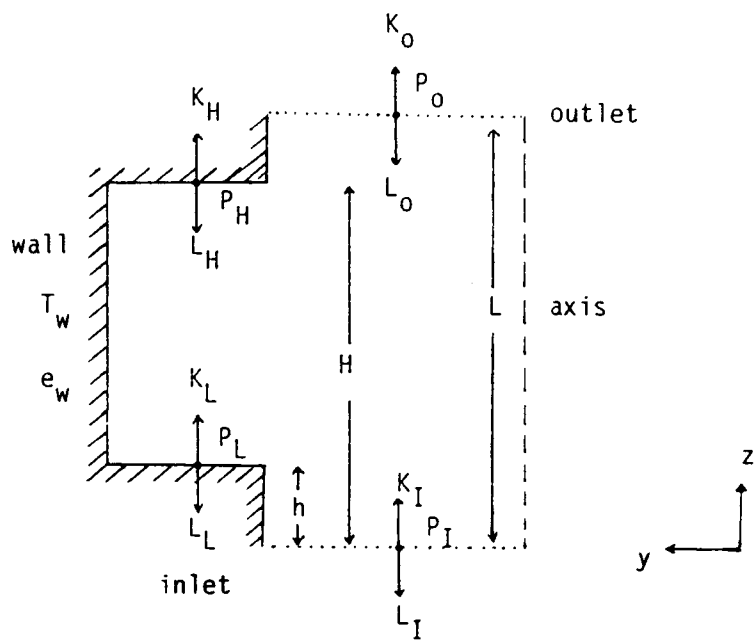
FIGURE 3.5: AXIAL DIRECTION BOUNDARY CONDITIONS
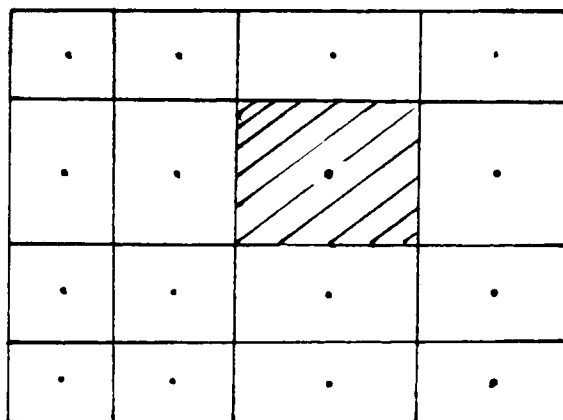
FIGURE 3.6: CONTROL VOLUME REPRESENTATION
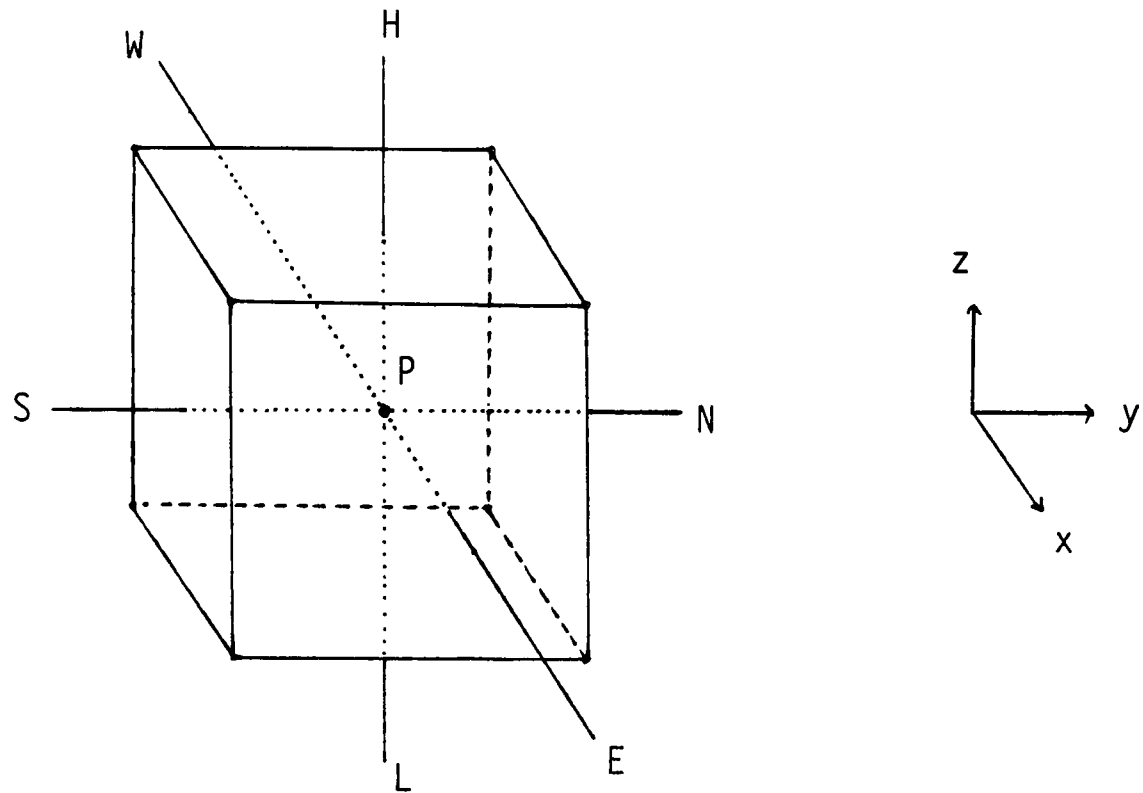
FIGURE 3.7: TYPICAL THREE-DIMENSIONAL CONTROL VOLUME
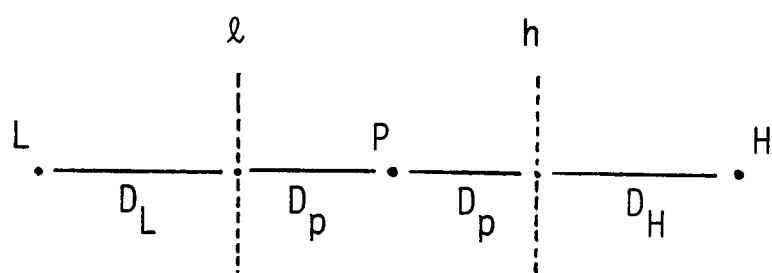

FIGURE 3.8: GENERAL CASE CONTROL VOLUME
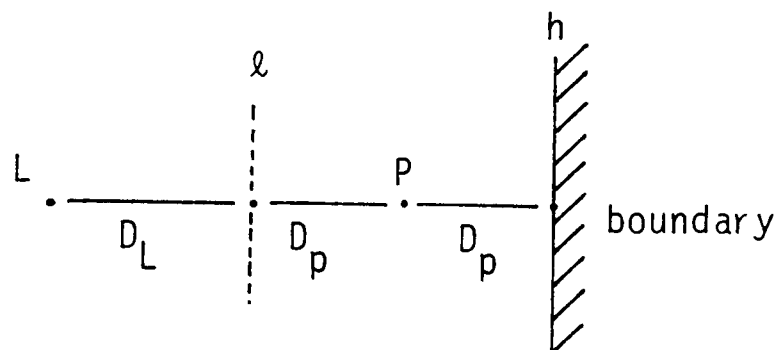
FIGURE 3.9: HIGH BOUNDARY
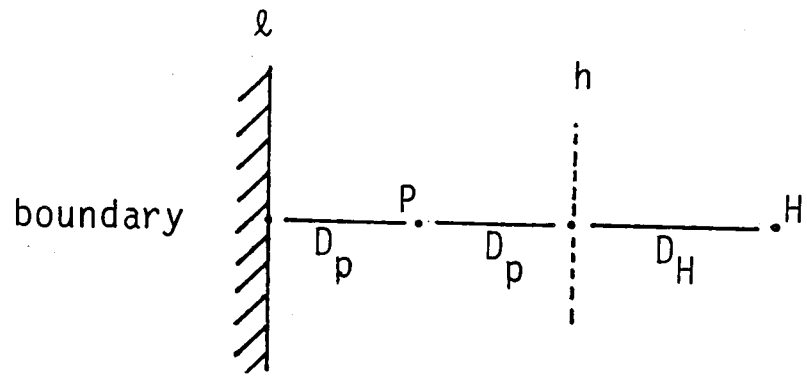
FIGURE 3.10: LOW BOUNDARY
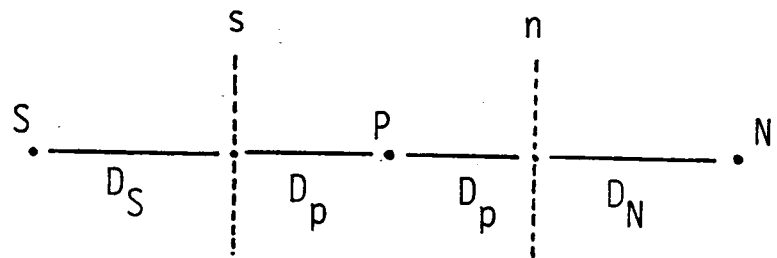
FIGURE 3.11: GENERAL CASE CONTROL VOLUME
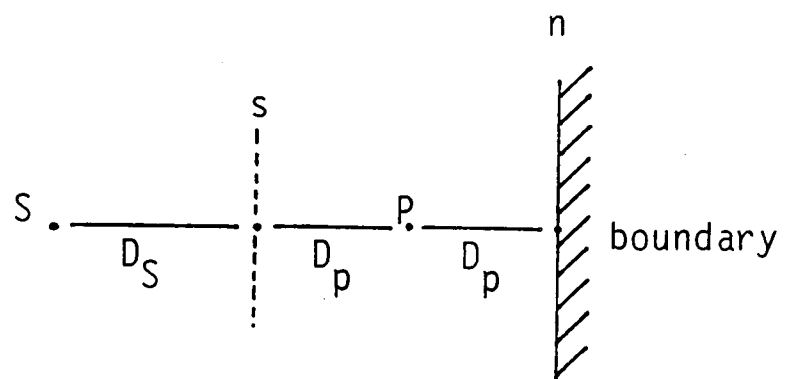
FIGURE 3.12: NORTH BOUNDARY
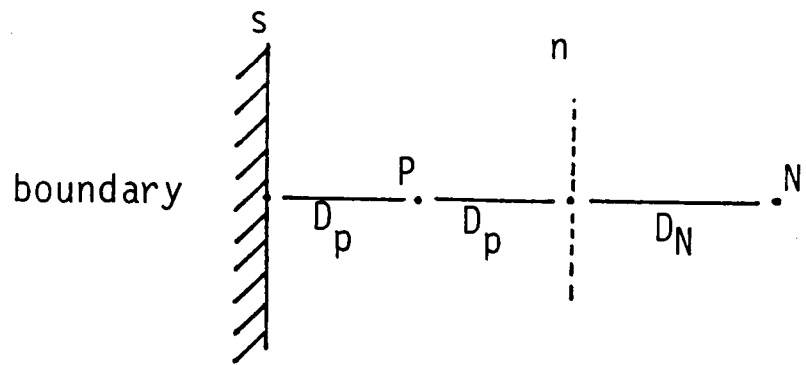
FIGURE 3.13: SOUTH BOUNDARY
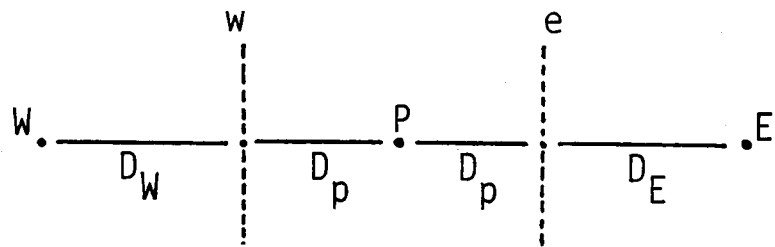
FIGURE 3.14: GENERAL CASE CONTROL VOLUME
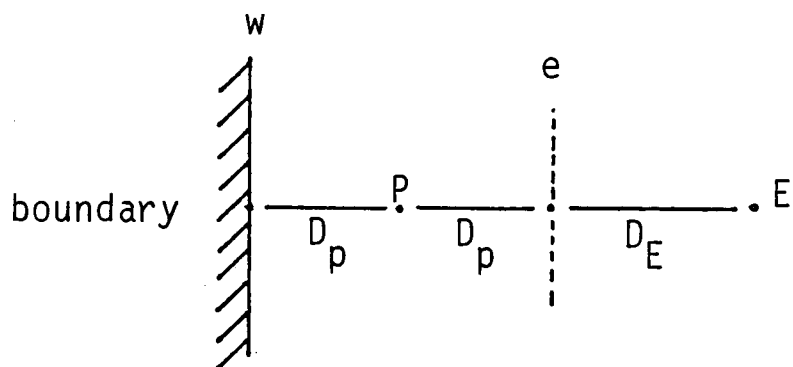

FIGURE 3.15: WEST BOUNDARY
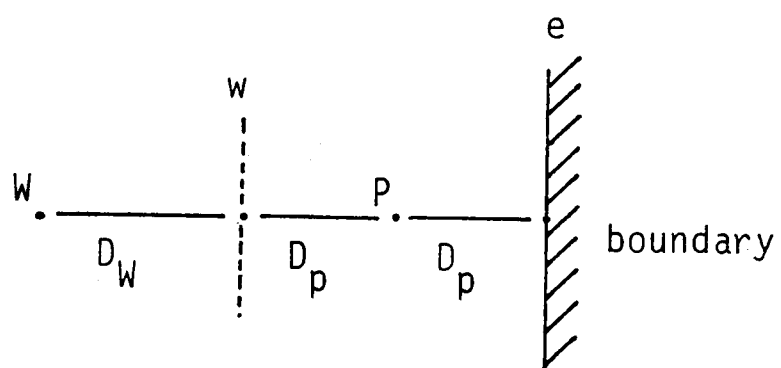
FIGURE 3.16: EAST BOUNDARY

CHAPTER 4 - THE COMBUSTION MODEL

4.1 Introduction - Review

Combustion is a major feature of the flow in furnaces. The aim of combustion modelling is to arrive at the calculation of the temperature, T, the mixture density, ρ, and the mass fractions of the chemical species involved, m_i.

Combustion is the process of interaction between fuel and oxidiser, which is accompanied by the liberation of heat and sometimes emission of light.

The importance of combustion processes in engineering is significant, being used for power production, in the process industry and for domestic and industrial heating. In the process industry much fuel is burned as an essential ingredient of the production of engineering materials, such as: iron, steel, glass, refined fuels and other hydrocarbon derivatives. Coal, oil and natural gas may be used as fuel and knowledge of the combustion process is a vital one in the design and operation of the relevant combustion systems.

Combustion is a very complex phenomena since the change from the reactants to the final products includes many intermediate reactions involving the formation and interactions of intermediate species and free radicals. Reactions can vary from simple ones to very complex ones, with consecutive steps or coupled ones (Kondrat'ev (1964)) involving primary reactions and secondary reactions. For example, Tsatsaronis (1978) has presented a reaction mechanism for methane-oxygen mixtures which contains 29 elementary reactions, involving 13 different chemical species. Turbulence further complicates the problems since it influences

the mixing of reactants and products and for this reason it has attracted considerable attention.

Spalding (1971) presented a model of turbulent combustion which involved the calculation of the magnitude of the fluctuating concentrations and adequately predicted the main features of turbulent diffusion flames. He also presented two further models, where in the first one, the time-mean reaction rate is related to the time-mean concentrations and temperature at the point in question, by a bimolecular Arrhenius expression. In the second model, the local reaction rate is taken to depend also on the rate of breakup of the eddies by the action of turbulence, and to be controlled by this rate when it is low enough. He concluded that the eddy-breakup term appears to be essential, if the dominance of hydrodynamic processes is to be correctly simulated. The eddy-breakup model is explained in more detail in the following sections.

Mason and Spalding (1973) presented an extension of the work by Spalding (1971), to calculate the rate of spread of flames through a turbulent combustible gas, using the k-ϵ model for the hydrodynamics and the eddy-breakup model for the chemical reaction rate. Comparing with experimental data, they concluded that the eddy-breakup model is capable of predicting the spread of turbulent flames behind baffles rather well.

Rhodes et al (1974) presented a series of predictive models for turbulent shear flows with simultaneous chemical reactions, using a probabilistic model for evaluating the influence of turbulent fluctuations on the chemical reactions of a hydrogen-air diffusion flame. They compared with

experimental results and concluded that the interaction between turbulence and chemical reaction is important, perhaps dominantly so in some flows.

Bray (1974) used the exact equations of turbulence for reacting flows, to derive an approximate form of the turbulence kinetic energy balance equation, for premixed, two-dimensional, turbulent flames, at low Mach numbers and high Reynolds number. He also experimentally observed effects of turbulence on a variety of turbulent flame configurations. He concluded by observing that certain phenomena - such as turbulence generation as a result of shear produced within the flame, turbulence energy removal due to velocity divergence resulting from heat release, diffusion of turbulence energy and reduction of turbulence Reynolds number - occur under the influence of combustion; and interaction between turbulence and combustion depends upon the balance between these often opposing effects.

Elghobashi and Pun (1974) studied turbulent diffusion flames in a small, axisymmetrical cylindrical furnace, using town gas and proposed a procedure for calculating the probability of chemical reaction in turbulent diffusion flames, which agreed well with experimental results.

Spalding (1972,1974) briefly reviewed models for turbulence, radiation, chemical kinetics and two-phase effects for predicting combustion-chamber flows. In particular, for the combustion model he discussed the idea on Arrhenius rate, having its basis on a physicochemical concept (collision frequency, activation energy) plus empiricism. He also discussed the idea of turbulent diffusion flames and the spread of a turbulent flame through already premixed gases.

He stressed the analogy with the dissipation of turbulence energy and of concentration fluctuations. He showed that predictions based on the eddy-breakup model hypothesis agree well with experimental data.

Pope (1976) described a preliminary investigation into the use of probability approach to model turbulent reacting flows. He paid attention to the effects of the turbulence on the reaction and concluded that in a combustion system, the average mass fraction and reaction rate of each species, and the average density and temperature may be determined from the average joint probability distribution of temperature and the species. He obtained solutions for homogeneous isotropic flow situations corresponding to diffusion and premixed flames. For the appropriate conditions, an expression for the average reaction rate was obtained which is similar to Spalding (1972) eddy-breakup model.

Spalding (1977(a)) presented a simple model for the rate of turbulent combustion, where the local rate of global reaction, in a turbulent gas of non-uniform fuel-air ratio, is expressed as a function of five parameters. These parameters are the time-average mixture fraction, the maximum and minimum values of the mixture fraction, occurring as a consequence of the fluctuations, and the time-average fuel concentrations at two nearby points. Predictions were made of the spread of both unmixed and premixed propane-air flames.

Lockwood (1977) extended existing combustion modelling for diffusion and for premixed turbulent reacting flows, to handle the general case of combined diffusion and premixed reaction and is intended for engineering use.

Spalding (1977(b)) presented the ESCIMO theory (for Engulfment, Stretching, Coherence, Interdiffusion, Moving Observer). The theory was explained as having 'biographical' (Lagrangian) and 'demographical' (Eulerian) aspects, which are almost independent of one another. Results were presented for several fluid-dynamically simple systems, such as the confined premixed flame, the free turbulent jet, etc. Spalding (1978) applied the ESCIMO theory of turbulent combustion to a one-step exothermic chemical reaction between premixed fuel and air in a steady-flow, well-stirred reactor and demonstrated the capabilities of the theory.

Gosman et al (1978) described a general computer-based procedure for the prediction of gaseous-fired cylindrical combustion chambers which can handle diffusion, partially-premixed and premixed combustion. The reaction rate is based on the 'macroscale model' described by Lockwood (1977) assuming a one-step global reaction between the gaseous fuel and oxygen.

Bray (1978) reviewed the interaction between combustion and turbulence from the point of view of a modeller, and discusses the effects of combustion on the structure of turbulence and effects of turbulence on chemical reaction rates.

Arbib et al (1980) developed a computer program for the solution of the set of elliptic non-linear partial differential equations that describe turbulent reacting flows of the kind encountered inside combustion chambers. Their investigation combined a two-equation model of turbulence with three global chemical reactions in realistic combustor

geometry, and obtained fair agreement between predictions and experimental data.

Williams and Libby (1980) reviewed works related to turbulent reacting flows with consideration of both premixed and non-premixed flows and with emphasis on the similarities in the formulations appropriate to the two cases, when the chemical reactions are fast.   An approach to the description of trace-species undergoing finite-rate chemical reactions is outlined and persisting difficulties in modelling the fluid-dynamics and transport processes in turbulent combustion, are stated.

Abou-Ellail and Abou-Arab (1981) studied co-axial diffusion flames for different velocity ratios of fuel and air.   They assumed global kinetics for the combustion model and that the reaction between fuel and oxidant takes place in a one-step, reversible reaction.

Khalil et al (1981) obtained results for a gas-fired furnace using three different models for combustion, namely for the diffusion, premixed and arbitrary fired flames using the models outlined in Hutchinson et al (1976).

Westbrook and Dryer (1981) reviewed some of the principles and techniques involved in the development and application of various kinetics models for hydrocarbon fuels (CO, CH_4, H_2, O_2, etc), which have been developed using data from a variety of experimental syustems.   They also emphasised the need for additional considerations on the non-Arrhenius temperature dependence of reaction rates, etc.

Ma et al (1982) applied the ESCIMO theory to the turbulent hydrogen-air diffusion flames with some degree of success.

Jones and Whitelaw (1982) provided a review for the calculation methods for reacting turbulent flows in relation to diffusion and premixed flames, with particular attention to the gaseous-combustion applications.

Spalding (1983(a)) discussed chemical reactions in turbulent fluids, characterising them as: 'deductive', 'zoological' and 'physiological', depending on the approach used, with attention on the ESCIMO theory.

Devapaul et al (1983) provided numerical predictions of flow characteristics of confined turbulent premixed flame, using the eddy-breakup model. They argued that the eddy-breakup model with modified constant, coupled with the Prandtl mixing length hypothesis, is capable of predicting the flow characteristics in the case of a turbulent premixed flame, stabilised by an auxiliary hot gas flow.

Nguyen and Pope (1984) presented calculations of turbulent diffusion flames and compared the results with experimental data for three turbulent flows: an inert methane jet, a hydrogen/air diffusion flame and a hydrogen-air/argon diffusion flame, obtaining good agreement between calculated and measured quantities including the pdf's.

Pope (1985) described pdf methods for turbulent reactive flows and tried to give a comprehensive and understandable account of the theoretical foundations of the pdf approach.

O'Brien (1986) discussed the recent extensions and contributions to the statistical theory of chemical reactants in turbulent flows.

In the 21st Symposium (International) on Combustion (1986) a number of people presented various works of turbulent reacting flows. Baum et al (1986) presented a mathematical model, with results, of the local transient diffusion-controlled reaction between initially unmixed species. Pope and Correa (1986) presented joint pdf calculations of a non-equilibrium turbulent diffusion flame. Further works can be found in the proceedings of the conference (to be published in 1987).

Work also has been carried out for the cases, where the non-gaseous phase combusts. More information on the subject can be found in: Spalding (1979(b)), (1982(b)), Smith (1982), Kansa and Perlee (1980), Lockwood et al (1980), Chung and Yun (1985), and in the proceedings of the 21st Symposium (International) on Combustion (1986).

4. 2   Existing Models - Background

Despite the complexity of the combustion process, the furnace engineer is usually interested only in the general representative features of the process such as time-averaged values of velocities, temperatures, concentrations and densities. Consequently, the assumption of a global one-step reaction mechanism between fuel and oxidant, as represented by Equation (4.1), is a very useful simplification, which aids the process of numerical prediction:

$$\text{Fuel} + \text{oxidant} \rightarrow \text{products} \qquad\qquad (4.1).$$

This assumption reduces the number of active species to only three, namely: fuel, oxidant and final product, for which the transport equations (2.8) can be solved.

In these equations, the rate of generation or consumption of the chemical species ℓ, R_ℓ per unit volume, appears as a source or sink term, S_ϕ, in the relevant equations. Many attempts have been made to model this term and one of the earlier ones is the expression of Kondrat'ev (1964). He gave an expression for the fuel reaction rate, R_{fu}, as a function of temperature, T, pressure P, the order of the reaction n, and the chemical species concentrations, as follows:

$$R_{fu} = f^n \ (T, \ P, \ concentrations) \tag{4.2}.$$

Another way of expressing the reaction rate is to take into account the collision or interaction of a single molecule of fuel with a single molecule of oxidant given that, at a particular temperature, the number of collisions is proportional to the local concentrations of reactants in the mixture. Thus:

$$R_{fu} = K_f \ m_{fu} \ m_{ox} \tag{4.3}.$$

Clearly for most chemical reactions the rate depends greatly on the temperature and this can be taken into account by a temperature dependent expression for K_f. Arrhenius (1889) suggested the following:

$$K_f = A \ \exp(-E/RT) \tag{4.4};$$

where A (called the pre-exponential factor) and E (the activation energy) are temperature independent parameters determined by experiments.

Values have been reported for many elementary reactions by various authors (see Chapter 6).

Reaction rates employing Equation (4.4) are said to be of the 'Arrhenius' form. However, for some reactions studied with high accuracy and when the temperature range is large it has been found that Equation (4.4) does not yield a very adequate representation (Libby and Williams (1980)), Gardiner (1984)). In such cases, more complex temperature functions, usually of the form:

$$K_f = BT^b \exp(-E/RT) \qquad\qquad (4.5);$$

have to be used. Equation (4.5) and other rate-coefficient functions which differ from (4.4), are said to describe 'non-Arrhenius' behaviour.

Spalding (1971), in his eddy-breakup model, for premixed turbulent flames, suggested a different approach in which the reaction rate can be expressed in terms of flow properties that can be calculated. This model is explained, in detail, in Section 4.4.

In practice, two types of combustion are distinguished: homogeneous and heterogeneous. The first type is typical of gaseous fuels and gaseous oxidant, where the reactants are mixed at the molecular level. Heterogeneous combustion is typical of liquid and solid fuels.

Homogeneous combustion can be modelled as either kinetically- or diffusion-controlled. In the kinetically influenced model the fuel and oxidant are premised, and the prepared fuel-oxidant mixture is supplied to the combustion zone. In the diffusion-controlled model they are not

premixed and combustion occurs as soon as fuel and oxidant mix.

4.3   The Diffusion-Controlled Model

Pun and Spalding (1967) and Spalding (1979(b)), developed the idea of
the Simple Chemically-Reacting System, (SRCS), by assuming a global,
one-step, infinitely fast chemical reaction between fuel and oxidant,
where they combine in stoichiometric proportion.   This model also
involved convenient simplifying assumptions about the species
thermodynamic and transport properties.

The diffusion-controlled model, employed in part of this work is based on
the SRCS model and it is presumed that whenever fuel and oxidant exist
together within a cell, the chemical reaction will proceed instantaneously
to completion in a single step, producing complete combustion products,
such that:

$$1Kg \ fuel + S \ Kg \ oxidant \ \rightarrow \ (1+S) \ Kg \ of \ products \qquad (4.6).$$
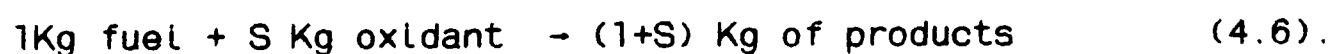
In this model, the effective exchange coefficients Γ_{eff} for all species are
assumed to be equal, although they need not be uniform (ie. they can
have different values at different spatial positions.   The second
assumption that has to be made is that fuel and oxidant always combine
in stoichiometric ratio as given by Equation (4.6).   A consequence of
the model is that the quantity:

$$\phi = m_{fu} - \frac{m_{ox}}{S} \qquad (4.7);$$

where m_{fu} and m_{ox} are the time-averaged mass fractions of fuel and
oxidant, respectively, and S is the stoichiometric oxidant requirements of

the unit mass of fuel, becomes a passive scalar (ie. it obeys the transport equation (2.8) with no source terms). This will be demonstrated later in this section.

It is convenient to work with a dimensionless ϕ, by defining the mixture fraction f, given by (Spalding (1980(a))):

$$f = \frac{\phi - \phi_1}{\phi_0 - \phi_1}$$

(4.8);

where the subscripts 0 and 1 designate ϕ at the fuel and oxidant stream inlets respectively, assuming a two-stream mixing process, as represented in diagram (4.1).

In the diagram (4.1) the fuel flows from stream S_0 (often entering in a pure state) at the rate of f Kg/s, and oxidant flows from the 'auxiliary' stream S_1, at the rate of 1-f Kg/s, to form a 'mixture' M, which flows at the rate of 1 Kg/s.

Equation (4.8) can also be written as:

$$f = \frac{(m_{fu} - \frac{m_{ox}}{S}) - (m_{fu} - \frac{m_{ox}}{S}) \text{ oxidant stream}}{(m_{fu} - \frac{m_{ox}}{S}) \text{ fuel stream} - (m_{fu} - \frac{m_{ox}}{S}) \text{ oxidant stream}}$$

(4.9).

The value of f at the combustion front is denoted by f_{ST} and at this point there is no fuel or oxidant present; its values being given by:

$$f_{ST} = \frac{m_{ox}^*}{Sm_{fu}^* + m_{ox}^*} \qquad (4.10);$$

where '*' values refer to the original concentrations injected through streams S_0 and S_1.

The mixture fraction is also a passive scalar, since it is a linear expression on ϕ and therefore satisfies the transport Equation (2.8) with no source terms; its transport equation is given by:

$$\nabla.(\rho \underline{u} f) = \nabla.(\Gamma_{eff} \nabla f) \qquad (4.11).$$

In many cases it is convenient to represent the mass concentration of each constituent species, m_i and diluent, in terms of f in the form of a stoichiometric diagram, which consists entirely of straight lines, since all relations are linear. In the more general case where the S_0 stream contains some product, the graph looks like Figure 4.2. It is easy to derive equations for the various lines and it is convenient to do so in terms of linear functions of f in terms of f_{ST}, where the value of f_{ST} can be calculated from equation (4.10) bearing in mind that at point P there is no fuel or oxidant present.

So:

$$0 \leqslant f < f_{ST} \quad \begin{cases} m_{fu} = 0 \\ \\ m_{ox} = \dfrac{m_{ox}^*(f_{ST}-f)}{f_{ST}} \end{cases} \qquad (4.12);$$

$$f_{ST} \leqslant f \leqslant 1 \quad \begin{cases} m_{ox} = 0 \\ \\ m_{fu} = \dfrac{m_{fu}^*(f-f_{ST})}{1-f_{ST}} \end{cases} \qquad (4.13);$$

-86-

$$m_{dil} = m^*_{dil} \, (1-f) \qquad\qquad (4.14).$$

The mass fraction of the remaining product species can now be found from:

$$m_{pr} = 1 - m_{dil} - m_{ox} - m_{fu} \qquad\qquad (4.15).$$

Then because the fuel and oxidant engage in a simple chemical reaction with a fixed stoichiometric ratio S, it follows that the reaction rates are related as follows:

$$\frac{1}{S} R_{ox} = R_{fu} \qquad\qquad (4.16).$$

Equation (4.16) can be used to show that ϕ in Equation (4.7) is a passive scalar.   This follows from the transport equations of fuel and oxidant which are:

$$\nabla \cdot (\rho \underline{u} m_{fu}) = \nabla \cdot (\Gamma_{eff} \nabla m_{fu}) + R_{fu} \qquad\qquad (4.17);$$

$$\nabla \cdot (\rho \underline{u} m_{ox}) = \nabla \cdot (\Gamma_{eff} \nabla m_{ox}) + R_{ox} \qquad\qquad (4.18).$$

Dividing (4.18) by S and subtracting it from (4.17) we now obtain:

$$\nabla \cdot [\rho \underline{u} (m_{fu} - \frac{m_{ox}}{S})] = \nabla \cdot (\Gamma_{eff} \nabla (m_{fu} - \frac{m_{ox}}{S})] + R_{fu} - \frac{R_{ox}}{S}$$

$$(4.19).$$

Using Equations (4.16) and (4.17) we now obtain:

$$\nabla \cdot (\rho \underline{u} \phi) = \nabla \cdot (\Gamma_{eff} \nabla \phi) \qquad\qquad (4.20);$$

which is the transport equations of ϕ, with no source terms.

4.4   The Kinetically-Influenced Model

In many flow situations such as when the gases are premixed, prior to the combustion chamber, the infinitely fast reaction assumption, is invalid and it is therefore necessary to provide for a finite rate of reaction. To do so, a source term is required in the conservation of chemical species equation (2.8), to account for the consumption or generation of the species at a finite rate.

Various models and approaches have been suggested (see Khalil (1982)) that vary from multi-step to one-step, reversible or irreversible reactions, accounting for various dependencies of the reaction rate with temperature, turbulence and other quantities.

In this section, finite rate, single-step reaction mechanisms with one- or two-simultaneous reversible or irreversible reactions, are considered. They are based on the eddy-breakup model of Spalding (1971), where the local reaction rate is proportional to the rate of formation and breakup of the turbulent eddies.

The essential ideas of the eddy-breakup model are: that the turbulent reacting mixture consists of interspersed sheets and filaments of fully reacted and completely unreacted material and that the rate of transformation of the gas from one state to the other depends upon the rate of stretching of the sheets and filaments.

This model appears to work reasonably well (Bradshaw et al (1981), Khalil (1982)) in situations where the reactants are premixed at the stoichiometric ratio before they enter the combustion chamber.   In his

model, Spalding recommends that the turbulent reaction-rate, R_{fu}, should be taken as the minimum of the laminar Arrhenius equations (4.3) and (4.4) and of:

$$R_{fu} = - C_R \, m_{fu} \, \rho \, \frac{\epsilon}{k} \qquad (4.21);$$

where C_R was taken to be a constant equal to 1. In reality C_R is not a constant (Pope (1976), Bradshaw (1981)) and various researchers have suggested several formulae for it. For example, Magnussen et al (1978) have suggested that C_R should be equal to:

$$C_R = 23.6 \, (\frac{\mu}{\rho} \frac{\epsilon}{k^2})^{1/4} \qquad (4.22).$$

Pope (1976) obtained a formula for C_R which is dependent on the average and maximum fluctuations of the scalar variable in question (i.e the fuel concentration) and is given by:

$$C_R = \frac{1}{2} \, C_2 \, \frac{\phi'}{\phi'_{max}} \, \ln \, (1 + \frac{2\phi'_{max}}{\phi'}) \qquad (4.23);$$

where $C_2 = 4.5$.

In equation (4.23), C_R varies between zero and 2.472 as compared with the constant values of 0.53 and 1.0, used by Mason and Spalding (1973) and Khalil et al (1975), respectively. Malin et al (1982) also used the values of 1.0 and this is the value adopted in this work.

Since the eddy-breakup model has been exclusively used for stoichiometrically premixed gases, the model must be modified here and extended for use with non-premixed gases. Furthermore, provision must

-89-

be made that the gases need not enter the combustion zone in stoichiometric proportions. The reaction is considered to be one-step with one- or two-simultaneous reversible and irreversible reactions. In order to achieve these tasks, various modifications have been introduced to the standard model, and they are explained in the next section.

4.4.1   The simple irreversible one-reaction kinetically-influenced model

Consider four species present in the combustion chamber, reactant A (oxidant), and inert D, injected through stream S_0 (Figure 4.1), and reactant B (fuel) and Product C, injected through port S_1. The reaction that takes place is:

$$aA + bB \rightarrow cC \qquad\qquad (4.24);$$
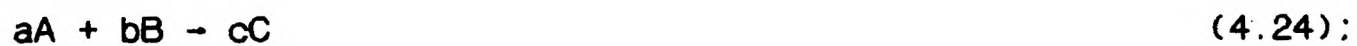
where a, b and c are the stoichiometric coefficients of the reaction.

Again, it is convenient to work with the dimensionless mixture fraction, f, (Spalding (1980(a)), equation (4.9)), which for the present case is given by:

$$f = \frac{m_B - \dfrac{m_A}{S} + \dfrac{m_A^*}{S}}{m_B^* + \dfrac{m_A^*}{S}} \qquad\qquad (4.25);$$

where '*'-values denote the initial values of the species at streams S_0 and S_1.

Mass fraction m_B of reactant B (fuel) and f, are assumed to have their own transport equations, which are of the standard form (2.8) and hence can be solved for using the standard procedure. The rest of the

variables, ie. mass fractions m_D, m_C and m_A of species D, C and A, respectively, can be calculated independently by the equations:

$$m_C = \frac{1 - m_B(1 - XYZ) - m_A(1 + X)}{1 + XY} \qquad (4.26);$$

$$m_D = [m_A + (m_C - m_B Z)Y]X \qquad (4.27);$$

$$m_A = m_A^*(1 - f) + S(m_B - f m_B^*) \qquad (4.28);$$

where:

$$X = \frac{m_D^*}{m_A^*} \qquad (a)$$

$$Y = \frac{a w_A}{c w_C} \qquad (b) \qquad (4.29);$$

$$Z = \frac{m_C^*}{m_B^*} \qquad (c)$$

where w_A and w_C are the molecular weights of substances A and C, respectively.

The following constraints are also applied:

$0 \leqslant f \leqslant 1$, with $f = 0$ at stream S_0 and $f = 1$, at stream S_1.

$0 \leqslant m_A \leqslant m_A^*$, with $m_A = m_A^*$ at stream S_0 and $m_A = 0$, at stream S_1.

$0 \leqslant m_B \leqslant m_B^*$, with $m_B = 0$ at stream S_0 and $m_B = m_B^*$, at stream S_1.

$0 \leqslant m_C \leqslant 1$, with $m_C = 0$ at stream S_0 and $m_C = m_C^*$, at stream S_1.

$0 \leqslant m_D \leqslant m_D^*$, with $m_D = m_D^*$ at stream S_0 and $m_D = 0$, at stream S_1.

These constraints were introduced to aid convergence of the iterative schemes.

The reaction rate employed is an extension of the one suggested by Spalding and is given by:

$$R_B = \tilde{m} \frac{\rho \epsilon}{k}$$ (4.30);

where m is taken to be:

$$\tilde{m} = \min(m_B, \frac{m_A}{S})$$ (4.31);

where m_B and m_A are the available reactants B and A respectively, and s is the stoichiometric ratio.

The motivation for Equation (4.31) is the fact that in the cases of non-stoichiometrically mixed gases, the reaction rate is dependent on the species that is in shortest supply.

4.4.1.1 Source terms for m_B

Because of the non-premixed nature of the model five cases must be considered:

Case 1: $m_B = 0$: no reaction.

Case 2: $m_A = 0$: no reaction.

Case 3: The temperatures inside the combustion chamber are outside the temperature range within which the reaction can take place, as dictated by the Gibb's free energy and the chemical thermodynamics of the reaction. Therefore no reaction occurs.

Case 4: m_A/S > m_B: Reaction rate is controlled by m_B, ie. excess of A or A and B at stoichiometric proportions.

Case 5: $m_A/S < m_B$: Reaction rate is controlled by m_A, ie. excess of species B.

The source term S_B is given by Equation (4.30) and to incorporate it into PHOENICS, it is put in the form:

$$S_B = C_B (V_B - m_B) \qquad (4.32);$$

where C_B and V_B are the coefficients and the value of S_B and are given in Table (4.1).

In summary, the main advantages of the above model are:

(i)   chemical species do not have to be in stoichiometric proportions before they mix;

(ii)   only two equations are directly solved for (ie. for variables f and m_B) and the others can be derived from them;

Case	Coefficient C_B	Value V_B
1	0	0
2	0	0
3	0	0
4	$\rho\epsilon/k$	0
5	$\rho\epsilon/k$	$f m_B^* - \dfrac{m_A^*}{S}(1-f)$

TABLE 4.1:   SOURCE TERM FOR REACTION (4.24)

(iii)   the model is consistent with available solving techniques and it is therefore, easy to incorporate in a general fluid flow package

such as PHOENICS.

4.4.2 The standard reversible-one-reaction model

Consider four species present in a combustion chamber: reactant A, entering through stream S_0, reactant B, products C and D, entering through stream S_1. The reversible reaction taking place is:

$$aA + bB \; \overset{(a)}{\underset{(b)}{\rightleftharpoons}} \; cC + dD \qquad (4.33).$$

In this model transport Equations (2.8) must be solved for three of the constituent species (eg. species A, B and C) while the fourth one (product D) is obtained using:

$$m_D = 1 - m_A - m_B - m_C \qquad (4.34).$$

For reaction (4.33(a)), there are three source terms to be considered, one for each of the species A, B and C, given by:

$$R_A = -\bar{m} \frac{\rho \epsilon}{k} \qquad (a)$$

$$R_B = -\bar{m} \, S_a \frac{\rho \epsilon}{k} \qquad (b) \qquad (4.35);$$

$$R_C = -\bar{m} \frac{cW_C}{aW_A} \frac{\rho \epsilon}{k} \qquad (c)$$

where $\bar{m}$ is taken to be:

$$\bar{m} = \min[m_A, \frac{m_B}{S_a}] \qquad (4.36);$$

since the reaction is limited by the reactant in shortest supply. The

stoichiometric ratio S_a, for reaction (4.33(a)) is given by:

$$S_a = \frac{bW_B}{aW_A} \qquad\qquad (4.37).$$

For reaction (4.33(b)), the source terms are:

$$R_A = \bar{m}\, \frac{aW_A}{cW_C}\, \frac{\rho\epsilon}{k} \qquad (a)$$

$$R_B = \bar{m}\, \frac{bW_B}{cW_C}\, \frac{\rho\epsilon}{k} \qquad (b) \qquad\qquad (4.38);$$

$$R_C = -\,\bar{m}\, \frac{\rho\epsilon}{k} \qquad (c)$$

where now, $\bar{m}$ is taken to be:

$$\bar{m} = \min[m_C, \frac{m_D}{S_b}] \qquad\qquad (4.39);$$

since the reaction is again controlled by the reactant in shortest supply. The stoichiometric ratio, S_b, for reaction (4.33(b)) is given by:

$$S_b = \frac{dW_D}{cW_C} \qquad\qquad (4.40).$$

4.4.2.1 Source terms

Since the gases are not premixed and are not in stoichiometric proportions, there are five cases to be considered for each direction of the reaction (4.33).

For reaction (4.33(a)) the cases are:

<u>Case 1</u>: $m_A = 0$: no reaction.

<u>Case 2</u>: $m_B = 0$: no reaction.

-95-

Case 3: Gas temperatures inside the combustion chamber are outside the temperature range that reaction can take place and therefore no reaction occurs.

Case 4: $m_B/S_a > m_A$: Species A in shortest supply, ie. reaction rate limited by m_A.

Case 5: $m_B/S_a < m_A$: Species B in shortest supply, ie. reaction rate limited by m_B.

Sources (4.35(a), (b) and (c)) are again put in the form of equation:

$$S_i = C_i(V_i - \phi) \qquad\qquad (4.41);$$

where coefficient C_i and values V_i for the species A, B and C are given in Table 4.2.

Case	Species A	Species B	Species C
4 $\bar{m}=m_A$	$R_A = -m_A \frac{\rho\epsilon}{k}$ $C_A = \rho\epsilon/k$ $V_A = 0.0$	$R_B = -m_A \frac{\rho\epsilon}{k} S_a$ $C_B = 10^{-10}$ $V_B = -m_A \frac{\rho\epsilon}{k} S_a 10^{10}$	$R_C = \frac{cW_C}{aW_A} m_A \rho\epsilon/k$ $V_C = \frac{cW_C}{aW_A} \frac{\rho\epsilon}{k} m_A 10^{10}$ $C_C = 10^{-10}$
5 $\bar{m}=\frac{m_B}{S_a}$	$R_A = -(\frac{m_B}{S_a}) \frac{\rho\epsilon}{k}$ $C_A = 10^{-10}$ $V_A = -(\frac{m_B}{S_a}) \frac{\rho\epsilon}{k} 10^{10}$	$R_B = -m_B \rho\epsilon/k$ $C_B = \rho\epsilon/k$ $V_B = 0.0$	$R_C = \frac{cW_C}{aW_A} \frac{m_B}{S_a} \frac{\rho\epsilon}{k}$ $C_C = 10^{-10}$ $V_C = \frac{cW_C}{aW_A} \frac{\rho\epsilon}{k} \frac{m_B}{S_a} 10^{10}$

TABLE 4.2:   SOURCE TERMS FOR REACTION (4.33(a))

For reaction (4.33(b) the cases to be considered are:

Case 1: $m_C = 0$: no reaction.

Case 2: $m_D = 0$: no reaction.

Case 3: Temperatures in the combustion chamber are outside the temperature range, where reaction can take place, ie. no reaction occurs.

Case 4: $m_C > m_D/S_b$: ie. excess of m_C, and reaction rate is controlled by m_D.

Case 5: $m_C < m_D/S_b$: ie. reaction rate controlled by m_C.

The source term coefficients C_i and values V_i for reaction (4.33(b)) are given in Table 4.3. Species D can be obtained by equation (4.34).

Case	Species A	Species B	Species C
$m_C > \dfrac{m_D}{S_b}$ $\bar{m} = \dfrac{m_D}{S_b}$	$R_A = \dfrac{aW_a}{cW_c} \dfrac{m_D}{S_b} \dfrac{\rho\epsilon}{k}$ $C_A = 10^{-10}$ $V_A = \dfrac{aW_A}{cW_C} \dfrac{m_D}{S_b} \dfrac{\rho\epsilon}{k} 10^{10}$	$R_B = \dfrac{bW_B}{cW_C} \dfrac{m_D}{S_b} \dfrac{\rho\epsilon}{k}$ $C_B = 10^{-10}$ $V_B = \dfrac{bW_B}{cW_C} \dfrac{m_D}{S_b} \dfrac{\rho\epsilon}{k} 10^{10}$	$R_C = -\dfrac{m_D}{S_b} \dfrac{\rho\epsilon}{k}$ $C_C = 10^{-10}$ $V_C = -\dfrac{\rho\epsilon}{k} \dfrac{m_D}{S_b} 10^{10}$
$m_C < \dfrac{m_D}{S_b}$ $\bar{m} = m_C$	$R_A = \dfrac{aW_A}{cW_C} m_C \dfrac{\rho\epsilon}{k}$ $C_A = 10^{-10}$ $V_A = \dfrac{aW_A}{cW_C} m_C \dfrac{\rho\epsilon}{k} 10^{10}$	$R_B = \dfrac{bW_B}{cW_C} m_C \dfrac{\rho\epsilon}{k}$ $C_B = 10^{-10}$ $V_B = \dfrac{bW_B}{cW_C} m_C \dfrac{\rho\epsilon}{k} 10^{10}$	$R_C = - m_C \rho\epsilon/k$ $C_C = \rho\epsilon/k$ $V_C = 0.0$

TABLE 4.3:   SOURCE TERMS FOR REACTION (4.33(b))

4.4.3   The two-simultaneous reactions model

Consider the two reactions:

$$aA + bB \xrightarrow{S_1} cC + dD \qquad \text{(a)}$$

$$\qquad\qquad\qquad\qquad\qquad\qquad (4.42);$$

$$eE + \bar{b}B \xrightarrow{S_2} \bar{c}C + \bar{d}D \qquad \text{(b)}$$
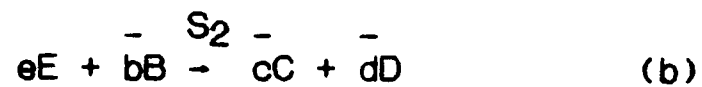
which can proceed simultaneously.

When reactants A and E are in excess compared with the quantity of reactant B present, we will assume that the masses of reactant B reacting with E and with A, per unit time, are in the ratio $\lambda:1$.   Without loss of generality we can assume $\lambda \geqslant 1$.

There are two stoichiometric ratios to be considered: S_1, for reaction (a), related to species A and S_2, for reaction (b), related to species E, given by:

$$S_1 = \frac{bW_B}{aW_A} \qquad\qquad\qquad (4.43);$$

and

$$S_2 = \frac{\bar{b}W_B}{eW_E} \qquad\qquad\qquad (4.44).$$

Species A and E are considered to be the two fuels in reactions (4.42) reacting with species B.

The reaction rates must be divided into a number of distinct cases. The simplest are:

Case 1: $m_B = 0$

        or   no reaction at all

(m$_A$=0 and m$_E$=0)

Case 2: $m_B \neq 0$ with:

        Case 2.1: $m_A = 0$

                and   reaction (4.42(b)) proceeds alone

                $m_E \neq 0$

        or

        Case 2.2: $m_A \neq 0$

                and   reaction (4.42(a)) proceeds alone

                $m_E = 0$

Case 3:   Temperatures of the gas mixture are outside the temperature

        range over which reaction (4.42) can proceed and hence there

        is no reaction.

For simplicity it is also assumed that the temperature ranges over which

the two reactions can proceed, are the same.

The more complicated case where m_A, m_E and m_B are non-zero and

temperature is inside the range at which reaction can proceed must now

be considered.   It can be subdivided into the cases shown in Table 4.4.

The minimum amount of species B, required for Species A and E to

react fully is: $S_1 m_A + S_2 m_E$, since species A and E require $S_1 m_A$ and

$S_2 m_E$ amount of m_B, respectively.   If this is available, m_B is said to be

in excess (Case 4.1).   When, however:

$$m_B < S_1 m_A + S_2 m_B \qquad (4.45);$$

then the available amount of species B, must be divided between A and E in the ratio $\lambda : 1$ (Case 4.2).

```
                    ┌─────────────────┐
                    │     Case 4      │
                    │  all reactants  │
                    │  are non-zero   │
                    └────────┬────────┘
                             │
              ┌──────────────┴──────────────┐
  Case 4.1    │                             │    Case 4.2
  ┌───────────┴──────┐            ┌─────────┴──────────┐
  │  excess of $m_B$ │            │  not enough $m_B$  │
  │       ie.        │            │        ie.         │
  │ $m_B > S_1 m_A + S_2 m_E$ │   │ $m_B < S_1 m_A + S_2 m_E$ │
  └──────────────────┘            └────────────────────┘
                   ┌──────────────────┐
                   │                  │
  Case 4.2.1       │                  │    Case 4.2.2
  ┌────────────────┴──┐      ┌────────┴───────────┐
  │ $m_B > S_1 m_A / \lambda + S_2 m_E$ │   │ $m_B < S_1 m_A / \lambda + S_2 m_E$ │
  │  not enough $m_E$  │      │ more than enough $m_E$ │
  └───────────────────┘      └────────────────────┘
```
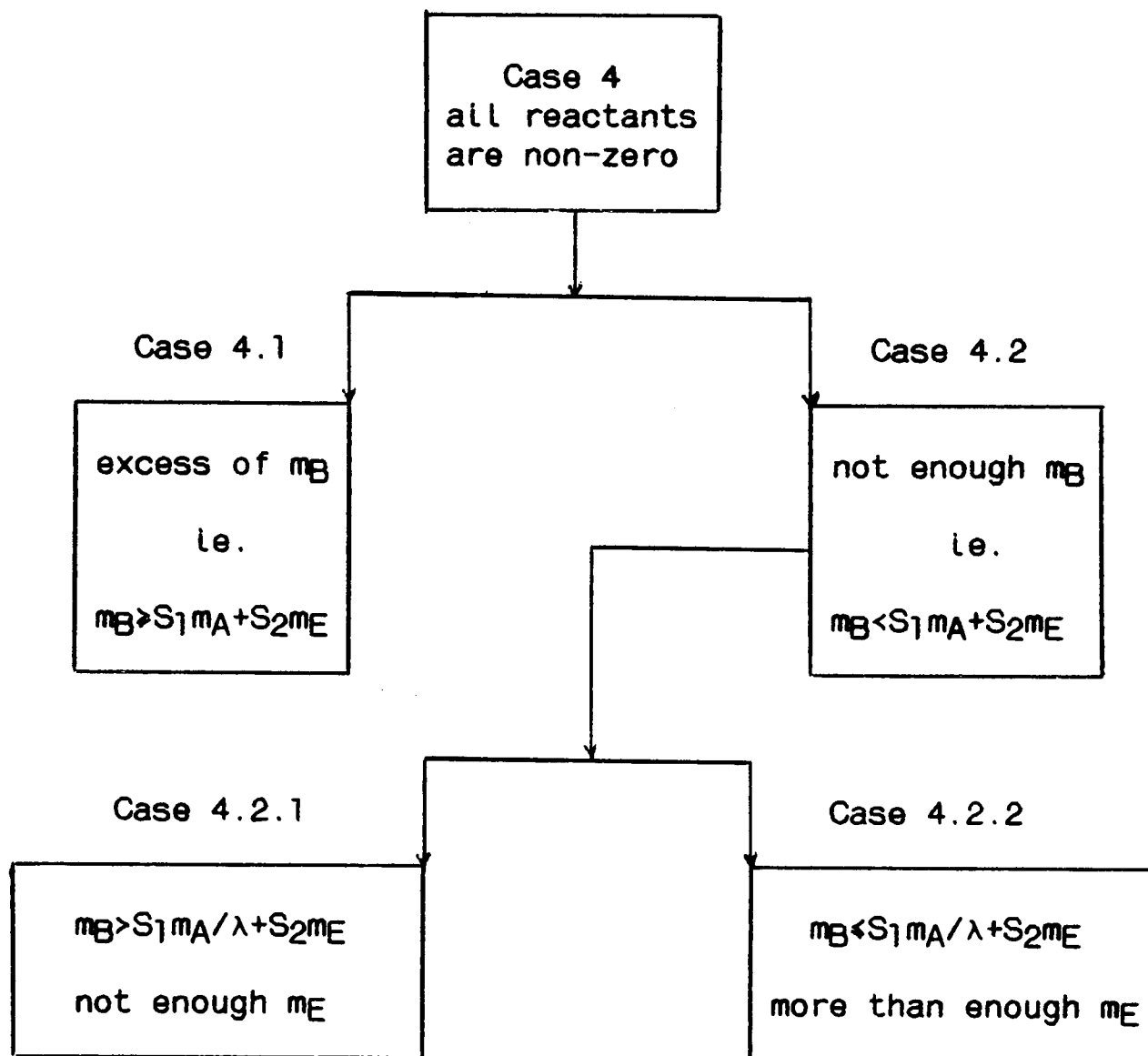
TABLE 4.4

In this case, species A and E would have required $S_1 m_A$ and $\lambda S_2 m_E$ amounts of species B respectively, with a total requirement of $S_1 m_A + \lambda S_2 m_E$ out of the available amount m_B.

Hence, the individual requirements of species A and E out of the available m_B will be:

(i)   amount of m_B reacting with m_A is:

$$\frac{S_1 m_A m_B}{S_1 m_A + \lambda S_2 m_E} \qquad\qquad (4.46).$$

(ii)   amount of m_B reacting with m_E is:

$$\frac{\lambda S_2 m_E m_B}{S_1 m_A + \lambda S_2 m_E} \qquad\qquad (4.47).$$

Because of the $\lambda : 1$ ratio, in favour of the available amount of species E, species E (ie. m_E) will then be determining the amounts of m_B each of the species A and E will be allocated for the reactions (4.42). Hence, there are two cases to be considered:

$$\frac{\lambda S_2 m_E m_B}{S_1 m_A + \lambda S_2 m_E} > S_2 m_E \qquad\qquad (4.48);$$

which gives:

$$m_B > \frac{1}{\lambda} S_1 m_A + S_2 m_E \qquad\qquad (4.49);$$

and

$$\frac{\lambda S_2 m_E m_B}{S_1 m_A + \lambda S_2 m_E} < S_2 m_E \qquad\qquad (4.50);$$

which gives:

$$m_B < \frac{1}{\lambda} S_1 m_A + S_2 m_E \qquad\qquad (4.51).$$

Equation (4.49) corresponds to Case 4.2.1 where, although there is not enough species B for both reactions, there is not enough species E

either.   Equation (4.51) corresponds to Case 4.2.2 where, this time there is more than enough m_E for reaction with the available m_B, and proper consideration is needed for the allocation of reactants.

In reactions (4.42) there are five species present and hence, species A, B, C and E are solved for and species D can be obtained using the equation:

$$m_D = 1 - m_A - m_B - m_C - m_E \qquad (4.52).$$

The reaction rates are based on the modified eddy-breakup model and for the non-premixed modifications are of the forms:

$$R_A = - \bar{m}_A \, \rho\epsilon/k \qquad (a)$$

$$R_B = - \bar{m}_B \, \rho\epsilon/k \qquad (b)$$

$$R_C = \bar{m}_C \, \rho\epsilon/k \qquad (c)$$

$$(4.53);$$

$$R_E = - \bar{m}_E \, \rho\epsilon/k \qquad (d)$$

where again reactions are controlled by the species in shortest supply and take account of the priority of reaction (4.42(b)) over (4.42(a)).

The coefficients C_i and values V_i of the sources (4.53) and the values of m_i are given in Tables 4.5.1, 4.5.2 and 4.5.3.

Species A	Species B
$R_A = - \frac{\rho\epsilon}{k} \bar{m}_A$	$R_B = - \frac{\rho\epsilon}{k} (S_1 m_A + S_2 m_E)$
$\bar{m}_A = m_A$	$\bar{m}_B = S_1 m_A + S_2 m_E$
$C_A = \rho\epsilon/k$	$C_B = 10^{-10}$
$V_A = 0.0$	$V_B = - [S_1 m_A + S_2 m_E] \frac{\rho\epsilon}{k} 10^{10}$

Species C	Species E
$R_C = \frac{\rho\epsilon}{k} [\frac{cW_C}{aW_A} m_A + \frac{\bar{c}W_C}{eW_e} m_E]$	$R_E = - \frac{\rho\epsilon}{k} \bar{m}_E$
$\bar{m}_C = [\frac{cW_C}{aW_A} m_A + \frac{\bar{c}W_C}{eW_E} m_E]$	$\bar{m}_E = m_E$
$C_C = 10^{-10}$	$C_E = \rho\epsilon/k$
$V_C = \frac{\rho\epsilon}{k} \bar{m}_C 10^{10}$	$V_E = 0.0$

TABLE 4.5.1: CASE 4.1, EXCESS OF m_B

Species A	Species B
$R_A = -\bar{m}_A \dfrac{\rho\epsilon}{k}$	$R_B = -\dfrac{\rho\epsilon}{k}\bar{m}_B$
$\bar{m}_A = \dfrac{m_B - S_2 m_E}{S_1}$	$\bar{m}_B = m_B$
$C_A = 10^{-10}$	$C_B = \rho\epsilon/k$
$V_A = -\bar{m}_A \dfrac{\rho\epsilon}{k} 10^{10}$	$V_B = 0.0$

Species C	Species E
$R_C = \dfrac{\rho\epsilon}{k}\bar{m}_C$	$R_E = -\dfrac{\rho\epsilon}{k}\bar{m}_E$
$\bar{m}_C = \dfrac{cW_C}{aW_A}\left(\dfrac{m_B - S_2 m_E}{S_1}\right) + \dfrac{\bar{c}W_C}{eW_E} m_E$	$\bar{m}_E = m_E$
$C_C = 10^{-10}$	$C_E = \rho\epsilon/k$
$V_C = \dfrac{\rho\epsilon}{k}\bar{m}_C 10^{10}$	$V_E = 0.0$

TABLE 4.5.2: CASE 4.2.1 WITH $m_B > S_1 m_A/\lambda + S_2 m_E$

Species A	Species B
$R_A = -\bar{m}_A \dfrac{\rho\epsilon}{k}$	$R_B = -\bar{m}_B \dfrac{\rho\epsilon}{k}$
$\bar{m}_A = \dfrac{m_A m_B}{S_1 m_A + \lambda S_2 m_E}$	$\bar{m}_B = m_B$
$V_A = 0.0$	$V_B = 0.0$
$C_A = (\dfrac{m_B}{S_1 m_A + \lambda S_2 m_E}) \dfrac{\rho\epsilon}{k}$	$C_B = \dfrac{\rho\epsilon}{k}$

Species C	Species E
$R_C = \bar{m}_C \dfrac{\rho\epsilon}{k}$	$R_B = -\bar{m}_E \dfrac{\rho\epsilon}{k}$
$\bar{m}_C = \dfrac{cW_C}{aW_A} \dfrac{m_B m_A}{S_1 m_A + \lambda S_2 m_E}$ $+ \dfrac{\bar{c}W_C}{eW_E} \dfrac{\lambda m_B m_E}{S_1 m_A + \lambda S_2 m_E}$	$\bar{m}_E = \dfrac{\lambda m_E m_B}{S_1 m_A + \lambda S_2 m_E}$
$V_C = \bar{m}_C \dfrac{\rho\epsilon}{k} 10^{10}$	$V_E = 0.0$
$C_C = 10^{-10}$	$C_E = (\dfrac{\lambda m_B}{S_1 m_A + \lambda S_2 m_E}) \dfrac{\rho\epsilon}{k}$

TABLE 4.5.3: CASE 4.2.2 WITH $m_B \ll S_1 m_A / \lambda + S_2 m_E$

4.4.4   The Arrhenius influence

As mentioned above, Spalding (1971) in his eddy-breakup model suggested that the reaction rate should be taken as the minimum of the eddy-breakup rate and of the laminar Arrhenius rate, which expresses the temperature dependence of the rates.

Khalil (1982) defines the eddy-breakup timescale T_S as:

$$T_S = \frac{k}{\epsilon} \qquad\qquad (4.54);$$

and the 'chemical time' T_k, as given by Borghi (1973):

$$T_k = [A_\rho (\sum_{i \neq fuel} m_i) \exp(-E/RT)]^{-1} \qquad\qquad (4.55).$$

The ratio:

$$N_D = \frac{T_S}{T_k} \qquad\qquad (4.56);$$

is called the Damkohler number N_D.   When $N_D < 1.0$, then the reaction is kinetically influenced, due to rapid mixing which is characterised by large values of ϵ/k and when $N_D > 1.0$ the reaction is controlled by mixing.   Libby and Williams (Eds.1980) state on the subject of N_D that many different Damkohler numbers can be defined depending on the choice of reactants, flow characteristics and other factors, and therefore they suggest that caution should be exercised in drawing conclusions on the basis of the numerical value of a particular N_D.   Nevertheless, the following conclusions can be drawn.

In the regions where T_s (Equation (4.54)) is larger than T_k (Equation (4.55)), the mixing of the reactants is slow and the reactants are at a suitable temperature and concentration to react as soon as they intimately mix. Therefore, the reaction is controlled by the eddy-breakup rate (Equation (4.21)). On the other hand, when T_s is very small, which corresponds to a large dissipation rate of eddies and rapid mixing, the reaction is controlled by the Arrhenius rate. This implies that the reactants are in intimate contact but their temperature and concentrations are not suitable for the reaction to proceed very fast. Therefore, in this case, the smallest rate is the Arrhenius rate.

Assuming a reaction of the form:

$$A + B \rightarrow C + D \qquad (4.57);$$

the Arrhenius reactions rate is given by:

$$R = k \rho^2 X_A X_B \qquad (4.58);$$

where ρ is the molar density of the species and X_i is the mole fraction of species i. The reaction coefficient k is given by equations (4.4) and (4.5), which express the 'Arrhenius' and 'non-Arrhenius' behaviour of the reaction, respectively.

A more explicit formula for the Arrhenius rate is used in the present work, as follows:

$$R = [k \rho^2 (\sum_{i \neq m_{fu}} \frac{m_i}{W_i}) \frac{1}{W m_{fu}}] m_{fu} \qquad (4.59);$$

which is derived from Equation (4.58). The usual units of R are (Kg/m^3s) moles and of k mℓ/molecule/sec or $cm^3/mol/sec$.

4.4.4.1 <u>Parameters that Influence the Arrhenius rate</u>

(1) <u>Uncertainty factor (UF)</u>

"The uncertainty factor (UF) given for each rate coefficient, k, is such that k x UF and k/UF provide probable approximate upper and lower bounds respectively to k at the temperature within the range 1000-3000K, for which the rate coefficient is least accurately known. Such uncertainty factors take account of the random errors quoted by different authors, or possible systematic errors and of the need to extrapolate available results into temperature ranges often widely different from those of the experimentals themselves, and are consequently somewhat subjective. Large uncertainty bounds associated with the rate coefficient of a given reaction do not necessarily imply that there may be substantial errors in calculations involving the reaction. A reaction with large uncertainty factor in its rate coefficients may in any case be so fast that it is close to chemical equilibrium: on the other hand, a different reaction also with large rate uncertainties, may in any case be so slow, that its contributions are overwhelmed by those of concomitant mixing processes".

<u>Note</u> - the above is an extract from Jensen and Jones (1978).

(2) <u>'Third bodies' or 'collision parameters' and 'collision efficiencies'</u>

A particularly difficult point in the description of chemical kinetics arises

in the case of reactions involving 'third bodies' or 'collision partners'. Different third bodies have different (and sometimes unknown) efficiencies in these reactions. In the present work, 'third bodies' are assumed to be the 'bath-gas' molecules, M, most likely to be found in a typical flame, excluding the fuel. The idea of 'collision efficiencies' introduces an extra term, β_C in the calculation of the Arrhenius reaction coefficient, k, such that:

$$k_{new} = \beta_C \, k_{old} \qquad\qquad (4.60).$$

A list of collision efficiencies, β_C, can be found in Gardiner (1984) and Braulch et al (1972,1973,1976). For example, Gardiner (1984) states that the recommended collision efficiencies relative to H_2 for k values in a $H_2/O_2/CO$ system are those given in Table 4.6.

	H_2	O_2	N_2	H_2O	CO	CO_2	CH_4	Ar
β_C	1.0	0.4	0.4	6.5	0.75	1.5	6.5	0.35

TABLE 4.6: COLLISION EFFICIENCIES TABLE

For a particular problem, where some or all of the species are present, a weighted average has to be taken given by:

$$\beta_w = \frac{\sum\limits_{i \neq fuel} \frac{m_i}{w_i} \beta_i}{\sum\limits_{i \neq fuel} \frac{m_i}{w_i}} \qquad\qquad (4.61);$$

where w_i is the molecular weight of the species i.

4.5   Thermodynamic Properties

4.5.1   Enthalpy equations

The enthalpy equation contains the contributions from sensible energy and chemical energy (kinetic effects are neglected).

For our purpose the specific enthalpy is defined as:

$$h = C_p T + \sum_i m_i H_i \qquad (4.62);$$

for composition-dependent but not temperature-dependent C_p, where H_i is the heat of reaction with respect to the fuel i.

The specific heat, C_p, is given by:

$$C_p = \sum_j C_{pj} m_j \qquad (4.63).$$

For temperature- and composition-dependent C_p, h is given by:

$$h = \int_{T=273}^{T} [C_p(T)] \, dT + \sum_i m_i H_i \qquad (4.64);$$

where $C_p(T)$ is the specific heat of the mixture at a temperature T and is given by:

$$C_p(T) = \sum_i (a_i + b_i T + c_i T^{-2} + d_i T^2) \qquad (4.65);$$

where:

$$a_i = \frac{m_i w_i}{\Sigma m_i w_i} A_i$$

$$(4.66).$$

$$b_i = \frac{m_i w_i}{\Sigma m_i w_i} B_i \qquad \text{etc}$$

The coefficients A_i, B_i, C_i, etc, are given in Barin et al (1982) and originate from the definition of $C_{p,i}(T)$, the specific heat of the species i, defined as (Barin et al (1982)):

$$C_{p,i}(T) = A_i + B_i T + C_i T^{-2} + D_i T^2 \qquad (4.67).$$

Integrating Equation (4.64) we obtain:

$$h \equiv \sum_i (a_i T + \frac{b_i}{2} T^2 - \frac{c_i}{T} + \frac{d_i}{3} T^3) + K \qquad (4.68);$$

where:

$$K = \sum_i m_i H_i - \sum_i (a_i \bar{T} + \frac{b_i}{2} \bar{T}^2 - \frac{c_i}{\bar{T}} + \frac{d_i}{3} \bar{T}^3) \qquad (4.69).$$

Given h, Equation (4.68) can be solved using the Newton-Ramson method to retrieve the temperature T.

Differentiating Equation (4.64) we obtain:

$$\frac{dh}{dT} = \bar{C}_p (T) \qquad (4.70);$$

or

$$\frac{h(T) - h(\bar{T})}{T - \bar{T}} = \bar{C}_p(T) \qquad (4.71).$$

Equation (4.71) can now be used to retrieve the specific heat of the mixture at temperature T, so that:

$$h(T) = \bar{C}_p(T) (T-\bar{T}) + h(\bar{T}) \qquad (4.72);$$

where $\bar{C}_p(T)$ is the effective specific heat of the mixture.

Equations (4.62) and (4.64) also satisfy the transport equation (2.8). Given the temprature T, the specific heat C_p and specific enthalpy h, can also be retrieved, by employing Equations (4.72) and (4.65).

4.5.2 Density calculations

The density of the gaseous phase is calculated using the perfect gas law:

$$\rho = \frac{p}{RT} \qquad (4.73);$$

where p is the operating pressure,

$$R = R_0/M \qquad (4.74);$$

where R_0 is the universal gas constant, and

$$\frac{1}{M} = \Sigma \frac{m_i}{w_i} \qquad (4.75).$$

S_0 f Kg/s

S_1
(1-f)Kg/s

1 Kg/s M
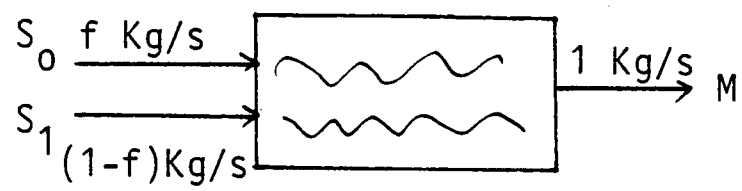
FIGURE 4.1: TWO-STREAM MIXING PROCESS

m^*_{dil}

$m_{dil} + m_{pr}$

m_{dil}

m^*_{fu}

m_{pr}

m_{pr}

m^*_{ox}

m_{ox}

m^*_{pr}

S_1-stream

f_{ST}

S_0-stream

0 P f 1
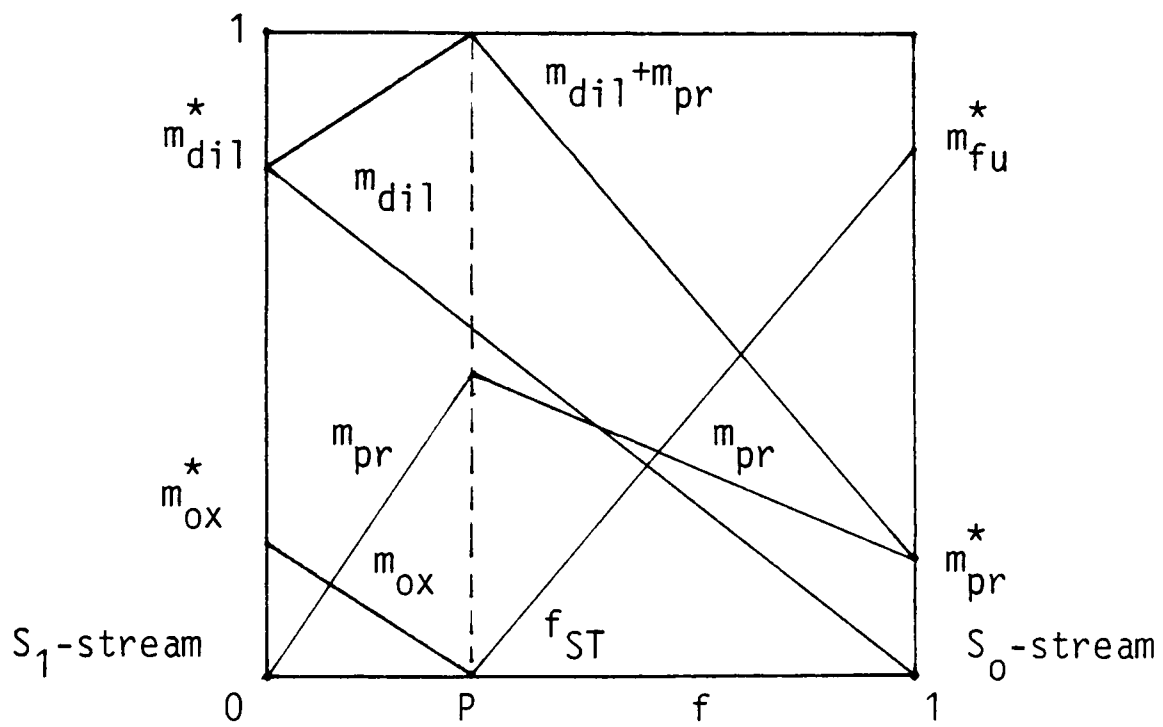
FIGURE 4.2: THE STOICHIOMETRIC DIAGRAM

-113-

CHAPTER 5 – THE OFF-GAS DUCTING SYSTEM

5.1   Introduction

The mathematical models and numerical procedures discussed in the previous sections, have been implemented within the PHOENICS framework, for simulating full-scale, modern, industrial off-gas ducting system of the type used in steelmaking.   Details of the geometrical configurations considered, the computational grids used, inlet-, outlet- and wall-boundary conditions and related parameters employed for the modelling of the off-gas ducting system processes, are given fully in the following sections.

The effects on the off-gas duct performance of such operating conditions, as the temperature and composition of the gases, loading, diameters and temperatures of the particles, influence of the inlet and auxiliary port positions and others, are also examined and results are presented and discussed.

The processes are considered to be either axisymmetric or three-dimensional.   They are turbulent and two-phase, where phase one refers to the gaseous phase, consisting of a mixture of gases, and phase two, is the particulate phase, consisting of pure iron particles assumed to be spherical and all of the same radius.

A number of different geometric configurations in two- and three-dimensions are considered and results of their simulations are presented and compared.

5.2   Inlet Conditions - Initial Values

Consider a cylindrical duct of radius R and polar coordinate axes as shown in Figure 5.1.

Inlet velocity profiles for the two phases must be provided and they are assumed to be equal. The inlet velocity distributions are taken to be defined by the following power law:

$$V(r) = V_{max} \left[1 - (\frac{r}{R})^n \right] \qquad (5.1);$$

where n is equal to 8, so as to give a typical turbulent profile. V_{max} can be obtained by employing Equation (5.1) to calculate a given volumetric flow, so that:

$$\text{Volumetric flow rate} = 2\pi V_{max} \int_0^R \left[1 - (\frac{r}{R})^n \right] r \, dr \qquad (5.2).$$

If we are given the mean inlet velocity V_{in} it follows that:

$$V_{max} = (\frac{n+2}{n}) V_{in} \qquad (5.3).$$

The kinetic energy of turbulence at the inlet k_{in} is assumed to be uniform and is estimated from the equation:

$$k_{in} = (0.01) V_{in}^2 \qquad (5.4);$$

and its dissipation rate, ϵ is calculated from Spalding (1982(a)):

$$\epsilon_{in} = C_D \frac{k_{in}^{3/2}}{l} \qquad (5.5);$$

where C_D is the turbulence model constant equal to 0.09 and ℓ is the characteristic lengthscale assumed to be R/10.

These two relations (5.4) and (5.5) give good representation of the mean level of the kinetic energy of turbulence and its dissipation rate in a fully developed pipe flow (Launder and Spalding (1974), Spalding (1982(a))).

The inlet enthalpies are those corresponding to the inlet temperature T_{in} and for the case of the gaseous phase is also related to the inlet chemical species concentrations m_i^*.

The radiation fluxes RX, RY and RZ are initialised to a value of the order of σT_{in}^4 W/m^2. This value corresponds to a constant temperature of T_{in} with no absorption or scattering of radiation.

The density of the pure iron particles is taken to be equal to 7897 Kg/m^3, their specific heat 750 J/Kg/K and their thermal conductivity 33 W/m/K. For the gaseous phase, the thermal conductivity is taken to be equal to 0.144 W/m/K.

The mass fraction of the particulate phase in gr/Nm^3 (say FECO) is obtained from the following equation, which is dependent on the local values of the velocities W_g and W_p, volume fractions R_g and R_p and densities ρ_g and ρ_p of the two phases:

$$FECO = \rho_o \frac{\rho_p \, R_p \, W_p}{\rho_g \, R_g \, W_g} \qquad (5.6)$$

where ρ_0 is the gas density under NTP. Equation (5.6) represents the ratio of the particle and gas mass fluxes through an area δA, multiplied by the NTP gas density to express the particle loading under normal conditions.

Latent heat of solidification is modelled as explained earlier, in Chapter 2, where the particle solidification temperature is taken to be equal to $1500^{\circ}C$ and the latent heat L, equal to 2.474×10^5 J/Kg.

Wall heat-transfer is accounted for using the prescribed model, described in Chapter 2. In cases where there are cooling tubes inside the off-duct, the wall heat-transfer is enhanced by multiplying the heat transfer rate per unit area (Equation (2.27)) by the appropriate area increase, arising from the bigger surface area of the cooling tubes with respect to the walls.

5.3   Outlet Boundary Conditions

Usually, the conditions at outlets are not known, but in most cases the outlet boundary is located in a region where the flow is expected to be everywhere outwards-directed and therefore insensitive to downstream conditions. It is then justifiable to set the coefficients linking the interior nodes to the neighbouring boundary ones to zero.

However, values of the velocity component normal to the outlet are obtained by prescribing an external pressure, so that the continuity equation is satisfied (eg. the correct outflow is computed from the difference in pressure between the prescribed external pressure and the calculated pressure in the outflow cell).

5.4　The Basic Model

Consider a simple off-duct configuration in three-dimensions, as shown in Figure 5.1, of radius R equal to 1.0m and of length L equal to 26.0m.

The inlet temperature of both phases is equal to $1575^{o}C$ and the wall is kept at a constant temperature of $300^{o}C$. The gaseous flow rate at inlet is 500 Nm^3/min (ie. 56.41 m^3/sec, under the given conditions), comprising of 66% CO, 11% CO_2, 13% H_2, 9% H_2O and 1% N_2. The specific heat of the gases is assumed to be constant and equal to 1552 $J/Kg/K$.

A basic model in two-dimensions is used as a starting point, eg. before the introduction of particle solidification, radiation and combustion. The purpose of exercising this model is to gain insight into the behaviour of the solutions *vis-a-vis* grid size, optimum relaxation parameters, and solution sweeps, which will be used for the complete model, without the additional complications and uncertainties of the full modelling.

5.4.1　Determining the optimal computational parameters

The selection of the optimum finite-difference grid, the relaxation parameters and the number of solution sweeps through the domain required for convergence is a complex task.

The aim is to establish the coarsest possible grid which, together with the appropriate relaxation parameters and the least possible number of sweeps, leads to practically accurate solutions of the original differential equations, without unrealistic computational demands. This is achieved in part by obtaining solutions with increasing number of grid nodes

and/or sweeps, until a stage is reached where the solution exhibits negligible changes with further increases in the number of nodes and/or sweeps.

The question of grid and sweep dependence for the early stages of the work was examined for the basic model only (because of computer time limitations), as for each test it was necessary to obtain a fully-converged solution in order to make a valid comparison of the results. Consequently, it is assumed that the grid sizes and optimum parameters for the simple two-dimensional case will also be suitable for the three-dimensional case. It would be desirable to confirm this by additional calculations using more refined grids in a three-dimensional case. However, the storage and CPU time requirements appear prohibitive in the context of the time-sharing mini-computer available for this work.

Runs were performed with the following grid sizes and number of iterations:

(1)   Particle of diameter 100μm and 100 g/Nm^2 concentration:

  (1a) 10x26 with 200 sweeps for convergence.

  (1b) 19x51 with 100 sweeps for convergence.

  (1c) 19x51 with 200 sweeps for convergence.

  (1d) 33x76 with 200 sweeps for convergence.

  (1e) 33x76 with 100 sweeps for convergence.

(2)   Particles of diameter 5μm and 10 g/Nm^3 concentration:

  (2a) 10x26 with 100 sweeps for convergence.

  (2b) 10x26 with 200 sweeps for convergence.

(2c) 19x51 with 200 sweeps for convergence.

(2d) 19x51 with 100 sweeps for convergence.

The 'reference cells' for the 10x26, 19x51 and 33x76 grids were (6,13), (11,25) and (18,36) respectively; these cells correspond to the same physical location in the domain.

Monotonic convergence was easily obtained for all cases, using a value of 0.1sec for the 'false-time step' relaxation parameter, applied for variables v_1, v_2, w_1, w_2, h_1 and h_2, to slow down their variation during the solution procedure.

The total CPU time for some of the above cases was:

(1a)	1413 sec	(2a)	723 sec
(1b)	2396 sec	(2b)	1445 sec
(1c)	4738 sec	(2c)	4876 sec
(1d)	10927 sec		

The first two grids, 10x26 and 19x51 above, required 200 sweeps for adequate convergence. Comparison of the results at the above reference cells is given in Tables 5.1 and 5.2.

Overall, the variables h_1, h_2, w_1, w_2, r_2, p_1 and p, for both particles sizes, have settled down well.

For the 100μm particle diameter agreement is good to about three significant figures for cases (1c) and (1d), and for the small particle size, the agreement is slightly better. Large (relative) changes in

radial velocities, v_1 and v_2, are acceptable since they are very small in comparison with the overall velocity magnitudes. Agreement in the turbulence variables k and ϵ is poor for both cases, especially for the larger particles. This is to be expected, since the turbulence model is highly sensitive to grid refinement. The variations with grid refinement, however, are not fed back strongly into the other flow quantities, which do not appear to be very strongly dependent on the predicted turbulence viscosity.

CASE GRID SWEEPS	1a 1x10x26 200	1b 1x19x51 100	1c 1x19x51 200	1d 1x33x76 200
VARIABLE				
H1	2.781×10^6	2.79×10^6	2.783×10^6	2.792×10^6
H2	1.349×10^6	1.339×10^6	1.352×10^6	1.337×10^6
KE	3.409	2.558	3.127	2.595
EP	7.728	4.962	6.614	4.974
V1	1.955×10^{-2}	1.675×10^{-2}	1.398×10^{-2}	1.624×10^{-2}
V2	2.353×10^{-2}	3.164×10^{-2}	1.866×10^{-2}	3.007×10^{-2}
W1	18.63	18.32	18.49	18.36
W2	17.19	16.72	17.01	17.05
R2	2.312×10^{-6}	2.295×10^{-6}	2.304×10^{-6}	2.226×10^{-6}
P1	9.805×10^4	9.805×10^4	9.805×10^4	9.805×10^4
RHO	0.1678	0.1672	0.1678	0.1671

TABLE 5.1: PARTICLES OF 100 μm DIAMETER AND $100g/Nm^3$ CONCENTRATION

CASE GRID SWEEPS	2a 1x10x26 100	2b 1x10x26 200	2c 1x19x51 200
VARIABLE			
H1	2.776×10^6	2.779×10^6	2.775×10^6
H2	1.342×10^6	1.340×10^6	1.341×10^6
KE	3.232	3.242	2.992
EP	7.130	7.154	6.161
V1	2.145×10^{-2}	2.152×10^{-2}	1.580×10^{-2}
V2	2.143×10^{-2}	2.151×10^{-2}	1.580×10^{-2}
W1	18.53	18.51	18.38
W2	18.50	18.45	18.33
R2	2.051×10^{-7}	2.081×10^{-7}	2.088×10^{-7}
P1	9.805×10^4	9.805×10^4	9.805×10^4
RHO	0.1680	0.1682	0.1680

TABLE 5.2: PARTICLES OF $5\mu m$ DIAMETER AND $10g/Nm^3$
CONCENTRATION

From the above studies it is concluded that cases (1c) and (2c) (ie. 19x51 grid) are the best appropriate to be employed; but that satisfactory results can be obtained using a 10x26 grid.

5.4.2 Heat losses for the basic model (no radiation)

Total heat losses have been calculated for different particle sizes and inlet particle concentrations and are as follows:

Particle Radius μm	Concentration g/Nm^3	Wp=Average Inlet velocity for particles Wg=Average Inlet velocity for gases	Heat Losses J/s
270	100	Wp=Wg	0.2343×10^7
100	100	Wp=Wg	0.2383×10^7
100	500	Wp=Wg	0.2373×10^7
100	1000	Wp=Wg	0.2334×10^7
100	100	Wp=1/2Wg	0.2382×10^7

TABLE 5.3:   BASIC MODEL TOTAL HEAT LOSSES

From those heat losses it is apparent that increase in the particle size or increase in the concentration decreases the heat losses.   In other words, particles tend to cool down more slowly than gases and an increase in their size or concentration reduces the rate of heat loss even more.

5.5   The Typical Off-Gas Duct

Figure 5.2 represents a simplified geometric model of a typical off-gas duct in two dimensions.

The actual equipment installed is of course more complex than this simplified model, but the essential geometrical features are taken into account.   For example, the model off-take has three main sections, as the actual equipment, as follows:

(i)   The skirt which is movable and in the form of a truncated

conical bundle of 124 cooling water tubes of diameter 60.3mm.

(II)   The primary zone which has a 2m diameter and is 3.3m high, consists of 124 tubes of 38mm diameter with 13mm fillet welded between each water-tube, as shown in Figure 5.3, which are part of the cooling system of the off-gas duct.

(iii)   The secondary zone which has 12 straight sides each 510mm in length, with 10 water-tubes on each side (also with fillet in between each water-tube, ie 12 sides 10x(38+13)), again part of the cooling system.

The cooling system, incorporated in the three sections, is designed to cope with a mixture of the off-gas and gas leaking in at the top of the skirt known as 'false-air', and its purpose is to keep the wall temperatures within acceptable limits.

In this model, primarily, we are interested in the primary and secondary zones. The increased surface-wall area, due to the cooling tubes, is taken into account by increasing appropriately the heat transfer coefficient at the walls. This increase provides an efficient and easy implementation taking into account the cooling effect of the water tubes. In the case of the skirt, gas leakage can occur above and below because of the pressure difference inside and outside the off-take duct. This leakage is represented in the model by the side-opening in Figure 5.2, positioned 3m above the entrance as shown. This leakage will be referred to as side-injection.

The results presented below in two-dimensions refer to the standard case of $50\mu m$ particle radius, $100gr/Nm^3$ particle inlet concentration with latent

heat and water-cooling tubes, based on the basic geometric model for a typical off-gas duct, with and without radiation.

The heat transfer coefficient at the walls was increased by 43.24% and 40.94%, for the primary and secondary zone respectively, for the appropriate sections of the off-take duct.

The cases examined are:

(I)   straight duct with and without side-injection and radiation; and

(II)   restricted particle inlet with and without radiation and side-injection.

The purpose of case (II) was to establish whether or not by restricting the particle inlet area from zero to half-radius, so that the particles are concentrated in the centre of the duct, away of the walls, it had any effect on the general flow properties.   Particles are assumed to enter the duct for case (II) at a mass flow rate equal to that of the standard case.

The volume flow rate through the side injection is 20% of the volume flow rate through the main inlet under NTP conditions.   The temperature of the side-injected gases is assumed to be $105^{\circ}C$.

All the computations reported below were carried out with a finite-domain grid having 10x26 control cells in the y- and z-directions, respectively. The distribution of grid cells is uniform in both directions.

For the results reported, convergence was good and it was unnecessary

to use relaxation. Two hundred domain sweeps were sufficient to ensure good convergence. The total CPU time used for cases including radiation was about 1800sec on the PRIME 750 minicomputer, compared with about 1500 seconds without radiation (200 sweeps, 10x26 grid).

5.6   Results without Radiation

5.6.1   Straight duct only

Figures 5.4 and 5.5 show the axial (w)-velocity components of the gaseous and particulate phases, respectively. The prescribed inlet profiles of about 22 m/sec can be seen at the inlet, and the exit velocities of both phases are about 18 m/sec. The particulate phase is slowing down faster than the gaseous phase because of gravity and lower velocities are found near the walls because of wall friction and low wall temperature. Highest velocities are found in the centre of the duct where the particles appear to be about 1 m/sec slower than the gases.

Figure 5.6 shows the temperature contours of the two phases in degrees Celsius. They are leaving the duct at about 1500°C in the centre. The solidification region (shaded) occupies a considerable area of the duct and the overall temperature drop between inlet and outlet is about 100°C with wall temperatures close to 1100°C near the top.

Figure 5.7 shows the particle mass fraction contours in gr/Nm^3. There are very low concentrations near the walls and fairly uniform concentrations over the rest of the duct. The highest concentrations are found about three-quarters of the way from the centreline to the wall at the lower end of the off-gas duct.

5.6.2 Straight duct with side-injection

Figures 5.8 and 5.9 show the axial (w)-velocities of the two phases, respectively. There is an increase in the velocities of the two phases of about 2 m/sec, over most of the duct, compared with the non-injection case, Figures 5.4 and 5.5. This is due to increased volumetric flow. The side-injection effect can be detected near the low walls and as before, the particles are slowing down faster than the gases. The exit velocities for both phases are about 19 m/sec, compared with about 18 m/sec for the non-injection case, Figures 5.4 and 5.5.

Figure 5.10 shows the temperature contours of the two phases. The exit temperatures are approximately 1270°C for both phases. Because of the cooling affect of the low temperature, side-injected gas, the temperatures are much lower than the non-injection case, Figure 5.6. As a result the solidification region (shaded) occupies a smaller region of the duct. Wall temperatures are lower than before with about 800°C near the injection port.

Figure 5.11 shows the particle mass fraction contours. The lowest values are found near the walls and the highest near the centreline of the duct, where the range of values is small, around the value of 105 gr/Nm^3. The effect of the side-injection is to create two regions of high concentrations. One small one near the entrance and another large one along the centreline of the duct. Hence, the net effect of the side-injection is that the particles are pushed towards the centreline of the duct, as expected. As a result they have minimal contact with the walls and therefore lose less heat than the gases. This explains the slightly higher temperature of the particulate phase at the exit (Figure

5. 10).

5.6.3   Particle restricted inlet

For the results presented in this section (and in Section 5.7.3 below),
whenever the particulate phase is very dilute (eg volume fraction less
than 10^{-7}) the axial velocity w, the radial velocity v and the enthalpy h,
of the particulate phase, are assigned the respective values w, v, h of
the gaseous phase.   The effects of these changes can be seen in the
results.   This was done because if the volume fraction is less than 10^{-7}
PHOENICS leaves w, v and h at arbitrary values.

Contours on all plots (except mass-fraction) which are below the dotted
line refer to the gaseous phase.

Figure 5.12 shows the axial (w)-velocity components of the two phases.
Again particles are slowing down faster than the gases.   As can be
seen from Figure 5.14, there are no particles near the walls and the
highest value of particle concentration is about half of the way from the
centreline to the wall.

Figure 5.13 shows the temperature contours.   The solidification
(shaded) region now occupies the upper part of the duct and compared
with Figure 5.6, both phases appear to be slightly hotter than before,
which is attributed to the fact that the particles are away from the
walls.

5.7   Results with Radiation

5.7.1   Straight duct

Figure 5.15 shows the axial (w)-velocity components of the two phases. Again the particulate phase is slowing down faster than the gaseous one and comparison with the non-radiation case, Figures 5.4 and 5.5, shows a more rapid decrease of the velocities, due to the lower temperatures and higher densities.   This is shown in Figures 5.9, 5.10 and 5.16. The exit velocities are now about 15 m/sec at the centre.

Figure 5.16 shows the temperature contours of the two phases.   They are leaving the duct with about 1090°C at the centre.   The solidification region (shaded) is now only at the lower part of the duct and although the temperature difference between the two phases at this region is considerable, the gap is closing very rapidly, giving a temperature difference at the exit of about 10°C.   Comparison with the non-radiation case, Figure 5.6, shows that radiation induces lower temperatures and a reduction of about 400°C in the exit temperatures of both phases, with considerable effect on the heat losses (see Section 5.9).

Figure 5.17 shows the particle mass-fraction contours.   It appears that the introduction of radiation produces no appreciable change in particle distribution, compared with Figure 5.7.

5.7.2   Straight duct with side-injection

Figure 5.18 shows the axial (w)-velocity components of the two phases. There is an increase in the velocities of both phases due to the side-injected gas, by about 2 m/sec over most of the region, compared with the non-injection case, Figures 5.8 and 5.9.   The side-injection

effect can be detected near the walls at the lower part of the duct and because of gravity, particles are slower than the gases, and the two phases have an exit velocity of about 17 m/sec.

Figure 5.19 shows the temperature contours (^{o}C) for the two phases. Wall temperatures are lower than the non-injection cases (Figure 5.16) due to the low temperature injected gas. The overall effect of the injection is a reduction in the temperatures of the two phases at the exit and over the rest of the duct, with an exit temperature of about 1020°C. There is a much smaller solidification region (shaded) at the lower part of the duct, very close to the side-slot, due to the influence of the low temperature side-injected gas. Temperature drop at exit between wall and centre of the duct is now about 300°C, compared with 400°C of Figure 5.6.

Figure 5.20 presents the particle mass-fraction contours with low values near the walls and highest near the centre of the duct.

5.7.3   Straight duct with restricted particle inlet

Figure 5.21 shows the axial velocity (w)-components of the two phases, and as before, particles are slowing down faster than the gases with exit velocities for the two phases of about 14 m/sec. Compared with Figure 5.15, it can be seen that in the present case the exit velocities are slower, due to the more heavy concentration of particles in the middle of the duct (Figure 5.23).

Figure 5.22 shows the temperature contours and the particle solidification area (shaded). Exit temperatures are about 1100°C, slightly higher than before (Figure 5.16).

Figure 5.23 shows the particle mass-fraction contours, with fairly uniform high concentration distributions in the centre and low at the walls.

5.7.4   Straight duct - radiation-side inlet, restricted-particle inlet

Figure 5.24 shows the axial (w)-velocity components of the two phases. It can be seen that the side-injected gas increases the velocities of both phases with the bigger increase observed in the gaseous phase. However, near the centre of the duct, immediately above the side-injection area, the particles appear to go faster than the gases, but very soon they slow down as they progress up the duct and their velocities are slower than that of the gases at the exit.

Figure 5.25 shows the temperature contours which again are very much the same as in the non side-injection case, Figure 5.22, except for the very low-temperatures near the injection area, due to the low side-injected gas temperature.

Figure 5.26 shows the particle mass-fraction contours.   The joint effect of the restricted inlet and side-injection is to push the particles to the centre of the duct, thus increasing their concentration.   It appears that there are virtually no particles in the region near the walls.

5.8   Comparison with Experimental Results

The exit temperatures of a typical off-gas duct were measured experimentally with the help of a thermocouple in an open (exposed) sheath.

Despite the advance techniques developed over the years for flow-field

modelling and diagnostics (Gupta and Lilley (1985)), the fact remains that experimental measurements in complex flow situations are very difficult to make, and in many cases, their accuracy is questionable. In the case of a normal gas environment with cool walls, the use of a thermocouple could lead to a significant underestimation of the gas temperature. However, if there are considerable amounts of dust present and the thermocouple is in the centre of the gas stream, then there will be little radiation heat transfer between the walls and the sheath and the measurements can be assumed to be reasonably accurate.

The measured temperatures (J Moodie (1984)) were found to be between $1000^{o}C$ and $1100^{o}C$ (ie 10% variation). The temperatures predicted by the model for all cases with radiation agree very well with the measured values, since they range between the above values. The predicted values with no radiation present depart considerably from the experimental values.

Case 5.7.2 is the closest geometric representation to the typical off-gas duct and in this case the predicted gaseous temperature of about $1020^{o}C$ is well within the measured values. Because of the complexity of the flow in realistic situations other experimental results were difficult to be obtained.

5.9   Standard Case - Heat Losses Parametric Study

In all the above calculations, the gas absorptivity coefficient (a_g), was taken to be equal to 0.15 (m^{-1}), the particle absorptivity coefficient (a_p), equal to 0.1, the particle scattering coefficient (s_p), equal to 0.01 and the wall emissivity (ϵ_w) equal to 0.8. These values were

provided by the collaborating establishment.

The heat losses for the standard case with radiation were found to be 0.8068×10^7 J/s, using the above values, compared with the value of 0.3523×10^7 J/s, for the standard case without radiation.

Parametric studies were performed to find the influence of the gas absorptivity, particle absorptivity, and the particle scattering coefficients, wall temperature and wall emissivity variations and low z-boundary condition variation, on the system total heat losses. These results are presented in the following tables.

5.9.1 Variation of a_p, s_p, a_g radiation parameters

The following tables present the influence of radiation parameters a_p (Table 5.4, Figure 5.27); a_g (Table 5.5, Figure 5.28); and s_p (Table 5.6) on the total heat losses.

From the tables below, it appears that a_g (Figure 5.28, Table 5.5) has the greatest effect on the total heat losses and the bigger its value the greater the heat losses.

$a_g=0.15$; $s_p=0.01$					
a_p	0.1	0.2	0.3	0.4	0.5
Heat losses J/s, $\times 10^7$	0.8068	0.8104	0.8175	0.824	0.827

TABLE 5.4: INFLUENCE OF a_p (DIMENSIONLESS), FIGURE 5.27

-133-

a_p=0.1; s_p=0.01					
a_g	0.05	0.1	0.2	0.25	0.3
Heat losses J/s, x10^7	0.5581	0.6959	0.8843	0.9403	0.9830

TABLE 5.5: INFLUENCE OF a_g (m^{-1}), FIGURE 5.28

a_p=0.1; a_g=0.15					
s_p	0.02	0.03	0.04	0.05	0.5
Heat losses J/s, x10^7	0.8105	0.8106	0.8108	0.8109	0.8230

TABLE 5.6: INFLUENCE OF s_p (DIMENSIONLESS)

The influence of a_p (Table 5.4, Figure 5.27) is very small compared to that of a_g. The influence of s_p (Table 5.6) was found to be so small that it can be disregarded as long as: $a_p/s_p \geq 10$.

In summary, for the standard case of 50μm radius and 100 gr/Nm^3 particle inlet concentration, a_g seems to be the dominant parameter for the heat losses, with minimal contributions from the particulate phase parameters.

5.9.2 Variation of wall temperature

Two sets of heat losses are presented, one with radiation and one without radiation, for comparison purposes:

T_W (C)	200	300	400
Heat losses J/s x 10^7	0.8315	0.8068	0.7838

TABLE 5.7:   INFLUENCE OF WALL TEMPERATURE (RADIATION CASE)

T_W (C)	200	300	400
Heat losses J/s x 10^7	0.3827	0.3523	0.3221

TABLE 5.8:   INFLUENCE OF WALL TEMPERATURE (WITHOUT RADIATION)

As expected, the results indicate (Tables 5.7 and 5.8, Figure 5.29), that for both radiating and non-radiation cases, the lower the wall temperature, the greater the total heat losses.

5.9.3   Wall emissivity (ϵ_w) variation

ϵ_w	0.0	0.5	0.8	1.0
Heat losses J/s x 10^7	0.3479	0.7825	0.8068	0.8147

TABLE 5.9:   INFLUENCE OF WALL EMISSIVITY (Figure 5.30)

These results suggest that the highest heat losses are obtained with $\epsilon_w = 1.0$ (ie with a black wall surface), and the lowest with $\epsilon_w = 0.0$ (ie

very highly polished surface).

It is interesting to note that the heat losses for $\epsilon_w = 0.0$ are very close to those for the standard non-radiating case, which are equal to 0.3523×10^7 J/s. This is because, when ϵ_w is very low the walls act as reflecting surfaces and little radiation escapes to the wall. As a result, radiation merely redistributes heat inside the duct.

5.9.4 Low z-direction boundary condition variation

The low z-boundary condition $dRZ/dz|_{z=0}$ is defined by Equation (3.31), as:

$$\frac{dRZ}{dz}\bigg|_{z=0} = (a_g + a_p' + s_p')K \qquad (5.7);$$

where $K = \alpha \, \epsilon_g \, \sigma \, T_{in}^4$ $\qquad (5.8);$

and:

α = radiation percentage crossing the plane z=0 from the furnace below.

ϵ_g = gas absorptivity at inlet (m^{-1}).

σ = Stefan-Boltzmann constant $(W/m^2/K)$.

T_{in} = gas temperature at inlet (K).

To determine the influence of the boundary condition two cases were considered:

Case 1

K=0, ie. no radiation is crossing the plane z=0, from the furnace below

giving heat losses equal to: 0.8089×10^7 J/s.

Case 2

$K = \sigma T_{in}^4$, assuming $\alpha = 1$ and $\epsilon_g = 1.0$ giving heat losses equal to: 0.7596×10^7 J/s.

Also from the standard case, where $\alpha = 0.5$ and $\epsilon = 0.1$, the heat losses were equal to 0.8068×10^7 J/s.

The results show that the higher the value of K the lower the heat loss. On the other hand, the higher the value of K, the higher will be the temperatures in the duct. This apparent anomaly can be explained as follows:

In the presence of radiation the heat lost per second by the particles and gases is not the same as the heat extracted through the wall. In fact:

$$
\begin{bmatrix} \text{Heat lost per second} \\ \text{by particles and gases} \end{bmatrix} = \begin{bmatrix} \text{Net heat absorbed} \\ \text{by wall per second} \\ \text{due to convection} \\ \text{and radiation} \end{bmatrix} - \begin{bmatrix} \text{Net radiation} \\ \text{flux out of top} \\ \text{and bottom of} \\ \text{duct} \end{bmatrix}
$$

5.9.5   Heat losses with particle size variation

Table 5.10 presents heat losses with respect to particle size variation down to 40μm. From the table it appears that heat losses are independent of the particle size down to 40μm radius. However, for smaller sizes, heat losses are expected to be considerably greater since the particle surface area is inversely proportional to particle radius (Equation (3.11)).

At this stage, convergence problems prevented the calculation of the heat losses for smaller particle sizes. However, when combustion was introduced (see Chapter 6) results were obtained for particle sizes down to $0.5\mu m$ (see Table 6.2, Figure 6.10) which showed the small particle size influence on the heat losses.

Particle Radius, μm	40	50	100	150
Heat Losses J/s x 10^7	0.8071	0.8068	0.8025	0.795

TABLE 5.10: PARTICLE SIZE INFLUENCE

5.9.6 Heat losses - summary

All the results above are based on the standard case with:

Particle inlet concentration	= 100 gr/Nm^3
Particle radius	= 50μm
Gas absorptivity coefficient (a_g)	= 0.15 m^{-1}
Particle absorptivity coefficient (a_p)	= 0.1
Particle scattering coefficient (s_p)	= 0.01
Wall emissivity (ϵ_w)	= 0.8
Wall temperature (T_w)	= 300°C

Table 5.11 presents a summary of the heat losses for radiation and non-radiation standard cases.

Case	Remarks	Heat Losses $J/s. \times 10^7$
Standard Duct - radiation	Section 5.7.1	0.8068
Standard Duct - no radiation	Section 5.6.1	0.3523
Side injection - radiation	Section 5.7.2	0.6025
Annular duct - no radiation	Section 5.6.3	0.3523
Annular duct - radiation	Section 5.7.3	0.7993
Annular duct - radiation - side injection	Section 5.7.4	0.6015

TABLE 5.11: SUMMARY - HEAT LOSSES

The standard case values with radiation agree well with experimental results (J Moodie (1984)). The grid used (10x26) was found to be adequate for the present calculations.

Side-injected gas and the particle annular inlet distribution seem to have little effect on the overall heat losses, as it was shown above.

The above results have demonstrated the success of the new radiation model, predicting temperatures at the top of the duct close to the measured values. The model also fits easily into the existing PHOENICS framework and is general in its application.

The above results show that the effect of radiation on a turbulent two-phase flow can be of considerable importance and that the most important factor is the gas absorptivity coefficient.

A number of boundary conditions were tried on the radiation model and it was found that they played little role in the determination of the results. In the end, it was decided to use the most obvious boundary conditions which were described above.

It has been found that the radiation fluxes converge more slowly than the other variables. In practice some Gauss-Seidel iterations for the radiation fluxes may be necessary for every one sweep for the other variables, for at least a few sweeps, adding an extra 15-20% to the total CPU time which was 1500 seconds.

5.10   Results with Variable Specific Heat

All the results previously reported were obtained using a constant specific heat for the gases. In order to establish the effect of variable specific heat (temperature and composition dependent), two cases were considered, one with radiation and one without radiation for the straight duct configuration.

Figures 5.31 and 5.33 show the temperature contours for the radiation and non-radiation cases respectively. Comparing these results with the respective constant specific heat cases, Figures 5.6 and 5.16, it can be seen that the predicted temperatures are lower than before by about 50^oC, with close agreement on the predicted wall temperatures. This can be seen from Figure 5.35 where exit gas temperatures are plotted against radial distance for constant and variable specific heat for the radiation case.

The predicted temperature difference of about 50^oC considerably affects

the velocities of the two phases shown in Figures 5.32 and 5.34 compared with the respective constant specific heat cases, Figures 5.4, 5.5 and 5.15.

These effects are attributed to the fact that the constant specific heat of 1552 J/kg/K originally used is too high and not consistent with the large temperature variations.
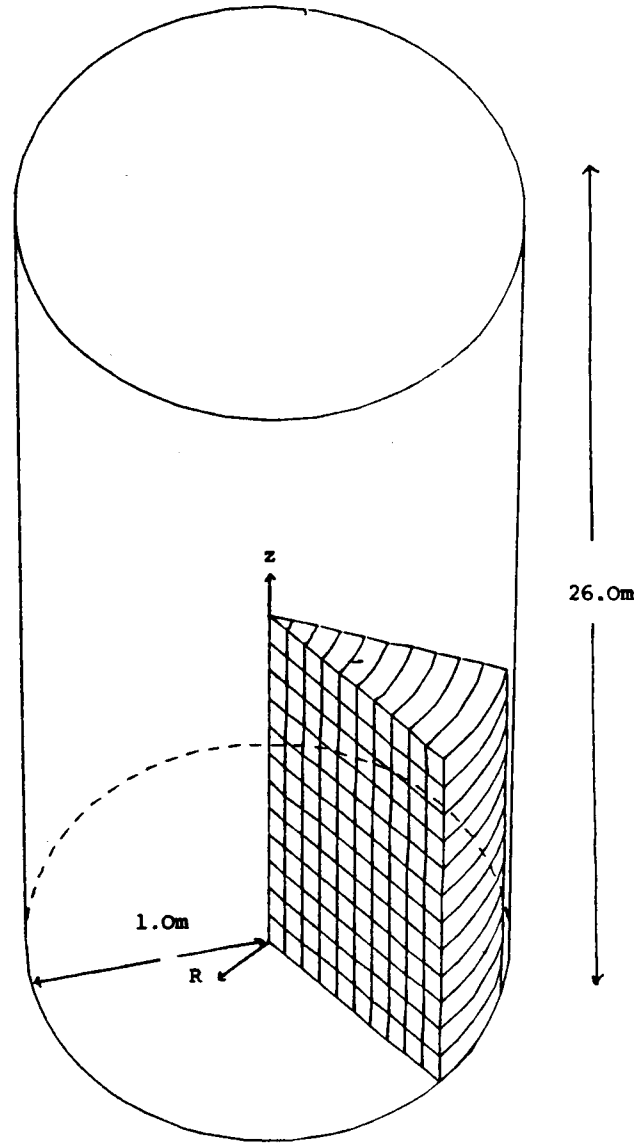
FIGURE 5.1: SIMPLE OFF-GAS DUCT
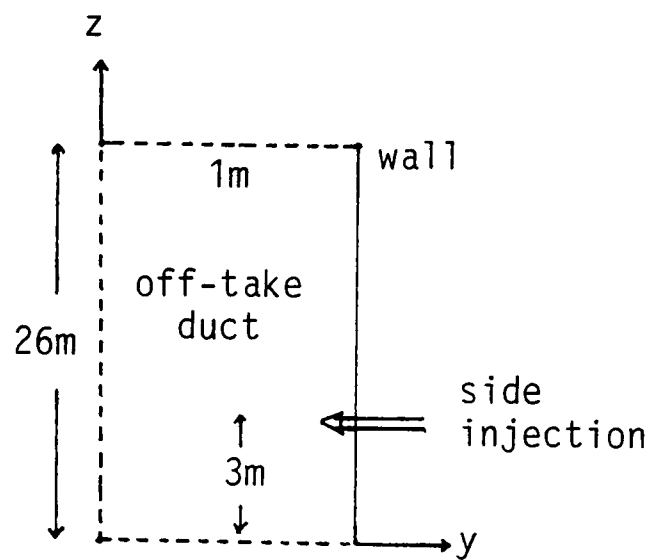
FIGURE 5.2: TYPICAL OFF-GAS DUCT
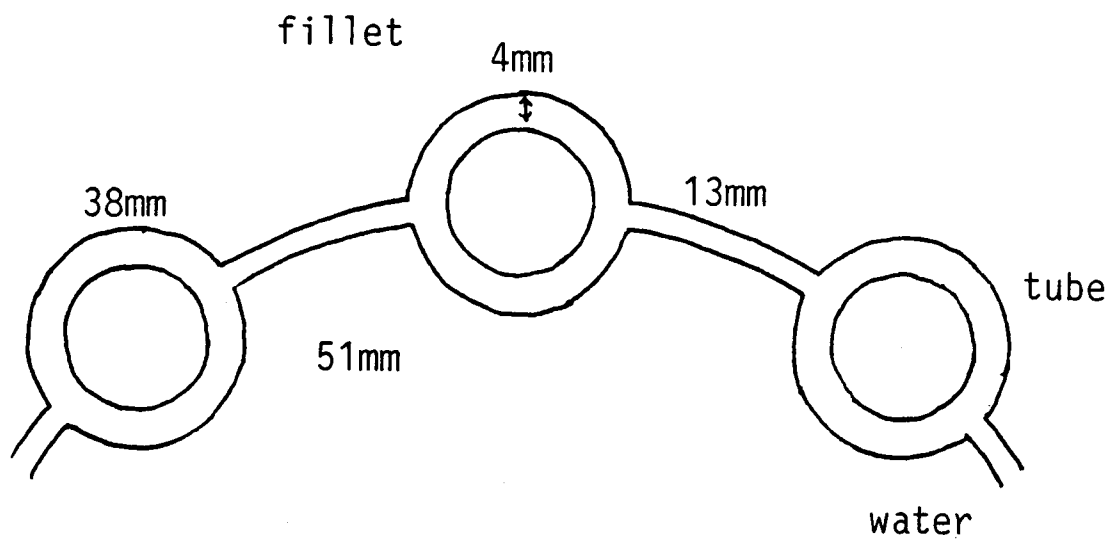
FIGURE 5.3: COOLING TUBES DESIGN
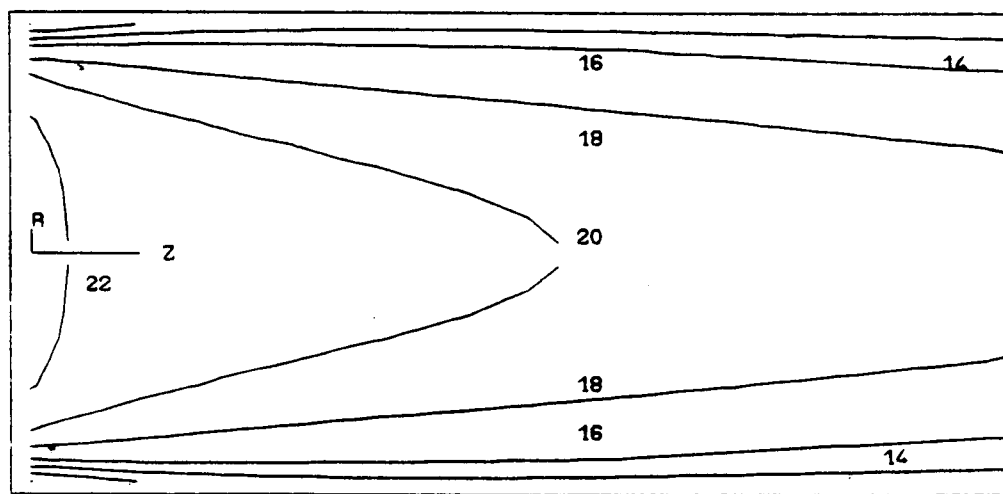
FIGURE 5.4: AXIAL VELOCITIES FOR GASES
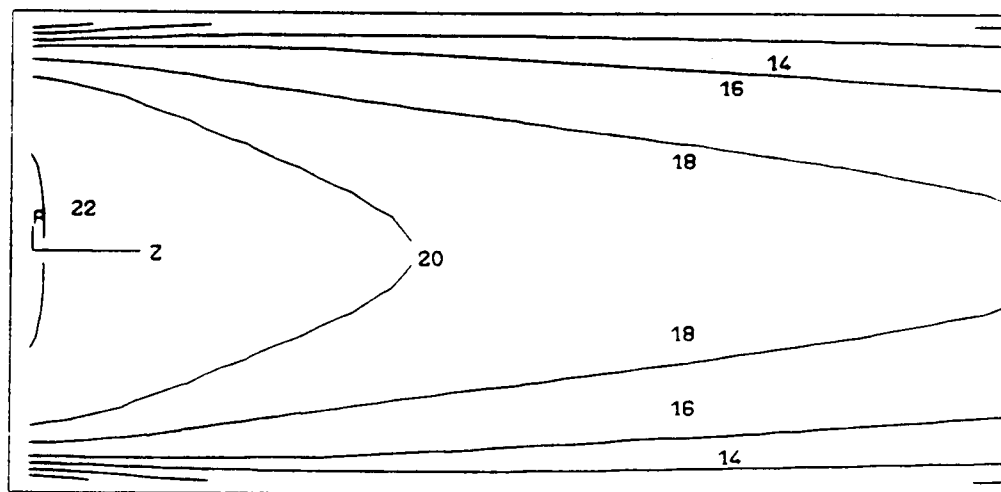
FIGURE 5.5: AXIAL VELOCITIES FOR PARTICLES
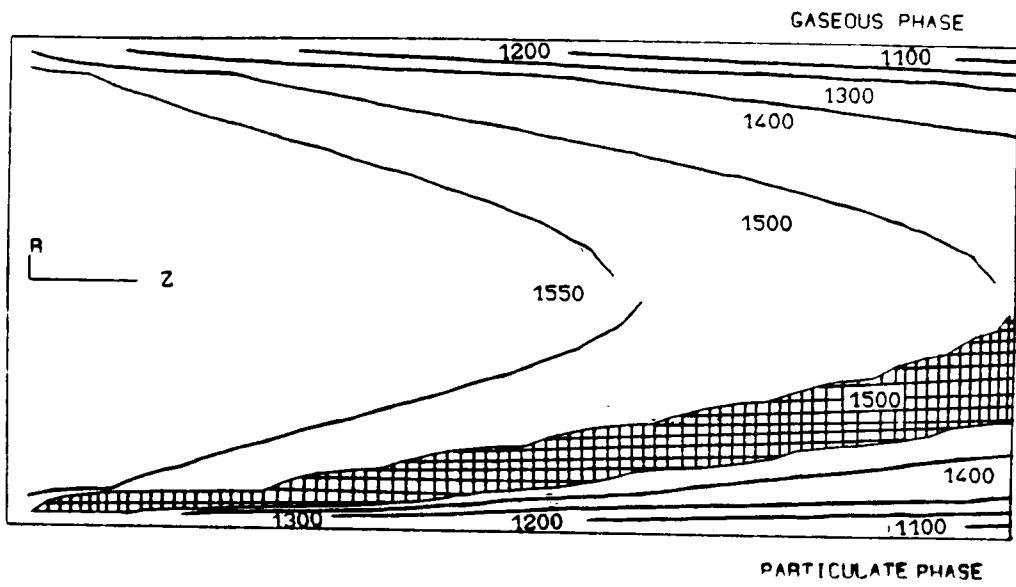
FIGURE 5.6: TEMPERATURE CONTOURS (C)
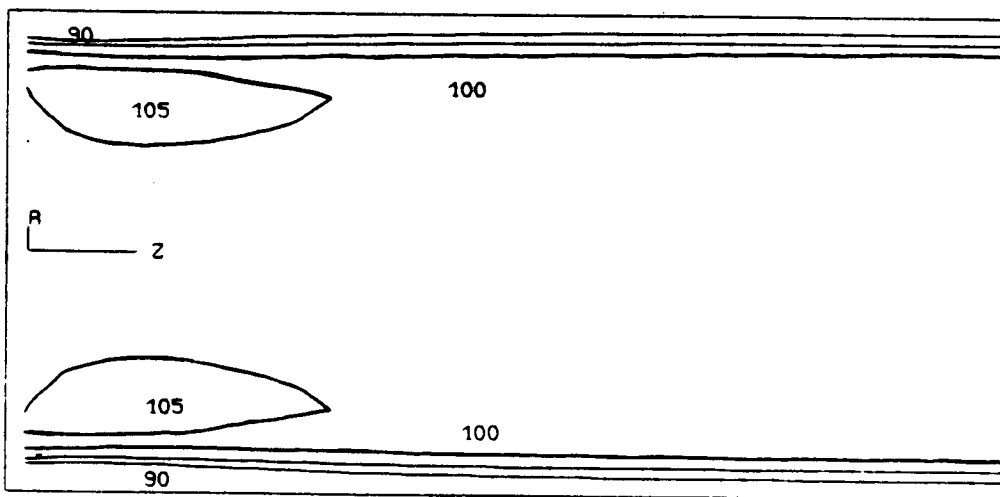
FIGURE 5.7: PARTICLE MASS-FRACTION CONTOURS
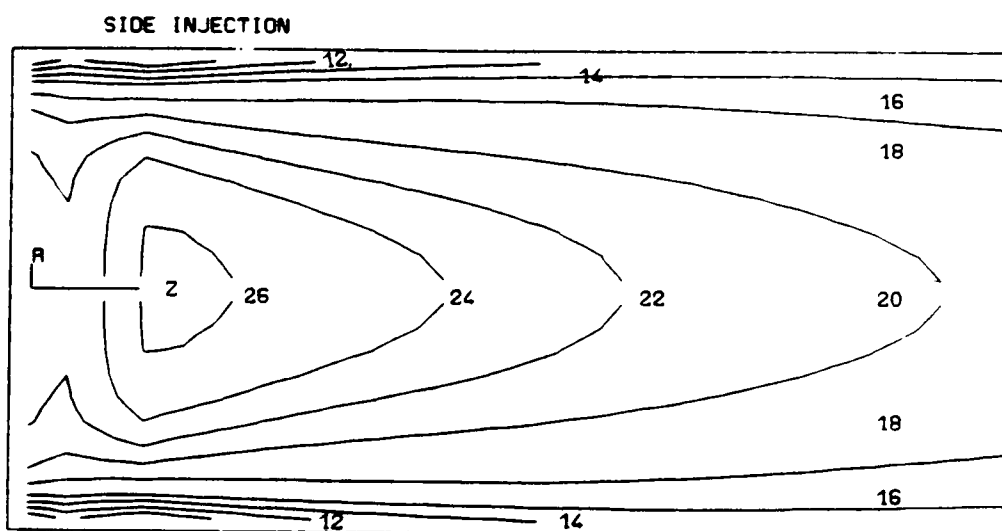
FIGURE 5.8: AXIAL VELOCITIES FOR GASES

SIDE INJECTION
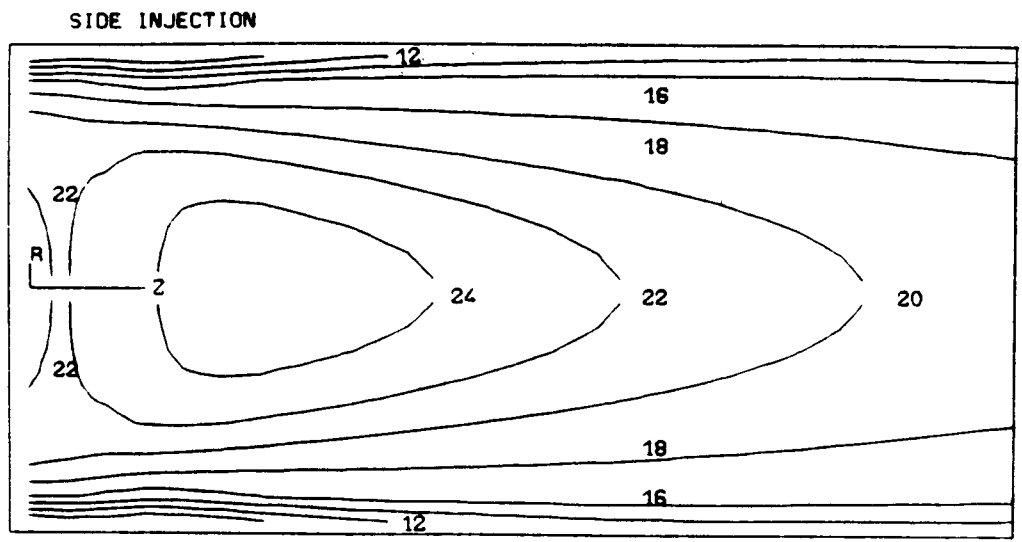
FIGURE 5.9: AXIAL VELOCITIES FOR PARTICLES

GASEOUS PHASE

PARTICULATE PHASE
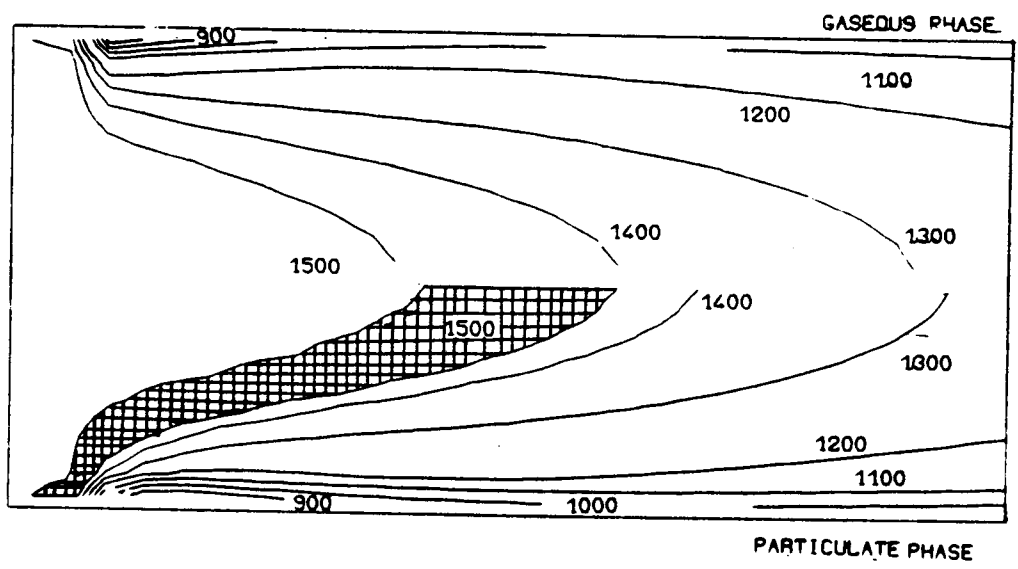
FIGURE 5.10: TEMPERATURE CONTOURS (C)

SIDE INJECTION
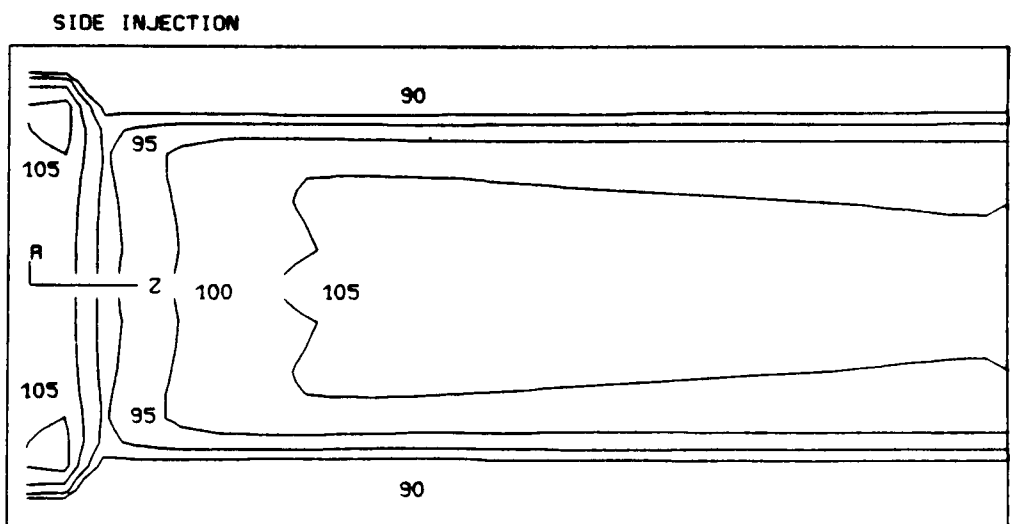
FIGURE 5.11: PARTICLE MASS-FRACTION CONTOURS

-145-
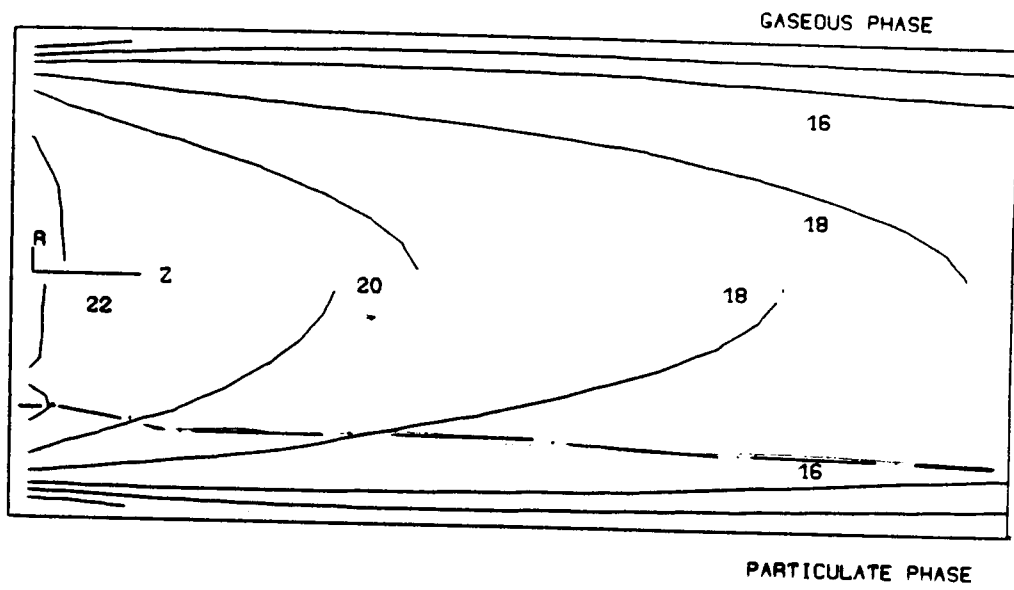
FIGURE 5.12: AXIAL VELOCITY COMPONENTS
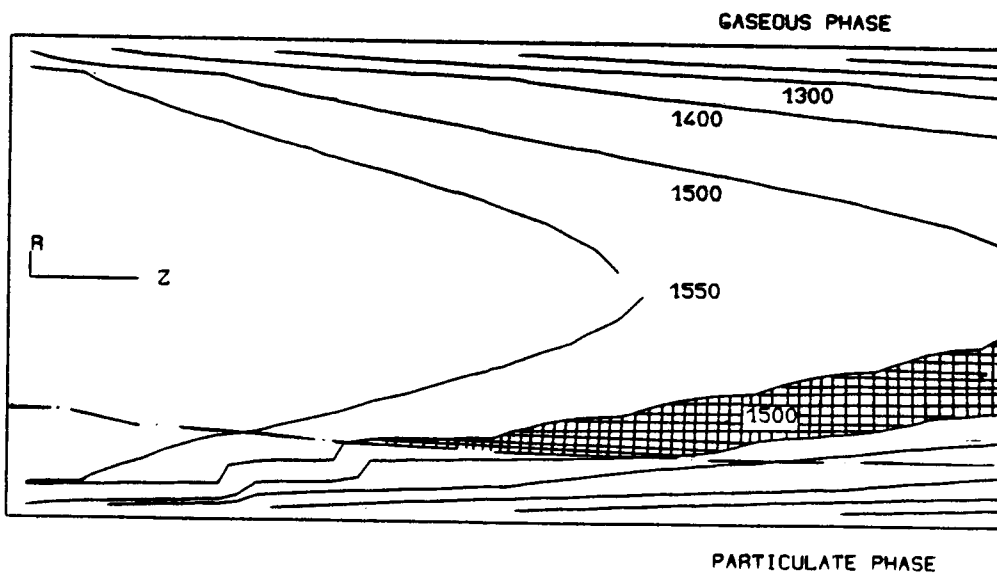
FIGURE 5.13: TEMPERATURE CONTOURS (C)
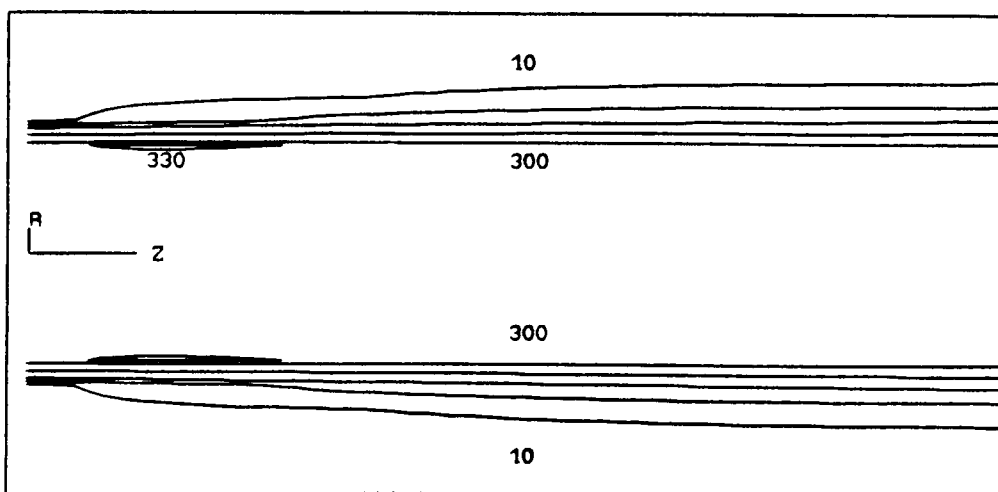
FIGURE 5.14: PARTICLE MASS-FRACTION CONTOURS

GASEOUS PHASE

PARTICULATE PHASE
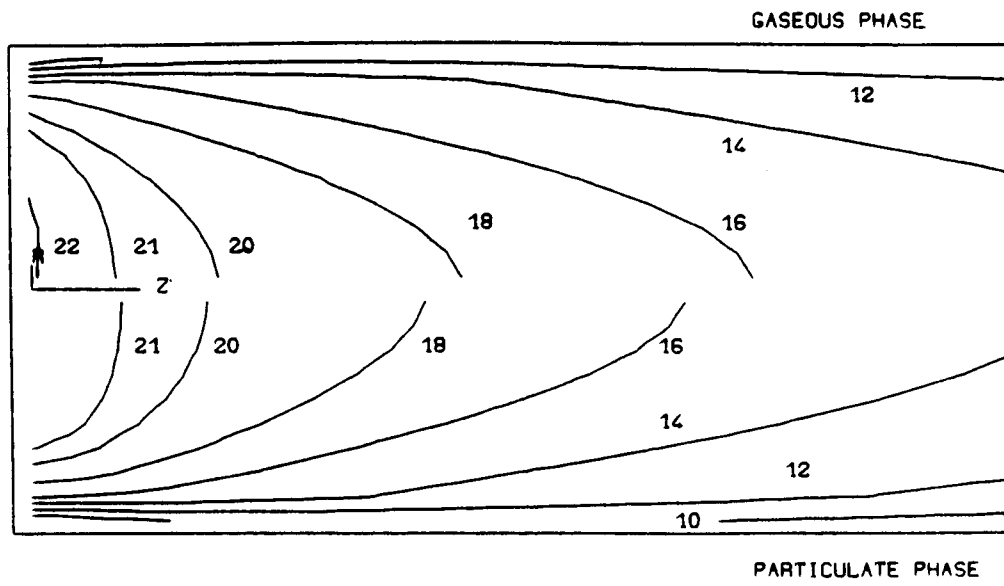
FIGURE 5.15: AXIAL VELOCITY COMPONENTS

GASEOUS PHASE

PARTICULATE PHASE
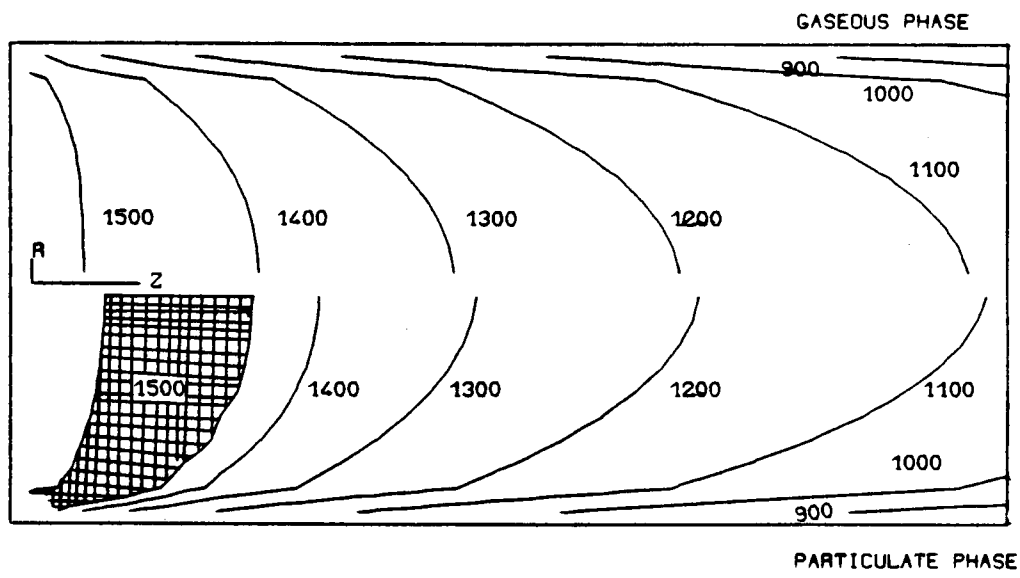
FIGURE 5.16: TEMPERATURE CONTOURS (C)
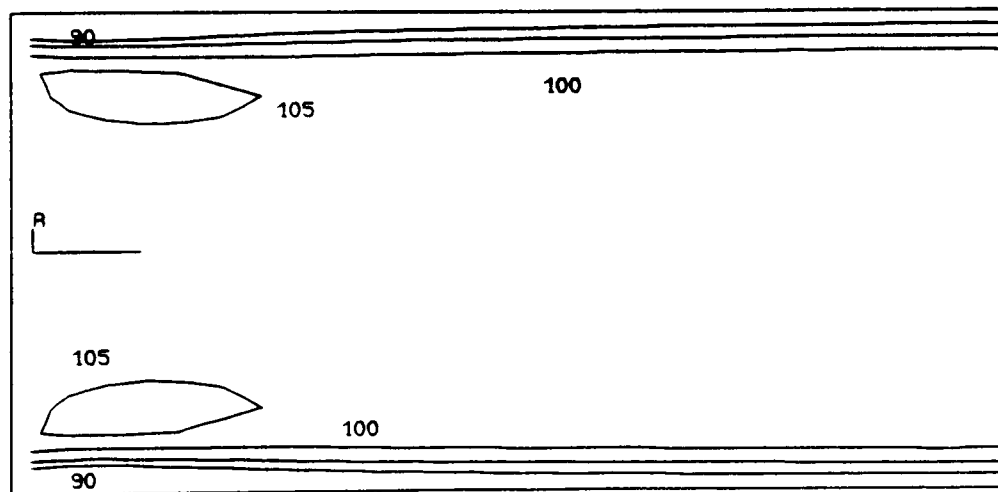
FIGURE 5.17: PARTICLE MASS-FRACTION CONTOURS
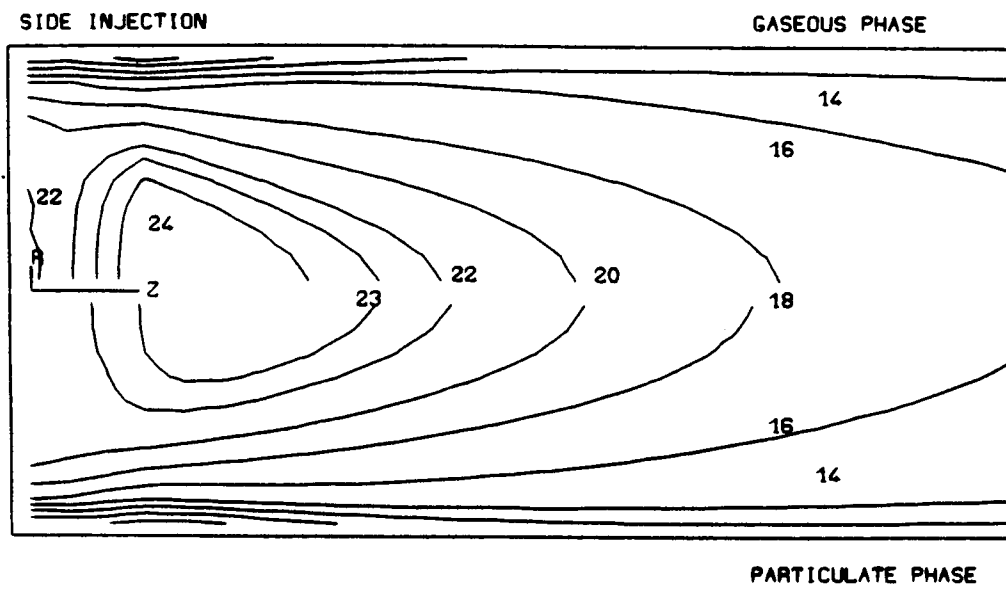
FIGURE 5.18: AXIAL VELOCITY COMPONENTS
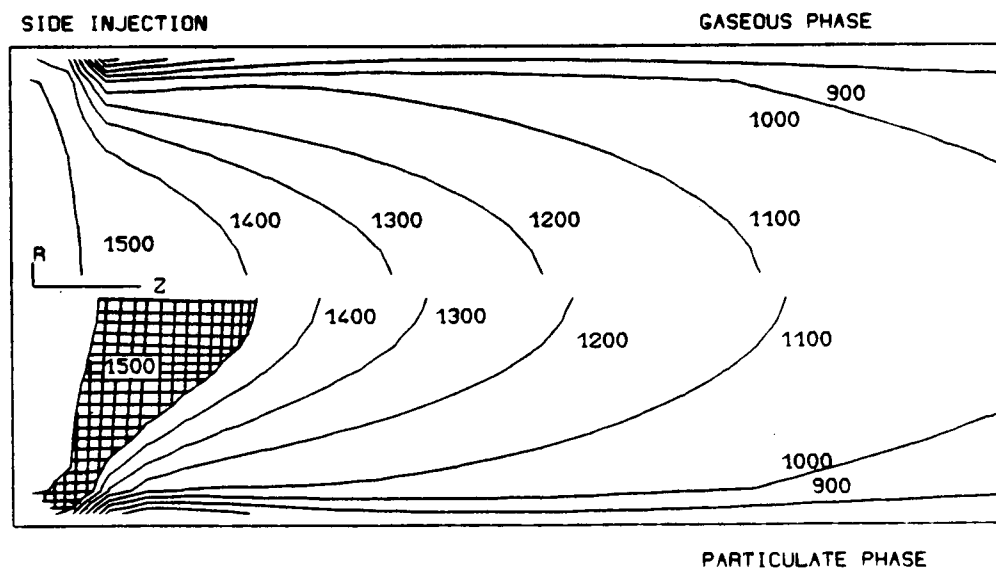
FIGURE 5.19: TEMPERATURE CONTOURS (C)
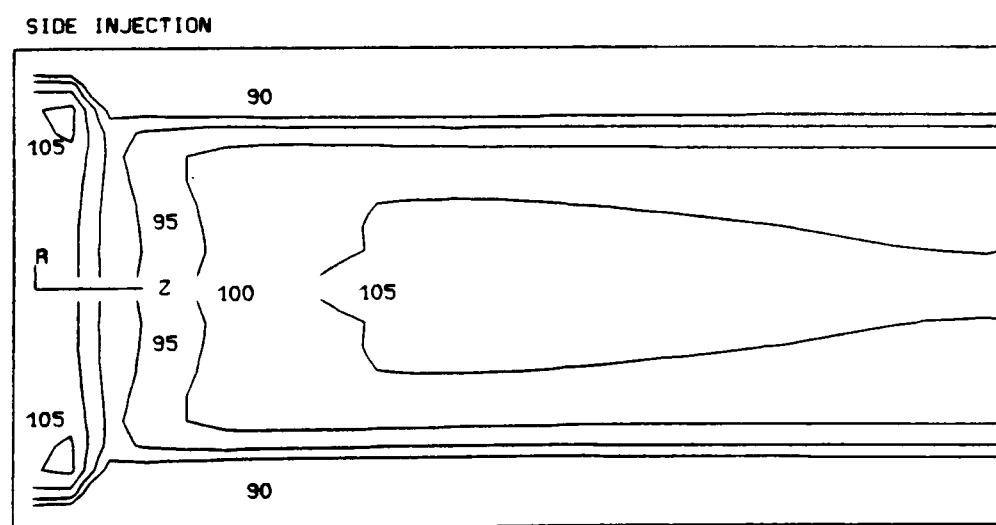
FIGURE 5.20: PARTICLE MASS-FRACTION CONTOURS

-148-
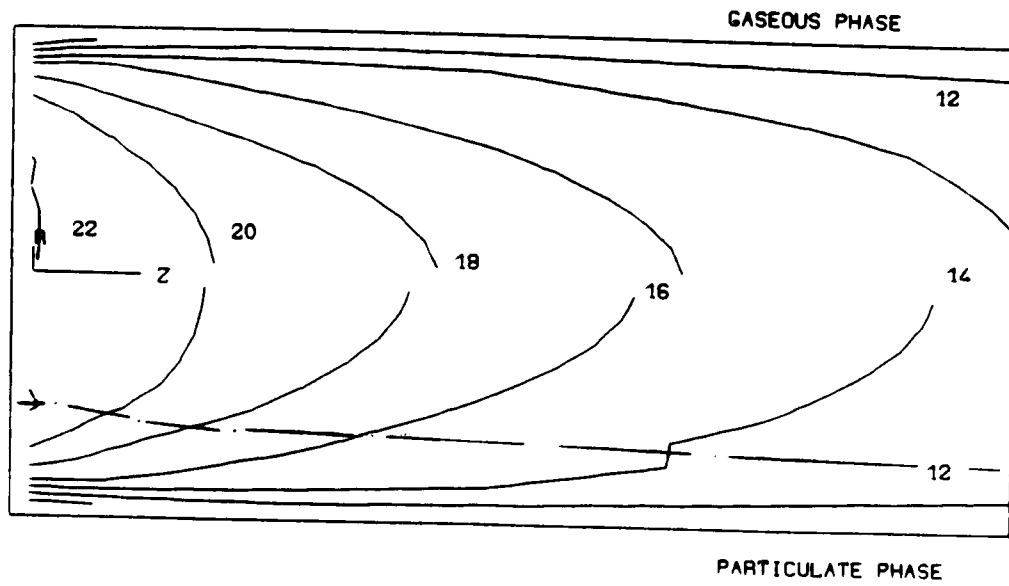
FIGURE 5.21: AXIAL VELOCITY COMPONENTS
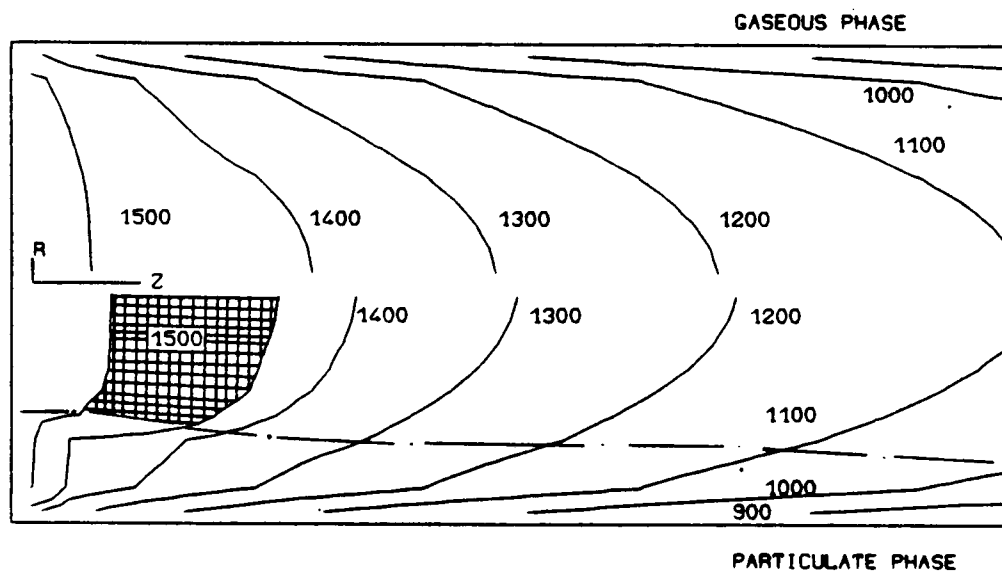
FIGURE 5.22: TEMPERATURE CONTOURS (C)
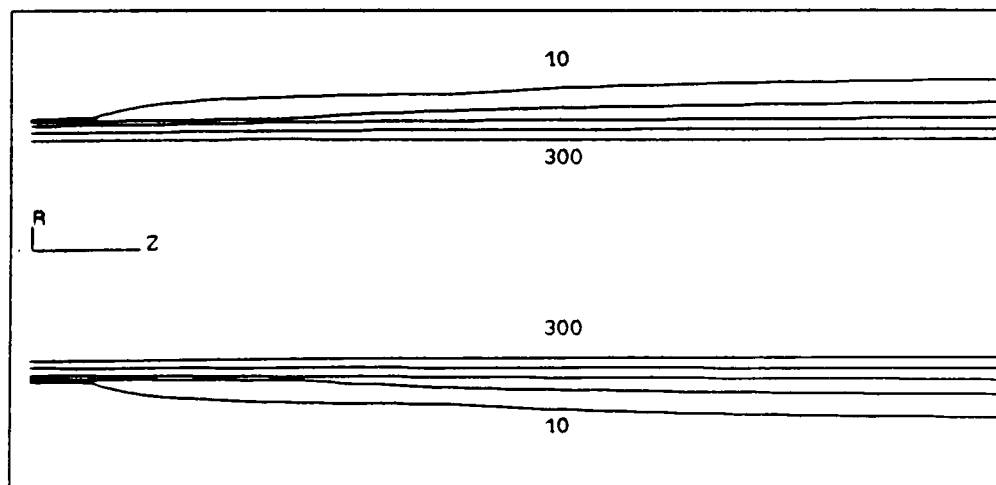
FIGURE 5.23: PARTICLE MASS-FRACTION CONTOURS

GASEOUS PHASE
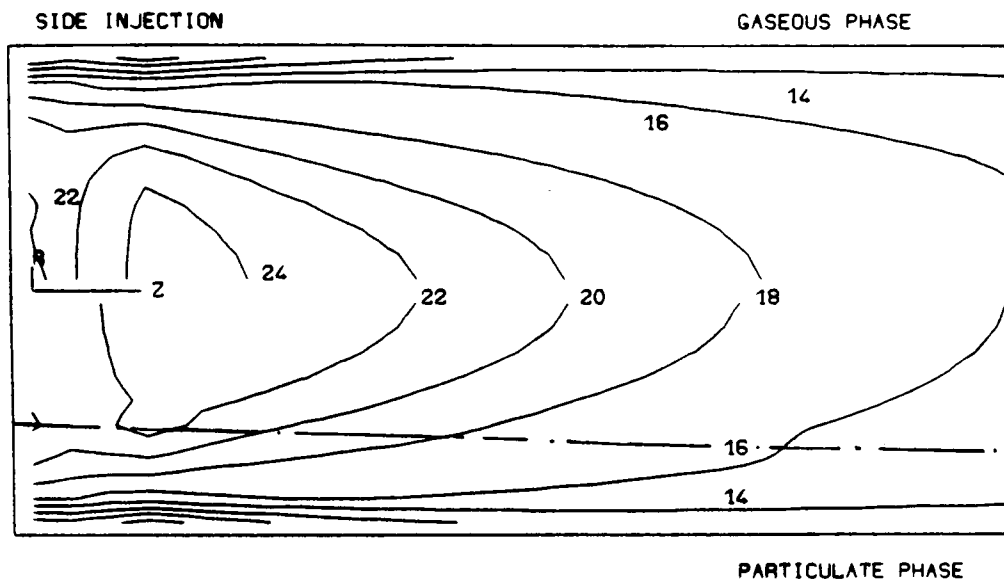
FIGURE 5.24: AXIAL VELOCITY COMPONENTS

SIDE INJECTION   GASEOUS PHASE

PARTICULATE PHASE
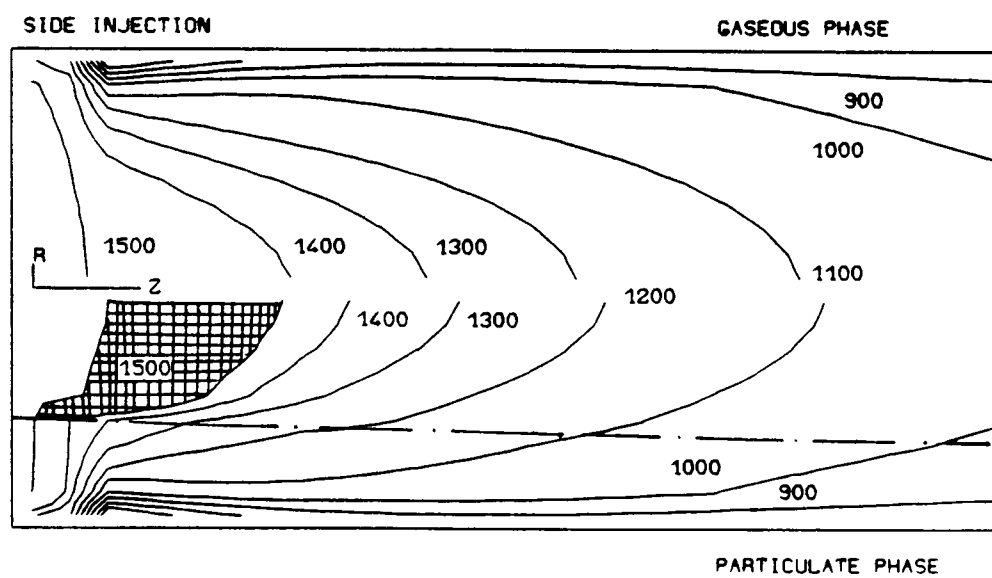
FIGURE 5.25: TEMPERATURE CONTOURS (C)

SIDE INJECTION
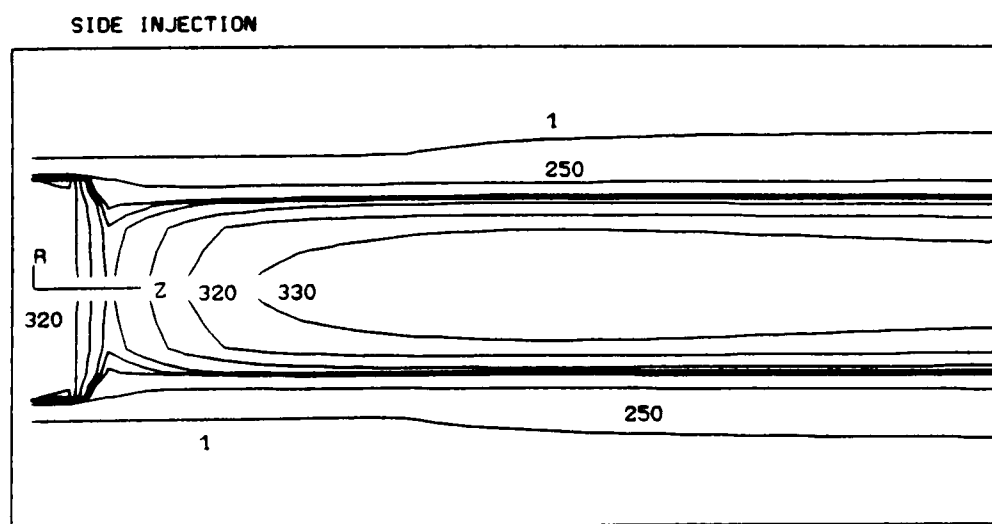
FIGURE 5.26: PARTICLE MASS-FRACTIONS
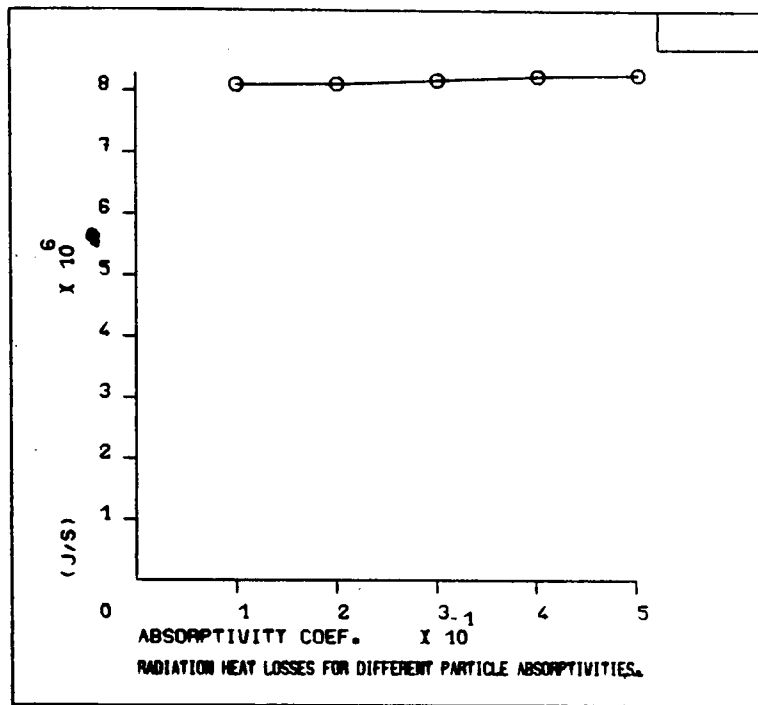
FIGURE 5.27: PARTICLE ABSORPTIVITY INFLUENCE
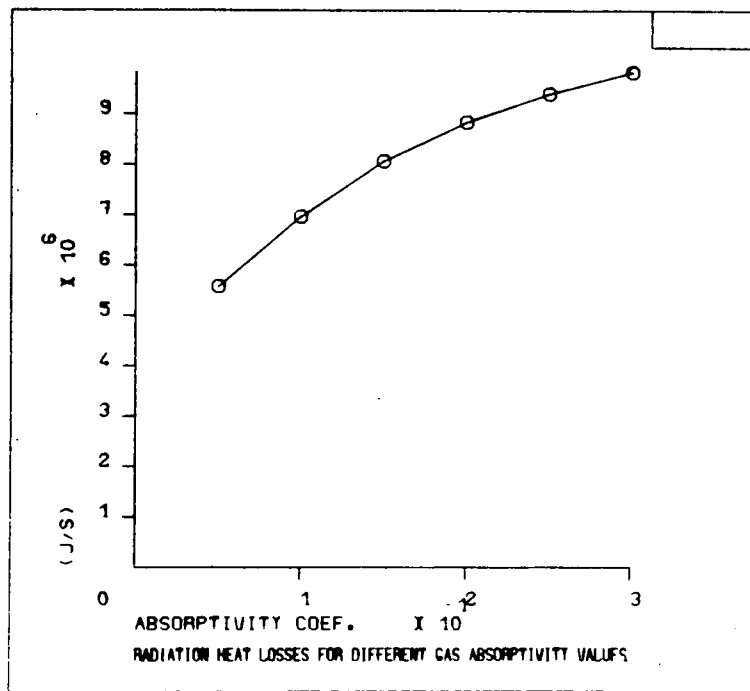
FIGURE 5.28: GAS ABSORPTIVITY INFLUENCE
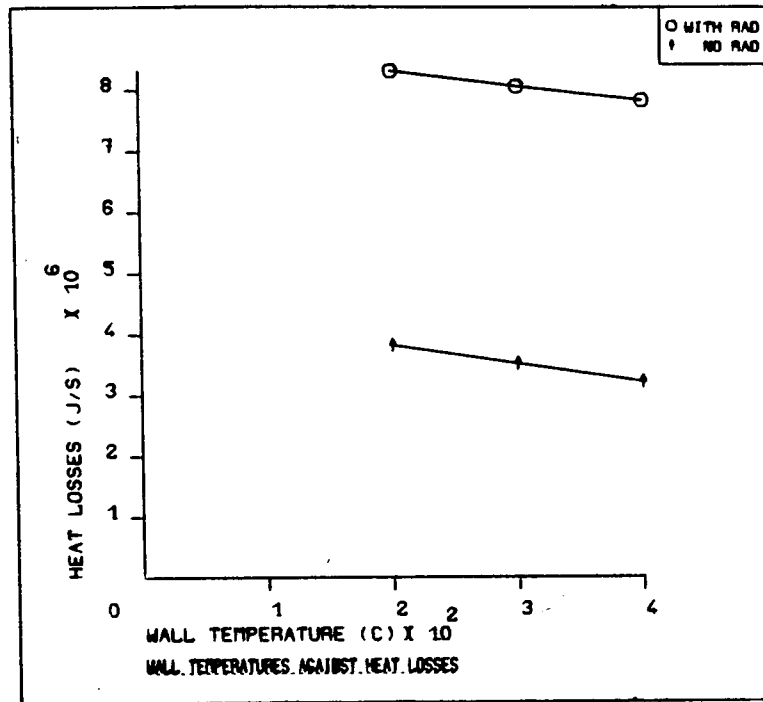
FIGURE 5.29: WALL TEMPERATURE INFLUENCE
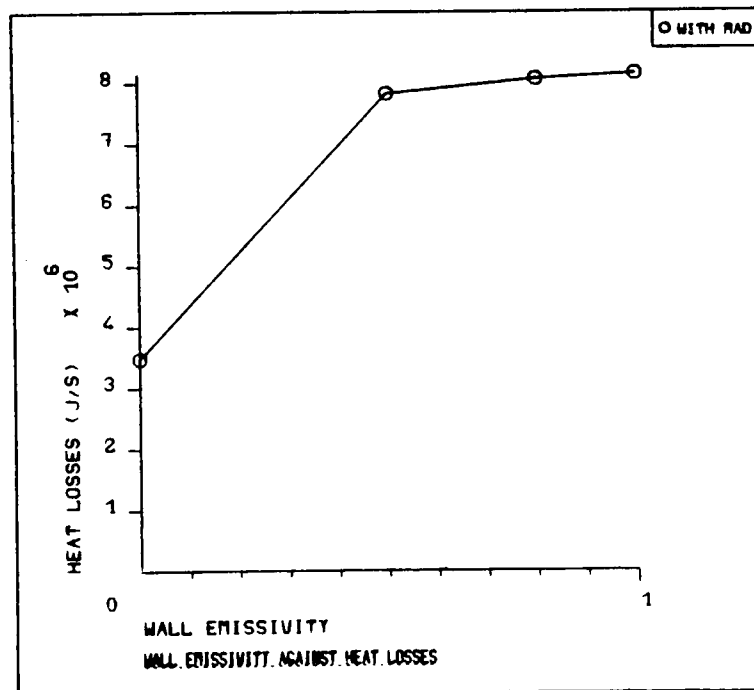
FIGURE 5.30: WALL EMISSIVITY INFLUENCE
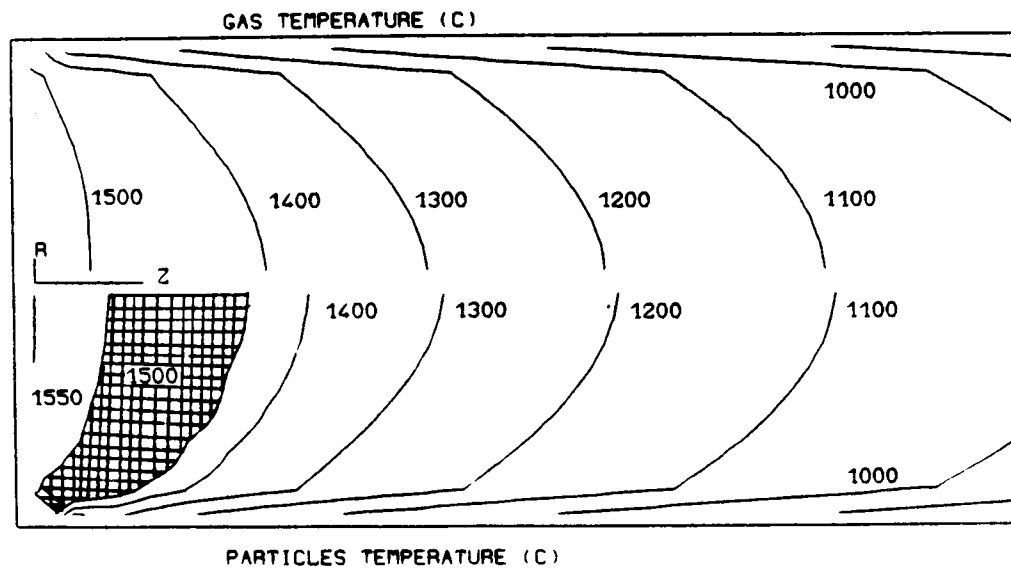
GAS TEMPERATURE (C)

FIGURE 5.31: TEMPERATURE CONTOURS (C)
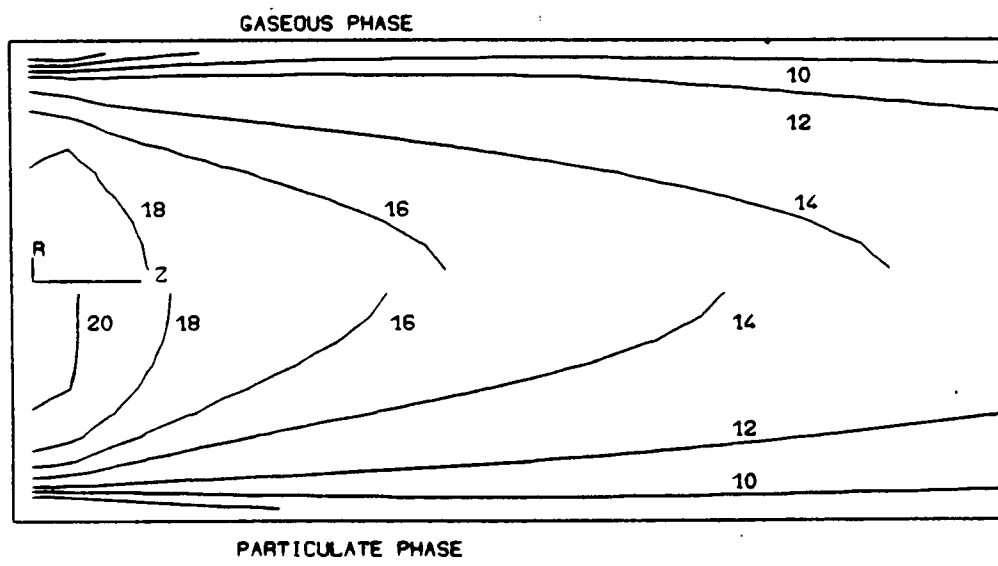
FIGURE 5.32: AXIAL VELOCITY COMPONENTS
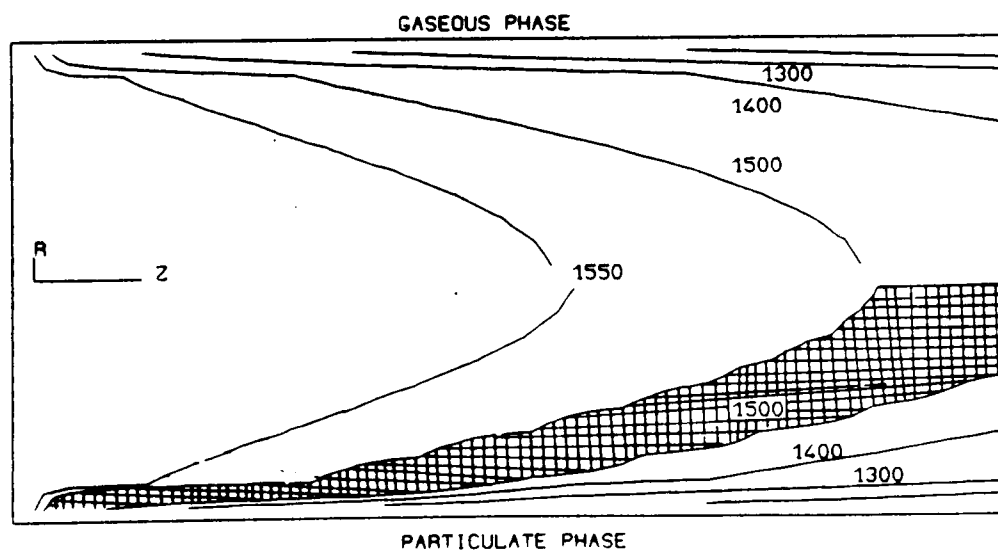
FIGURE 5.33: TEMPERATURE CONTOURS (C)

GASEOUS PHASE

PARTICULATE PHASE
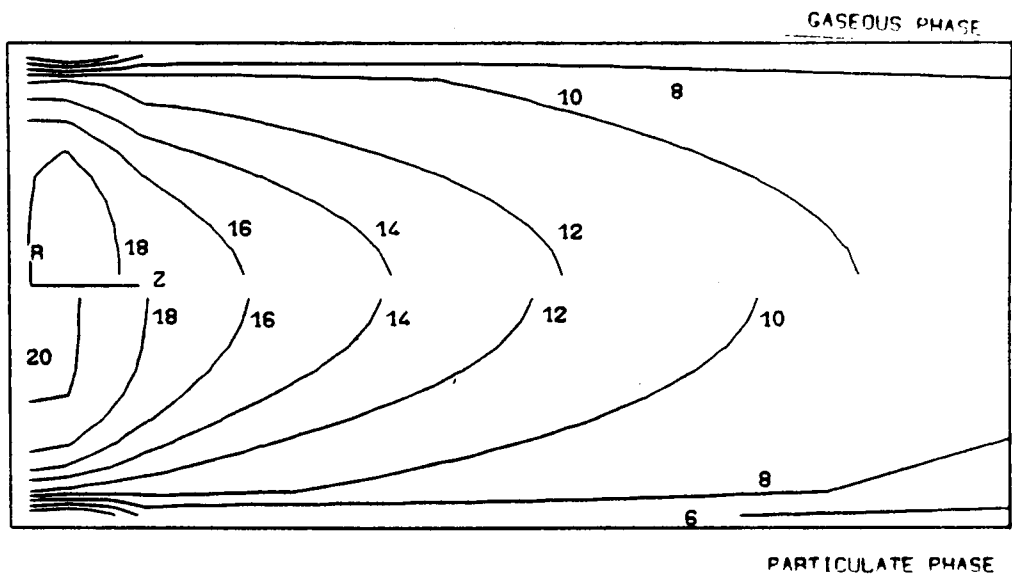
FIGURE 5.34: AXIAL VELOCITY COMPONENTS

EXIT TEMPERATURES FOR CONSTAND AND VARIABLE CP FOR GASES
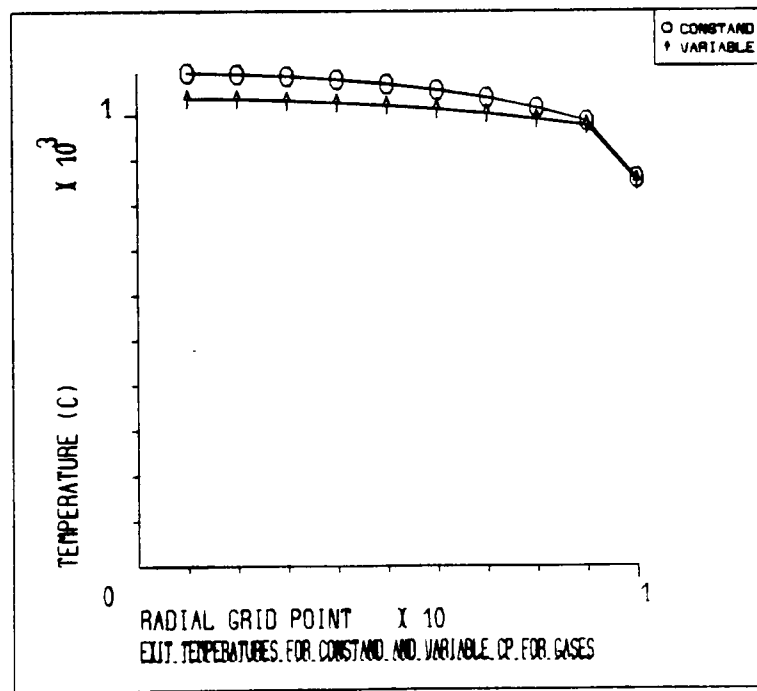
FIGURE 5.35: EXIT GASEOUS TEMPERATURES FOR CONSTANT AND VARIABLE SPECIFIC HEAT

CHAPTER 6 - THE INDUSTRIAL FURNACE MODELLED WITH COMBUSTION

6.1 Introduction

In this chapter the implementation of the combustion models introduced in Chapter 4 is described. Results are presented for a variety of two- and three-dimensional configurations with one- or two-phase flows. The effect of variations in inlet gas composition and other inlet parameters is studied. In all cases radiation is included.

6.2 The Diffusion- and Kinetically-Influenced Models Implementation

The models were applied to a typical off-gas duct as shown in Figure 5.2. The inlet volume flows are the same as in Chapter 5, ie. 500 Nm^3/min but the new inlet composition (by volume) is 90% CO and 10% CO_2, with an inlet temperature of 1575°C. Air (23.2% O_2 and 76.8% N_2, by mass) at a temperature of 104°C is injected through the side slot at a rate corresponding to 20% of the main volumetric flow.

The reaction taking place is:

$$2CO + O_2 + (N_2) \rightarrow 2CO_2 + (N_2)$$
$$\text{(fuel)} \quad \text{(oxidant)} \quad \text{(inert)} \rightarrow \text{(product)} \quad \text{(inert)}$$

(6.1);
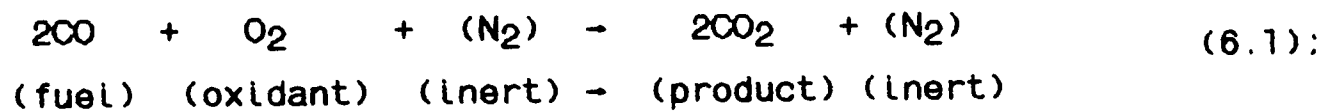
and the initial mass-fractions are given in Table 6.1:

species	CO	CO_2	O_2	N_2
m^x_i	0.851	0.149	0.232	0.768

TABLE 6.1: SPECIES INITIAL MASS FRACTIONS

The heat of combustion of CO is taken to be H_{fu} = 16.5x10^6 J/Kg (Barin et al (1982)) and f_{ST}, as given by Equation (4.10), is calculated to be equal to 0.3232. For the diffusion controlled model (Section 4.3) the stoichiometric diagram is shown in Figure 6.1.

For the simple kinetically-influenced model, Equation (4.21) is used to model the reaction (6.1). In the present case, the stoichiometric coefficients a, b and c of Equation (4.24) have values of 2, 1 and 2, respectively. The computer program computes the mass fraction m_{CO} of CO and the mixture fraction f, using conservation principles, and the mass fractions of the rest of the species are obtained from Equations (4.26) to (4.28).

Reaction (6.1) is an exothermic one and as a precaution a maximum reaction cut-off temperature of 3000°C was introduced for the diffusion model. This value was found to aid convergence since when omitted the diffusion model predicted highly unrealistic temperatures in the reaction zone, frequently resulting in divergence. Also, because of the very high generated temperatures, it is not necessary to include the Arrhenius rate.

Figures 6.2 to 6.5 present the results for the diffusion model. These should be compared with Figures 6.6 to 6.9 which show the results of the simple kinetically-influenced model for the same reaction.

Figure 6.2 shows the axial(w)-velocity components of the two phases. There is an increase in the inlet velocities of the two phases, greater for the gaseous phase than the particles, especially in the region of the

injection. This is largely due to the high temperatures and low densities generated by the chemical reaction. The exit velocities are about the same for the two phases, ie. 18 m/sec and compared with the non-reacting case, Figure 5.18, there is a small difference of about 1 m/sec (although the inlet gas composition is different).

Figure 6.3 presents the temperature contours for the two phases. The peak temperatures are about $3000^O C$ and $2700^O C$ for the gaseous and particulate phases, respectively. Due to high temperatures, generated heat losses are very high for both phases. The solidification region (shaded) is situated near the top end of the duct. Wall temperatures are very high in the lower half of the duct and much lower in the top part. Exit temperatures are about the same for both phases, slightly higher for the particulate phase with about $1387^O C$ in the centre of the exit compared with $1376^O C$ for the gaseous phase. The temperature drop along the centre line of the duct is about $300^O C$. Overall, particles cool down slower than the gases.

Figure 6.4 gives the particle mass fraction contours with high concentrations in the centre and lowest near the walls.

Figure 6.5 shows the mixture fraction f contours with the lowest values near the injection slot, where there is little fuel present, and the highest away from the injection plane where oxidant concentration is low. The exit value of f is about 0.9.

Figure 6.6 shows the predicted axial(w)-velocity components of the two phases using the simple kinetically-influenced model. Overall, the

results are very similar to the diffusion model predictions, Figure 6.2, except in the region of the reaction zone, where velocities are much lower than before. This is because of the lower predicted temperatures and consequently higher densities. Exit velocities are slightly less than before by about 0.45 m/sec. This is due to the temperature being 40° lower than predicted by the diffusion model.

Figure 6.7 shows the temperature contours. The two phases are again leaving the duct at approximately the same temperature (about $1350^{\circ}C$). The solidification region (shaded) is now occurring just above the centre of the duct, slightly below the region where it occurred in the diffusion model, Figure 6.3. Highest temperatures are attained at the side-injection where reaction occurs with peak values of $2100^{\circ}C$ and $2000^{\circ}C$ for the gases and particles, respectively. Results are very similar to those of the diffusion model with the important exception that peak temperatures are much lower now. This is consistent with Bradshaw et al (1981) who reported that although the diffusion model can give qualitatively correct results, it overestimates temperatures in the reaction region by amounts that can exceed $500^{\circ}C$.

Figure 6.8 shows the particle mass fraction contours and agreement with the diffusion model is very good.

Figure 6.9 shows contours at the mixture fraction, f, and mass fraction of CO. The mixture fraction attains its highest value at the inlet and its lowest near the injection point, where the reaction rate is at its highest. This corresponds to the highest and lowest values of CO, respectively. Apart from the region close to the injection slot there is good agreement

with the diffusion model results.

Of the two models, the simple kinetically-influenced model gives the best agreement with experimental results, especially in the case of temperature field predictions (J Moodie (1984)). Unfortunately, these experimental results are considered to be classified and confidential by the collaborating establishment and cannot be presented here.

The kinetically-influenced model predicts a peak temperature of $2100^{o}C$ for the gaseous phase at the reaction zone with about 30% of CO combusted to CO_2. The theoretical (adiabatic) prediction for the case where enough air is drawn to combust 30% of CO to CO_2 (as in this case), has given a temperature of $2230^{o}C$. Allowing for the present non-adiabatic case with wall heat losses, it can be seen that the predicted peak temperature is in good agreement with expectations.

In conclusion, the diffusion model is not recommended for serious quantitative studies. The results produced confirm the warning reported by Bradshaw et al (1981). It should only be used as a simple and general guide to the overall flow properties.

The simple kinetically-influenced model is more complicated than the diffusion model and it requires more computer storage. However, it produces far more realistic results without having to employ drastic relaxation and temperature cut-off parameters, as in the diffusion model. It can also be modified relatively easily to deal with reactions incorporating natural gas.

In Chapter 5 it was mentioned that the calculation of the total heat losses was only possible for particles as small as 40μm radius, due to convergence problems. Efforts to produce results for smaller particle sizes were successful only with the simple kinetically-influenced model. It also appears that the presence of combustion aids convergence.

Five different particle sizes were considered, ranging from 0.5μm to 100μm radius and the results are given in Table 6.2 and Figure 6.10. As expected, heat losses are greatest for the smaller particle sizes due to the particle increased surface area, which is inversely proportional to the particle radius. For the very small particle sizes (ie. 0.5μm), heat losses increase dramatically. For even smaller particle sizes, the model breaks down and heat losses are probably better predicted by the Mie theory (see for example, Edwards (1981)).

Particle Radius, μm	0.5	5	20	50	100
Heat Losses J/s, $\times 10^8$	0.3457	0.1759	0.1702	0.1700	0.1681

TABLE 6.2: TOTAL HEAT LOSSES

6.3 Methane Injection

The geometry of Figure 5.2 and the same inlet volumetric flows and temperatures are considered. The inlet gas composition is 90% CO and 10% CO_2 (by volume). The walls are assumed to be insulated and methane (CH_4) is injected through the side-slot at a rate of 10% of the

main volume flow rate, at a temperature of 104°C.

The reaction taking place is:

$$CO_2 \quad + \quad CH_4 \quad \overset{(a)}{\underset{(b)}{\rightleftharpoons}} \quad 2CO \quad + \quad 2H_2 \qquad\qquad (6.2).$$

(oxidant) (fuel)   (product)   (product)
                         1   2
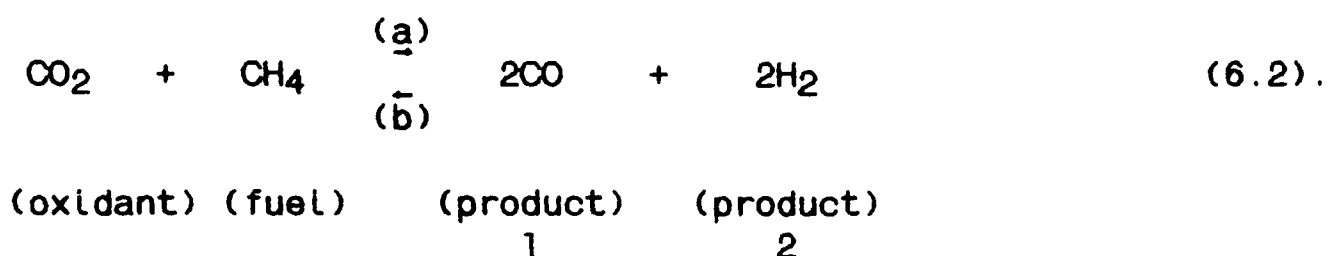
The model used previously is still appropriate and it is convenient to regard CO_2 as the 'oxidant' and CH_4 as the 'fuel'. The heat of reaction of CO_2 has been taken equal to -5.7936×10^6 J/Kg.

The model described in Section (4.4.2) is employed to this reversible reaction, and the stoichiometric coefficients a, b, c and d defined in Equation (4.33) are 1, 1, 2 and 2, respectively.

Two cases are considered: one with only reaction (6.2a) active, and one where the reaction (6.2) is reversible with rates depending on the local temperature and gas composition.

The theoretical 'critical' temperatures of reaction (6.2) are determined by calculating the standard free energy ΔG_T (Glasstone (1960)), which provides a means of determining whether a particular reaction is possible or not under a given set of conditions. It has been found theoretically that reaction (a) will take place for temperatures above 916°K and reaction (b) for temperatures below 916°K. This 'critical' temperature was calculated from data given in Barin et al (1982).

In the model employed, the equations for mass fractions of species CO_2, CH_4 and CO are solved, and species H_2 is obtained from Equation (4.34).

The initial mass fractions m_i^x and volume fractions at the inlet are summarised in Table 6.3.

Species	CO_2	CO
Mass fraction m_i^x	0.149	0.851
% Volume fraction	10	90

TABLE 6.3:   INLET CONCENTRATIONS

6.3.1   Results with reaction 6.2(a) only

Figure 6.11 shows the temperature contours of the two phases. Temperatures drop very rapidly for both phases, and the exit value is approximately 820°C. The solidification region (shaded) is at the lower end of the duct and wall temperatures are close to 700°C-800°C. Lower temperatures occur at the injection point (where the reaction rate is greatest) because of the endothermic reaction. Gases cool faster than the particles but the temperature difference appears to diminish near the exit.

Figure 6.12 shows the axial velocity components of the two phases. Gases appear to move faster than the particles near the exit because of

gravity acting on the particulate phase, although the two phases enter with the same velocities. Lower velocities are found near the walls and exit velocities are about 15 m/sec.

Figure 6.13 shows the mass fraction contours of CH_4 and CO_2. Highest values of CH_4 are found near the injection port and for CO_2 near the inlet below the injection. CO_2 is almost consumed at the exit and there is still some CH_4 left, suggesting that CH_4 was originally in slight excess. Reaction appears to be very fast, with the two species consumed very rapidly near the injection where they mix. Consequently, the temperatures drop rapidly in this area.

Figure 6.14 shows the mass fraction of CO and the gas density contours. There is an increase in the values because of the generation of CO with a highest value of approximately 0.89. Near the central region of the duct lowest values are found near the injection port, because of the dilution with CH_4. Exit values are approximately 0.86. Gas density is highest at the injection area, where temperature is lowest, because of the high reaction activity and the exit value is approximately 0.26 Kg/m^3.

6.3.2   Results with the reversible reaction (6.2)

Figure 6.15 shows the temperature contours of the two phases. Results are the same as with the one way reaction case, Figure 6.11, with the important exception that at the injection area, there is a local peak in the gas temperature because of the heat generated by the exothermic reaction (b). This suggests that the local temperature was lower than the critical one and hence reaction (b) took over, thus generating heat. The generated heat also increased the particle local temperature by a

small amount.

Figure 6.16 shows the CH_4 and CO_2 mass-fraction contours. Results again are very similar to the one way reaction (a), Figure 6.13. The small increase in CH_4 and CO_2 values near the injection point where the reaction changes direction, can just be detected, but overall there was no signficant change.

Figure 6.17 shows the CO mass-fraction and gas density contours. Again, overall contours are almost the same as in the one-way reaction (a) except near the injection port, where reaction (b) dominates over a small region only.

6.4   Methane Injection - New Dimensions

Another off-gas duct with dimensions as shown in Figure 6.18 was also considered.

The inlet gas volume flow rate is 4000 Nm^3/hr at a temperature of 1575°C, consisting of 90% CO and 10% CO_2, as before. Methane (CH_4) is injected through the injection port shown at 100 m/sec and 21°C. Walls are assumed to be insulated and the same model of Section 6.3, reaction (6.2), (reversible case), is used.

Three cases are considered: 10%, 7% and 5% of injected CH_4, to establish the best operating conditions.

6.4.1   10% CH_4 Case

Figure 6.19 shows the axial velocity component contours for the two

phases. There is an increase in the axial velocities near the inlet because of the side-injected CH_4. Exit velocities are about 36.5 m/sec for both phases. At the lower and centre parts of the duct, particles move faster than the gases. This is because of the more rapid temperature drop in the gaseous phase due to the endothermic reaction taking place. Even near the walls, velocities are high because the insulated walls lead to higher temperatures and hence lower densities.

Figure 6.20 shows the temperature contours of the two phases. The solidification region (shaded) occupies the lower end of the duct, above the injection port, where the temperature difference between the two phases is considerable. This difference diminishes near the exit where the gas temperature is about $50^{o}C$ lower than that of the particles. Overall, the temperature drop between inlet and outlet is approximately $650^{o}C$ showing the effect of the endothermic reaction 6.2(a). Temperatures are not low enough for reaction (6.2(b)) to proceed.

Figure 6.21 shows the volume fractions of the CH_4 and CO_2 species. Highest values of CH_4 are found at the injection port but CH_4 is consumed very rapidly as it reacts with the available CO_2. Only small amounts of CO_2 and CH_4 are left at the exit.

Figure 6.22 shows the volume fractions of the CO species. Lower values are found near the injection and higher near the exit.

6.4.2   7% CH_4 Case

Figure 6.23 shows the axial velocities of the two phases, which are slightly higher than for the 10% case. Figure 6.19 by approximately 2

m/sec, due to the higher temperatures. This is because there is less CH_4 to react and therefore less heat can be extracted from the system.

Figure 6.24 shows the temperature contours of the two phases. The solidification region now occupies a slightly bigger region compared with Figure 6.20 of the 10% case, due to the higher temperatures. Exit temperatures are higher than before, Figure 6.20.

Figure 6.25 shows the volume fractions of the CH_4 and CO_2 species. CH_4 is almost extinct and can only be found in a small region around the injection port. CO_2 appears to be in excess, since a lot of it is left unreacted, compared with the 10% case, Figure 6.21.

Figure 6.26 shows the volume fraction contours of the CO species. Compared with the 10% case there is more CO in the system.

6.4.3   5% CH₄ Case

Figures 6.27 to 6.30 show the velocity, temperature and species concentrations for the 5% case. Overall, they follow the pattern established with the 10% and 7% cases. Since less CH_4 is available for reaction, temperatures and velocities are higher. As a result of this, the solidification region is now much greater than the 7% and 10% case, and there is more CO_2 left unreacted at the end. The region around the injection port in which there is signficant amounts of CH_4 is much smaller. Exit temperatures are just below 1200°C and wall temperatures are higher than before. Again reaction 6.2(b) never takes place because temperatures are always higher than the critical temperature.

.

6.5   The Two-Reaction Model

The two reaction model is applied to the duct shown in Figure 6.18. The inlet temperature is 1600°C with the inlet gas composition given in Table 6.4.   The walls are made of refractory brick and this is modelled at a uniform temperature of 300°C.   Natural gas (CH_4) is injected through the side port at a volumetric rate of 5% of the volumetric main inlet flow and temperature of 21°C.

Species	CO	CO_2	H_2O	H_2
% Volume	58.54	15.24	7.59	18.63
Mass fraction	0.66	0.27	0.055	0.015

TABLE 6.4:   INITIAL GAS COMPOSITIONS

The reactions taking place are:

$$CO_2 + CH_4 \rightarrow 2CO + 2H_2 \qquad (a)$$

$$(6.3);$$

$$H_2O + CH_4 \rightarrow CO + 3H_2 \qquad (b)$$
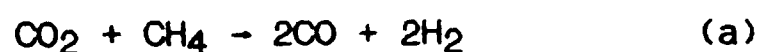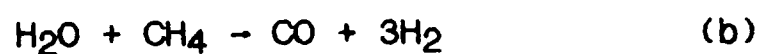
and the two-reaction model, described in Section 4.4.3 is employed. Species A, B, C, D and E in Equation (4.42) are CO_2, CH_4, CO, H_2 and H_2O, respectively, and the stoichiometric coefficients a, b, c, d, e, $\bar{b}$, $\bar{e}$ and $\bar{d}$ are 1, 1, 2, 2, 1, 1, 1 and 3, respectively.   It is also assumed that the amounts of CH_4 reacting with CO_2 and H_2O is in the ratio 1 to 2 and hence λ as defined in Section 4.4.3 is equal to 2.

The heats of reaction of the CO_2 and H_2O species are taken to be -5.786×10^6 J/Kg and -1.2595×10^7 J/Kg, respectively (Barin et al (1982)).

The theoretical critical temperatures below which the reactions (6.3) cannot proceed are 916^OK and 801^OK, respectively. However, experimental results (J Moodie (1985)) suggest that the presence of the particulate phase raises these values to aproximately 1000^OK. After some numerical experimentation the kinetically-influenced model was used with reaction rate multiplied by the ramp function $[(T-1000)/100]$ for temperatures in the range 1100^OK to 1000^OK. This greatly aided convergence.

Figure 6.31 shows the axial velocity components of the two phases. Particles appear to move faster than the gases at the centre of the duct, by about 2 m/sec, because of the temperature difference in the region between the two phases. At the higher end of the duct both phases have approximately the same velocity.

Figure 6.32 shows the temperature contours. The solidification region (shaded) occurs at the lower part of the duct, above the side-injection port, where the temperature difference between the phases is considerable. This is because of the high reaction rate of the endothermic reaction giving rise to a rapid temperature drop. The temperature difference between the phases immediately above the solidification region is about 100^OC with the exit temperatures of both phases about 1150^OC.

Figures 6.33 and 6.34 show the percentage volume fraction contours of the CH_4, CO_2 and H_2O, CO species, respectively. The CH_4 concentration is high near the injection point and almost non-existent further away, since it has reacted with CO_2 and H_2O, to produce CO and H_2. Exit values are approximately 10% CO_2, 57.9% CO, 5% H_2O and 27.1% H_2, which agree well with experimental results (J Moodie (1985)). Table 6.5 gives the theoretical percentage volume fraction of the species at the exit, assuming that all CH_4 reacts and $\lambda=2$. It can be seen there is good agreement with the predicted values. Total heat losses are: 0.3547×10^6 J/s with approximately 75% due to the gases and 25% to the particles.

Species	% volume fraction
CO_2	11.07
CO	57.43
H_2O	4.43
H_2	27.07

TABLE 6.5: THEORETICALLY PREDICTED EXIT VALUES

6.6 Co-current and Counter-current Sonic Tuyeres

In this section CH_4 is injected at sonic velocity, co-currently or counter-currently with the main flow, from a tuyere positioned in the centre of the duct, as shown in Figure 6.35.

The sonic velocity of CH_4 is obtained from (Krivandin and Markov (1980)):

$$w = \sqrt{\frac{2\gamma}{\gamma+1}RT_o} \qquad\qquad (6.4):$$

where R is the CH_4 gas constant of 519 J/Kg/K, T_o is the injection temperature of 294^OK, and γ is the ratio of specific heat at constant pressure to that at constant volume which for CH_4 is equal to 1.32. Thus, the sonic velocity of CH_4 for the given temperature of 294^OK is equal to 416.69 m/sec.

The inlet gas composition is 90% CO and 10% CO_2 and CH_4 is injected at a 7% rate. The kinetically-influenced model of Section 4.4.2 is employed, with no reverse reaction, since experimental evidence suggests that it does not take place (J Moodie (1985)). The walls are assumed to be insulated and made of refractory bricks.

6.6.1 Co-current CH_4 sonic tuyere

Figure 6.36 shows the temperature contours of the two phases. The particle solidification region (shaded) occupies the lower end of the duct extending diagonally from the tuyere injection to the wall. Lower temperatures are found around the tuyere, because of the low temperature of injected CH_4 and of the endothermic reaction taking place. Exit temperatures are about 1000^OC for both phases and temperature drop for the gaseous phase is more rapid than for the particulate phase, especially in centre of the duct.

Figure 6.37 shows the axial velocity components of the two phases. Highest velocities are found at the injection port, approximately 230 m/sec and 100 m/sec for the gaseous and particulate phase, respectively. Exit velocities are about 45 m/sec for both phases.

Figure 6.38 shows the CH_4 and CO_2 percentage volume fraction concentrations. Highest CH_4 values are found near and around the tuyere. Highest values of CO_2 are found near the inlet of the duct, below the tuyere. CH_4 and CO_2 are consumed very rapidly and at the exit there is approximately 2.5% CO_2 and no CH_4 left. There is more CO_2 near the walls and less near the centreline.

Figure 6.39 shows the CO percentage volume fraction contours, with lowest value at the injection area and highest nearest the inlet.

6.6.2 Counter-current sonic tuyere

Figure 6.40 shows the temperature contours for the counter-current case. The solidification region (shaded) now occupies a slightly smaller region than the co-current case, Figure 6.36, slightly below the previous position. Exit temperatures are approximately 70°C lower than before and the overall temperature gradient is steeper than before, Figure 6.36.

Figure 6.41 shows the axial velocity contours of the two phases. Velocities are smaller than the co-current case, Figure 6.37, since CH_4 is injected counter-currently with exit velocities of about 45 and 40 m/sec for the gaseous and the particulate phase, respectively. At the injection point the gaseous velocity is approximately -50 m/sec.

Figure 6.42 shows the percentage volume fractions of CH_4 and CO_2 and Figure 6.43 the percentage volume fractions of CO. Contours follow a similar pattern with the co-current case, Figures 6.38 and 6.39, with the important exception that CH_4 and CO_2 are disappearing more rapidly and therefore CO values are higher.

6.6.3   Average slab values

It is common practice in the process industry to calculate the post-combustion value ($\%CO_2$ + $\%H_2O$) and utilise this value to calculate the oxidation rate of the off-gas, defined as (von Bogdandy et al (1984)) the sum of CO_2 and H_2O, related to the sum ($CO_2+H_2O+H_2+CO$). Hence, the 'total-post-combustion' value is given by:

$$TPC = \frac{\%CO_2 + \%H_2O}{\%CO_2 + \%H_2O + \%H_2 + \%CO} \times 100 \qquad\qquad (6.5).$$

The average slab values of CH_4, CO_2, CO, H_2O, H_2, TPC and gas temperature, have been calculated for both cases and are given in Tables 6.6 and 6.7.   Graphical representations of the average TPC and gas temperatures, against the height of the duct are given in Figures 6.44 to 6.47.   From these results, it appears that the counter-current case induces lower temperatures by 69°C at the exit, whilst the exit composition of the gases and TPC values are almost the same.   The important difference between the two cases is detected at the injection region.   The counter-current case induces a sudden drop in the gas temperature (Figure 6.46) and TPC values (Figure 6.47) and then smooths out, compared with the smooth gradient of the co-current case (Figures 6.44 and 6.45).   This is because of the rapid mixing of the gases in the counter-current case.   The same pattern can also be seen in the values of the species in Tables 6.6 and 6.7.

h(m)	T(C)	CO2	CH4	CO+N2	H2	TPC
0.250	1568	10.030	0.8774E-16	89.970	0.0000E 00	10.030
0.750	1561	10.030	0.2798E-13	89.970	0.0000E 00	10.030
1.250	1554	10.030	0.9355E-11	89.970	0.0000E 00	10.030
1.750	1547	10.030	0.3261E-08	89.970	0.0000E 00	10.030
2.250	1540	10.030	0.1176E-05	89.970	0.6858E-06	10.030
2.750	1535	10.030	0.9443E-03	89.970	0.1126E-02	10.030
3.112	1508	9.759	0.7628E 00	89.180	0.2932E 00	9.834
3.337	1465	9.215	0.1261E 01	88.480	0.1049E 01	9.332
3.562	1429	8.728	0.1353E 01	88.140	0.1777E 01	8.848
3.787	1396	8.252	0.1307E 01	87.930	0.2512E 01	8.361
4.177	1330	7.165	0.1094E 01	87.540	0.4206E 01	7.244
4.732	1267	6.095	0.8919E 00	87.140	0.5872E 01	6.149
5.287	1212	5.141	0.7115E 00	86.790	0.7356E 01	5.178
5.842	1169	4.410	0.5453E 00	86.550	0.8499E 01	4.434
6.397	1138	3.902	0.4002E 00	86.400	0.9297E 01	3.917
6.952	1118	3.574	0.2880E 00	86.320	0.9815E 01	3.584
7.507	1105	3.373	0.2092E 00	86.280	0.1013E 02	3.380
8.062	1095	3.250	0.1532E 00	86.270	0.1033E 02	3.255
8.617	1089	3.173	0.1132E 00	86.260	0.1046E 02	3.176
9.172	1083	3.123	0.8451E-01	86.260	0.1054E 02	3.125
9.727	1078	3.089	0.6365E-01	86.260	0.1059E 02	3.091
10.280	1073	3.066	0.4838E-01	86.260	0.1063E 02	3.067
10.840	1069	3.049	0.3711E-01	86.260	0.1066E 02	3.050
11.390	1066	3.037	0.2872E-01	86.260	0.1068E 02	3.038
11.950	1062	3.028	0.2244E-01	86.260	0.1069E 02	3.029
12.500	1059	3.021	0.1768E-01	86.260	0.1070E 02	3.022
13.060	1056	3.016	0.1405E-01	86.260	0.1071E 02	3.017
13.610	1053	3.012	0.1125E-01	86.260	0.1072E 02	3.013
14.170	1051	3.009	0.9067E-02	86.260	0.1072E 02	3.009
14.720	1049	3.007	0.7353E-02	86.260	0.1073E 02	3.007

TABLE 6.6:   AVERAGE SLAB VALUES

h(m)	T(C)	CO2	CH4	CO+N2	H2	TPC
0.250	1569	10.030	0.9312E-15	89.970	0.0000E 00	10.030
0.750	1563	10.030	0.3055E-12	89.970	0.0000E 00	10.030
1.250	1558	10.030	0.1080E-09	89.970	0.0000E 00	10.030
1.750	1552	10.030	0.4148E-07	89.970	0.0000E 00	10.030
2.250	1547	10.030	0.1754E-04	89.970	0.0000E 00	10.030
2.750	1561	10.010	0.1147E-01	89.960	0.1928E-01	10.020
3.250	1192	5.123	0.5351E 01	82.850	0.6674E 01	5.412
3.750	1172	4.257	0.1474E 01	85.680	0.8590E 01	4.320
4.250	1145	3.720	0.7336E 00	86.020	0.9524E 01	3.747
4.750	1135	3.456	0.4185E 00	86.150	0.9975E 01	3.471
5.250	1131	3.315	0.2626E 00	86.210	0.1021E 02	3.324
5.750	1129	3.231	0.1751E 00	86.240	0.1036E 02	3.237
6.250	1129	3.179	0.1221E 00	86.250	0.1044E 02	3.182
6.750	1129	3.144	0.8831E-01	86.260	0.1050E 02	3.146
7.250	1129	3.119	0.6579E-01	86.270	0.1054E 02	3.121
7.750	1128	3.102	0.5028E-01	86.270	0.1057E 02	3.104
8.250	1128	3.089	0.3927E-01	86.280	0.1059E 02	3.090
8.750	1128	3.079	0.3124E-01	86.280	0.1061E 02	3.080
9.250	1127	3.071	0.2523E-01	86.280	0.1062E 02	3.072
9.750	1127	3.064	0.2064E-01	86.280	0.1064E 02	3.065
10.250	1126	3.058	0.1706E-01	86.280	0.1065E 02	3.059
10.750	1125	3.053	0.1422E-01	86.280	0.1065E 02	3.053
11.250	1124	3.048	0.1194E-01	86.280	0.1066E 02	3.049
11.750	1124	3.044	0.1008E-01	86.280	0.1067E 02	3.045
12.250	1123	3.040	0.8547E-02	86.280	0.1067E 02	3.041
12.750	1122	3.037	0.7276E-02	86.280	0.1068E 02	3.037
13.250	1121	3.033	0.6212E-02	86.280	0.1069E 02	3.034
13.750	1120	3.030	0.5315E-02	86.270	0.1069E 02	3.030
14.250	1119	3.027	0.4554E-02	86.270	0.1069E 02	3.027
14.750	1118	3.025	0.3907E-02	86.270	0.1070E 02	3.025

TABLE 6.7:   AVERAGE SLAB VALUES

It is interesting to note that unlike previous cases with wall injections, in the present cases, the lowest temperatures were at the centre of the duct. Also, experimental evidence (J Moodie (1984) indicated a gas temperature of about 1150°C, 3m above the tuyere, which agrees well with the predicted values of approximately 1160°C and 1129°C for the co-current and counter-current cases, respectively.

6.7 Restricted Inlet Cases

In this section, results are presented for two-dimensional and three-dimensional cases for the restricted inlet geometry shown in Figure 6.48.

Methane injection is sonic and radially through the whole circumference. Particles are not included in these calculations.

There are two main cases:

(a)   4000 m^3/hr with 70% CO and 30% CO_2 with 5, 7 and 10% CH_4 rate corresponding to oxygen operation in the duct.

(b)   8000 m^3/hr with 35% CO, 15% CO_2 and 50% N_2. Methane flows are of 2.5%, 5%, 7% and 10% rate and the nitrogen is due to air operation in the duct.

In both cases the walls are insulated, the reaction taking place is:

$$CO_2 + CH_4 \rightarrow 2CO + 2H_2 \qquad\qquad (6.6);$$

and the reaction stops at 916°K.

6.7.1   <u>Case (a)</u>

Figures 6.49 shows the velocity vectors for the gaseous phases for the 5% CH_4 case. For the three CH_4 concentrations velocity vectors are similar and there is a recirculation zone above the sloped wall, as expected with the reattachment point approximately 3.75m above the inlet.

Figures 6.50 to 6.52 show the axial velocity component of the gaseous phase for the 5, 7 and 10% CH_4 cases. At the exit, the velocities are approximately 3.3 m/sec in the centre and 2.9 m/sec near the wall for all three cases, with the velocities of the 5% case slightly higher from the other two all over the domain. This is because the higher the throat-injected amount of CH_4, the greater the impact on the main flow velocities (ie. it slows them down). Inside the recirculation zone, near the wall, the velocity is approximately -5 m/sec. Overall, the velocities drop very rapidly because of the expansion of the duct above the throat.

Figures 6.53 to 6.55 show the gas temperature contours of three cases, respectively. Average exit temperatures are 921.3, 872.6 and 785.7^{O}C, respectively, for the 5, 7 and 10% CH_4 cases (also seen in Tables 6.8 to 6.10). The largest temperature drop is in the 10% case, since there is more CH_4 to react and consequently more heat extracted from the system. Temperatures inside the recirculation region are approximately 1102, 1010 and 864°C respectively for 5, 2 and 10% CH_4. Temperature profiles become flat at about 5.30m above the inlet and have a steep gradient near the walls. Overall, the temperature drops very rapidly from the injection point to halfway up the duct and then it drops very slowly. This is because there is little CH_4 left in the top part of the duct and therefore little heat extraction.

Figures 6.56 to 6.58 show the percentage volume fraction of CH_4 and Figures 6.59 to 6.61 for CO_2 for the 5, 7 and 10% CH_4 cases, respectively. In all three cases, highest values of CH_4 are found near the injection point and lowest away from it. The available CH_4 is consumed very rapidly as it spreads out. At the exit there is not much left as it can be seen from Tables 6.8 to 6.10. Lowest values of CO_2 are found inside the recirculation zone and highest in the centre. Average CO_2 exit values are 22.42, 19.88 and 16.46% for the 5, 7 and 10% CH_4 cases, respectively (also seen in Tables 6.8, 6.9 and 6.10).

Tables 6.8 to 6.10 give the average slab values of the temperature, chemical species and TPC for the 5, 7 and 10% cases, respectively.

h(m)	T(C)	CO2	CH4	CO+N2	H2	TPC
0.125	1570	30.000	0.8676E-05	70.000	0.6590E-03	30.000
0.375	1566	30.000	0.8233E-03	70.000	0.1625E-02	30.000
0.625	1561	29.880	0.5848E-01	69.950	0.1090E 00	29.900
0.875	1425	26.640	0.3040E 01	67.750	0.2563E 01	27.480
1.050	1292	23.550	0.2330E 01	68.090	0.6031E 01	24.110
1.150	1205	22.140	0.1311E 01	68.720	0.7824E 01	22.440
1.250	1151	21.820	0.7191E 00	69.110	0.8350E 01	21.980
1.350	1119	21.900	0.4088E 00	69.320	0.8363E 01	21.990
1.450	1102	22.080	0.2464E 00	69.440	0.8236E 01	22.130
1.750	1104	22.150	0.1448E 00	69.520	0.8188E 01	22.180
2.250	1114	22.250	0.1029E 00	69.550	0.8094E 01	22.280
2.750	1117	22.350	0.7470E-01	69.580	0.7998E 01	22.370
3.250	1110	22.420	0.5237E-01	69.590	0.7931E 01	22.430
3.750	1099	22.450	0.3715E-01	69.610	0.7909E 01	22.460
4.250	1084	22.450	0.2589E-01	69.610	0.7909E 01	22.460
4.750	1067	22.450	0.1755E-01	69.620	0.7918E 01	22.450
5.250	1049	22.440	0.1232E-01	69.620	0.7925E 01	22.440
5.750	1032	22.430	0.8917E-02	69.630	0.7931E 01	22.440
6.250	1016	22.430	0.6645E-02	69.630	0.7935E 01	22.430
6.750	1000	22.430	0.5079E-02	69.630	0.7937E 01	22.430
7.250	985	22.430	0.3966E-02	69.630	0.7940E 01	22.430
7.750	971	22.430	0.3156E-02	69.630	0.7941E 01	22.430
8.250	957	22.430	0.2552E-02	69.630	0.7942E 01	22.430
8.750	945	22.430	0.2094E-02	69.630	0.7943E 01	22.430
9.250	932	22.430	0.1740E-02	69.630	0.7944E 01	22.430
9.750	921	22.420	0.1461E-02	69.630	0.7944E 01	22.430

TABLE 6.8:   AVERAGE SLAB VALUES

h(m)	T(C)	CO2	CH4	CO+N2	H2	TPC
0.125	1570	30.000	0.1180E-04	70.000	0.8239E-03	30.000
0.375	1566	30.000	0.1121E-02	70.000	0.2766E-02	30.000
0.625	1561	29.840	0.7997E-01	69.930	0.1495E 00	29.860
0.875	1375	25.460	0.4075E 01	66.990	0.3478E 01	26.540
1.050	1194	21.400	0.3058E 01	67.490	0.8048E 01	22.080
1.150	1091	19.590	0.1708E 01	68.330	0.1037E 02	19.930
1.250	1041	19.160	0.9355E 00	68.840	0.1106E 02	19.340
1.350	1019	19.250	0.5319E 00	69.120	0.1110E 02	19.350
1.450	1011	19.450	0.3210E 00	69.270	0.1096E 02	19.520
1.750	1015	19.540	0.1889E 00	69.360	0.1091E 02	19.580
2.250	1026	19.660	0.1342E 00	69.410	0.1079E 02	19.690
2.750	1031	19.790	0.9719E-01	69.440	0.1068E 02	19.810
3.250	1027	19.870	0.6791E-01	69.460	0.1059E 02	19.890
3.750	1019	19.900	0.4808E-01	69.480	0.1057E 02	19.910
4.250	1007	19.910	0.3346E-01	69.490	0.1057E 02	19.910
4.750	993	19.900	0.2267E-01	69.500	0.1058E 02	19.910
5.250	979	19.890	0.1591E-01	69.500	0.1059E 02	19.900
5.750	965	19.890	0.1152E-01	69.500	0.1060E 02	19.890
6.250	951	19.880	0.8594E-02	69.510	0.1060E 02	19.890
6.750	939	19.880	0.6573E-02	69.510	0.1060E 02	19.880
7.250	926	19.880	0.5138E-02	69.510	0.1061E 02	19.880
7.750	914	19.880	0.4093E-02	69.510	0.1061E 02	19.880
8.250	903	19.880	0.3314E-02	69.510	0.1061E 02	19.880
8.750	892	19.880	0.2723E-02	69.510	0.1061E 02	19.880
9.250	882	19.880	0.2265E-02	69.510	0.1061E 02	19.880
9.750	872	19.880	0.1905E-02	69.510	0.1061E 02	19.880

TABLE 6.9:   AVERAGE SLAB VALUES

h(m)	T(C)	CO2	CH4	CO+N2	H2	TPC
0.125	1570	30.000	0.1617E-04	70.000	0.7466E-03	30.000
0.375	1566	30.000	0.1537E-02	70.000	0.3872E-02	30.000
0.625	1561	29.770	0.1103E 00	69.910	0.2067E 00	29.810
0.875	1303	23.820	0.5462E 01	65.960	0.4760E 01	25.190
1.050	1049	18.530	0.3952E 01	66.750	0.1076E 02	19.300
1.150	919	16.240	0.2176E 01	67.870	0.1371E 02	16.600
1.250	874	15.670	0.1188E 01	68.540	0.1460E 02	15.860
1.350	864	15.750	0.6750E 00	68.900	0.1467E 02	15.850
1.450	866	15.970	0.4076E 00	69.100	0.1452E 02	16.040
1.750	872	16.070	0.2393E 00	69.210	0.1449E 02	16.110
2.250	884	16.210	0.1690E 00	69.260	0.1437E 02	16.230
2.750	892	16.350	0.1216E 00	69.290	0.1424E 02	16.370
3.250	892	16.450	0.8421E-01	69.320	0.1414E 02	16.470
3.750	888	16.490	0.5930E-01	69.340	0.1411E 02	16.500
4.250	881	16.490	0.4121E-01	69.350	0.1411E 02	16.500
4.750	872	16.490	0.2785E-01	69.360	0.1412E 02	16.490
5.250	862	16.480	0.1952E-01	69.370	0.1413E 02	16.480
5.750	852	16.470	0.1413E-01	69.380	0.1414E 02	16.470
6.250	843	16.470	0.1054E-01	69.380	0.1414E 02	16.470
6.750	833	16.460	0.8066E-02	69.380	0.1415E 02	16.470
7.250	825	16.460	0.6313E-02	69.380	0.1415E 02	16.460
7.750	816	16.460	0.5036E-02	69.390	0.1415E 02	16.460
8.250	808	16.460	0.4086E-02	69.390	0.1415E 02	16.460
8.750	800	16.460	0.3364E-02	69.390	0.1415E 02	16.460
9.250	792	16.460	0.2806E-02	69.390	0.1415E 02	16.460
9.750	785	16.460	0.2366E-02	69.390	0.1415E 02	16.460

TABLE 6.10:   AVERAGE SLAB VALUES

6.7.2   Case (b)

In order to reduce computer storage requirements, the N_2 is taken together with the available CO, since they both have the same molecular weight and N_2 is present only as an inert species.

Figure 6.62 shows the velocity vectors for the 2.5% CH_4 case.   For the four cases, vector plots are similar and there is a recirculation zone above the sloping wall, as expected, with the reattachment point approximately 3.75m above the inlet, as with case (a).

Figures 6.63 to 6.66 show the axial velocity component for the 2.5, 5, 7 and 10% CH_4 cases, respectively.   At the exit the velocities are approximately 6.1 m/sec at the cell nearest to the walls, and 7.2 m/sec in the centre for the 2.5, 5 and 7% cases; and 5.3 m/sec at the cell nearest the walls and 6.5 m/sec in the centre for the 10% CH_4 case. From these results it appears that the 10% case is approximately 0.7 m/sec slower than the other three and this is because the 10% radially-injected CH_4 has a greater effect on the main flow temperature. Also, in all four cases, the velocity drop is very sudden from inlet to just above the sloping wall, and then the decrease slows down.   Inside the recirculation zone near the wall, the velocity is approximately -10 m/sec.

Figures 6.67 to 6.70 show the temperature contours for the 2.5, 5, 7 and 10% cases respectively.   Average exit temperatures are approximately 1104, 1023, 948.1 and 768.5°C for the four cases, respectively (also seen in Tables 6.11 to 6.14).   The largest temperature drop is in the 10% case, since there is more CH_4 to react with the available CO_2 and consequently more heat extracted from the system.   Temperatures inside

the recirculation region are approximately 1275, 1138, 1023 and 761°C, respectively for the four cases. At the radial injection-point the temperatures are 1412, 1271, 1166 and 984°C respectively for the four cases. Temperature profiles become flat at about 5.75m above inlet for the 2.5, 5 and 7% case and at about 6.25m above inlet for the 10% case, with a big gradient near the walls. Overall, the temperature drops very rapidly from the injection point to about halfway up the duct and then very slowly. This is because there is little CH_4 left in the top part of the duct to react and the temperature is also very low for the reaction to proceed. The biggest temperature drop is found inside the recirculation zone, where the reaction is taking place at a higher rate because of the high amounts of CH_4 and CO_2.

Figures 6.71 to 6.74 show the percentage CH_4 volume fractions and Figures 6.75 to 6.78 the CO_2 volume fractions for the 2.5, 5, 7 and 10% CH_4 cases, respectively. In all four cases highest values of CH_4 are found near the injection point, the smallest for the 2.5% case and the biggest for the 10% CH_4 case. The available CH_4 is consumed very rapidly near and around the sloping wall and at the exit there is almost no methane left, as can also be seen from Tables 6.11 to 6.14. CH_4 spreads out in a similar manner in all four cases, with highest concentrations inside the lower end of the recirculation zone. Exit average values of CO_2 are 11.92, 9.208, 7.262 and 4.713%, respectively for the four cases. The highest consumption of CO_2 is found in the 10% CH_4 case and the lowest values inside the recirculation zone where the reaction rate is at its highest.

Tables 6.11 to 6.14 give the average slab values for the chemical

species and gas temperature. H_2 is generated in higher amounts in the 10% case with exit values of 4.23, 7.94, 10.61 and 10.99% for the four cases, respectively. These values are from an initial zero percentage H_2 concentration. The average exit values of CO and N_2 are given together with about 83.86, 82.85, 82.12 and 84.29% combined value at the exit. The average slab temperature drops below the 1000°C at approximately 6.25m and 9.5m above inlet for the 7 and 10% CH_4 respectively. For the 2.5 and 5% cases, the average slab temperature is always above 1000°C.

h(m)	T(C)	CO2	CH4	CO	H2
0.125	1572	15.000	0.4373E-05	35.000	0.0000E 00
0.375	1570	15.000	0.4183E-03	35.000	0.0000E 00
0.625	1566	14.950	0.2982E-01	34.970	0.5301E-01
0.875	1489	13.780	0.1601E 01	33.280	0.1331E 01
1.050	1415	12.470	0.1259E 01	33.070	0.3206E 01
1.150	1360	11.830	0.7180E 00	33.260	0.4200E 01
1.250	1318	11.670	0.3959E 00	33.450	0.4490E 01
1.350	1290	11.690	0.2258E 00	33.590	0.4488E 01
1.450	1273	11.770	0.1364E 00	33.690	0.4406E 01
1.750	1275	11.800	0.8055E-01	33.750	0.4374E 01
2.250	1283	11.840	0.5758E-01	33.780	0.4317E 01
2.750	1285	11.890	0.4214E-01	33.810	0.4259E 01
3.250	1279	11.920	0.2979E-01	33.830	0.4218E 01
3.750	1269	11.930	0.2138E-01	33.840	0.4205E 01
4.250	1256	11.930	0.1479E-01	33.850	0.4205E 01
4.750	1241	11.930	0.1019E-01	33.850	0.4210E 01
5.250	1225	11.930	0.7234E-02	33.850	0.4215E 01
5.750	1209	11.920	0.5297E-02	33.850	0.4218E 01
6.250	1194	11.920	0.3989E-02	33.850	0.4220E 01
6.750	1180	11.920	0.3079E-02	33.850	0.4222E 01
7.250	1166	11.920	0.2426E-02	33.850	0.4223E 01
7.750	1152	11.920	0.1947E-02	33.850	0.4223E 01
8.250	1140	11.920	0.1587E-02	33.850	0.4224E 01
8.750	1127	11.920	0.1312E-02	33.860	0.4224E 01
9.250	1116	11.920	0.1097E-02	33.860	0.4225E 01
9.750	1104	11.920	0.9267E-03	33.860	0.4225E 01

TABLE 6.11: AVERAGE SLAB VALUES

h(m)	T(C)	CO2	CH4	CO+N2	H2
0.125	1572	15.000	0.8549E-05	85.000	0.3951E-03
0.375	1570	14.990	0.8180E-03	85.000	0.9273E-03
0.625	1565	14.910	0.5840E-01	84.930	0.1080E 00
0.875	1417	12.670	0.3010E 01	81.750	0.2564E 01
1.050	1276	10.250	0.2313E 01	81.410	0.6037E 01
1.150	1197	9.092	0.1306E 01	81.770	0.7830E 01
1.250	1160	8.797	0.7192E 00	82.120	0.8361E 01
1.350	1144	8.835	0.4103E 00	82.380	0.8375E 01
1.450	1138	8.955	0.2480E 00	82.550	0.8243E 01
1.750	1142	9.007	0.1466E 00	82.650	0.8193E 01
2.250	1151	9.082	0.1046E 00	82.720	0.8098E 01
2.750	1155	9.157	0.7634E-01	82.770	0.8001E 01
3.250	1153	9.210	0.5372E-01	82.800	0.7932E 01
3.750	1147	9.229	0.3845E-01	82.820	0.7909E 01
4.250	1138	9.231	0.2651E-01	82.830	0.7909E 01
4.750	1127	9.225	0.1825E-01	82.840	0.7918E 01
5.250	1115	9.220	0.1296E-01	82.840	0.7926E 01
5.750	1103	9.217	0.9490E-02	82.840	0.7932E 01
6.250	1092	9.214	0.7151E-02	82.840	0.7935E 01
6.750	1081	9.212	0.5523E-02	82.840	0.7938E 01
7.250	1070	9.211	0.4357E-02	82.840	0.7940E 01
7.750	1060	9.210	0.3500E-02	82.840	0.7942E 01
8.250	1050	9.210	0.2856E-02	82.850	0.7942E 01
8.750	1041	9.209	0.2363E-02	82.850	0.7943E 01
9.250	1032	9.209	0.1979E-02	82.850	0.7944E 01
9.750	1023	9.208	0.1674E-02	82.850	0.7944E 01

TABLE 6.12: AVERAGE SLAB VALUES

h(m)	T(C)	CO2	CH4	CO+N2	H2
0.125	1572	15.000	0.1172E-04	85.000	0.4345E-03
0.375	1570	14.990	0.1122E-02	85.000	0.1710E-02
0.625	1564	14.870	0.8023E-01	84.900	0.1505E 00
0.875	1361	11.850	0.4016E 01	80.650	0.3483E 01
1.050	1168	8.663	0.3020E 01	80.260	0.8062E 01
1.150	1068	7.174	0.1691E 01	80.750	0.1038E 02
1.250	1032	6.782	0.9294E 00	81.210	0.1108E 02
1.350	1024	6.817	0.5298E 00	81.540	0.1112E 02
1.450	1025	6.959	0.3203E 00	81.760	0.1097E 02
1.750	1030	7.018	0.1890E 00	81.880	0.1091E 02
2.250	1040	7.109	0.1345E 00	81.960	0.1080E 02
2.750	1047	7.199	0.9770E-01	82.020	0.1068E 02
3.250	1047	7.264	0.6836E-01	82.070	0.1060E 02
3.750	1044	7.287	0.4873E-01	82.090	0.1057E 02
4.250	1037	7.289	0.3356E-01	82.110	0.1057E 02
4.750	1028	7.282	0.2306E-01	82.110	0.1058E 02
5.250	1019	7.276	0.1636E-01	82.120	0.1059E 02
5.750	1011	7.272	0.1197E-01	82.120	0.1060E 02
6.250	1002	7.269	0.9021E-02	82.120	0.1060E 02
6.750	993	7.267	0.6968E-02	82.120	0.1061E 02
7.250	985	7.265	0.5498E-02	82.120	0.1061E 02
7.750	977	7.264	0.4420E-02	82.120	0.1061E 02
8.250	969	7.263	0.3610E-02	82.120	0.1061E 02
8.750	962	7.263	0.2989E-02	82.120	0.1061E 02
9.250	955	7.262	0.2506E-02	82.120	0.1061E 02
9.750	948	7.262	0.2122E-02	82.120	0.1061E 02

TABLE 6.13: AVERAGE SLAB VALUES

h(m)	T(C)	CO2	CH4	CO+N2	H2
0.125	1572	15.000	0.1765E-04	85.000	0.4753E-03
0.375	1570	14.990	0.1691E-02	85.000	0.2546E-02
0.625	1561	14.830	0.1210E 00	84.850	0.1935E 00
0.875	1262	11.260	0.5772E 01	79.030	0.3939E 01
1.050	914	7.670	0.4467E 01	85.820	0.2045E 01
1.150	792	5.521	0.2861E 01	86.630	0.4988E 01
1.250	758	4.744	0.1680E 01	85.950	0.7627E 01
1.350	759	4.537	0.9571E 00	85.310	0.9200E 01
1.450	769	4.518	0.5503E 00	84.560	0.1037E 02
1.750	773	4.558	0.3023E 00	85.880	0.9264E 01
2.250	785	4.635	0.2068E 00	85.750	0.9407E 01
2.750	794	4.736	0.1452E 00	85.960	0.9161E 01
3.250	800	4.790	0.9780E-01	85.650	0.9457E 01
3.750	801	4.808	0.6812E-01	85.550	0.9577E 01
4.250	800	4.805	0.4621E-01	85.430	0.9718E 01
4.750	797	4.785	0.3140E-01	85.200	0.9988E 01
5.250	793	4.768	0.2210E-01	85.000	0.1021E 02
5.750	790	4.754	0.1609E-01	84.840	0.1039E 02
6.250	787	4.744	0.1208E-01	84.710	0.1053E 02
6.750	784	4.736	0.9312E-02	84.610	0.1064E 02
7.250	781	4.729	0.7343E-02	84.530	0.1074E 02
7.750	779	4.725	0.5904E-02	84.460	0.1081E 02
8.250	776	4.721	0.4828E-02	84.410	0.1087E 02
8.750	773	4.717	0.4006E-02	84.360	0.1092E 02
9.250	771	4.715	0.3366E-02	84.320	0.1096E 02
9.750	768	4.713	0.2859E-02	84.290	0.1099E 02

TABLE 6.14: AVERAGE SLAB VALUES

6.8 Three-Dimensional Sloping Wall Configuration – Six Sonic Tuyeres

In this section results are presented for three-dimensional runs with six sonic tuyeres. The inlet volume flow rate is 8000 Nm^3/hr composed of 15% CO_2, 35% CO and 50% N_2, by volume, injected at 1575°C. Methane (CH_4) is injected radially through the six sonic tuyeres at a rate of 7% of the main-flow rate at 294°K temperature. The geometry is shown in Figures 6.79(a) and (b).

There are two cases to be considered:

(a) Wall-injection: ie. the tuyeres are positioned at the top end of the sloping wall as shown in Figure 6.79(a).

(b) Throat injection: ie. tuyeres positioned at the bottom end of the

sloping wall as shown in Figure 6.79(a).

The six tuyeres are positioned at intervals of 60° and symmetry of 30° exists, as shown in Figure 6.79(b). Because of the 30° symmetry, the results presented below for both cases, are for the θ-planes 3.75^o, 11.25^o, 18.75^o and 26.25^o degrees. For both the wall- and throat-injection cases, a 30° slab is considered with CH_4 injected at the cell adjacent to the wall and to one of the symmetry planes. To allow for the symmetry only one half of the actual tuyere flow rate is introduced into the cell. The centre of this cell corresponds to θ=3.75^o, at 1.45 and 0.875m above the inlet for the wall and throat cases, respectively.

6.8.1 Wall-injection

Figures 6.80 to 6.83 show the velocity vectors and the temperature contours for θ=3.75^o, 11.25^o, 18.75^o and 26.25^o, respectively. There is a large recirculation zone above the sloping wall with the reattachment point approximately 3.46m above the inlet.

At the injection plane θ=3.75^o, the large velocity vectors above the sloping wall correspond to the CH_4 wall-injection, and as we move away to θ=11.25^o, etc planes, the size of the vectors decreases.

The exit temperature has a flat profile at 1067°C. Inside the recirculation zone the temperature is approximately 848°C, and on the same z-plane at the centreline 1491°C. At the reattachment point the temperature is 1066°C and 1145°C on the same z-plane, at the centreline of the duct. At the injection zone, θ=3.75^o the temperature is 780°C on the cell nearest the wall and 972° 976° and 977°C at

$\theta = 11.25^\circ$, 18.75° and 26.25°, respectively. The lowest temperature of approximately $715^\circ C$ is found in the centre point of the sloping wall, approximately 0.6m from the centreline and about 1.40m above the inlet. At this point the reaction rate is at its highest and therefore heat extraction is also at its highest. The temperature drops very rapidly along the centreline to about $1100^\circ C$ halfway up the duct and then very slowly, since the reaction rate is very low. Above that point, highest temperatures are found along the centreline and lowest closest to the wall. Overall, the temperature profiles look similar for all θ-planes.

Figures 6.84 to 6.87 show the percentage volume fractions for the CH_4 and CO_2 species for the θ-planes, respectively. Chemical species profiles look similar for all θ-planes, with the exception of the highest value of CH_4 at the injection plane, which is 14, 5.5, 3.5 and 2.6% for the θ-planes, respectively. Methane is consumed very rapidly inside the recirculation zone and halfway up the duct is almost exhausted (0.01%). CO_2 spreads out in a similar manner for all θ-planes and highest values are found along the centreline of the duct. Lowest values inside the recirculation zone, where it has reacted with the available CH_4. Exit value of CO_2 is approximately 7.3%.

Figures 6.88 to 6.90 show the vector plots for z-planes at heights of 1.40, 1.45 (injection plane), and 1.50 above inlet. The largest radial velocities are found in the region of the injection plane.

6.8.2 Throat-Injection

Figures 6.91 to 6.94 show the velocity vectors and the temperature contours for planes $\theta = 3.75^\circ$, 11.25°, 18.75° and 26.25°, respectively.

There is a large recirculation zone above the sloping wall with the reattachment point approximately 3.63m above the inlet, compared with the 3.46m for the wall injection.

The exit temperature has a flat profile as in the wall-injection case, with a temperature of approximately $1063^{\circ}C$. Inside the recirculation zone the temperature is approximately $1072^{\circ}C$, and on the same z-plane at the centreline, $1217^{\circ}C$. At the reattachment point, the temperature is approximately $1077^{\circ}C$ and $1114^{\circ}C$ on the same z-plane at the centreline of the duct. At the injection plane $\theta=3.75$, the temperature is $1051^{\circ}C$ at the throat wall and $1553^{\circ}C$ at the centreline, on the same level. The lowest temperature of approximately $999^{\circ}C$ is found at 1.15m above the inlet at the cell nearest the throat wall. Temperatures drop very rapidly along the centreline to about $1100^{\circ}C$ halfway up the duct and then very slowly, since the reaction rate is low above that point. Highest temperatures are found along the centreline and lowest close to the walls. Overall temperature profiles look similar for cell θ-planes, as in the wall-injection case.

Figures 6.95 to 6.98 show the percentage volume fractions for the CH_4 and CO_2 species for the four θ-planes, respectively. Species profiles look similar for all θ-planes, with the exception of the highest CH_4 value at the injection plane, which is 17, 7, 3.5 and 2.5%, respectively for the four θ-planes. Methane is consumed very rapidly around the lower edge of the sloping wall and halfway up the duct it is exhausted. CO_2 spreads out in a similar manner for all θ-planes, the highest values are found along the centreline, and the lowest inside the recirculation zone as in the wall case. Exit value of CO_2 is approximately 7.3% as in the

wall case.

Figures 6.99 to 6.102 show the velocity vectors for the z-planes at heights: 0.875 (Injection plane), 1.05, 1.25 and 1.45 respectively. The velocity vectors are shown at the injection plane (Figure 6.99) and some of the planes above it. Figures 6.101 and 6.102 also show the velocity vectors inside the recirculation zone. The biggest velocity vectors are found at a height 1.05m (Figure 6.100), 0.175m above the throat-injection.

6.8.3 Comparison of the two cases

The two cases described, wall- and throat-injection, exhibit similar characteristics. Average exit temperatures and average species concentration are similar for both cases.

The major difference between the wall and throat-injection cases is that the reattachment point is lower for the wall case (3.46m) than it is for the throat-injection case (3.63m). Also, the wall case attains lower temperatures than the throat-case, especially inside the recirculation zone.

The average exit volume fraction values of all chemical species present, is approximately 7.3, 0, 82.44 and 10.26 for CO_2, CH_4, $CO+N_2$ and H_2, respectively.

6.9 Off-Gas Reaction Vessel I (RV1)

This plant is shown in Figure 6.103. Figure 6.103(a) shows a side-view of the plant and Figure 6.103(b) the injection tuyere plane.

There are six sonic tuyeres situated at regular intervals of 60° as shown in Figure 6.103(b), ie. at 30°, 90°, 150°, 210°, 270° and 330°. The injection plane is at 0.5075m above the inlet.   Symmetry of 180° exists and therefore it suffices to model only half of the plant.   The exit is situated at the side of the plant, as shown in Figure 6.103.

Two cases are considered:

(a)   Six tuyeres directed along the radii.

(b)   Six tuyeres inclined at 5° to the radii, as shown in Figure 6.103(b).

In both cases the walls are made of refractory brick and as such are assumed to be insulated.   The results presented below are for θ-planes: 10°, 20°, 30°, 60°, 90° and 150°.   The inlet volume flow rates and CH_4 injection, as well as in the inlet temperatures, are the same as in Section 6.8.

6.9.1.   Tuyeres along the radii

Figures 6.104 to 6.109 show the velocity vectors and the temperature contours for the above θ-planes, respectively.   Figure 6.104 shows the flow at the centre of the exit plane and Figure 6.105 at the edge of the exit plane.   In these two planes some of the flow leaves immediately through the exit and some progresses up to the top and then turns around near the wall and joins the escaping flow.   Figures 6.106 to 6.109 show the flow recirculating above the sloping walls, with the plane farthest away from the exit plane, exhibiting the biggest recirculation zone.

The temperature contours follow a similar pattern for all θ-planes, with the temperature higher in the centre and lowest inside the recirculation zone. The exit temperature at the centre of the outlet plane ($\theta=10^{\circ}$) varies between $1086^{\circ}C$ to $1205^{\circ}C$ for the lower and top end of the outlet, respectively. The lowest temperatures of $769^{\circ}C$, $824^{\circ}C$ and $837^{\circ}C$ are found at the injection plane 0.705m above inlet, for tuyeres 1, 2 and 3, respectively. These temperatures correspond to the cells nearest the wall-tuyeres at 0.5125m from centreline. The temperatures at the top wall cells vary between $1298^{\circ}C$ and $1245^{\circ}C$ for the centreline and the walls, respectively. Above the side outlet the temperature is uniform in the centreline at approximately $1357^{\circ}C$ and varies between $1242^{\circ}C$ and $1255^{\circ}C$ on the walls for the above θ-planes, respectively, with the lowest temperature of $1242^{\circ}C$ above the 10° θ-plane. Above the injection plane at 0.6125m above the inlet, and 0.5125m from the centreline, at the lower end of the recirculation zone, the temperature varies between $1002^{\circ}C$ and $1235^{\circ}C$, between $\theta=10^{\circ}$ and $\theta=150^{\circ}$ and it is uniform for all θ-planes at $1557^{\circ}C$ at the centreline. Overall, there is a steep temperature gradient up to halfway up the domain. Above that point the temperature gradient is lower. The largest temperature drop occurs inside the recirculation zone, where most of the reaction is taking place.

Figures 6.110 to 6.115 show the percentage volume fraction of the CO_2 and CH_4 species for the above θ-planes, respectively. Overall, CH_4 and CO_2, spread out in a similar way for all θ-planes. Much of CH_4 is 'short-circuiting' and escapes through the side outlet and the rest reacts with the available CO_2. There is not much CH_4 at the top part of the domain and the highest values are found at the injection plane with 18, 23, 29, 12, 26 and 25% for the θ-planes, respectively. The amount of

CH_4 escaping is about 2%, with the highest value of CH_4 concentration found at the lower end of the side-outlet. Lowest values of CO_2 are found inside the recirculation zone (lower part), where most of the reaction with CH_4 takes place. Highest values of CO_2 are found along the centreline.

Figures 6.116 to 6.123 show vector plots at z-planes: 0.465, 0.5075 (injection plane), 0.6125, 0.85 (outlet plane), 1.05 (outlet plane), 1.25 (outlet plane), 1.70 and 2.55m above the inlet. They show the radial movement of the flow anticlockwise up to the injection plane, (0.5075m), Figure 6.117, and then gradually above it, turning clockwise near the wall. Near the top the flow is completely clockwise, Figure 6.123.

The grid used for the above calculations is (NX*NY*NZ) equal to 7x12x14. Numerical results are also available for a refined grid of 17*12*21 but because of graphic storage limitations graphic output was not obtained. Comparison of the two sets of results shows good overall agreement. Both cases predict the CH_4 short-circuiting at the outlet region with the two values differing by about 10% (higher value for the fine grid). Top-plate temperatures are predicted to vary between: 1108 – 1169°C for the fine grid and: 1245 – 1298°C for the coarse grid. These differences in temperature range on the top-plate, are attributed to the fact that the nodal values are closer to the top-plate for the fine grid (ie. more grid points).

At the outlet the temperatures vary from 1067° to 1141°C for the fine grid and from 1086°C to 1205°C for the coarse grid giving a difference of

about $60^{\circ}C$ between the two grid sizes.

6.9.2 Tuyeres at 5° degrees to radii

The position and the directions of the six inclined tuyeres is shown in Figure 6.103. The same reference θ-planes are again considered, as in Section 6.9.1.

Results are very much similar to the 6.9.1 case. The lowest temperatures are again found in the tuyeres regions, with the exception that lowest temperatures are slightly higher than before. They are 787°, 847° and $882^{\circ}C$ for tuyeres 1, 2 and 3, respectively, compared with 769°, 824° and $837^{\circ}C$ for the previous case 6.9.1. Temperatures at the top plate vary between 1312° and $1258^{\circ}C$ for the centreline and the walls respectively, compared with $1298^{\circ}C$ and $1245^{\circ}C$ for the previous case. The temperature at the centre of the outlet plane ($\theta=10^{\circ}$), varies between $1088^{\circ}C$ and $1217^{\circ}C$, for the lower and the top end of the outlet, respectively, compared with 1086° and $1205^{\circ}C$ of the previous case. Overall, this case gives temperatures approximately $25^{\circ}C$ higher than the previous case 6.9.1. The velocity vectors also behave in a similar manner to the previous case.

The chemical species CO_2 and CH_4 behave in a similar manner as previously and their profiles look the same. The only important exception is that mixing is not as good as previously and hence less CH_4 reacts with the available CO_2 in the recirculation region, CH_4 and CO_2 taking longer to react. This has an effect on the average temperatures which are approximately $25^{\circ}C$ higher.

The radial velocity vector plots for the different planes show a similar radial movement, as before, with the exception at the injection plane, 0.5075m above the inlet (Figure 6.124). In this case the radial velocities are slightly bigger. Figure 6.124 is the only one presented for this section, that shows major differences from previously.

Overall, the two cases give comparable results. Very little experimental results were available (J Moodie (1986)) and those only concerned the exit temperatures and CH_4 exit values. Experiments showed that the exit temperatures varied between 1000^oC and 1200^oC and approximately 3% of CH_4 was 'short-circuited'. These results agree well with the model results and confirmed the presence of significant unreacted CH_4 amounts.

The radial exit velocities in both cases vary between 25.59 to 39 m/sec and 26.47 to 40 m/sec for the 6.9.1 and 6.9.2 cases, respectively. Case 6.9.2 velocities are slightly higher because of the slightly higher temperatures.

6.10   Incorporating the Arrhenius Rate Minimum

In all the cases presented so far the reaction rate was taken to be given by the eddy-breakup model, discussed in Chapter 4. In this section the Arrhenius rate is incorporated into the models and the actual rate is taken to be the minimum of the eddy-breakup rate and of the Arrhenius rate.

Results are presented for various two-dimensional geometries and inlet compositions employing the one- and two-reaction models, discussed in Chapter 4. In all cases the flow is considered to be one-phase (ie.

gases only).

As mentioned above, the chemical system under consideration is made up of CH_4, CO_2, CO, H_2O, H_2 and N_2 with CH_4 being the 'driving-force' in the reactions. These reactions are termed as high temperature hydrocarbon reactions and as such are complicated chemical processes.

The usual first steps in building a model of a complex reaction system are to assemble the available information about the mechanism and to devise a provisional mathematical model, generally consisting of a set of non-linear equations, which can be solved to give predicted concentration profiles of the species present. Using experimental results the models can be refined with respect to its mechanism and its parameters. One of the most important model refinements is the introduction of the Arrhenius rate, which is considered to be an important factor in the reaction mechanism, as discussed in Chapter 4, since reaction rates are, in general, strongly dependent on temperature. The temperature dependency is in the form of the reaction rate coefficient, K_f (see Equations 4.4 and 4.5) given by:

$$K_f = \begin{cases} A \exp(-E/RT) & \text{for Arrhenius behaviour} \\ BT^b \exp(-E/RT) & \text{for non-Arrhenius behaviour} \end{cases} \qquad (6.7).$$

The study of K_f, the reaction rate coefficient, has been one of the primary subjects of kinetic investigations over the last 20 years (Gardiner, (1984) and as a result there is massive literature on kinetics. Yet many kinetic data are not satisfactory for the purpose intended, indeed some are no good at all (Bernasconi (1986)). A number of authors give recommended rate coefficients for the Arrhenius rates which are

either taken from experiments described in the scientific literature or estimated by comparison with rate coefficients for analogous reactions. In the latter case, they are merely informed guesses.

The choice of the kinetic data from the literature is strongly dependent on the type of reaction under consideration, which can be classed as a simple (one-step reaction) or a complex reaction having consecutive steps, coupled reactions, parallel reactions, etc with intermediate steps (Kondrat'ev (1964)). In this case one should know the compositions and structures of the reactants, the products and byproducts, and whether alternative sets of products are formed competitively.

Clearly, for the one-step reaction, the reaction law rate will be dependent only on the original chemical species and for the complex reactions, will be dependent on the original and intermediate chemical species. Despite the complexity of the second case (complex reaction), sometimes it is possible to establish a simple approximate treatment of the reaction, which can still be useful, especially in the absence of reliable information. At the same time, from the general ideas of kinetics of complex reactions, it has been concluded (Kondrat'ev (1964)) that reactions with consecutive steps may also have rates independent of the concentration of some reacting substances. In order that the rate should not depend (Kondrat'ev (1964)) on the concentration of some particular reacting substance, it is sufficient for the rate of the limiting step of the reaction to be independent of the concentration of this substance. For example, in the simplest case, consider the reaction A+B $\rightarrow$ C, taking place in the two stages:

$$K_1 \qquad\qquad\qquad K_2$$
$$A \rightarrow x \quad \text{and} \quad x + B \rightarrow C,$$

where K_1 and K_2 are rate constant.

From the law of mass action, which states that the rate of chemical reaction is proportional to the product of the molar concentrations of the reacting substances, the rate of reaction of the substance x is given by:

$$\frac{d(x)}{dt} = K_1(A) - K_2(x)(B) \qquad\qquad (6.8);$$

where ( ) represents molar concentration of a chemical species in dilute solution. But the second term in (6.8) is equal to zero at the start of a reaction and increases with time, becoming equal to the first term (which decreases with consumption of the initial substance A) at a definite moment of time. At this moment of time we have $d(x)/dt=0$. From this moment the concentration of the intermediate substance x decreases parallel to the decrease in concentration of the initial substance and the value of $d(x)/dt$ is automatically kept close to zero. So $d(x)/dt$ can be assumed to be zero under steady-state conditions (Kondrat'ev (1964)) and Equation (6.8) is now:

$$\frac{d(x)}{dt} = K_1(A) - K_2(x)(B) = 0.$$

Therefore:

$$\text{reaction rate} = \frac{d(C)}{dt} = -\frac{d(A)}{dt} = K_1(A)$$

ie. the rate of reaction is dependent only on the concentration of substance A.

In the present work the reactions under consideration are:

$$CO_2 + CH_4 \rightarrow 2CO + 2H_2 \qquad (a)$$

$$H_2O + CH_4 \rightarrow CO + 3H_2 \qquad (b)$$

(6.9):

and depending on the reaction model used (see Chapter 4), either only one reaction is considered (ie. only (a)) or both.

Both reactions are very complex with many intermediate steps; nevertheless, it is possible to establish the main features governing their reactions, under the given conditions, despite the fact that there is very little information available.

Edelman and Hasha (1978), Bowman (1974), Dixon-Lewis and Islam (1982), Jensen and Jones (1978), Westbrook et al (1977), Bilger (1977), Skinner et al (1972), Creighton (1977), Engleman (1976), Gardiner, (1984) and many others give Arrhenius rate coefficient values for various high-temperature hydrocarbon reactions.. Although the above reactions (a) and (b) do not appear explicitly anywhere in the relevant reaction rate literature, their intermediate steps do.

For example, reaction (a) is thought to have the following steps:

$CH_4 + CO_2 \longrightarrow CH_3 + H + CO_2$

$CO + O + H$

$CHO + H_2$

RESULTS

$2CO + 2H_2 \longleftarrow H_2 + CO$

In our case for the chemical system of CH_4, CO_2, CO, H_2O, H_2 and N_2, for reactions (a) and (b), the predominant factor is the dissociation of CH_4 in $CH_3 + H$, ie:

$$CH_4 + M \rightarrow CH_3 + H + M \qquad (6.10);$$

where M is taken to be the 'bath' of the rest of the species. At the same time all the other intermediate steps are ignored under the assumption that the rate of the limiting step of the reaction is independent of the concentration of the other substances, and therefore according to Kondrat'ev (1964), it only depends on the CH_4 as seen from above.

This important simplifying assumption is considered in view of the complexity of the problem, the available computer time and storage and the overall efficiency of the software developed.

A short survey of the Arrhenius rates found in the literature is given in Table 6.15. They all refer to Equation (6.7), ie:

$$K_f = BT^b \exp(-E/RT) \qquad (6.11);$$

for the reaction (6.10).

Jensen and Jones (1978) give the forward rate K_F and the equilibrium rate K_E for the reaction $CH_3+M+H \rightarrow CH_4+M$.

For the given values the reaction rate K_R for our case is obtained using the quotient law, (which states that the ratio of the forward reaction rate coefficient to the rate coefficient of the backward reaction is equal to the equilibrium constant). The values given for K_F and K_E are: 2×10^{-21} T^{-3} and 4×10^{-27} $\exp(5.46\times10^4/T)$, respectively, with units of ml/molecule/sec.

This rate is of the 'non-Arrhenius' type and Jensen and Jones (1978), suggests that the weighted average 'collision efficiency' β_W (see Chapter 4) for the 'bath gas' is not recommended, because the rate coefficient K is already averaged for the most effective third bodies (eg. CO_2, H_2O, N_2, etc). Also because of the large temperature range $1000-3000^\circ K$ the uncertainty factor (UF) is reported to be 100.

In this work, the rate is based on that given by Gardiner (1984) with M=Ar, since it was the most recent and that given by Jensen and Jones (1978), with UF=100 and M=Ar, since it was the only non-Arrhenius rate exression found. For both these, rate results were obtained for comparison.

Reference	B	b	E/R	UF	M	Notes
Edelman and Harsha (1978)	2×10^{17}	0	44.5×10^3	–	–	Units of cm^3/mol/sec temperatures above $1000^{\circ}K$.
Gardiner, (1984)	2×10^{17}	0	44.5×10^3	± 3.1622	Ar	For temperature 1500-$3000^{\circ}K$ but also useful for 1000-$1500^{\circ}K$. Units of cm^3/mol/sec.
Westbrook et al (1977)	2×10^{17}	0	44.5×10^3	–	–	Units of cm^3/mol/sec. Temperature range 1000-$1350^{\circ}K$.
Skinner et al (1972)	4×10^{17}	0	44.5×10^3	–	Ar	Value of B has been multiplied by a factor of 2 to give better agreement with experimental results. Units of cc/mol/sec. Temperature range below $1700^{\circ}K$.
Bowman (1974)	1.4×10^{17}	0	44.5×10^3	–	–	High temperature range 1900-$2400^{\circ}K$. Units of cm^3/mol/sec
Jensen and Jones (1978)	5×10^{-5}	-3	5.46×10^4	100	Ar	Temperature range 1000-$3000^{\circ}K$ - see text.
Gardiner et al (1974)	2.3×10^{14}	0	3.25×10^4	–	Ar	Temperature range 2000-$2700^{\circ}K$. Units of cm^3/mol/sec.

TABLE 6.15: SELECTION OF ARRHENIUS RATES

The 'collision efficiency' β_C (see Chapter 4) is obtained from Table 4.6 and for our particular system is:

	Ar	H_2	CO_2	CO	CH_4	H_2O	N_2
β_C	1.0	2.857	4.286	2.143	18.571	18.571	1.143

TABLE 6.16: COLLISION COEFFICIENTS

In practice the 'Arrhenius' rate acts as a minimum, and is used only at the lower end of the temperature range, to stop the reaction. At higher temperatures the eddy-breakup rate applies. Both rates behave in this way, but as it will be seen from the reported results below, the choice of the rate, coupled with the choice of UF, can influence the temperature below which the Arrhenius rate takes over. The Arrhenius rate can be lower than the eddy-breakup rate everywhere, or just at the lower end of the temperature range depending on our choice of rate and UF.

Two geometry configurations were considered: (a) based on the geometry and input parameters described in Section 6.7 with throat injection and one reaction only with 4000 Nm^3/hr inlet volumetric flow rate and 5% injected CH_4; and, (b) based on the off-gas reaction vessel II (RV2) described below.

6.10.1 Case (a) geometry with Arrhenius minimum

For this case four runs were performed:

Run 1: Rate given by Gardiner (1984) with β_W term.

Run 2: Same as Run 1 with UF=3.1622.

Run 3: Rate given by Jensen and Jones (1978) with UF=100 (results also presented in Section 6.10.3).

Run 4: No Arrhenius rate present with cut-off temperature of $1100^{\circ}K$ to replace old results (previous results reported in Section 6.2, had cut-off temperature of $916^{\circ}K$).

The results presented are for the averaged exit slab values and are given in Table 6.17

	RUN 1	RUN 2	RUN 3	RUN 4
T(C)	1254	1219	1044	1137
CO_2	23.72	20.79	12.75	22.42
CH_4	2.934	2.33	0.725	1.799×10^{-3}
CO	60.28	55.35	41.79	69.63
H_2	13.066	21.597	44.78	7.941

TABLE 6.17: AVERAGED EXIT VALUES

For Run 1, examination of the full results reveal that the Arrhenius rate is less than the eddy-breakup rate everywhere in the region and as a result the reaction rate is very small and CH_4 is almost unreacted at the exit. Also, the temperature drop is steady and uniform from inlet to exit.

Run 2, gives results similar to Run 1 with slightly less CH_4 at the top and $35^\circ C$ lower exit temperature because of the effect of the UF term.

For Run 3, the Arrhenius rate is less than the eddy-breakup rate for only part of the region (where temperatures are lowest). This results in a sudden drop in the temperature at the lower part of the duct because of the turbulent reaction rate mechanism and above it a steady uniform temperature drop, where the Arrhenius rate prevails. Far more CH_4 results than in the previous two cases and at the exit there is only a small amount unreacted, ie 0.7%. Also the exit temperature is $210^\circ C$ lower than Run 1 mainly because of the endothermic reaction.

Run 4, is a rerun of the previous case to reproduce old results with a cut-off temperature of $1100^\circ K$, with no Arrhenius rate present. As shown before, it is predicted that CH_4 is totally consumed at the end, with an exit temperature of approximately $1130^\circ K$.

Detailed experimental measurements were not available for this case. However, the results using the rate proposed by Jensen and Jones (1978) with UF=100 in conjunction with the eddy-breakup rate where closest to known exit conditions (J Moodie (1986)).

6.10.2   Off-Gas Reaction Vessel II (RV2)

Consider the two-dimensional geometry of Figure 6.125. There is counter-current injection of methane with sonic velocity in the centre of the duct, as shown in Figure 6.125, at a temperature of $294^\circ K$. The lower part of the walls (ie. up to 1.0m above the inlet) is insulated, the 'lip' is at a temperature of $300^\circ C$, the lower sloping wall and the wall up

to 2.0m above it are kept at a temprature of 800°C and for the next 3.0m above it, the wall temeprature is 150°C (due to water-cooling). The rest of the wall (ie. the section near the outlet) is again insulated. The inlet temperature is 1600°C and all the dimensions of the various sections of the duct are shown in Figure 6.125. The initial volumetric percentage composition of the gases is given in Table 6.18.

Species	CO	CO$_2$	H$_2$	H$_2$O	N$_2$
% volume	24	8	4	6	58

TABLE 6.18:   INITIAL GAS COMPOSITION

For reasons explained in earlier sections, the composition of CO is taken together with the composition of N$_2$. At the end of the calculations the respective compositions of the two species are retrieved.

Nitrogen is flushed at 200 Nm^3/hr, with a velocity of 20 m/sec at a temperature of 300°K by the side of the lip, adjacent to the lower end of the sloping wall, as shown in Figure 6.125.

In this section the two reaction model is employed as explained in Chapter 4.

The first section of the results presented below refers to the comparison of the outlet results given when the two rates by Gardiner (1984) and Jensen and Jones (1978) are employed. The initial volumetric flow rate is 8000 Nm^3/hr and the injected CH$_4$ is 5% (ie. 400 Nm^3/hr). The

averaged exit slab values are given in Table 6.19, and Run 1 refers to the rate given by Gardiner (1984) and Run 2 to the non-Arrhenius rate of Jensen and Jones (1978), with UF=100.

	RUN 1	RUN2
T(C)	1092	1032
CO_2	7.259	6.308
CH_4	3.906	1.910
H_2O	5.346	4.136
H_2	4.741	8.205
$CO+N_2$	78.748	79.441

TABLE 6.19: AVERAGED EXIT VALUES

Comparison of the results revealed that for Run 1, the Arrhenius rate is less than the eddy-breakup everywhere in the domain, and as a result the reaction rate is very small with most of CH_4 unreacted. The temperature drop between inlet and outlet is approximately 508°C.

Employing the rate given by Jensen and Jones (1978), in Run 2, the Arrhenius rate is less than the eddy-breakup rate for only part of the region (ie. for the lower end of the temperature range). The effect that this has on the reaction rate is that for high temperatures (ie. above 1400°K) the reaction rate of CH_4 is very large, resulting in a lot of CH_4

consumption and a sudden drop in the temperature. At the lower end of the temperature range, the Arrhenius rate takes over and the reaction rate is very slow, resulting in little consumption in CH_4 and a small temperature drop. The reaction comes to a halt at a temperature of approximately 1100^OK, since the non-Arrhenius rate is almost zero. Graphical results for this case are presented below in this section.

Again detailed experimental measurements are not available, but it appears that the rate proposed by Jensen and Jones (1978), with UF=100 in conjunction with the eddy-breakup rate, is the most appropriate to be used for our temperature range. This is because it produces results that appear to be more plausible and closer to the results expected by the collaborating establishment (J Moodie (1986)).

The high value of the uncertainty factor (UF) equal to 100, used in this work is attributed to the catalytic effect of the iron particles, which in reality are present in the duct. This is also supported by Takenaka et al (1981) in their paper which indicated that under the operating conditions of the off-gas duct the catalytic action of the iron particles would be high. J Moodie (1986) in a private communication, pointed out that under some conditions iron was deposited on the walls and little oxidation occurred, leading to strong catalytic action. This again supports the high value of the uncertainty factor.

For the RV2 case, a parametric study was performed based on the rate reported by Jensen and Jones (1978) with UF=100, by varying the inlet conditions of CH_4, and of the main flow and by increasing the size of the 'lip' as well as changing the position of the CH_4 sonic tuyere to establish

the optimal operating conditions.

Optimal operating conditions are considered to be the ones where, most (or all) of the injected CH_4 has reacted and CO and H_2 are produced in greatest quantities and the temperature has dropped to between 1000° and 1100^oC.

All results must be compared with the standard case with 8000 Nm^3/hr with 5% CH_4 and gas composition as given in Table 6.18. The exit conditions for the standard case were reported in Table 6.19 for Run 2.

The parametric studies performed were:

Study 1: Standard case, but with insulated walls.

Study 2: Standard case, but counter-current tuyere positioned at 1.0m above inlet, as opposed to 2.2m of the standard case.

Study 3: Standard case, but counter-current tuyere positioned at 0.75m above inlet and lip extended vertically by 10cm to 30cm, as opposed to 20cm of the standard case.

Study 4: Same as study 3, but with 2% CH_4 instead of the 5%.

Study 5: Standard case, but with 4000 Nm^3/hr main flow rate, and 5% CH_4 instead of the 8000 Nm^3/hr.

Study 6: Same as study 5, but with 12000 Nm^3/hr with 5% CH_4.

Study 7: Throat sonic tuyere positioned on the side wall at 1.0m above inlet with 8000 Nm^3/hr and 5% CH_4.

Study 8: Same as study 3, but with a small horizontal buffer at the top of the lip, as shown in Figure 6.126.

The average exit values obtained from the above studies are given in Table 6.20.

From these results (Table 6.20) it can be seen that Study 1 with insulated wall gives the lowest CH_4 average exit value (ie. $\approx 0.25\%$). This is because the absence of wall-cooling keeps the temperature inside the domain high enough for the reaction to continue towards CH_4 extinction.

STUDY	1	2	3	4	5	6	7	8	RUN 2 TABLE 6.19
T(C)	1179	1023	1026	1089	931.5	1075	949.4	1038	1032
CO_2	5.546	6.038	5.908	6.808	6.427	6.215	5.326	6.183	6.308
CH_4	0.245	1.371	0.99	0.139	2.378	1.694	3.805	1.706	1.910
H_2O	3.231	3.828	3.642	4.681	4.353	4.018	3.006	4.036	4.136
H_2	8.641	9.259	9.404	7.452	7.139	8.888	8.596	8.658	8.205
$CO+N_2$	82.337	79.504	80.056	80.920	79.658	79.185	79.267	79.417	79.441

TABLE 6.20: PARAMETRIC STUDY EXIT VALUES

Studies 2 and 3 give the next lowest exit CH_4 values, with study 3 the best of the two.   By extending the lip by 10cm and lowering the tuyere to a position 0.75m above the inlet, the mixing and the reaction are forced to take place in a high temperature region before the flow opens up and before wall-cooling effects drop the temperature to a point where the reaction stops.

A 2% CH_4 concentration results in a near extinction of CH_4 in Study 4 and an exit temperature of approximately 1089°C, compared to 1179, 1023, and 1026°C, for Studies 1 to 3, respectively.

For the rest of the studies (ie. 5 to 8) large quantities of CH_4 are unreacted. Variations of inlet flow conditions and CH_4 concentrations play a minimum role in the consumption. Overall, it appears that to achieve high CH_4 consumption, CH_4 must be introduced in a high temperature region well away from any wall-cooling effects. Study 3 appears to give the best results of all studies for the 8000 Nm^3/hr and 5% CH_4 case.

Study 1 with insulated walls was re-run with UF=1 and comparison of the results was made with Study 1 results which employ UF=100.

The average exit values of this run are given in Table 6.21 along with the results of UF=100 of Study 1.

These results indicate that for UF=1, most of the CH_4 is unreacted (ie. exit value ≃2.17%) with a much higher exit temperature of about 1252°C compared to the respective values of CH_4 and temperature for UF=100, which are 0.245% and 1179°C. The other species also differ considerably. This is because the value of the reaction rate (minimum of eddy-breakup and Arrhenius rate) is much smaller for UF=1 for most of the region. Table 6.22 gives the overall maximum and minimum values for UF=100 and UF=1, for the temperature, the eddy-breakup rate and the Arrhenius rate.

	UF=100 (Study 1)	UF=1
T(C)	1179	1252
CO_2	5.546	6.360
CH_4	0.245	2.173
H_2O	3.231	4.255
H_2	8.641	8.551
CO	25.8125	24.3154
N_2	56.5245	54.3456
TPC	20.30	24.41

TABLE 6.21:   INSULATED CASE RESULTS WITH UF=100 AND UF=1

Overall MAX			Overall MIN	
UF = 100	UF = 1		UF = 100	UF = 1
1873	1873	T($^\circ$K)	1135	1183
40.07	39.57	Eddy-rate	0.5389	0.5251
2373	23.79	Arrhenius rate	0.608×10^{-4}	0.376×10^{-5}
40.07	20.95	min(Ar,Ed)	0.608×10^{-4}	0.376×10^{-5}

TABLE 6.22:   OVERALL MAX/MIN VALUES

All the above results give an indication of the importance of the uncertainty factor UF in the reaction rate, and at the same time, show the difference it can make in the results, according to the value it takes in the model.   Especially in the case of the amount of CH_4 that has reacted, the models predictions differ considerably as shown above.

The values of the Arrhenius rate, the eddy-breakup rate and of the minimum of the two are divided by the mass fraction of CH_4 (m_{fu}). The logarithms to the base 10 is then calculated and the result is plotted against temperature (K) in Figures 6.127 to 6.132.   These values are from Study 1, for the insulated case for UF=1 and UF=100.   The purpose of this exercise was to establish the temperature at which the two rates cross each other on the axis and the temperature range in which one or the other rate is the minimum for the two cases of UF=1 and UF=100.

Figures 6.127 to 6.129 and Figures 6.130 to 6.132 refer to UF=100 and UF=1, respectively.   EDY and ARR stand for the eddy-breakup and Arrhenius rates, respectively.   They are all plotted on the same scale for comparison purposes.

Graphs for the log_{10} (ARR/MFU) values against temperature (K) for both cases, Figures 6.127 and 6.130 respectively, give smooth curves, with higher Arrhenius rates for the UF=100 case.   The lowest rate values correspond to T=1135°K and 1183°K for the two cases, respectively.

Graphs for the log_{10} (EDY/MFU) values against temperature (K) for both cases, Figures 6.128 and 6.131 give a scatter of points for each

temperature unlike the Arrhenius rate. This is because of the definition of the eddy-breakup rate, Equation (4.21), which is also dependent on k, ϵ and ρ.

Figures 6.129 and 6.132 show the $\min[\log_{10}(ARR/MFU), \log_{10}(EDY/MFU)]$ for UF=100 and UF=1, respectively. For UF=100, Figure 6.129, it can be seen that the Arrhenius rate is the minimum for temperatures approximately less than $1573^{\circ}K$ (ie. $1300^{\circ}C$), with some heavy overlapping with the eddy-breakup rate for temperatures $1500^{\circ}-1573^{\circ}K$. Above the $1573^{\circ}K$ temperature the eddy-breakup rate is always the minimum.

For UF=1, Figure 6.132, the Arrhenius rate is the smaller rate for most of the temperature range (up to approximately $1850^{\circ}K$), and only near the highest temperature values (ie. $1870^{\circ}K$) is the eddy-breakup rate the smaller again, with some overlapping temperatures in excess of $1800^{\circ}K$.

From the above results it appears that the choice of the UF value can influence the position of the minimum of the Arrhenius rate and of the eddy-breakup rate and consequently the actual reaction rate. The value of UF=100, as mentioned above, is the most realistic one for our temperature range in the presence of catalytic iron, and gives a balanced and smooth transition between the two rates. This is evident from the temperature ranges that the two rates are active.

The whole study seems to indicate conditions under which the reforming of natural gas would and would not take place. A temperature of $1200^{\circ}C$ seems critical and in reality would only be achieved with well-insulated

walls, however, such a plant is not feasible (J Moodie (1986) since particulate build-up on refractory walls would be severe.

6.10.3 Representative results

In this section some representative graphical results are given for the RV2 case (Run 2, Section 6.10.2) and for Run 3, of Case (a) of Section 6.10.1.

Figure 6.133 shows the vector plots for the RV2 case, with the sonic counter-current tuyere, just detected along the centre axis near the centre of the domain.   There is a large recirculation zone above the lower sloping wall with the reattachment point approximately 6.05m above the inlet, almost touching the top sloping wall.   The exit velocities are approximately 60 m/sec.   There appears also to be two very small recirculation zones above the 'lip', where the large recirculating flow joins the main flow just above the lip.   Figure 6.134 also shows the large recirculating zone, where the streamlines are plotted.   The displacement of the streamlines at the centre of the duct, along the axis, indicate the position of the counter-current tuyere.

Figure 6.135 shows the temperature contours.   The lowest temperature of approximately 450°C occurs at the injection point of N_2, by the 'lip', because of the very low temperature of the injected N_2.   At the CH_4 tuyere injection point, the temperature is approximately 1000°C and the wall temperature varies between 945°C at the lower part, to a peak value of 1005°C approximately 2.9m above inlet (ie. halfway up the duct) to 948°C, 5.76m up the duct, just below the upper sloping wall. Temperature drops very slowly along the central axis up to just below the

counter-current tuyere and then very rapidly, because of the reaction taking place. The lowest temperature inside the large recirculation zone is approximately 865°C, 1.275m above inlet and 0.45m from the centreline, almost above the 'lip'. The biggest horizontal temperature gradient is found in the lower part of the duct above the lower sloping wall and the smallest at the top part near the exit, where there is not much chemical activity. The average exit temperature is approximately 1032°C.

Figures 6.136 and 6.137 show the percentage volume fractions of the CH_4 and CO_2, H_2O chemical species, respectively. Highest CH_4 concentration is naturally found near the injection point and as it spreads out it decreases rapidly. Average exit value is approximately 1.9%, indicating that there is a lot of CH_4 unreacted. This is because the temperature drops to a point where the reaction cannot proceed any more, especially in the top part of the duct. The highest chemical activity and consequently the largest consumption of CH_4 is found inside the large recirculation zone, at the lower part, where mixing takes place. CO_2 and H_2O follow similar patterns and their highest values are found near the inlet. Their average exit values are approximately 6.31% and 4.14%, respectively.

Table 6.23 gives the average slab values of the temperature and the chemical species.

Figures 6.138 and 6.139 refer to the Run 3, of Case (a) of Section 6.10.1, and they show the temperature and CH_4, CO_2 contours, respectively. This case as explained earlier, employs a one-reaction

model with throat-injection. The average exit temperature is approximately 1044°C and the average exit values of CO_2 and CH_4 are approximately 12.75% and 0.73%, respectively. These figures can be compared directly with Figures 6.53, 6.56 and 6.59 of Section 6.7, with no Arrhenius rate present. They exhibit a lot of similarities with the exception of CH_4 concentration and temperature. This is because the presence of the Arrhenius rate slows the reaction, thus leaving some CH_4 unreacted, which in turn influences the temperature, since there is no more heat extracted from the system. Overall, there is a slightly higher exit temperature than before, (approximately 50-60°C) and more CH_4 at the end, since in the previous case, Figure 6.56, it was predicted the CH_4 has been exhausted almost halfway up the duct.

Table 6.24 gives the average slab values of temperature, chemical species and TPC.

6.10.4 Comparison with experimental results for RV2 case

All the above results for the RV2 case employed input data/parameters and gas composition provided by the collaborating establishment, with the purpose of indicating the general characteristics of the flow and providing reference predictions for the subsequent experiments.

h(m)	T(C)	CO2	CH4	CO	H2	H2O
0.125	1598	7.972	0.2726E-11	26.100	4.102	5.984
0.375	1595	7.972	0.2619E-09	26.100	4.099	5.984
0.625	1593	7.972	0.1709E-07	26.100	4.099	5.984
0.875	1591	7.972	0.8222E-06	26.100	4.099	5.984
1.020	916	5.142	0.5008E 00	25.690	3.706	3.725
1.060	895	5.755	0.1030E 01	25.260	5.156	4.042
1.100	909	6.242	0.1329E 01	25.020	6.048	4.328
1.140	911	6.485	0.1488E 01	24.890	6.517	4.467
1.180	930	6.584	0.1576E 01	24.820	6.758	4.517
1.225	970	6.608	0.1551E 01	24.840	6.741	4.539
1.275	987	6.651	0.1545E 01	24.850	6.781	4.570
1.450	1018	6.719	0.1490E 01	24.890	6.827	4.621
1.750	1043	6.750	0.1396E 01	24.970	6.807	4.651
2.050	1070	6.770	0.1341E 01	25.010	6.789	4.671
2.437	1090	6.735	0.1944E 01	24.520	6.663	4.634
2.912	1099	6.700	0.1964E 01	24.510	6.794	4.590
3.387	1094	6.650	0.2106E 01	24.390	6.923	4.530
3.862	1083	6.603	0.2206E 01	24.310	7.050	4.476
4.337	1069	6.561	0.2250E 01	24.270	7.182	4.427
4.812	1052	6.518	0.2237E 01	24.280	7.338	4.377
5.287	1036	6.462	0.2156E 01	24.350	7.567	4.313
5.762	1027	6.372	0.1987E 01	24.490	7.952	4.209
8.607	1026	6.218	0.1701E 01	24.720	8.607	4.032
6.150	1020	6.188	0.1673E 01	24.740	8.721	3.998
6.325	1033	6.305	0.1906E 01	24.550	8.215	4.133
6.575	1032	6.308	0.1910E 01	24.550	8.205	4.136

TABLE 6.23: AVERAGE SLAB VALUES FOR RV2

h(m)	T(C)	CO2	CH4	CO+N2	H2
0.125	1571	30.000	0.7927E-05	70.000	0.6611E-03
0.375	1568	30.000	0.7681E-03	70.000	0.8612E-03
0.625	1564	29.900	0.5585E-01	69.990	0.5226E-01
0.875	1430	26.970	0.3009E 01	68.660	0.1367E 01
1.050	1329	22.840	0.2972E 01	62.980	0.1122E 02
1.150	1262	19.720	0.2456E 01	56.990	0.2083E 02
1.250	1211	17.570	0.2004E 01	52.290	0.2814E 02
1.350	1172	16.140	0.1649E 01	49.040	0.3318E 02
1.450	1143	15.180	0.1380E 01	46.810	0.3663E 02
1.750	1129	14.660	0.1276E 01	45.370	0.3869E 02
2.250	1126	14.350	0.1222E 01	44.430	0.3999E 02
2.750	1121	14.100	0.1160E 01	43.750	0.4100E 02
3.250	1113	13.840	0.1098E 01	43.110	0.4196E 02
3.750	1108	13.580	0.1098E 01	42.340	0.4298E 02
4.250	1095	13.380	0.1011E 01	42.140	0.4347E 02
4.750	1087	13.250	0.9632E 00	42.000	0.4379E 02
5.250	1079	13.150	0.9237E 00	41.900	0.4403E 02
5.750	1073	13.070	0.8899E 00	41.840	0.4421E 02
6.250	1068	13.000	0.8606E 00	41.800	0.4434E 02
6.750	1063	12.950	0.8347E 00	41.770	0.4445E 02
7.250	1059	12.900	0.8117E 00	41.750	0.4453E 02
7.750	1055	12.860	0.7910E 00	41.750	0.4460E 02
8.250	1052	12.830	0.7723E 00	41.740	0.4466E 02
8.750	1049	12.800	0.7553E 00	41.740	0.4470E 02
9.250	1046	12.780	0.7397E 00	41.740	0.4474E 02
9.750	1044	12.750	0.7253E 00	41.740	0.4478E 02

TABLE 6.24: AVERAGE SLAB VALUES FOR SECTION 6.10.1

Two test cases were also used which were directly comparable with experimental measurements.

(1)   Insulated case with initial composition given in Table 6.25.

CO	CO_2	H_2	H_2O	N_2	T_{in}
29.1	10.3	2.2	3.7	54.7	$1550^{o}K$ to $1680^{o}K$

TABLE 6.25:   INITIAL CONDITIONS FOR INSULATED CASE

The initial inlet volume flow rate is 8600 Nm^3/hr with 580 Nm^3/hr CH_4 injected counter-currently.

(2)   Water-cooled case, with initial composition given in Table 6.26.

CO	CO_2	H_2	H_2O	N_2	T_{in}
20.6	7.5	5.0	6.8	60.1	$1550^{o}K$ to $1650^{o}K$

TABLE 6.26:   INITIAL CONDITIONS FOR WATER-COOLED CASE

The initial volume flow rate of the off-gas is 9200 Nm^3/hr, with 600 Nm^3/hr CH_4 injected counter-currently.

The exit values obtained using the developed models and the experimental

data are given in Table 6.27. It should be pointed out that the computed results refer to cases with UF=100.

	CO	CO_2	H_2	H_2O	N_2	CH_4	T	
Predictions	31.17	6.188	8.796	1.596	51.5	0.75	1146	Insulated
Experiments	32.9	5.5	7.3	3.2	50.1	1.0	1150-1250	case
Predictions	22.20	5.76	10.90	4.6	53.81	2.73	1054	Water-cooled
Experiments	24.2	6.6	6.7	5.9	52.1	4.5	1020	case

TABLE 6.27: EXPERIMENTAL AND PREDICTED EXIT RESULTS

Closer examination of these results reveals that the predictions quantitatively agree well with the experiments and predict the general characteristics of the flow. Overall, temperatures agree well and the exit values are close to measured values. Most of the chemical species also show good agreement with the exception that the model predicts that too much H_2O reacts. This discrepancy is attributed to the original assumption of the split of CH_4 between H_2O and CO_2 used and the value of $\lambda=2$ in Section 4.6.

From these results it appears that although the simple mechanism employed gives quantitatively good results, the actual λ parameter is a little high, resulting in overestimation of reacted H_2O and underestimation of CO_2. These results however, are encouraging in view of the overall complexity of the model, the lack of reliable kinetic data, and their

relation to the other flow parameters.   The overall objective of the software developed has been achieved.

6.11   Water-Gas Equilibrium

A further development of the two-reaction model described in Chapter 4 is the inclusion of a third reaction, the water-gas reaction (6.12).

$$CO_2 + H_2 \rightarrow CO + H_2O \qquad\qquad (6.12);$$

in the system of reactions (6.9(a) and (b)).

The importance of reaction (6.12) arises from the assumption that reaction 6.9(a) and (b) depend on the water-gas equilibrium (ie. on the equilibrium of reaction (6.12)).

The controlling mechanism in the water-gas equilibrium is the equilibrium constant K_E of (6.12), which can be found in tables (see, for example, Engleman (1976)).   From definition, for any given temperature, T, the equilibrium constant has a value which is always constant for the given T. Therefore the amounts of CO_2, H_2, CO and H_2O from (6.12) present in the mixture of gases will always be such that K_E will be constant for the given temperature T.   The equilibrium constant K_E is defined in terms of the partial pressures of the gases in question and given by:

$$K_E = \frac{P_{CO}\; P_{H_2O}}{P_{CO_2}\; P_{H_2}} \qquad\qquad (6.13);$$

where P_i are the partial pressures of CO, H_2O CO_2 and H_2 species. The partial pressure P_i of a species i is determined by the total pressure,

P_{tot}, of the mixture and the molar fraction of the component, ie:

$$P_i = P_{tot} \frac{n_i}{\Sigma n_i} = P_{tot} \, N_i \qquad (6.14);$$

where n_i is the number of moles of the given component and N_i is its molar fraction.   It is also assumed that mixture is made up from ideal gases.

For our case, K_E is given by:

$$K_E = \frac{P_{CO} \, P_{H_2O}}{P_{CO_2} \, P_{H_2}} = \frac{\left(\dfrac{m'_{CO}}{w_{CO}}\right) \left(\dfrac{m'_{H_2O}}{w_{H_2O}}\right)}{\left(\dfrac{m'_{CO_2}}{w_{CO_2}}\right) \left(\dfrac{m'_{H_2}}{w_{H_2}}\right)} \qquad (6.15);$$

Algebraic manipulation of (6.15) gives:

$$K_E = \frac{m'_{CO} \, m'_{H_2O}}{m'_{CO_2} \, m'_{H_2}} \, A \qquad (6.16);$$

where A is a constant given in terms of the molecular weights:

$$A = \frac{w_{CO_2} \, w_{H_2}}{w_{CO} \, w_{H_2O}} \qquad (6.17).$$

The equilibrium constant K_E is also given as (Engleman (1976)):

$$K_E = 10^{\log A} \, T^B \, \exp(-C/RT) \qquad (6.18);$$

where:

$$\log A \quad = -4.621;$$

B   = 0.87;

C   = -9.839.

Equation (6.18) gives the value of K_E for a given temperature T.

So, for Equations (6.9(a)) and (b), to satisfy the water-gas equilibrium, a system of equations have to be solved, readjusting the species, according to the water-gas equilibrium.

Originally in the system, after reactions 6.9(a) and (b) have taken place, there are: m_{CO}, m_{CH_4}, m_{CO_2}, m_{H_2O} and m_{H_2} amounts of species. Assuming next that a readjustment has taken place to satisfy the water-gas equilibrium, the amount of species present will be: m'_{CO}, m'_{CH_4}, m'_{CO_2}, m'_{H_2O} and m'_{H_2}.

A balance of the elements gives:

(1)   For carbon:

$$\frac{12}{w_{CO}} m_{CO} + \frac{12}{w_{CO_2}} m_{CO_2} = \frac{12}{w_{CO}} m'_{CO} + \frac{12}{w_{CO_2}} m'_{CO_2} \qquad (6.19);$$

(2)   For oxygen:

$$\frac{16}{w_{CO}} m_{CO} + \frac{32}{w_{CO_2}} m_{CO_2} + \frac{16}{w_{H_2O}} m_{H_2O} = \frac{16}{w_{CO}} m'_{CO} + \frac{32}{w_{CO_2}} m'_{CO_2} + \frac{16}{w_{H_2O}} m'_{H_2O}$$

$$(6.20).$$

(3)   For hydrogen:

$$m_{H_2} + \frac{2}{w_{H_2O}} m_{H_2O} = m'_{H_2} + \frac{2}{w_{H_2O}} m'_{H_2O} \qquad (6.21).$$

Algebraic manipulation of Equations (6.19) to (6.21) gives m'_{CO}, m'_{H_2}, and m'_{H_2O} in terms of the known quantities m_{CO}, m_{CO_2}, m_{H_2} and m_{H_2O} (Equation 6.22) and the unknown (as yet) m'_{CO_2}.

$$m'_{CO} = m_{CO} + \frac{w_{CO}}{w_{CO_2}} \, m_{CO_2} - \frac{w_{CO}}{w_{CO_2}} \, m'_{CO_2} \qquad (a);$$

$$m'_{H_2} = \frac{2}{w_{CO_2}} \, m'_{CO_2} - \frac{2}{w_{CO_2}} \, m_{CO_2} + m_{H_2} \qquad (b); \qquad (6.22).$$

$$m'_{H_2O} = m_{H_2O} - \frac{w_{H_2O}}{w_{CO_2}} \, m'_{CO_2} + \frac{w_{H_2O}}{w_{CO_2}} \, m_{CO_2} \qquad (c);$$

The only unknown in Equations (6.22) is m'_{CO_2} and this is obtained by equating Equations (6.16) and (6.18) and by eliminating with back substitution the species m'_{H_2}, m'_{H_2O} and m'_{CO} by employing Equations (6.19) to (6.21).

The result of this algebraic manipulation is a quadratic equation in m'_{CO_2} given by:

$$\alpha \, m'^2_{CO_2} + \beta m'_{CO_2} + \gamma = 0 \qquad (6.23);$$

where:

$$\alpha = 2C_1 - \frac{w_{CO} \, w_{H_2O}}{w_{CO_2}} \qquad (6.24);$$

$$\beta = m_{CO_2} \left[2w_{CO} \frac{w_{H_2O}}{w_{CO_2}} - 2C_1 \right] + w_{H_2O} \, m_{CO} + w_{CO} \, m_{H_2O} + C_1 \, w_{CO_2} \, m_{H_2}$$

$$(6.25);$$

$$\gamma = - [m_{CO} + \frac{w_{CO}}{w_{CO_2}} m_{CO_2}] \, [w_{CO_2} \, m_{H_2O} + w_{H_2O} \, m_{CO_2}] \qquad (6.26);$$

and $C_1 = K_E$ given by Equation (6.18).

The quadratic Equation (6.23) will give two roots (values) for m'_{CO_2}, for which they should be real, ie. need $\beta^2 - 4\alpha\gamma \geqslant 0$.

When the above model was implemented it was found that Equation (6.23) always has real roots and one root is always between zero and one (as it should be) and the other one outside this range, usually negative.

The rest of the species m'_{CO}, m'_{H_2O} and m'_{H_2} can now be calculated from Equations (6.22).

This model was introduced in the calculations for a typical test case with 5% throat injection of CH_4. The initial average gas composition is 35.2% CO_2, 10.05% CO, 54.75% H_2O and the inlet temperature is $1575^{\circ}C$. Results were obtained with and without water-gas equilibrium with the same initial conditions for both cases, and are given in Tables 6.28 and 6.29 for the inlet average and average exit conditions, respectively.

	T(°C)	CO_2	CO	H_2	H_2O	CH_4
Without water-gas reaction	1575°	35.20	10.05	0.0	54.75	0.0
With water-gas reaction	1575°	43.44	1.829	8.191	46.54	0.0

TABLE 6.28: INLET CONDITIONS

	T(°C)	CO_2	CO	H_2	H_2O	CH_4
Without water-gas reaction	974.4	26.96	16.06	17.29	39.69	0.0
With water-gas reaction	943.5	30.87	12.12	21.25	35.76	0.0

TABLE 6.29: EXIT CONDITIONS

At the inlet, although both cases started with the same initial composition, the water-gas reaction forced the species to be readjusted so as to satisfy the water-gas equilibrium. At the exit the temperatures differ by approximately 30°C and because of the water-gas equilibrium readjustment, final species composition, CO, H_2O, CO_2 and H_2 is slightly different. Methane on the other hand is predicted in both cases to have the same value (ie totally consumed). Overall, the water-gas equilibrium case needed less iterations for convergence but increased the

CPU time. Because the water-gas model readjusts the initial composition of the species, and thus makes them different for the values prescribed by the collaborating institution, it was decided that the previous model was more appropriate for the present calculations. In any case, the exit results are not significantly different from the non-water-gas original results (Table 6.29).
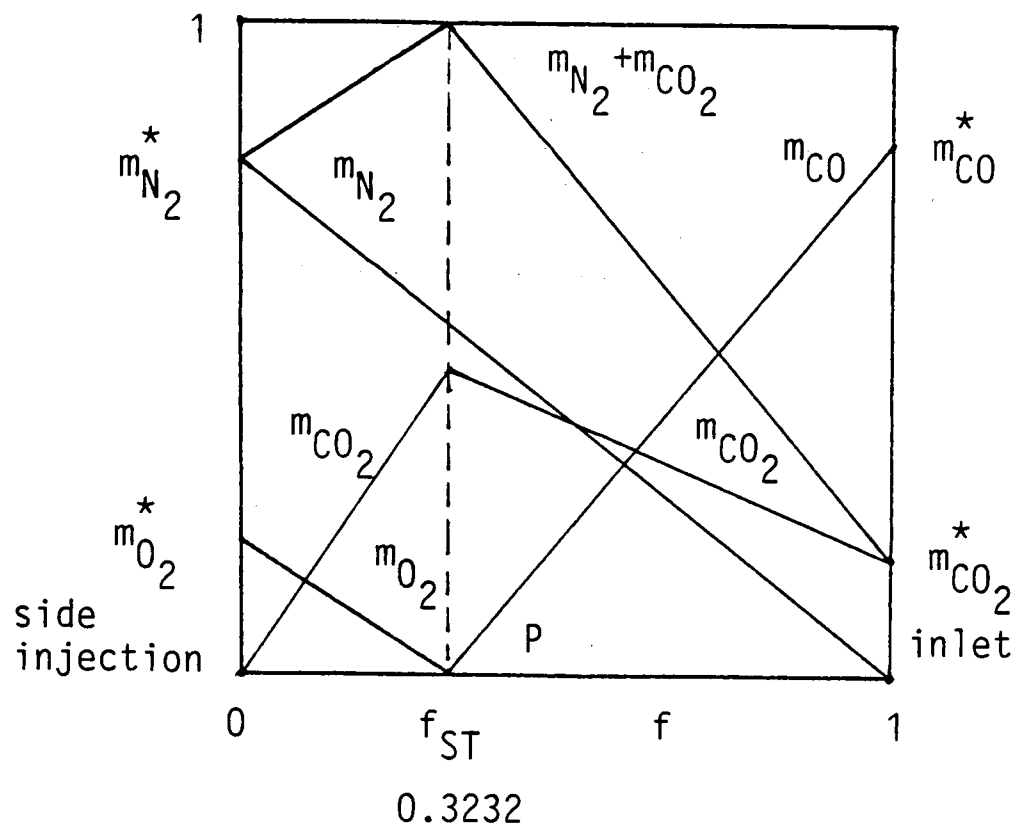
FIGURE 6.1: STOICHIOMETRIC DIAGRAM
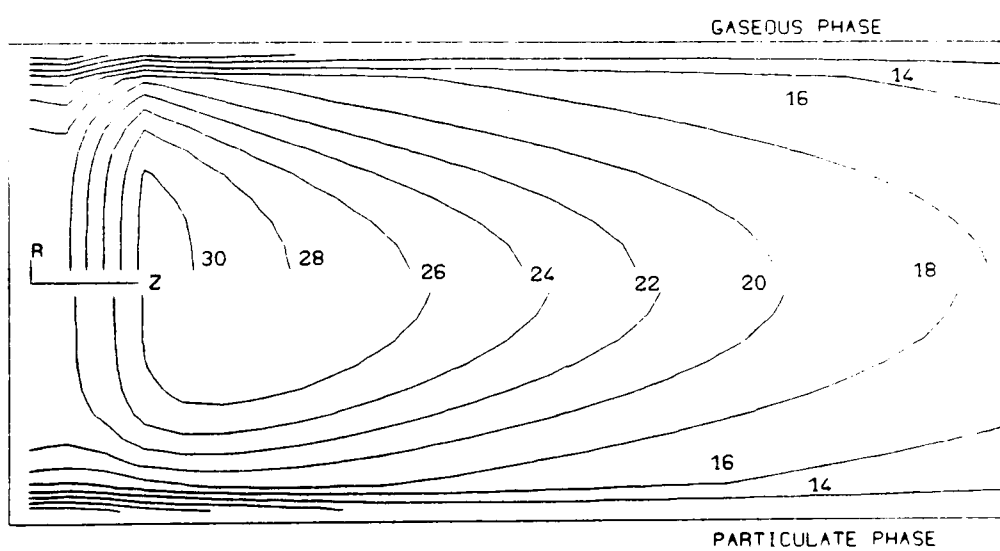
FIGURE 6.2: AXIAL VELOCITY COMPONENTS
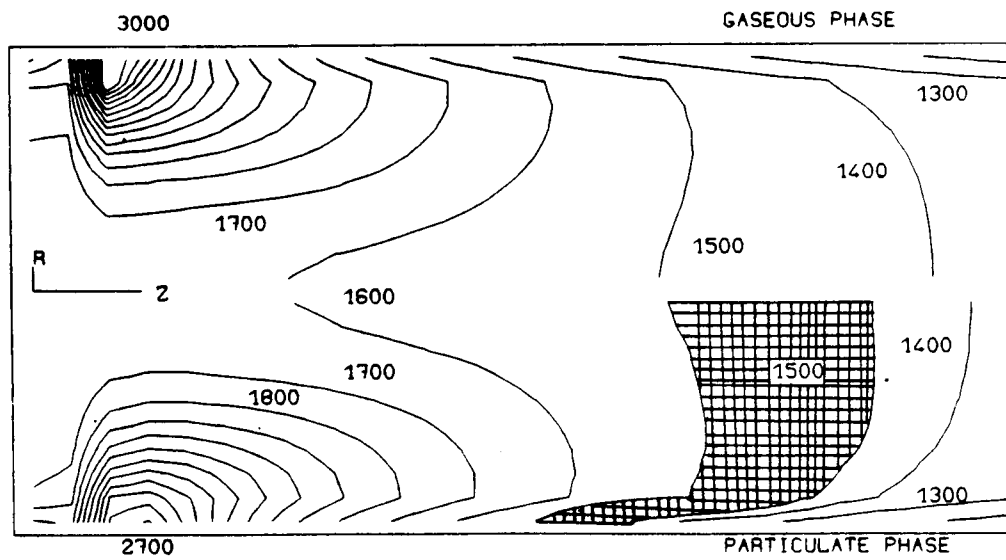
FIGURE 6.3:   TEMPERATURE CONTOURS (C)
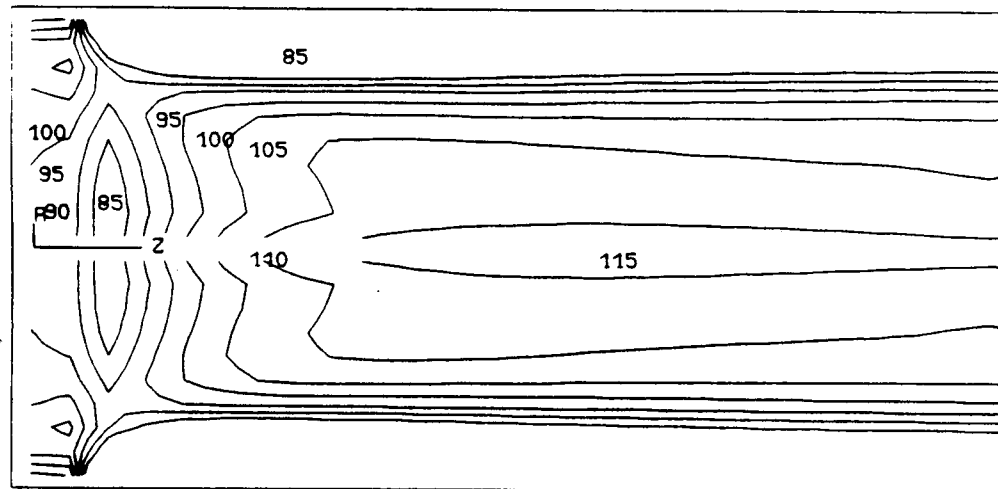
FIGURE 6.4:   PARTICLE MASS FRACTIONS
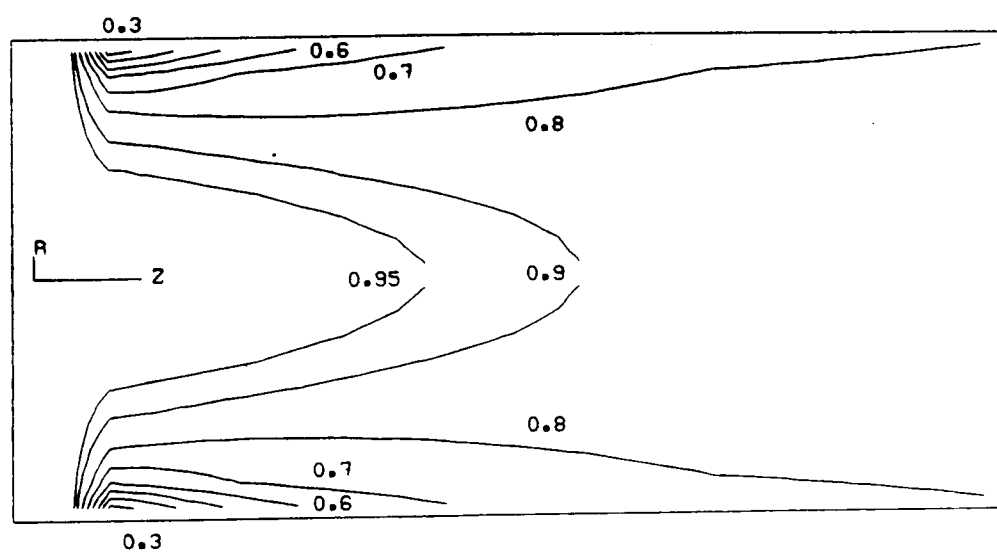
FIGURE 6.5:   MIXTURE FRACTION f

GASEOUS PHASE

26 24

22 20 18

24

16 14

14 16

PARTICULATE PHASE
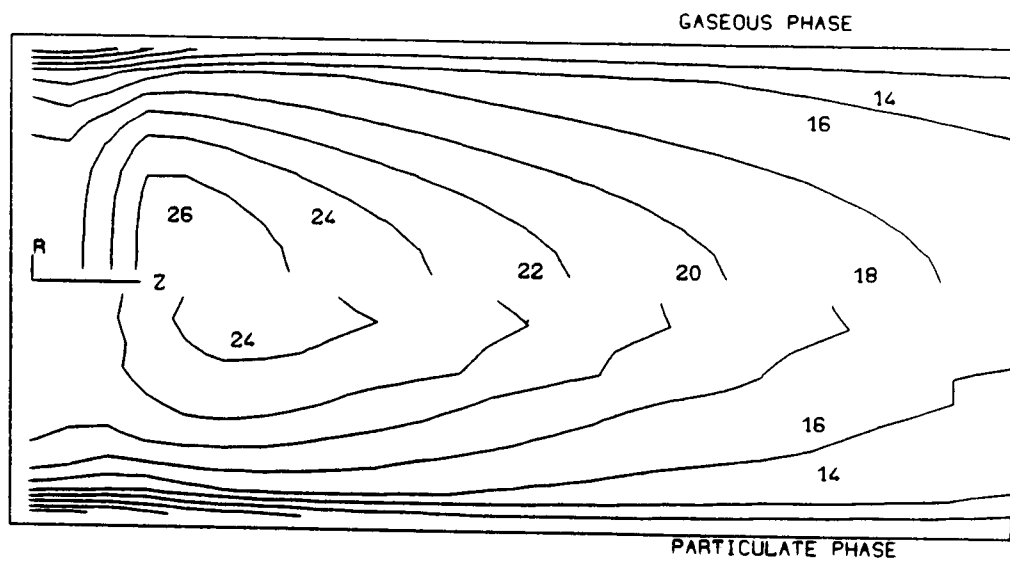
FIGURE 6.6: AXIAL VELOCITIES

2100   GASEOUS PHASE

1900   1300
1800
1700

1600
R   1500   1400
Z

1600   1500

1700

1800
1900

PARTICULATE PHASE
2000
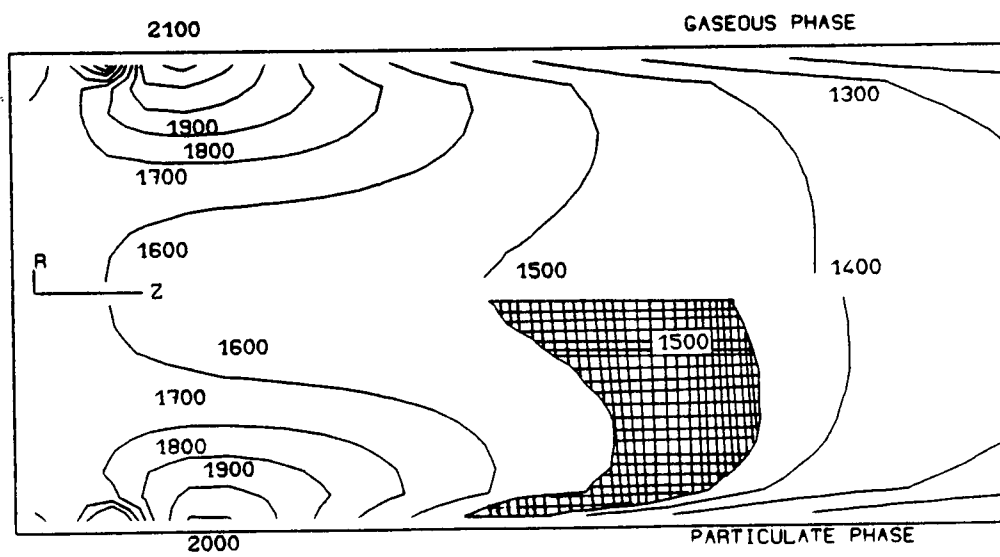
FIGURE 6.7: TEMPERATURE CONTOURS (C)

20
100   50
90
95
95   100
R
Z   105   110
95
90 95
100
100   90
50
20
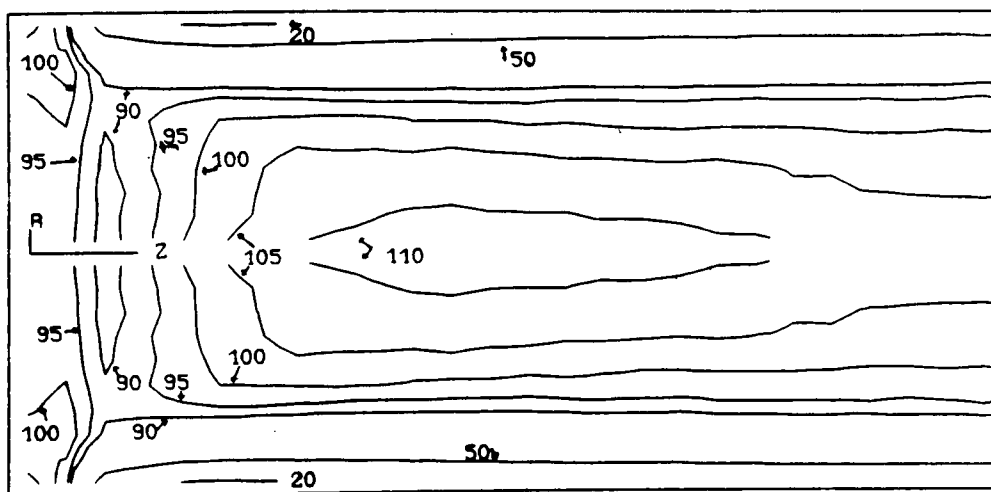
FIGURE 6.8: PARTICLE MASS FRACTIONS
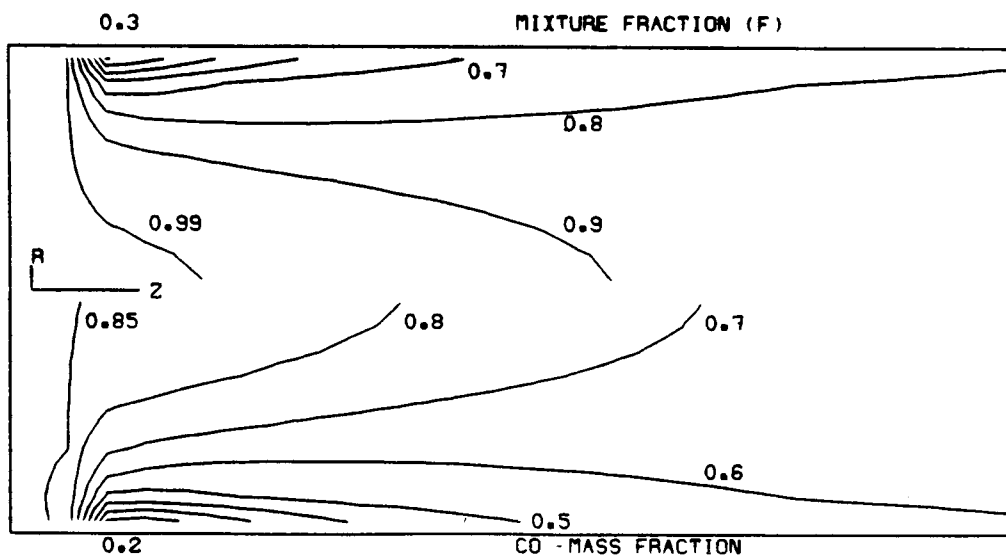
FIGURE 6.9:   MIXTURE FRACTION f AND CO MASS-FRACTIONS
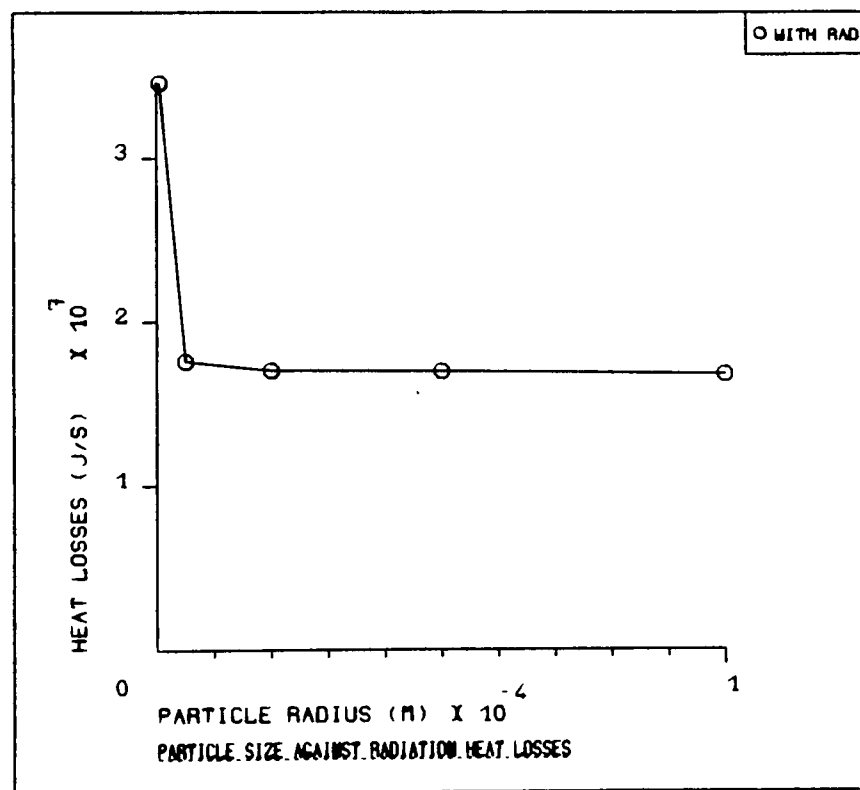
FIGURE 6.10: PARTICLE SIZE INFLUENCE ON HEAT LOSSES

PARTICULATE PHASE

GASEOUS PHASE
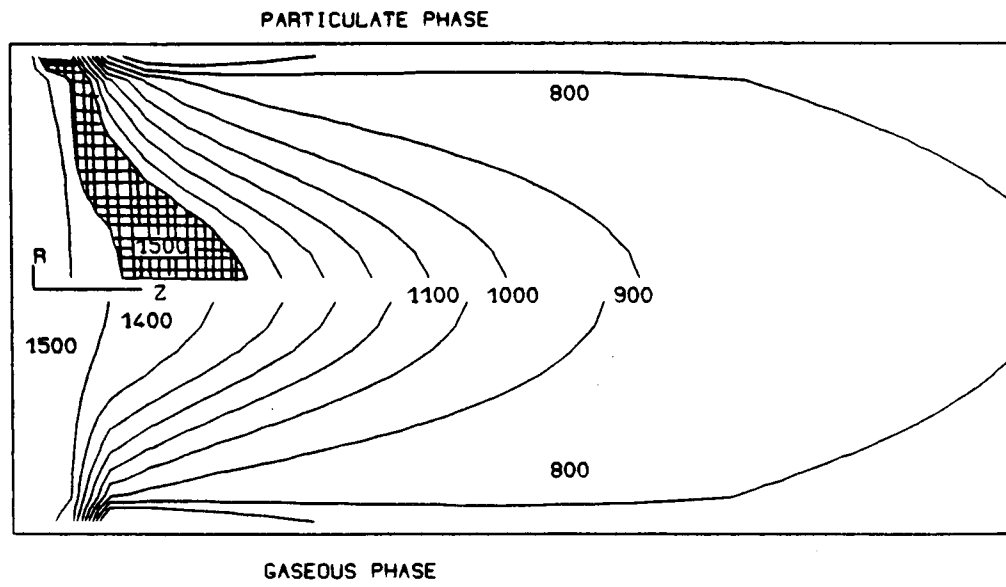
FIGURE 6.11: TEMPERATURE CONTOURS (C)

GASEOUS PHASE

PARTICULATE PHASE
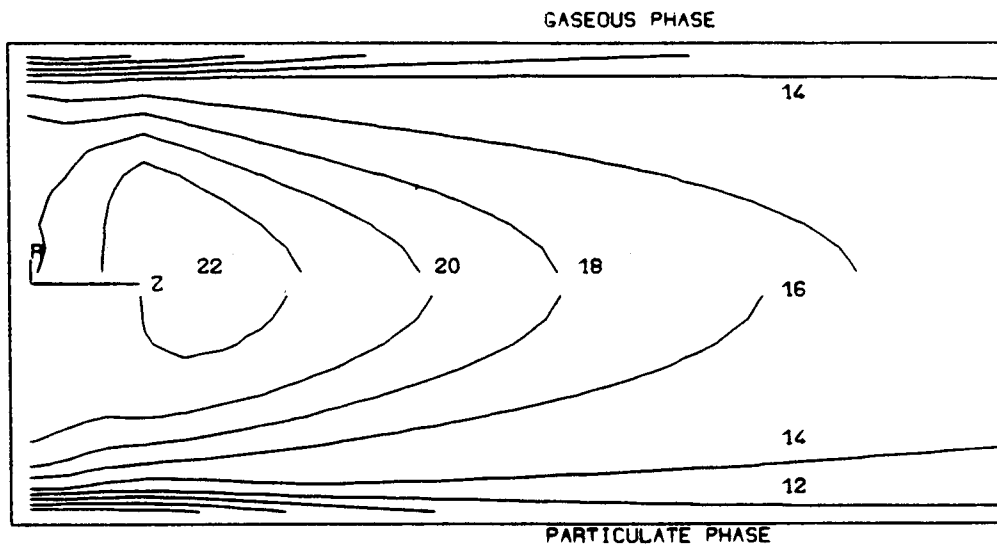
FIGURE 6.12: AXIAL VELOCITIES

CH4 -MASS FRACTION
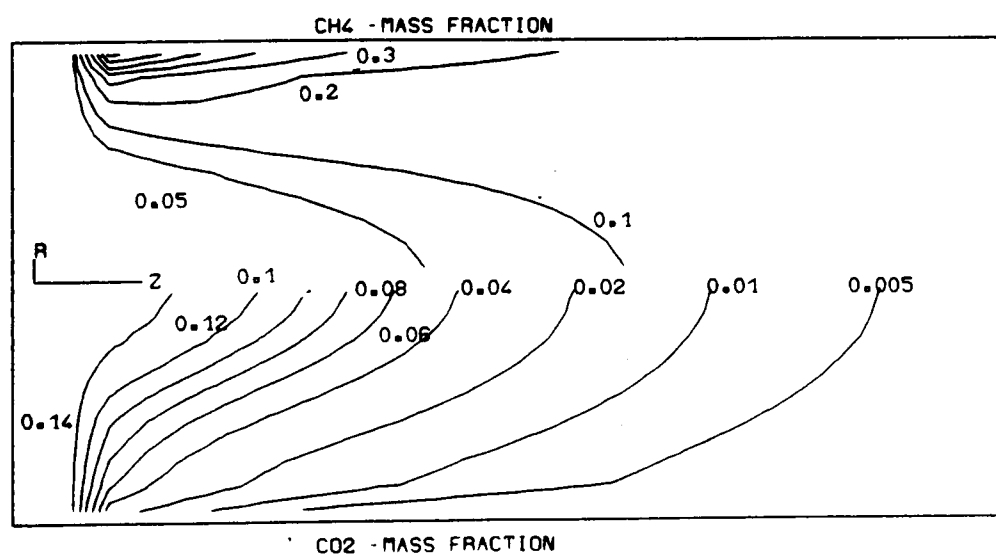
CO2 -MASS FRACTION

FIGURE 6.13: CH$_4$ AND CO$_2$ MASS FRACTIONS

CO - MASS FRACTION

0.3

0.8   0.82
             0.84
          0.86
       0.88
    0.89
0.22 0.23 0.24 0.25   0.26
0.20 0.21

0.30   DENSITY CONTOURS, KGR/M**3
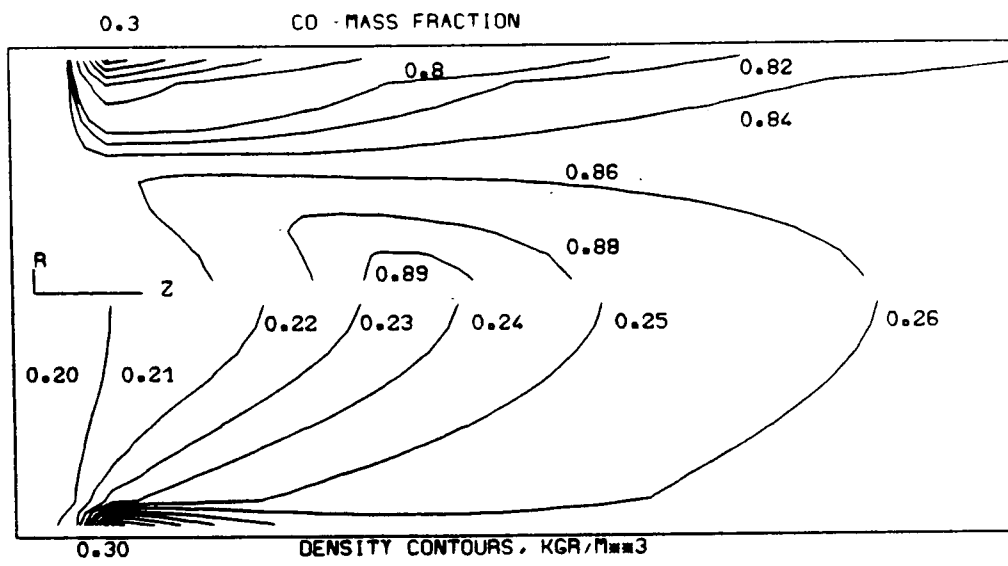
FIGURE 6.14: CO MASS FRACTIONS AND DENSITY CONTOURS

GASEOUS PHASE

900
          800
1550
  1500
R 1500 1400 1100 1000 900
   Z 1500
          800

PARTICULATE PHASE
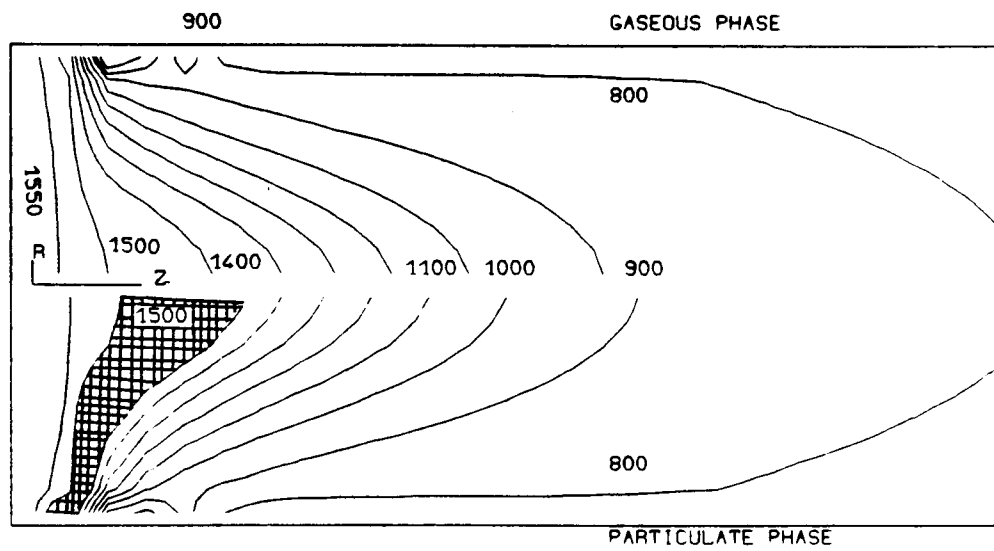
FIGURE 6.15: TEMPERATURE CONTOURS (C)

MCH4 - MASS FRACTION

0.7
          0.3
          0.2
             0.1
   0.01
R
  Z 0.1 0.08 0.06
  0.12
0.14
        0.04 0.02
                  0.01

0.15   0.001
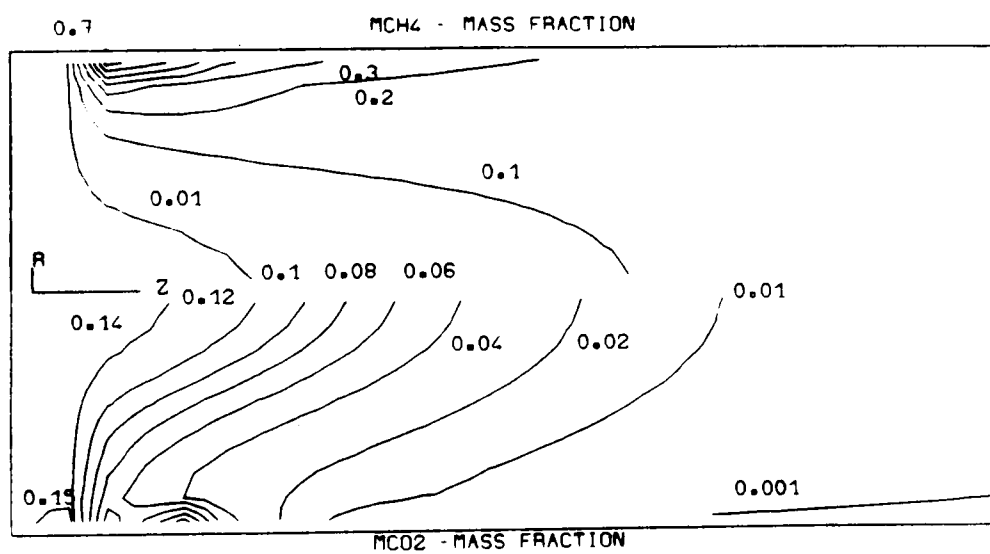
MCO2 - MASS FRACTION

FIGURE 6.16: CH$_4$ AND CO$_2$ MASS FRACTIONS
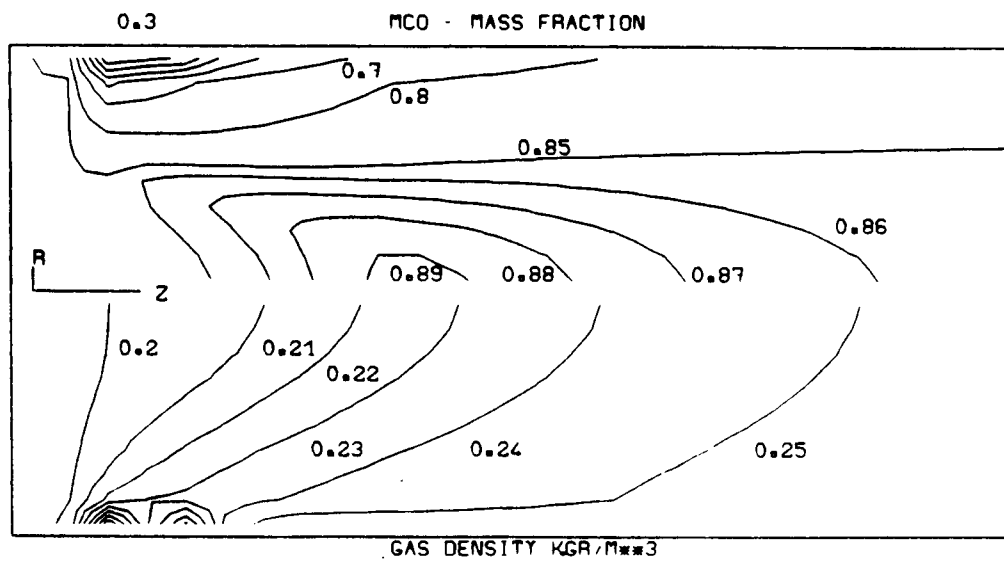
FIGURE 6.17: CO MASS FRACTIONS AND DENSITY CONTOURS
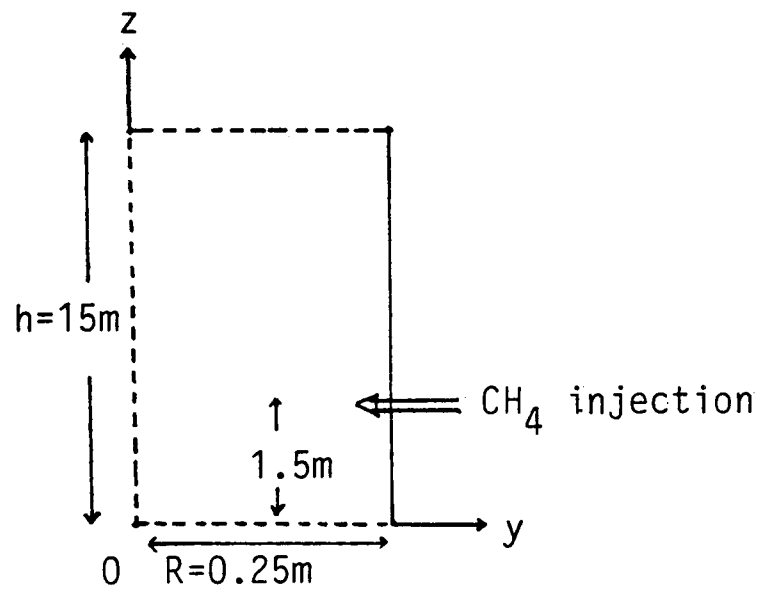
FIGURE 6.18: NEW GEOMETRY
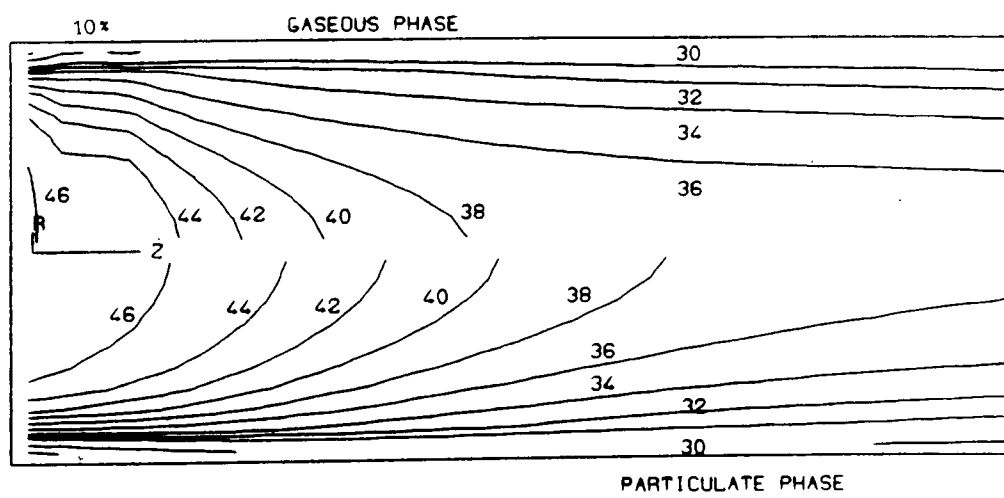
FIGURE 6.19: AXIAL VELOCITIES
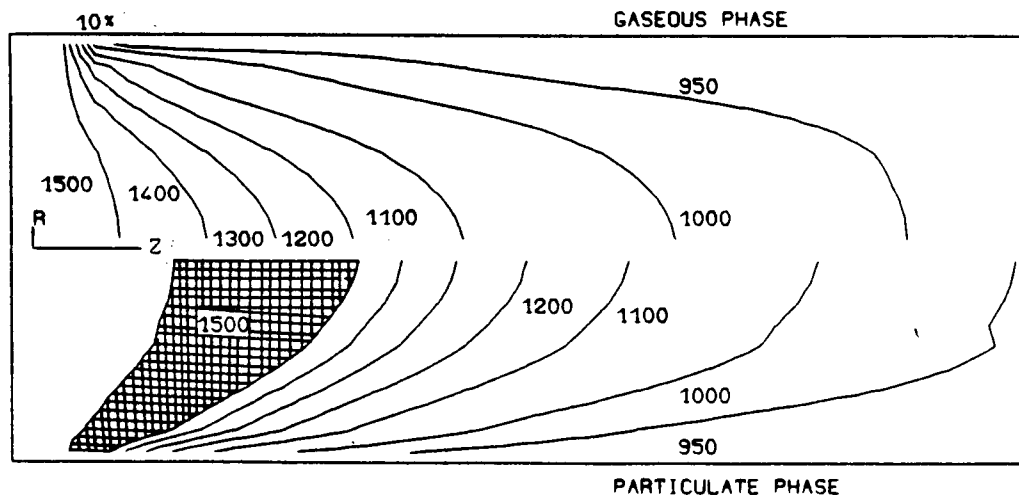
FIGURE 6.20: TEMPERATURE CONTOURS (C)
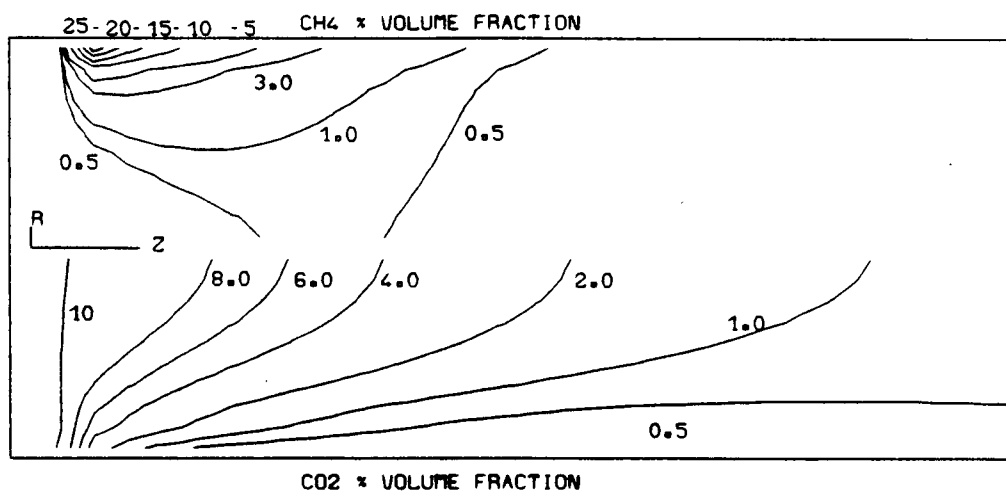
FIGURE 6.21: CH₄ AND CO₂ VOLUME FRACTIONS
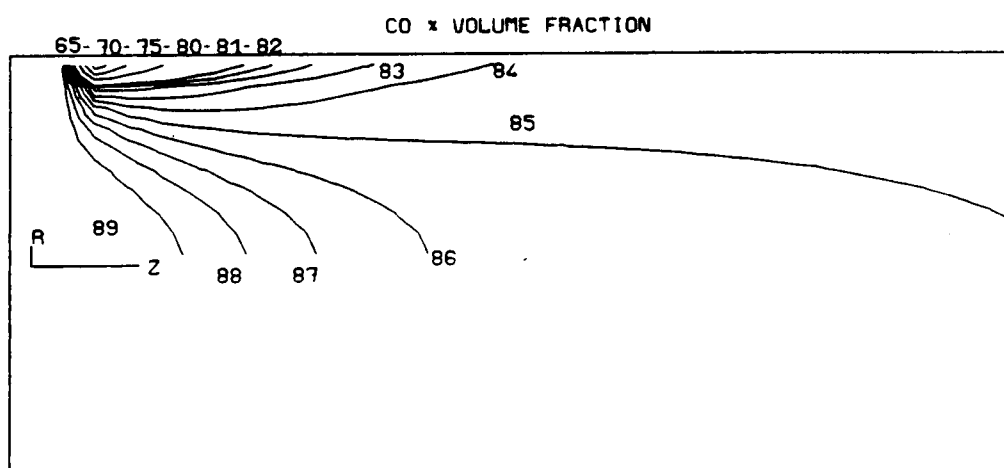
FIGURE 6.22: CO VOLUME FRACTIONS

-231-
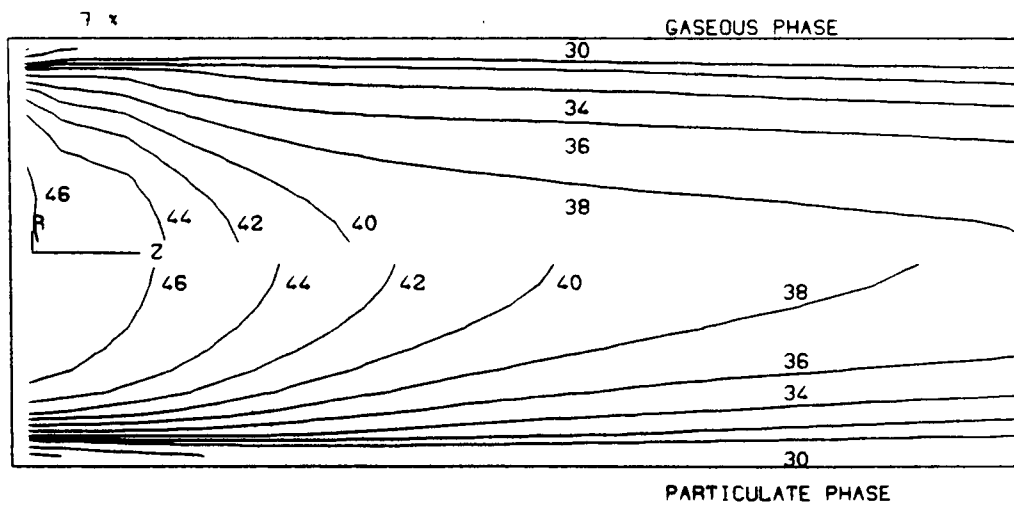
FIGURE 6.23: AXIAL VELOCITIES
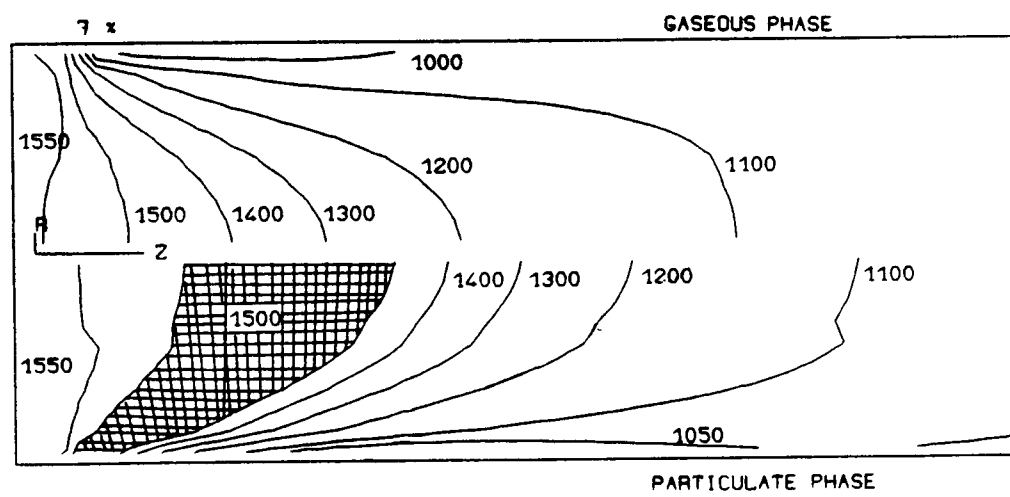
FIGURE 6.24: TEMPERATURE CONTOURS (C)
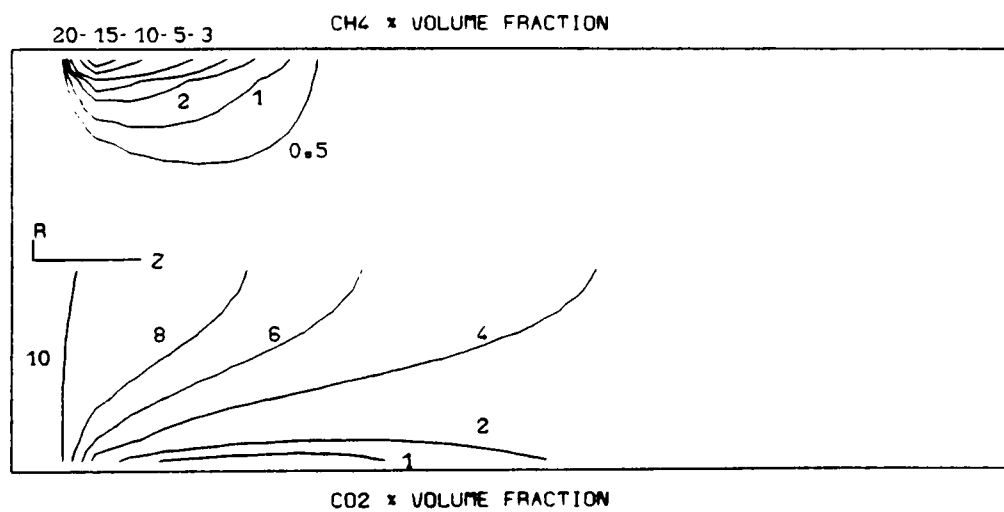
FIGURE 6.25: CH_4 AND CO_2 VOLUME FRACTIONS
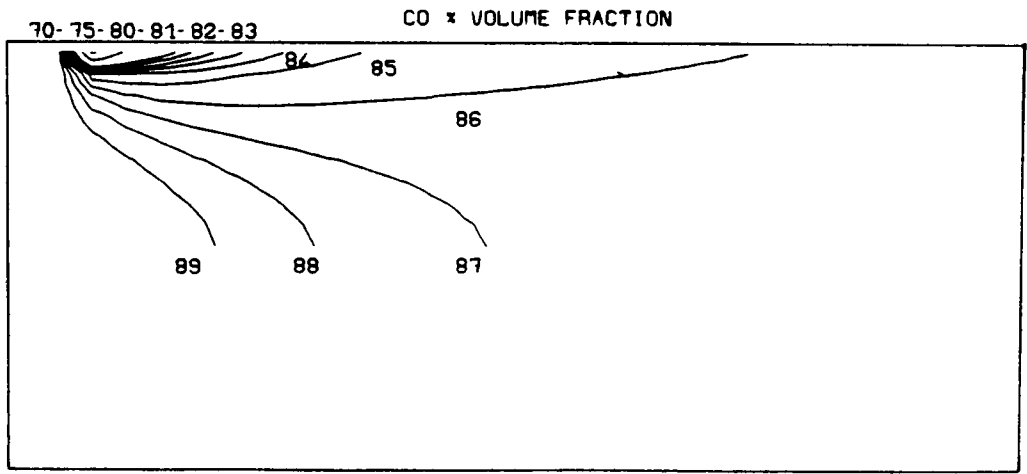
FIGURE 6.26: CO VOLUME FRACTIONS
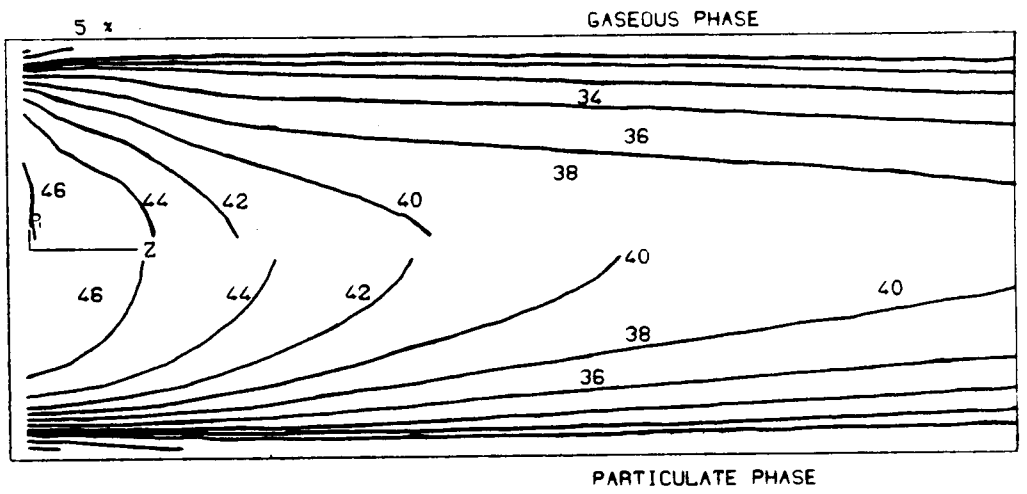
FIGURE 6.27: AXIAL VELOCITIES
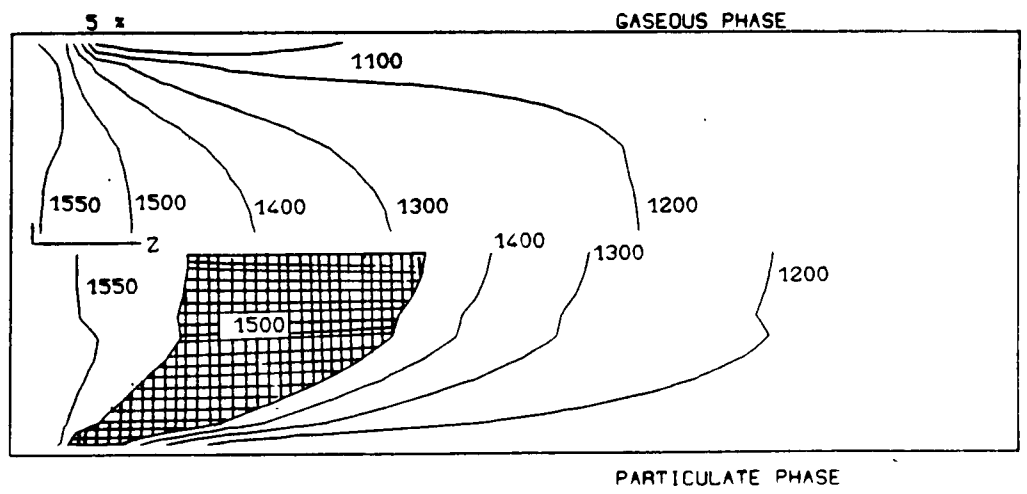
FIGURE 6.28: TEMPERATURE CONTOURS (C)
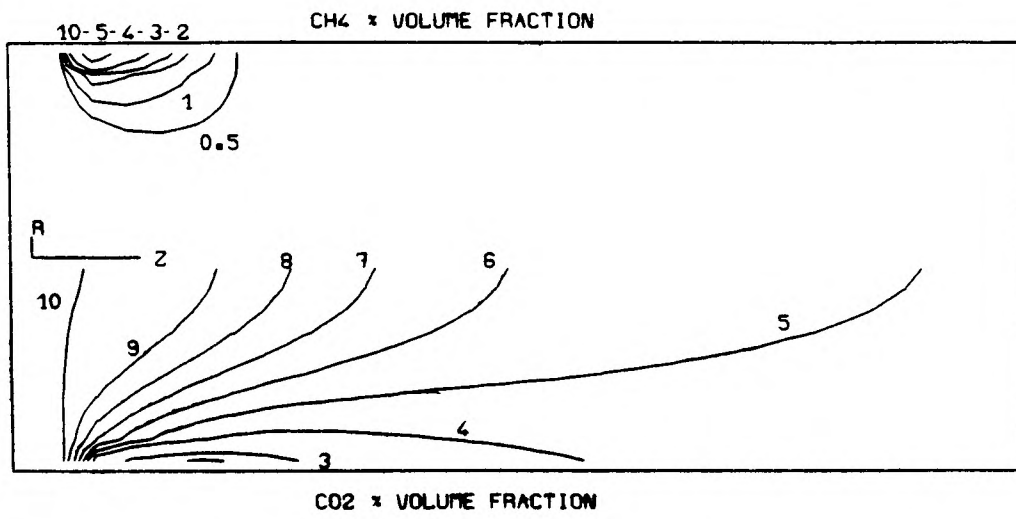
FIGURE 6.29: CH₄ AND CO₂ VOLUME FRACTIONS
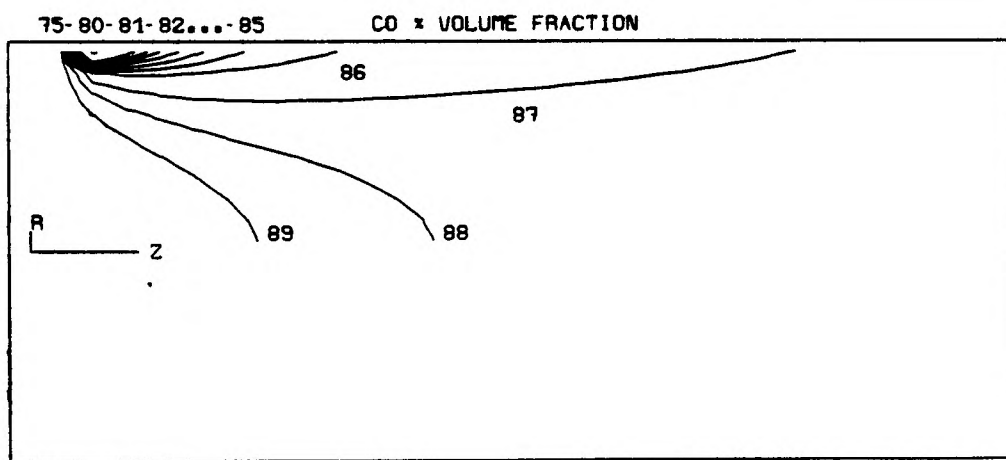
FIGURE 6.30: CO VOLUME FRACTIONS
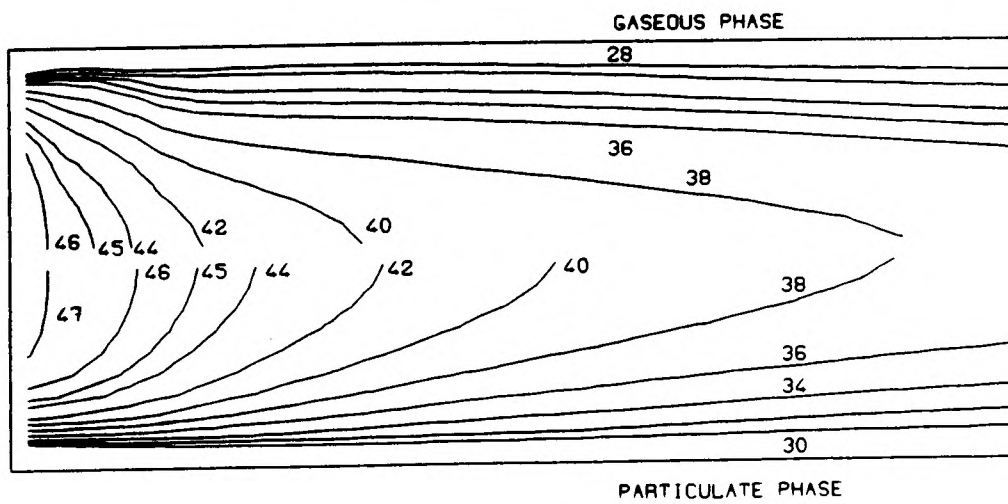
FIGURE 6.31: AXIAL VELOCITIES

GASEOUS PHASE
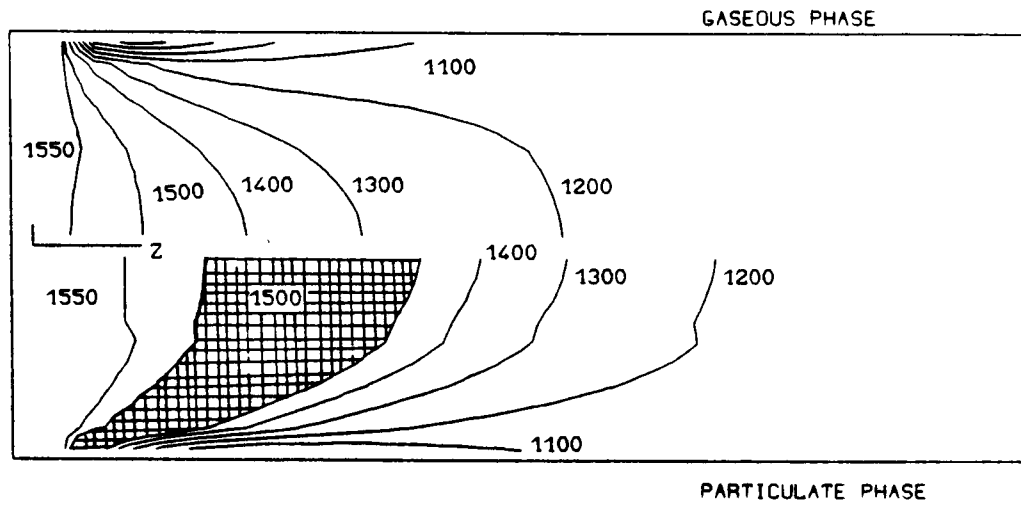
FIGURE 6.32: TEMPERATURE CONTOURS (C)

PARTICULATE PHASE

CH4 % VOLUME FRACTION

CO2 % VOLUME FRACTION
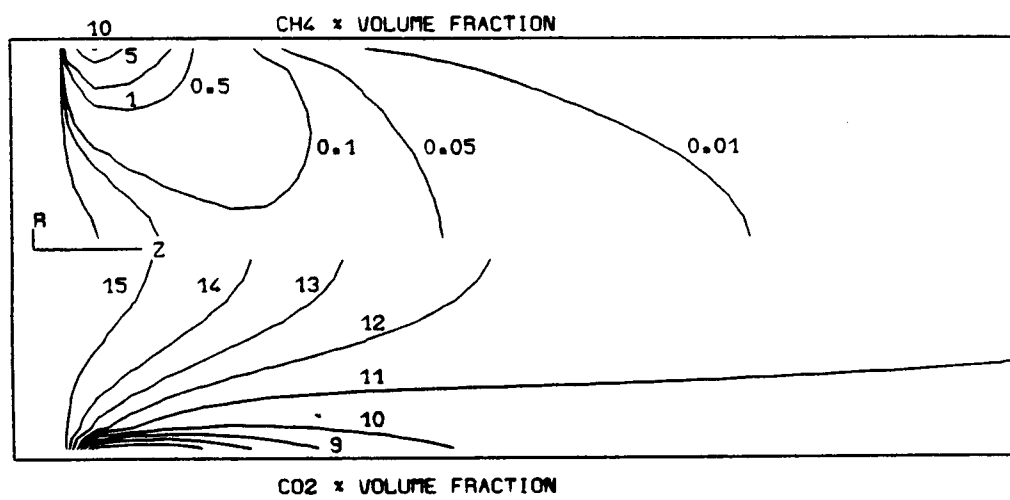
FIGURE 6.33: CH₄ AND CO₂ VOLUME FRACTIONS

H2O % VOLUME FRACTION
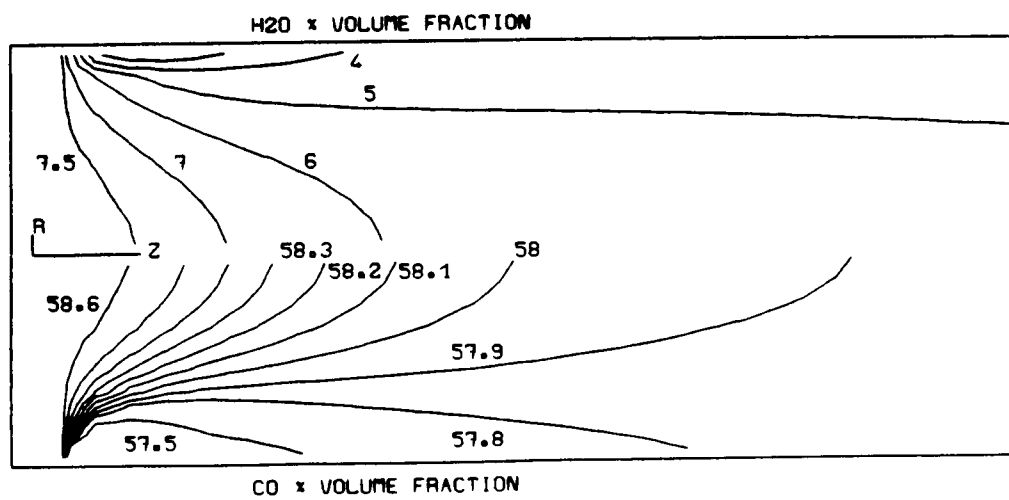
CO % VOLUME FRACTION

FIGURE 6.34: H₂O AND CO VOLUME FRACTIONS

-235-
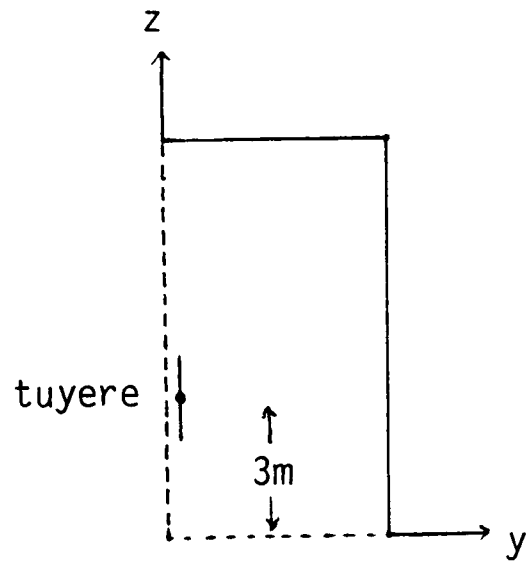
FIGURE 6.35: TUYERE POSITION

GASEOUS PHASE

PARTICULATE PHASE
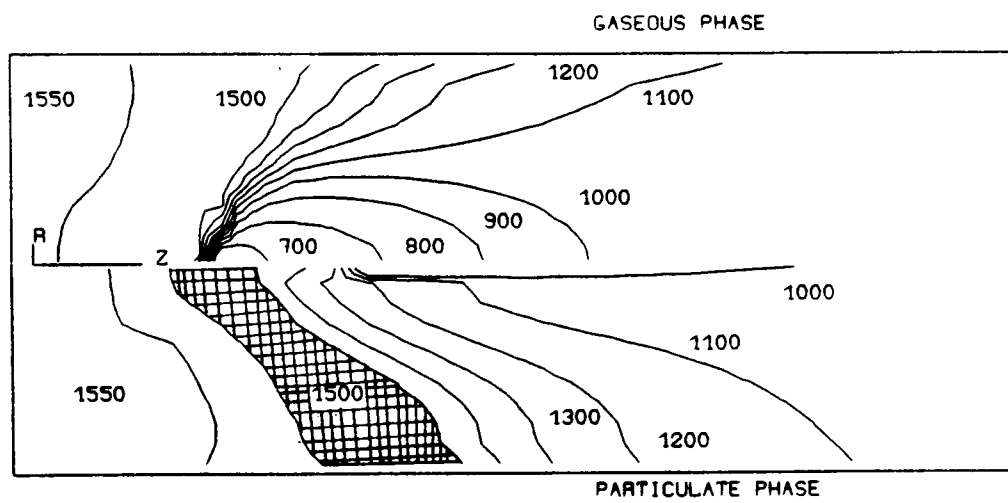
FIGURE 6.36: TEMPERATURE CONTOURS (C)

GASEOUS PHASE

PARTICULATE PHASE
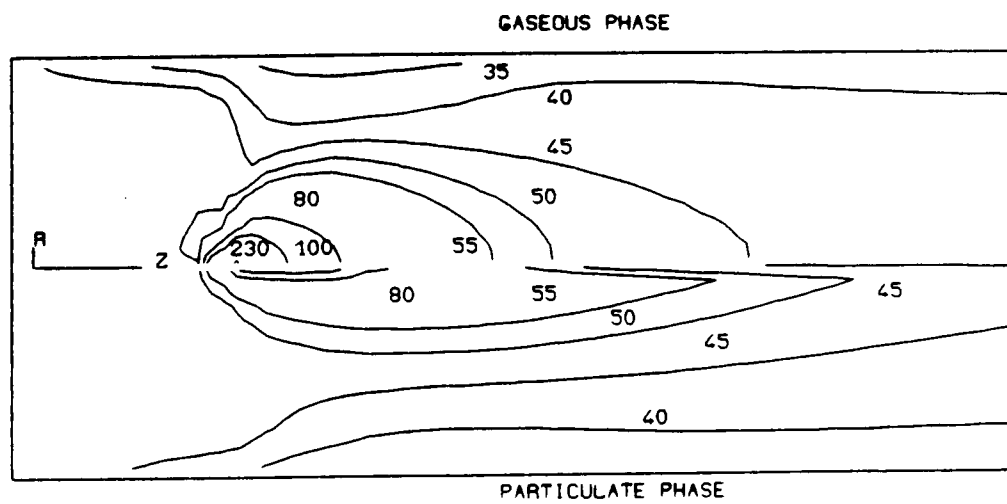
FIGURE 6.37: AXIAL VELOCITIES

-236-
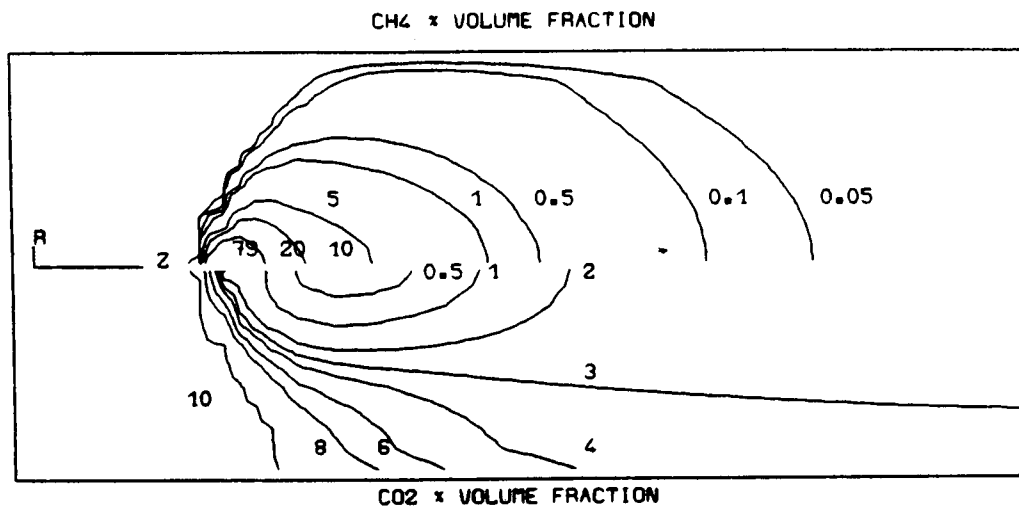
FIGURE 6.38: CH₄ AND CO₂ VOLUME FRACTIONS
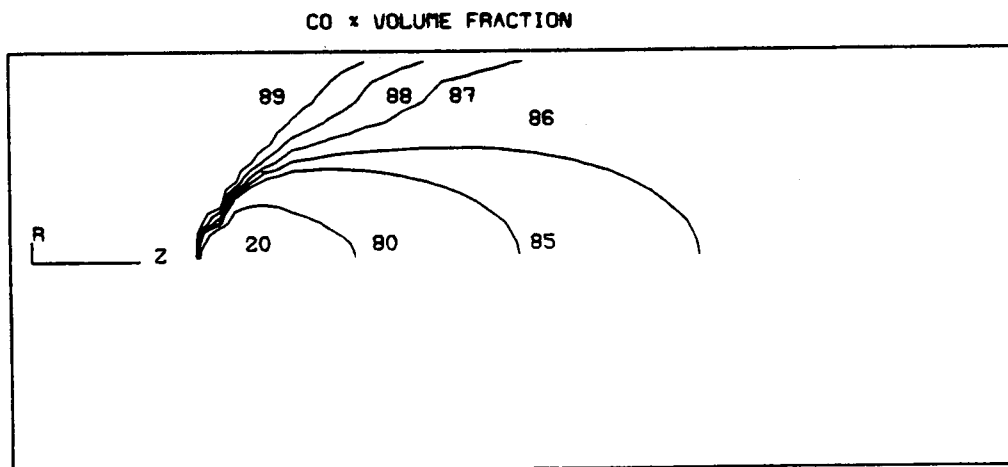
FIGURE 6.39: CO VOLUME FRACTIONS
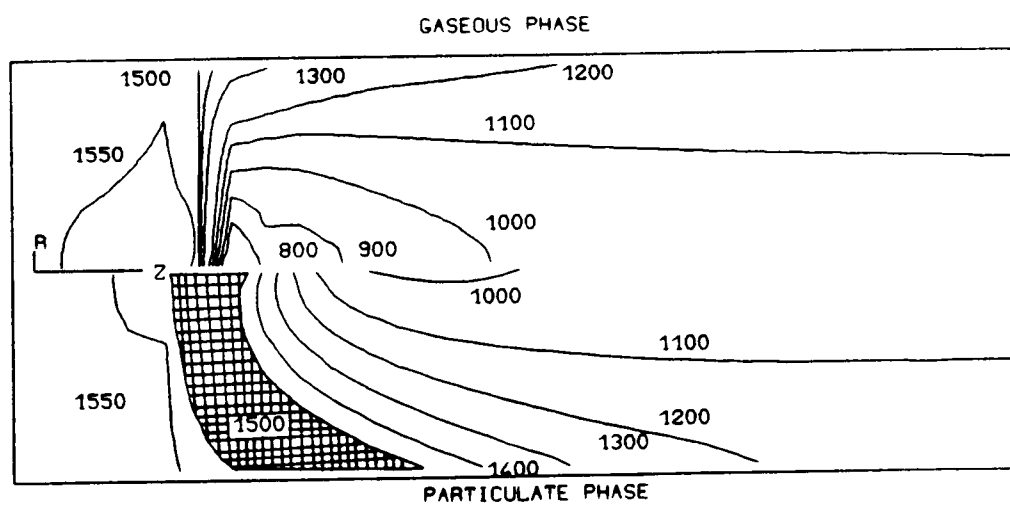
FIGURE 6.40: TEMPERATURE CONTOURS (C)

GASEOUS PHASE

PARTICULATE PHASE
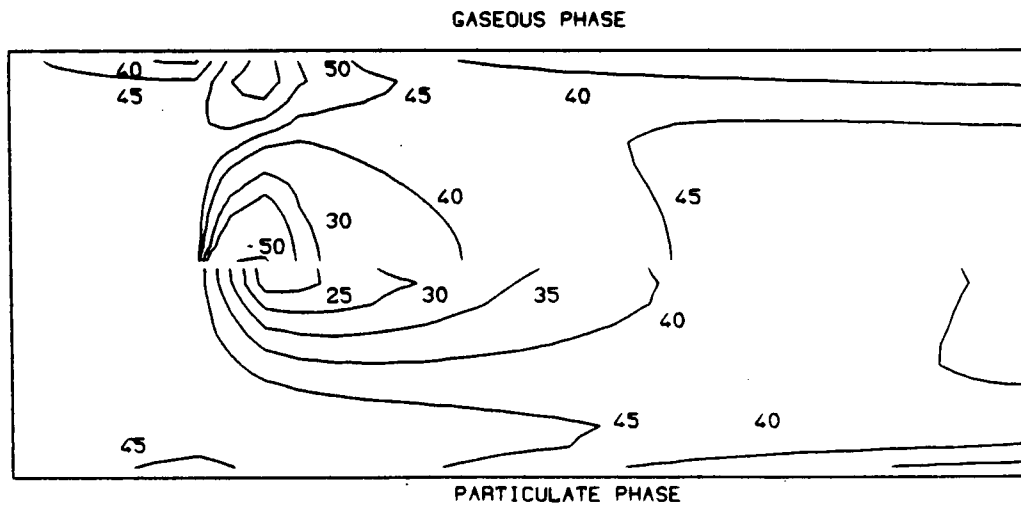
FIGURE 6.41: AXIAL VELOCITIES

CH4 % VOLUME FRACTION

CO2 % VOLUME FRACTION
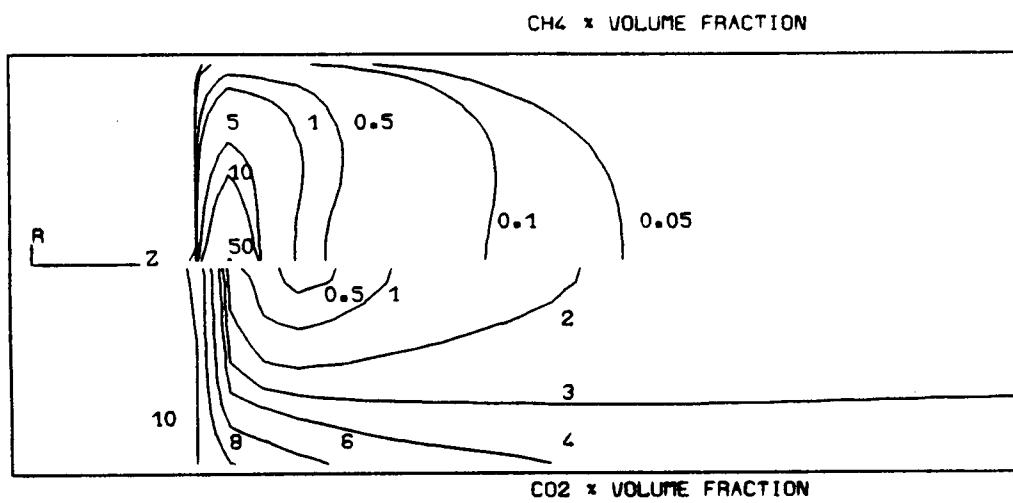
FIGURE 6.42: CH$_4$ AND CO$_2$ VOLUME FRACTIONS
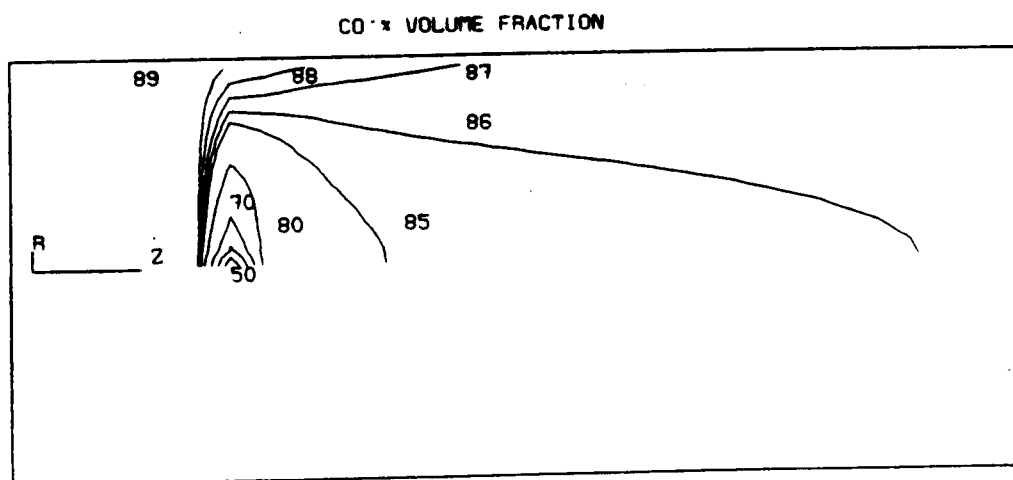
CO % VOLUME FRACTION

FIGURE 6.43: CO VOLUME FRACTIONS
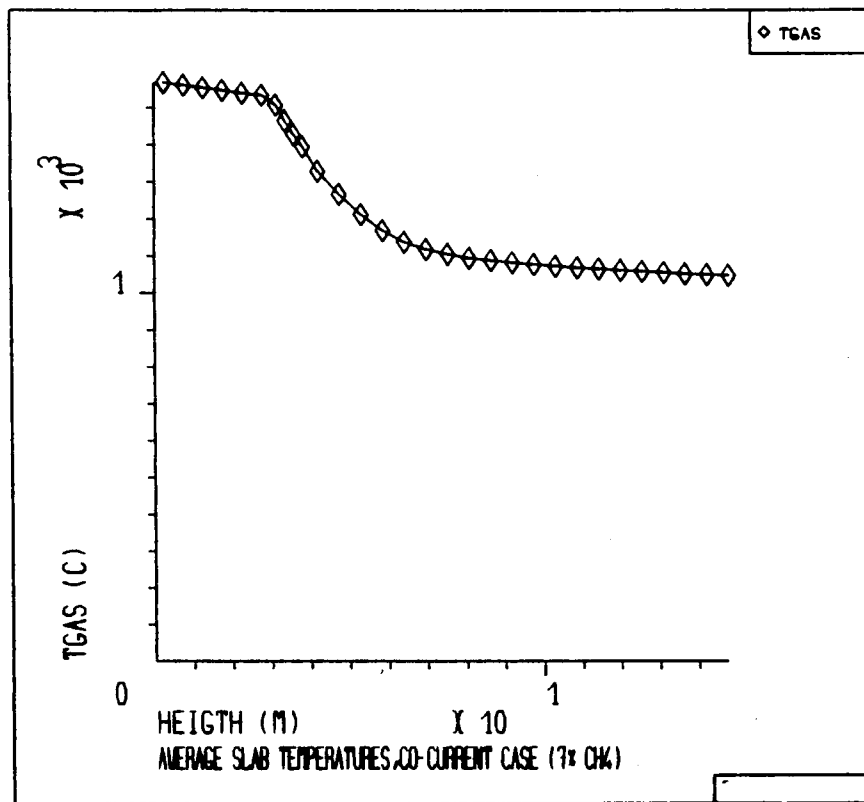
FIGURE 6.44: CO-CURRENT AVERAGE SLAB TEMPERATURES
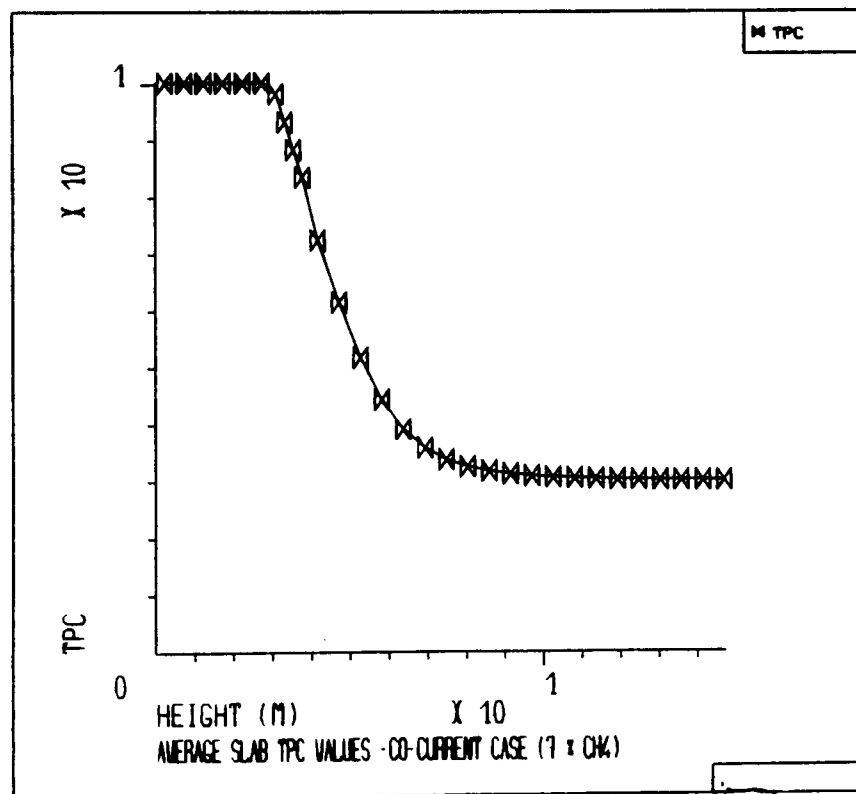
FIGURE 6.45: CO-CURRENT AVERAGE SLAB TPC
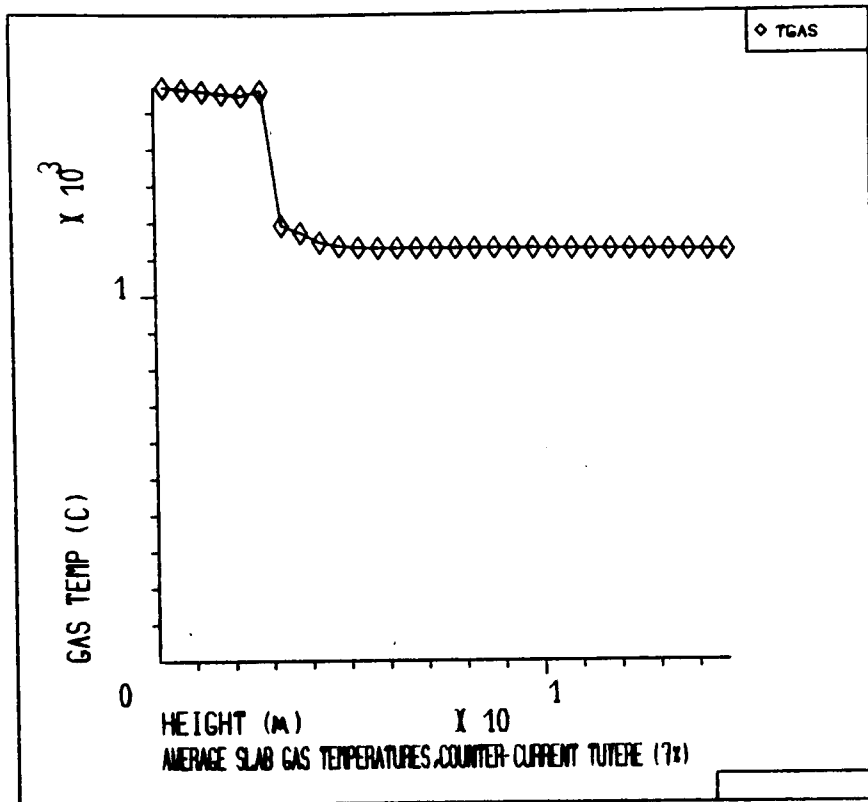
FIGURE 6.46: COUNTER-CURRENT AVERAGE SLAB TEMPERATURES
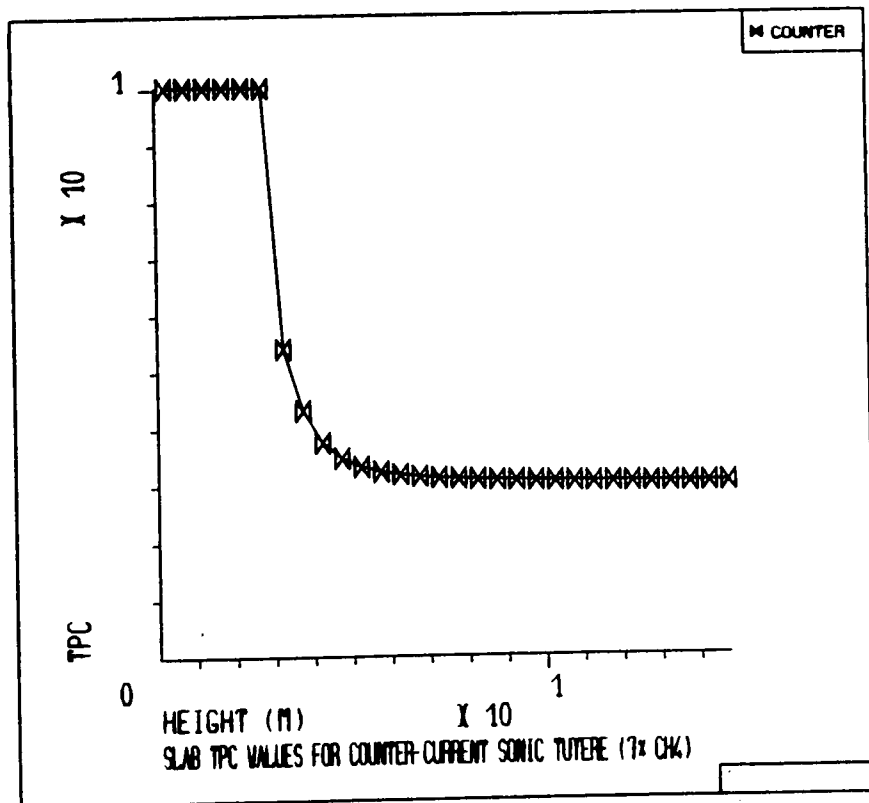
FIGURE 6.47: COUNTER-CURRENT AVERAGE SLAB TPC
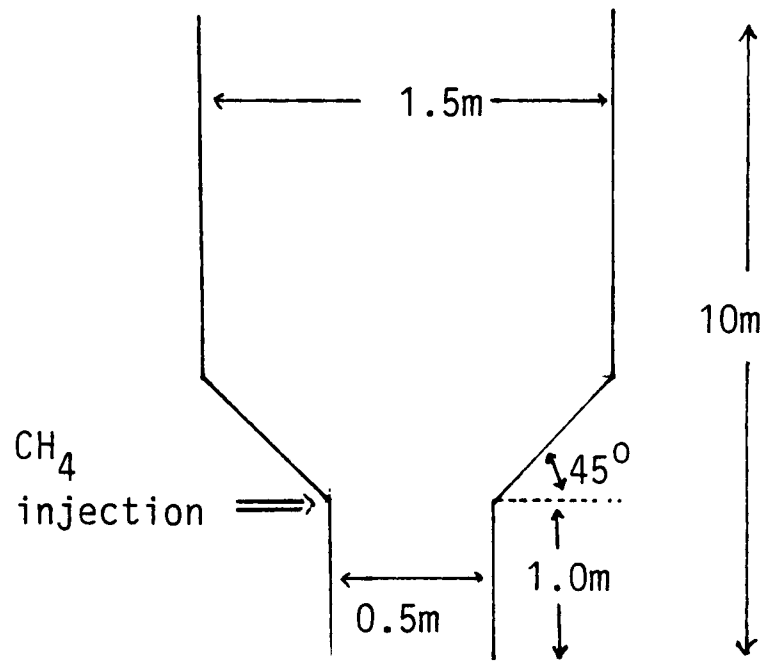
FIGURE 6.48: RESTRICTED INLET GEOMETRY
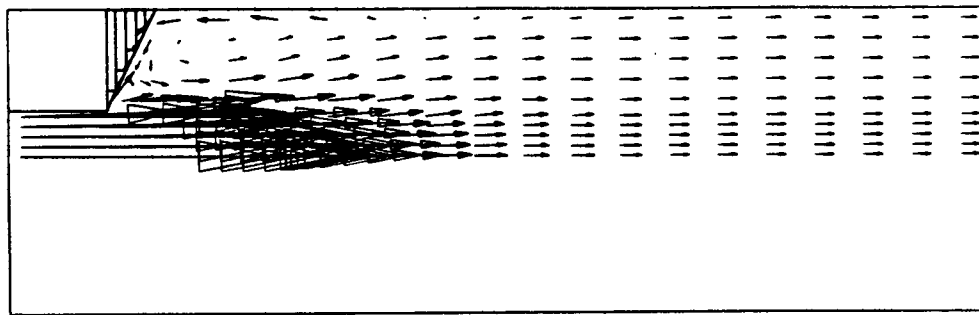
FIGURE 6.49: VELOCITY VECTORS
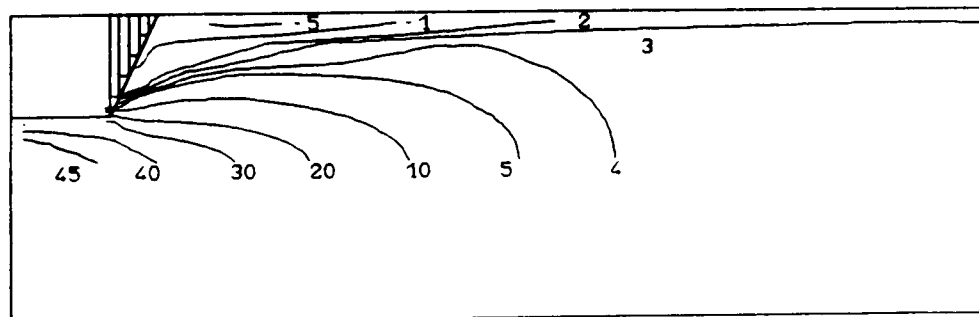
FIGURE 6.50: AXIAL VELOCITIES (5% CH_4)
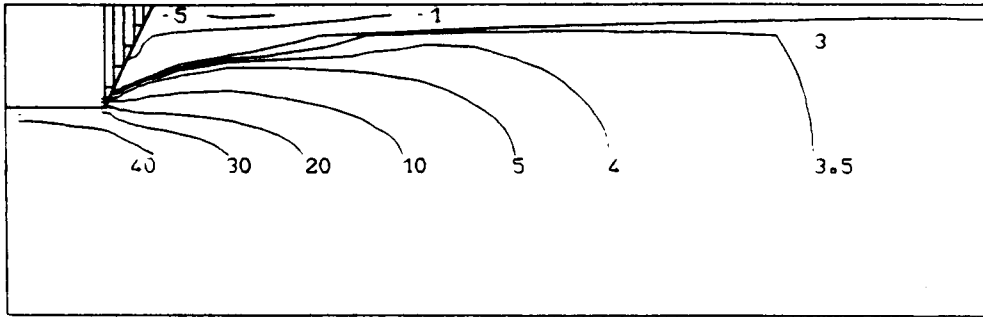
FIGURE 6.51: AXIAL VELOCITIES (7% CH$_4$)
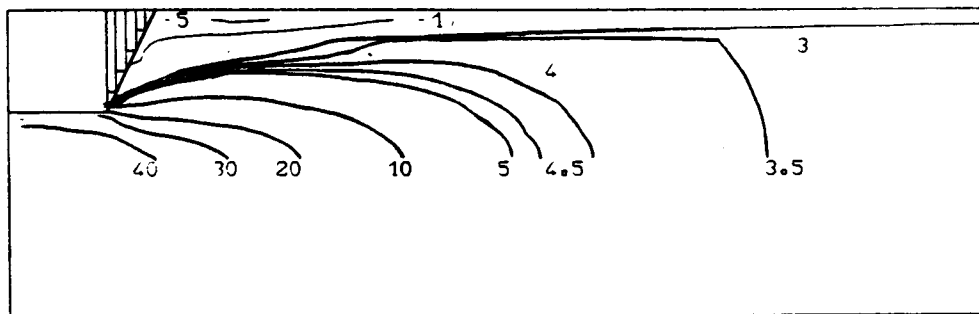
FIGURE 6.52: AXIAL VELOCITIES (10% CH$_4$)
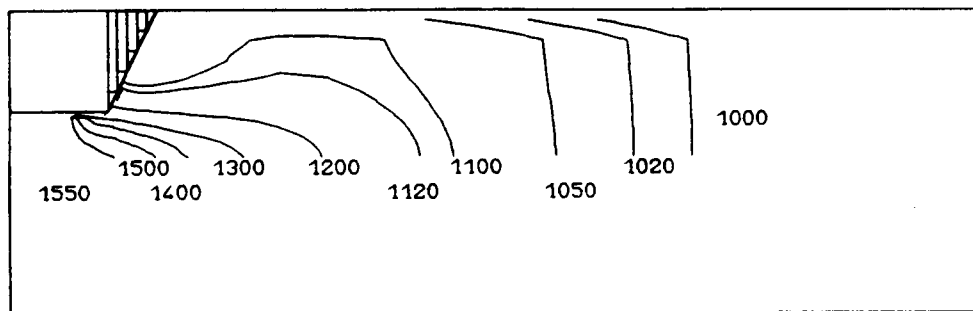
FIGURE 6.53: TEMPERATURE CONTOURS (C), (5% CH$_4$)
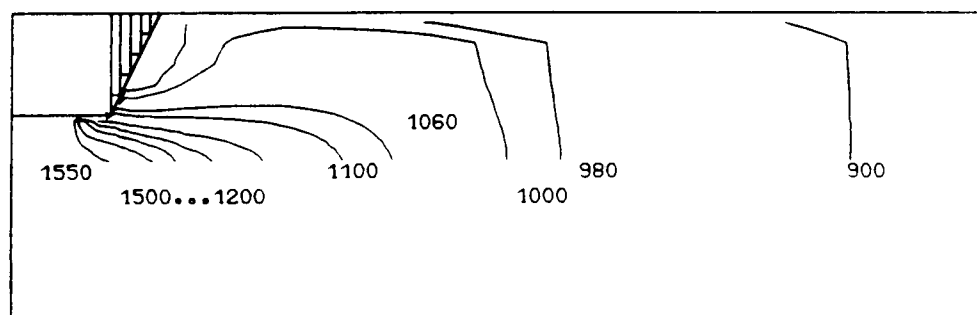
FIGURE 6.54: TEMPERATURE CONTOURS (C) (7% CH$_4$)
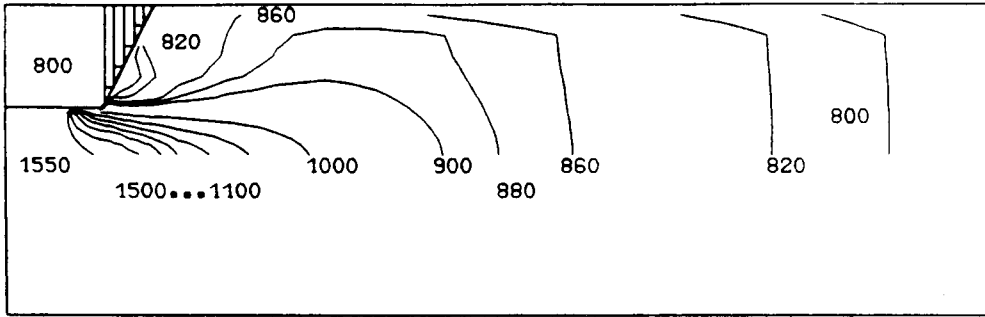
FIGURE 6.55: TEMPERATURE CONTOURS (C), (10% CH4)
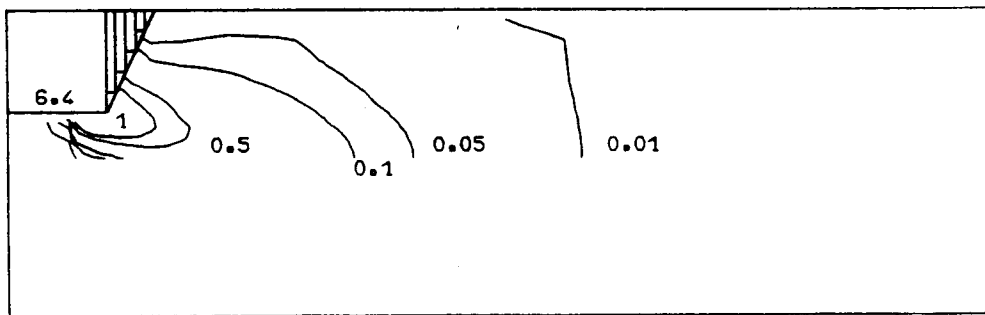
FIGURE 6.56: CH4 VOLUME FRACTIONS (5% CH4)
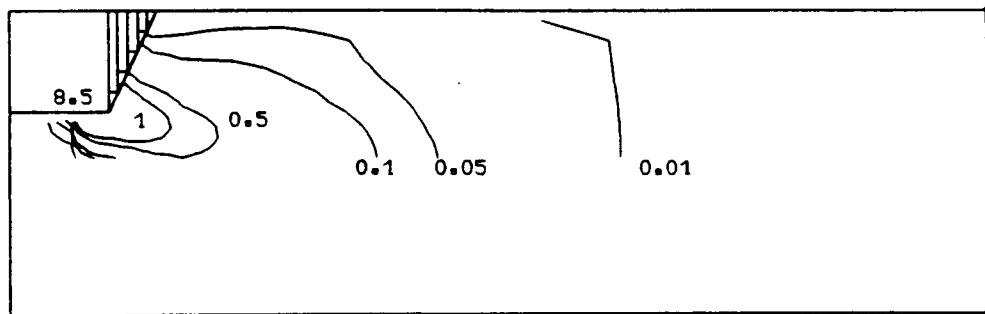
FIGURE 6.57: CH4 VOLUME FRACTIONS (7% CH4)
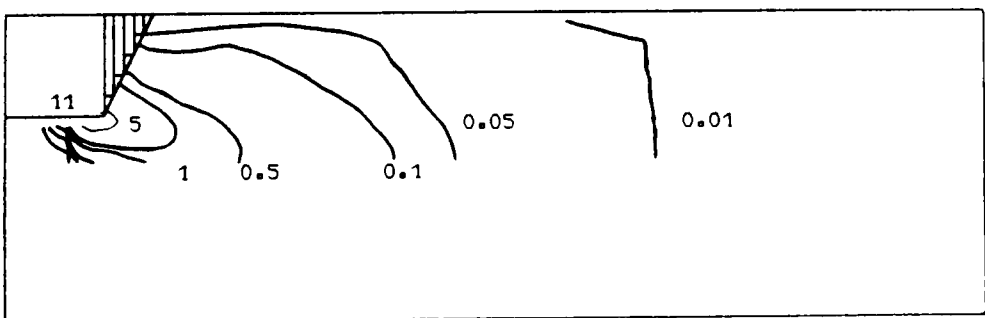
FIGURE 6.58: CH4 VOLUME FRACTIONS (10% CH4)
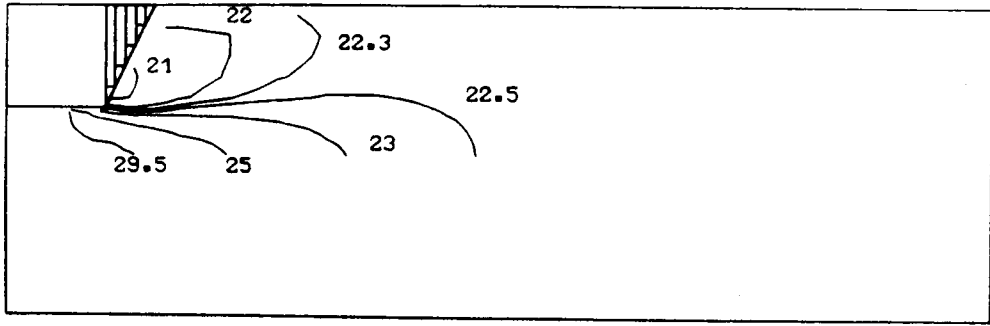
FIGURE 6.59: CO$_2$ VOLUME FRACTIONS (5% CH$_4$)
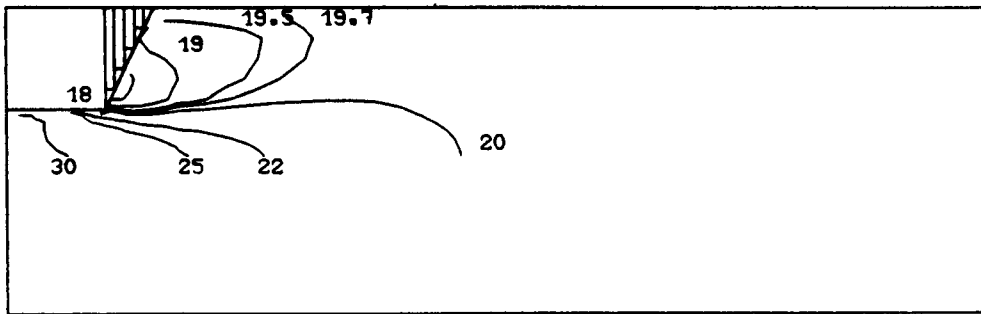
FIGURE 6.60: CO$_2$ VOLUME FRACTIONS (7% CH$_4$)
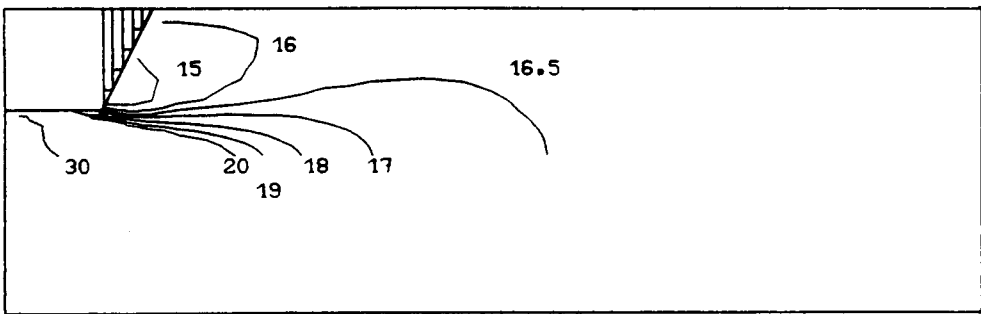
FIGURE 6.61: CO$_2$ VOLUME FRACTIONS (10% CH$_4$)
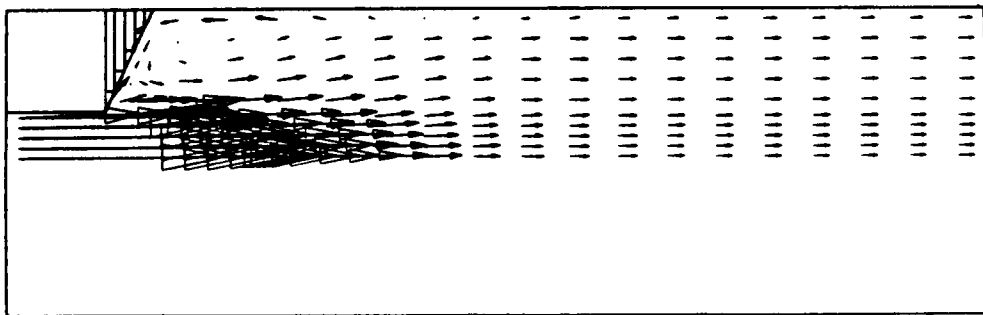
FIGURE 6.62: VELOCITY VECTORS
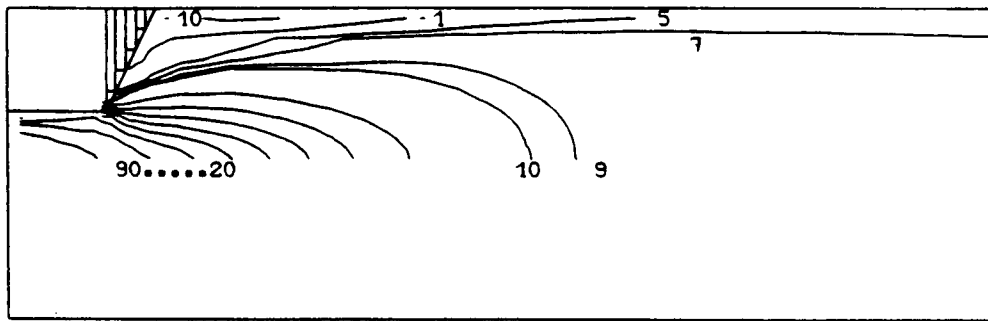
FIGURE 6.63: AXIAL VELOCITIES (2.5% CH₄)
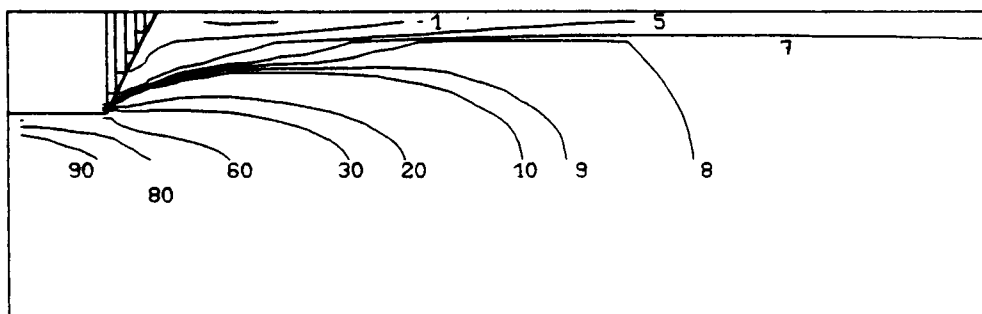
FIGURE 6.64: AXIAL VELOCITIES (5% CH₄)
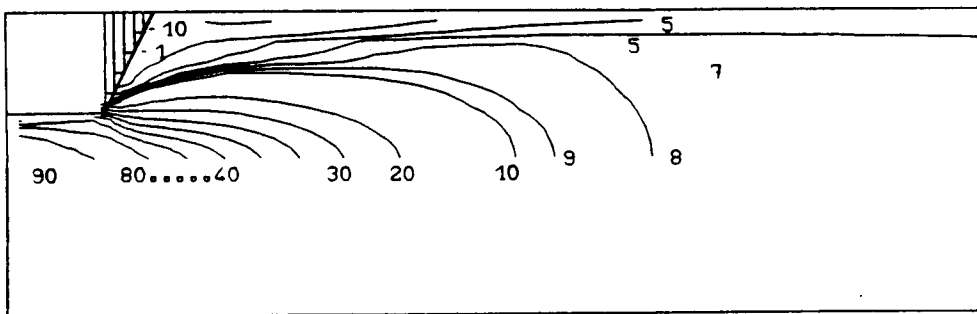
FIGURE 6.65: AXIAL VELOCITIES (7% CH₄)
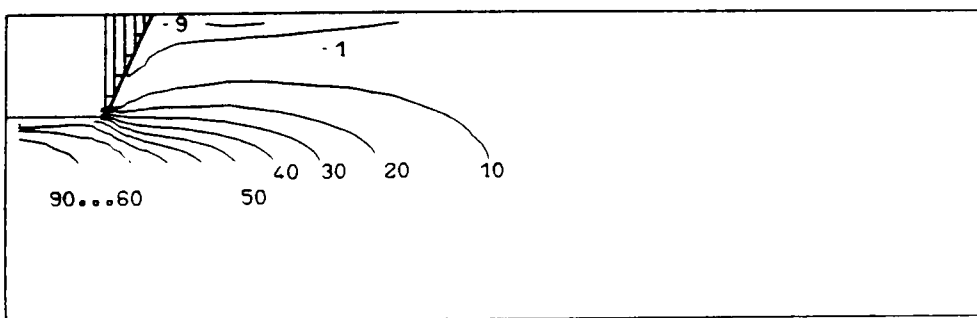
FIGURE 6.66: AXIAL VELOCITIES (10% CH₄)
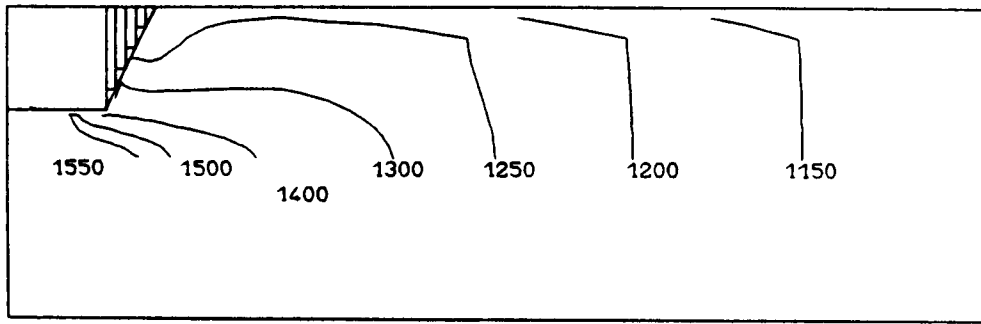
FIGURE 6.67: TEMPERATURE CONTOURS (2.5% CH4)
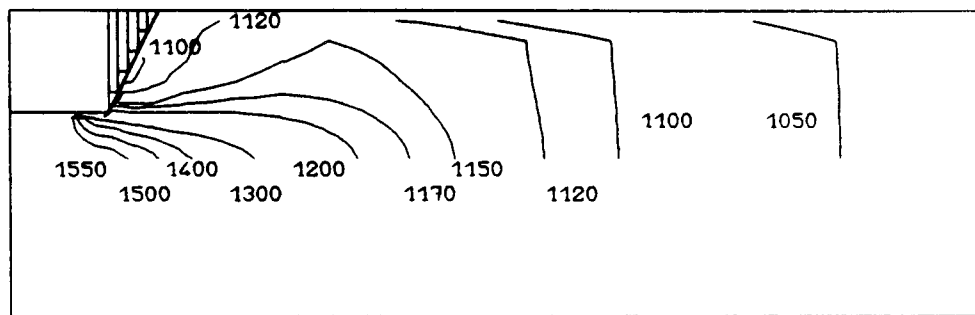
FIGURE 6.68: TEMPERATURE CONTOURS (5% CH4)
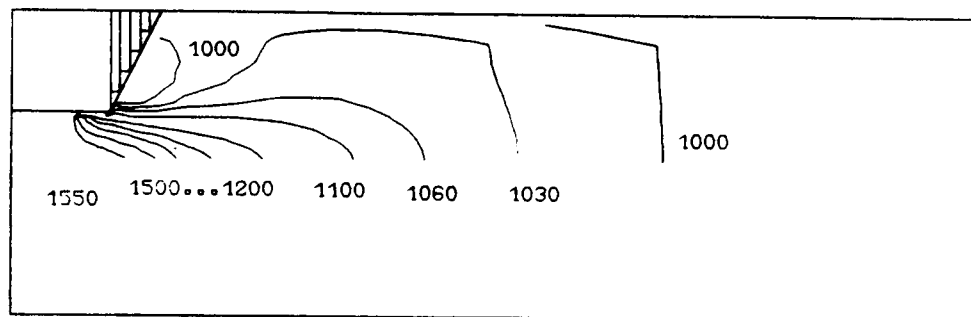
FIGURE 6.69: TEMPERATURE CONTOURS (7% CH4)
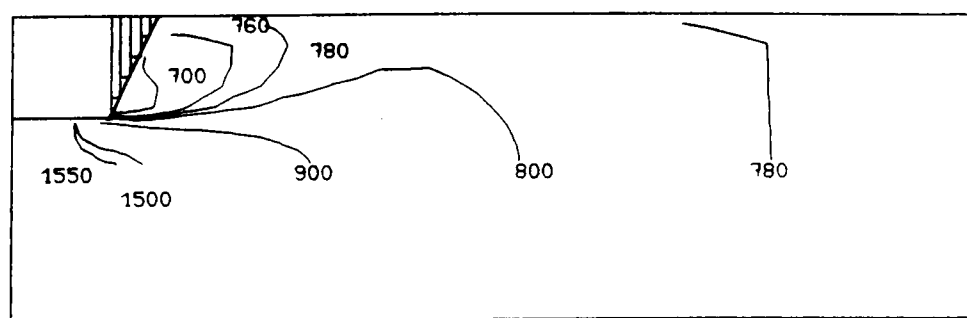
FIGURE 6.70: TEMPERATURE CONTOURS (10% CH4)
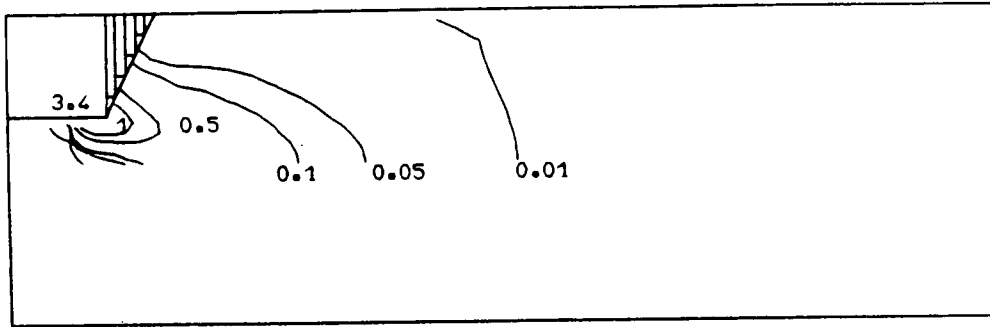
FIGURE 6.71: CH$_4$ VOLUME FRACTIONS (2.5% CH$_4$)
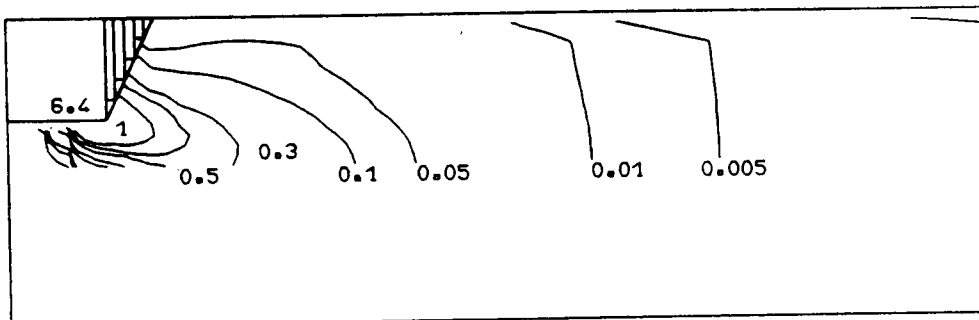
FIGURE 6.72: CH$_4$ VOLUME FRACTIONS (5% CH$_4$)
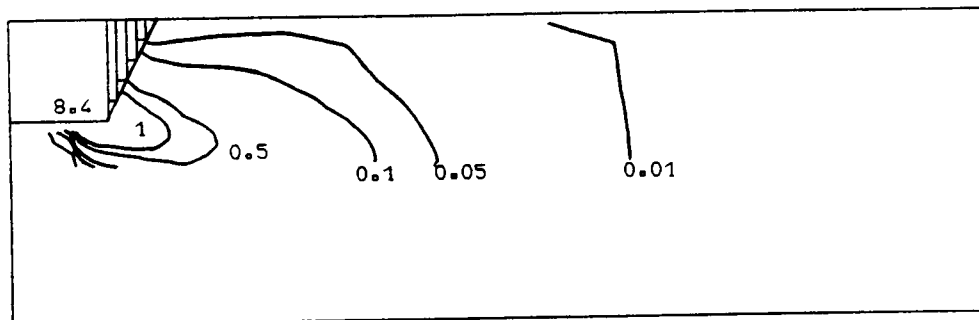
FIGURE 6.73: CH$_4$ VOLUME FRACTIONS (7% CH$_4$)
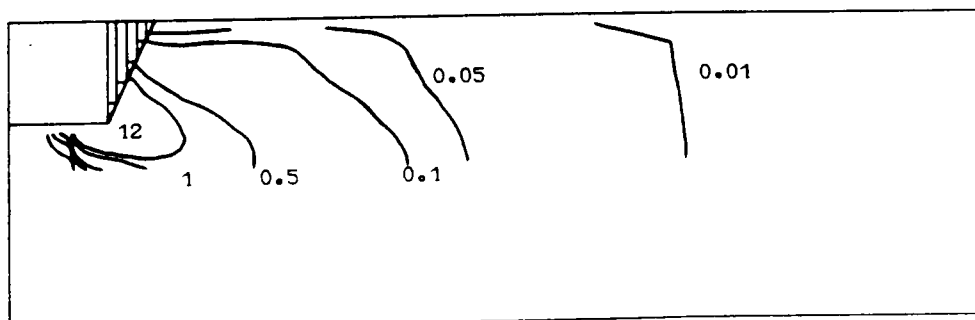
FIGURE 6.74: CH$_4$ VOLUME FRACTIONS (10% CH$_4$)
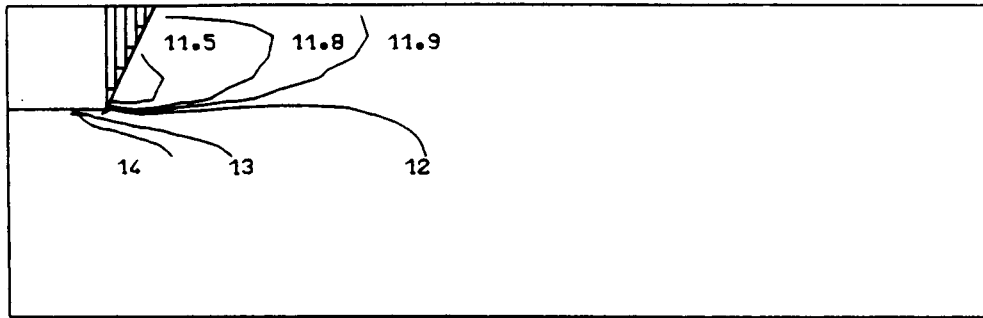
FIGURE 6.75: CO_2 VOLUME FRACTIONS (2.5% CH_4)
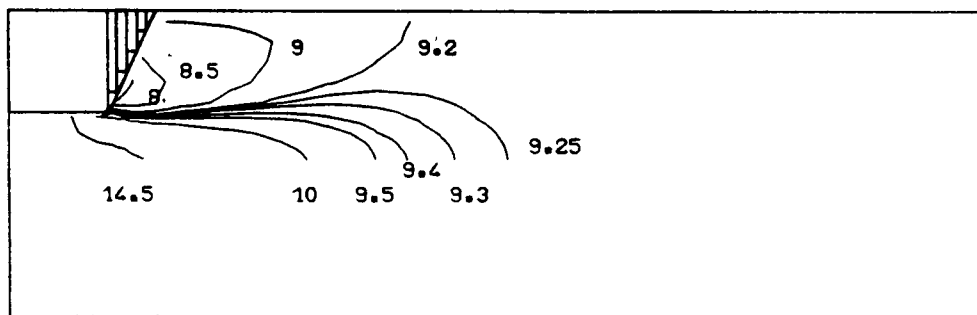
FIGURE 6.76: CO_2 VOLUME FRACTIONS (5% CH_4)
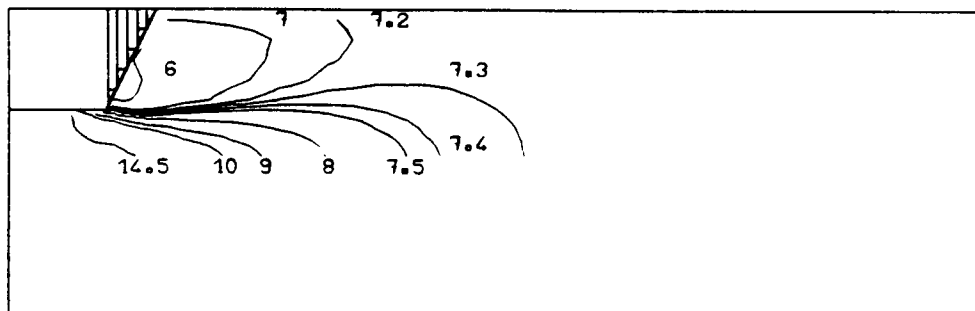
FIGURE 6.77: CO_2 VOLUME FRACTIONS (7% CH_4)
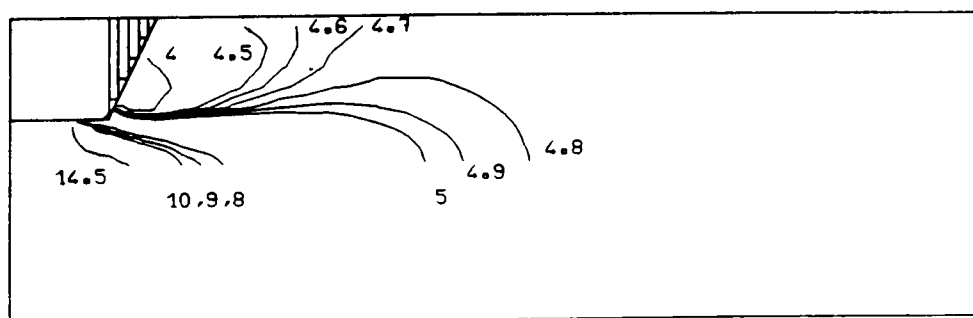
FIGURE 6.78: CO_2 VOLUME FRACTIONS (10% CH_4)

Wall injection

Throat injection

1.5m

10m

0.5m

1.0m

0.5m

(a) side view

tuyere positions

3

2

4

1

30°

5

6

(b) plane view
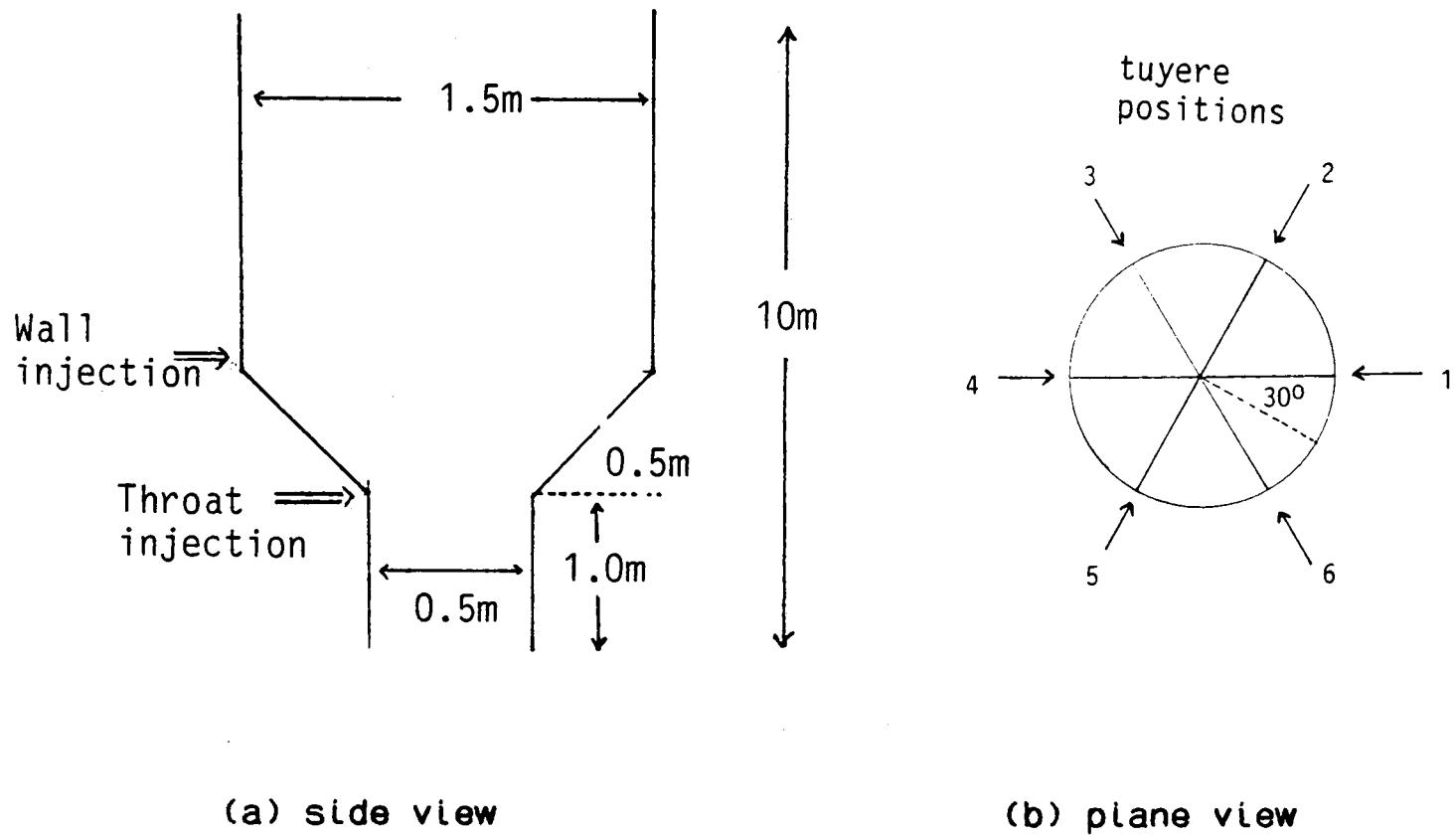
FIGURE 6.79: THREE-DIMENSIONAL GEOMETRY

1080   1100   1200   1550

1070   1040

1060

TEMPERATURE CONTOURS (C)
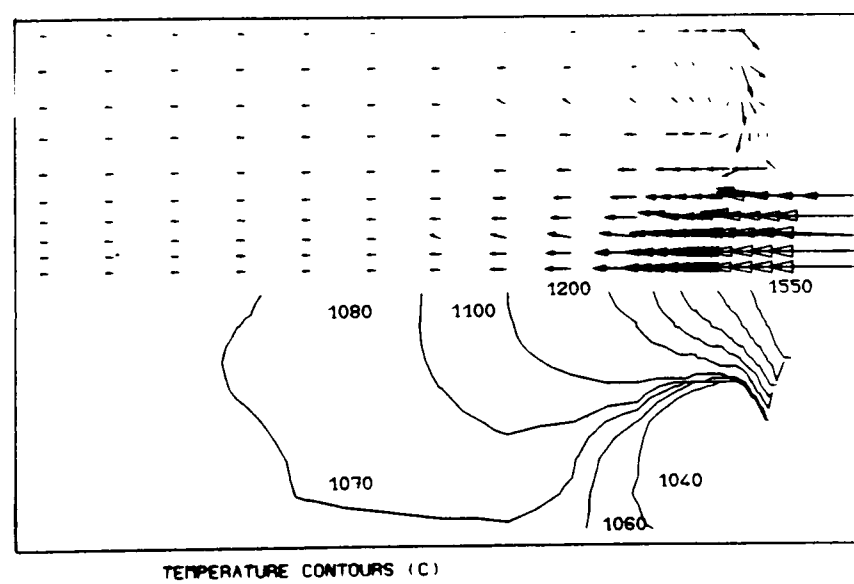
FIGURE 6.80: VELOCITY VECTORS AND TEMPERATURES AT θ=3.75°

TEMPERATURE CONTOURS (C)
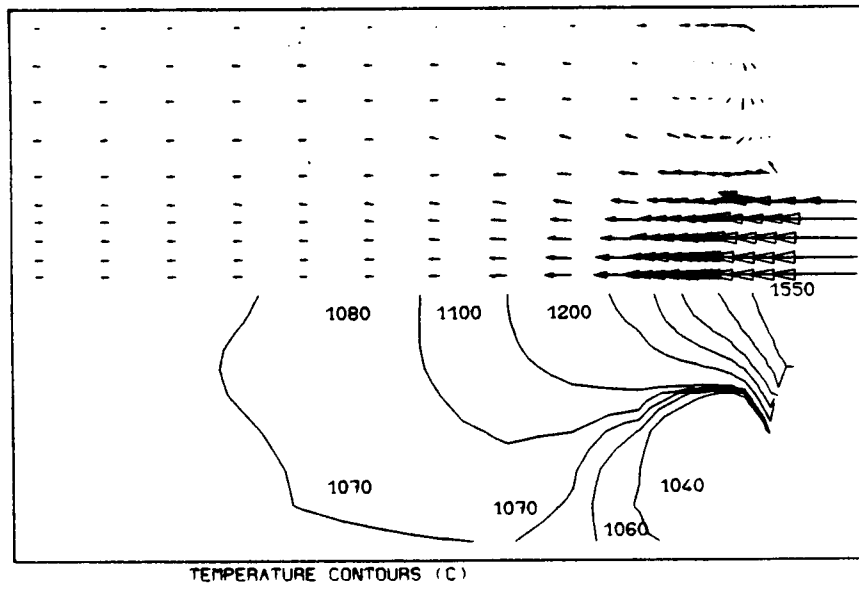
FIGURE 6.81: VELOCITY VECTORS AND TEMPERATURES AT θ=11.25°

TEMPERATURE CONTOURS (C)
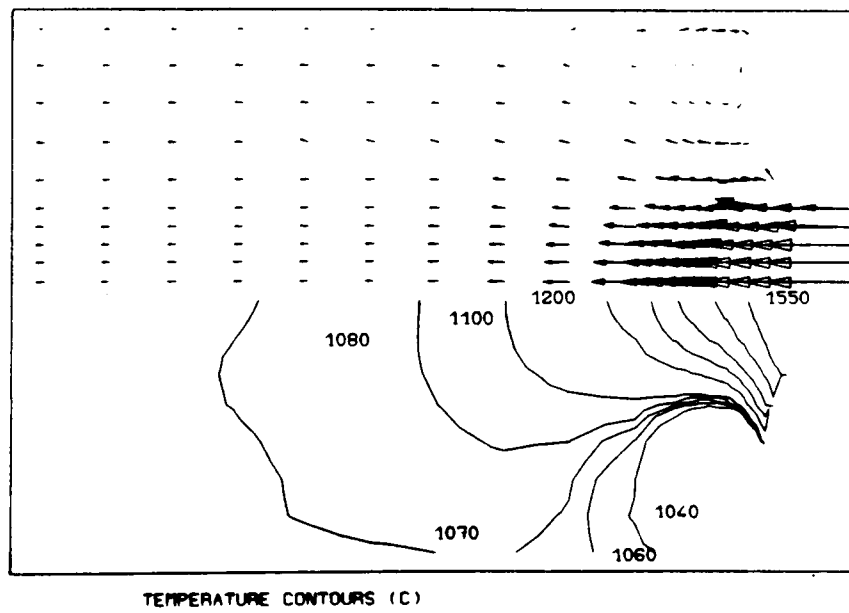
FIGURE 6.82: VELOCITY VECTORS AND TEMPERATURES AT θ=18.75°

TEMPERATURE CONTOURS (C)
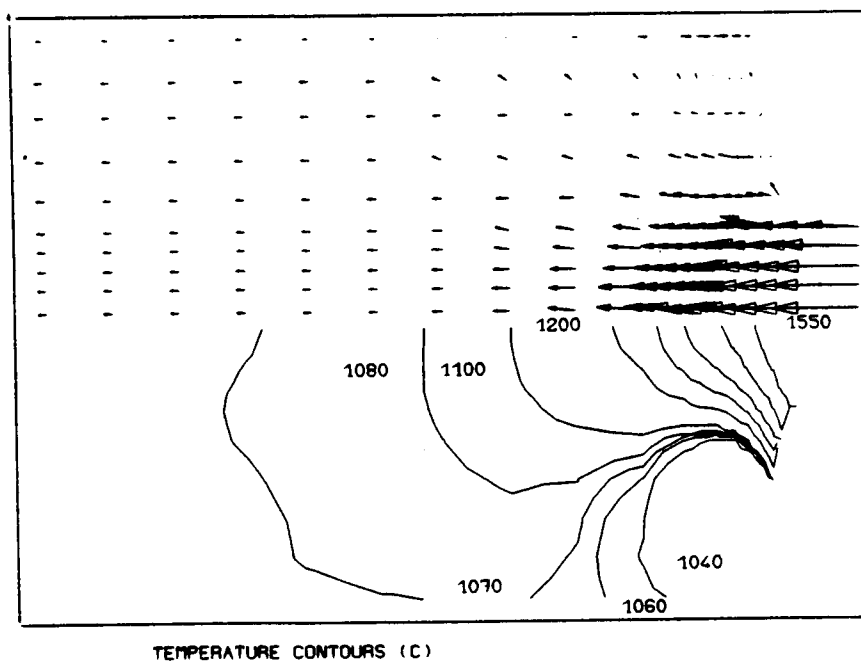
FIGURE 6.83: VELOCITY VECTORS AND TEMPERATURES AT θ=26.25^o


CO2 % VOLUME FRACTION

CH4 % VOLUME FRACTION
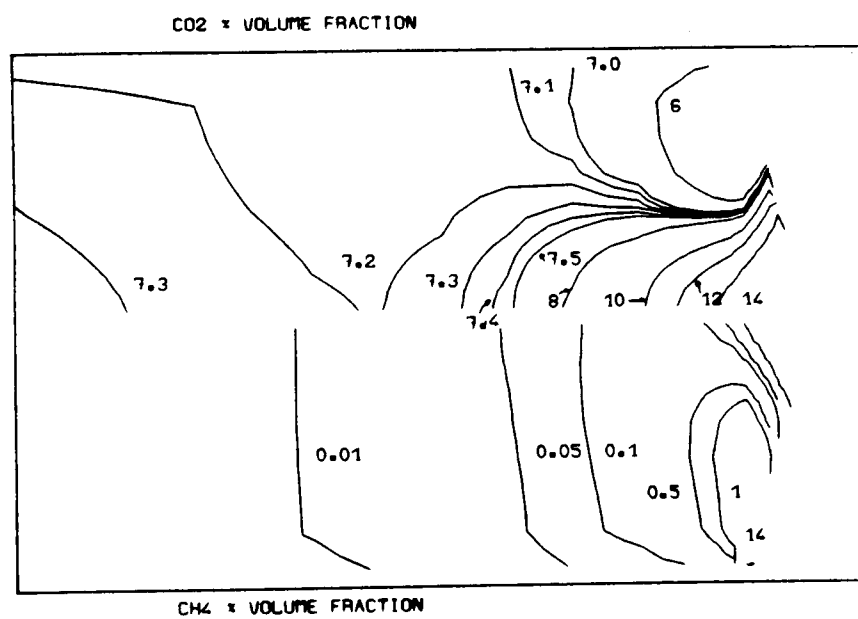
FIGURE 6.84: CH_4 AND CO_2 VOLUME FRACTIONS AT θ=3.75^o

CO2 % VOLUME FRACTION

CH4 % VOLUME FRACTION
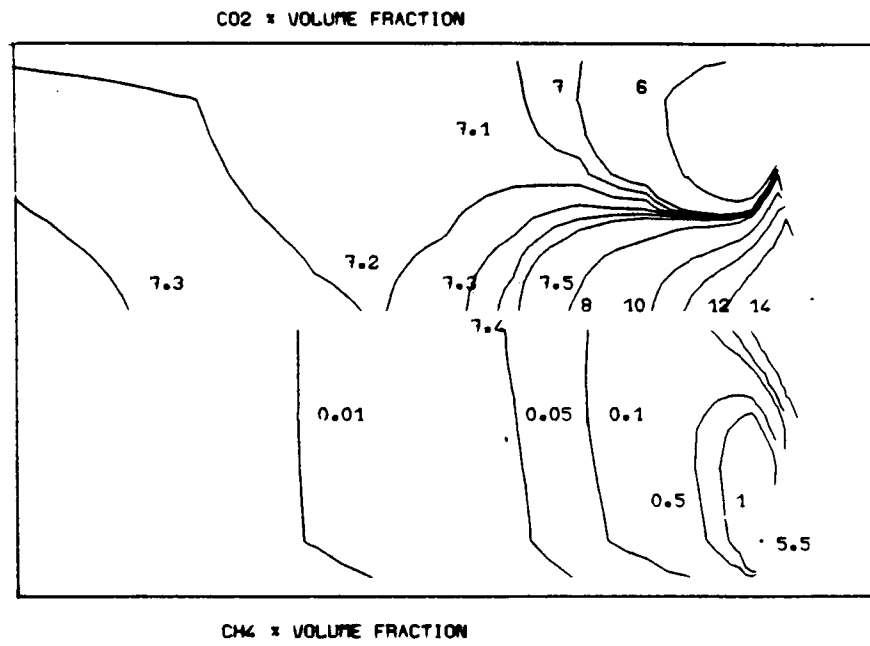
FIGURE 6.85: CH$_4$ AND CO$_2$ VOLUME FRACTIONS AT θ=11.25°

CO2 % VOLUME FRACTION

CH4 % VOLUME FRACTION
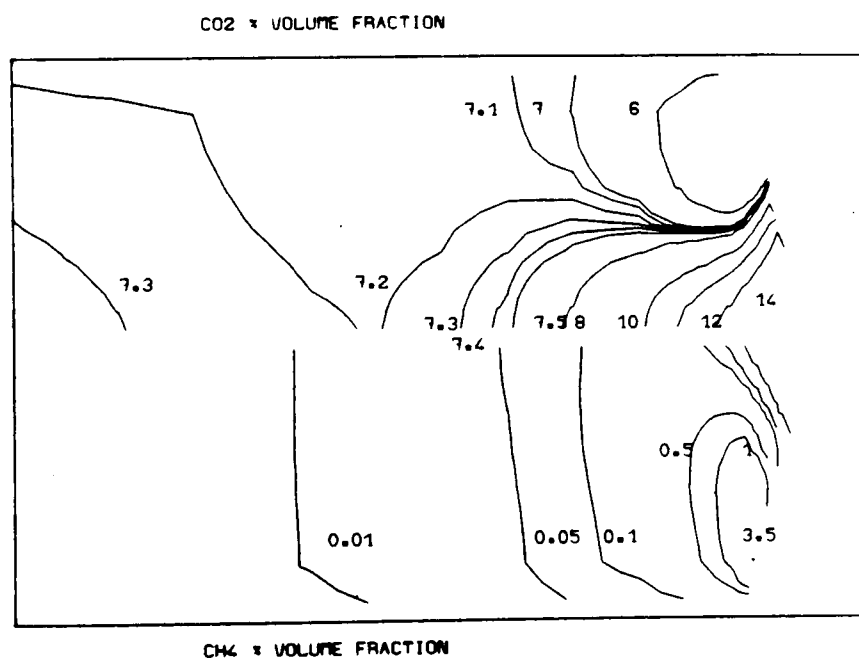
FIGURE 6.86: CH$_4$ AND CO$_2$ VOLUME FRACTIONS AT θ=18.75°

-252-

CO2 % VOLUME FRACTION

CH4 % VOLUME FRACTION
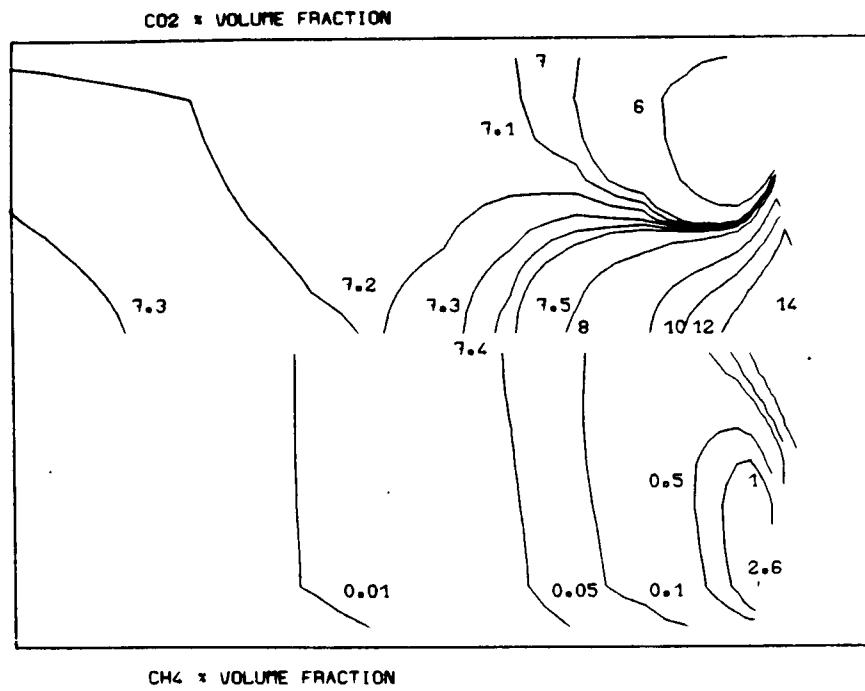
FIGURE 6.87: CH4 AND CO2 VOLUME FRACTIONS AT θ=26.25°
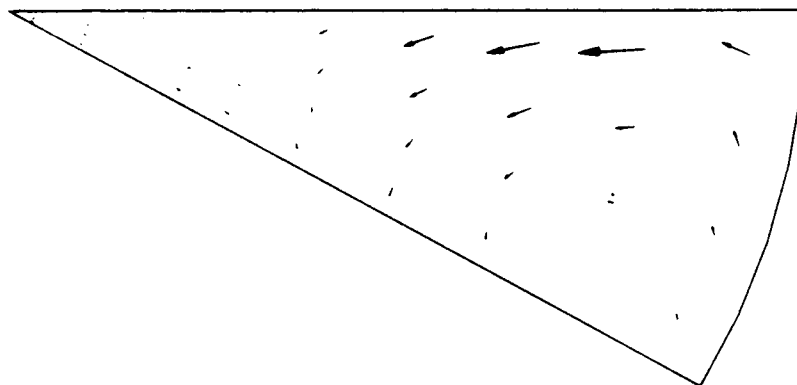
FIGURE 6.88: RADIAL VELOCITY VECTORS AT 1.40m
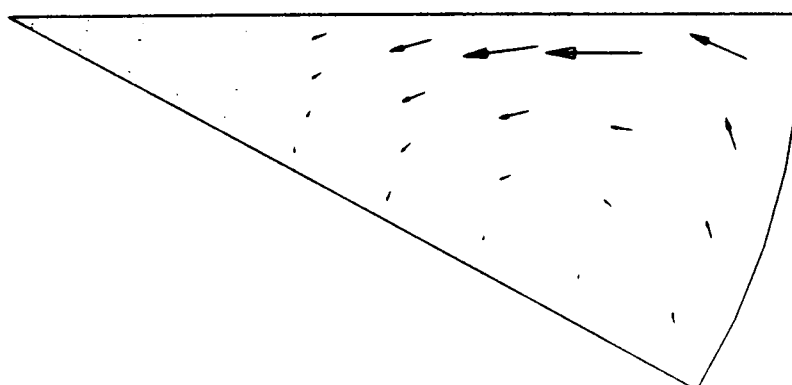
FIGURE 6.89: RADIAL VELOCITY VECTORS AT 1.45m
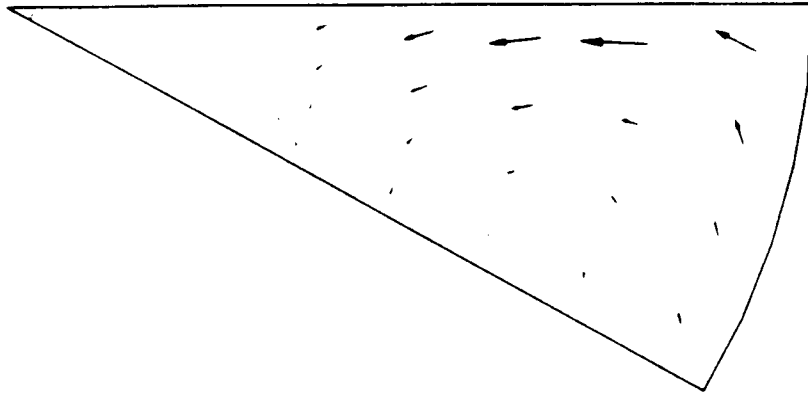
FIGURE 6.90: RADIAL VELOCITY VECTORS AT 1.50m

TEMPERATURE CONTOURS (C)
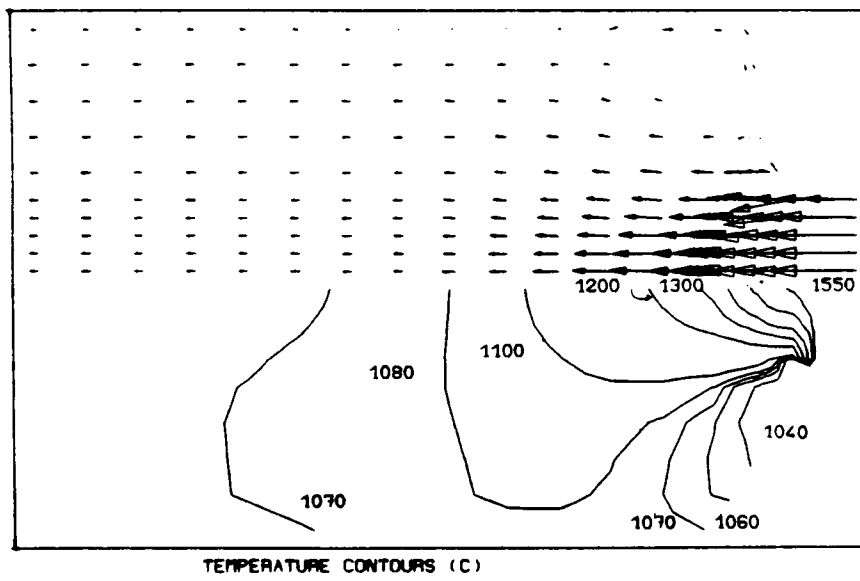
FIGURE 6.91: VELOCITY VECTORS AND TEMPERATURES AT θ=3.75°

TEMPERATURE CONTOURS (C)
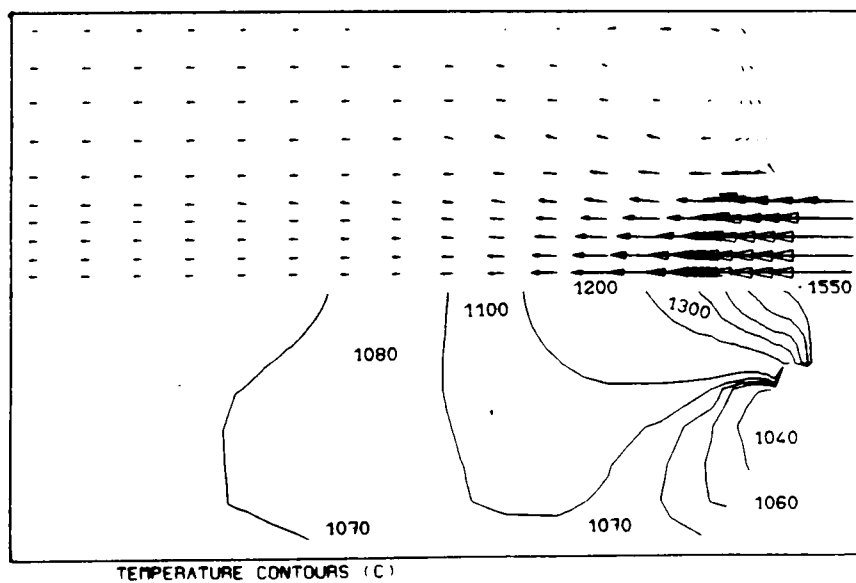
FIGURE 6.92: VELOCITY VECTORS AND TEMPERATURES AT θ=11.25°

TEMPERATURE CONTOURS (C)
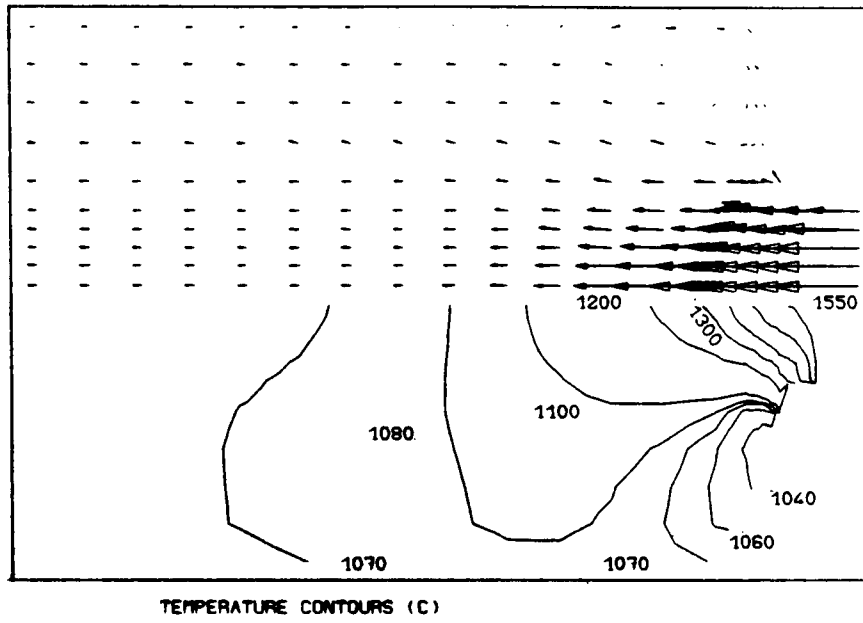
FIGURE 6.93: VELOCITY VECTORS AND TEMPERATURES AT θ=18.75°

TEMPERATURE CONTOURS (C)
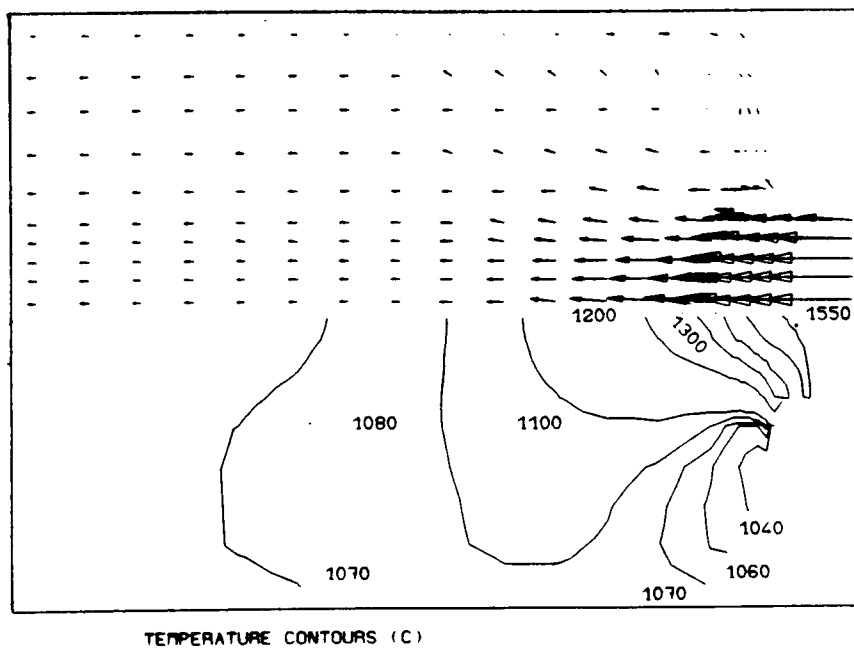
FIGURE 6.94: VELOCITY VECTORS AND TEMPERATURES AT θ=26.25°
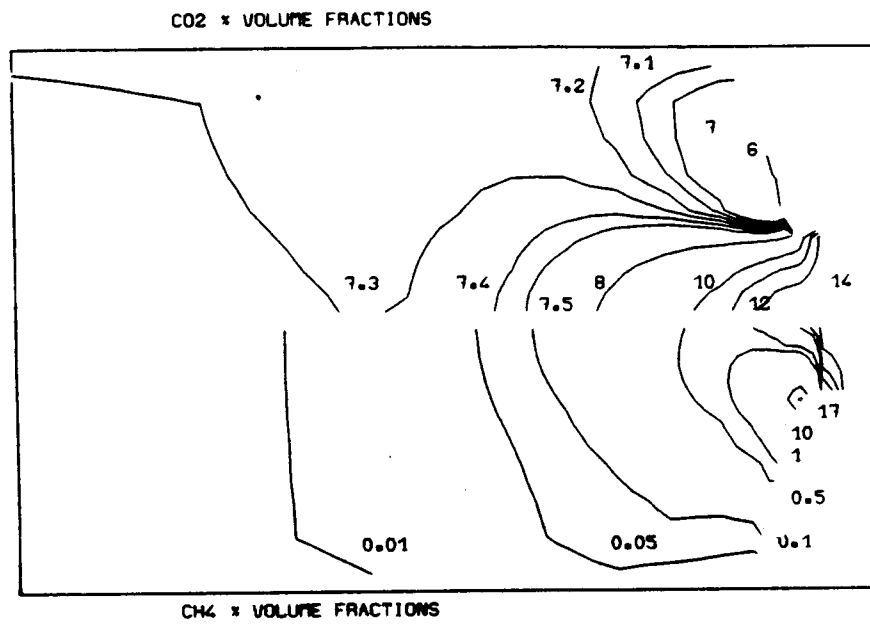
FIGURE 6.95: CH₄ AND CO₂ VOLUME FRACTIONS AT θ=3.75°
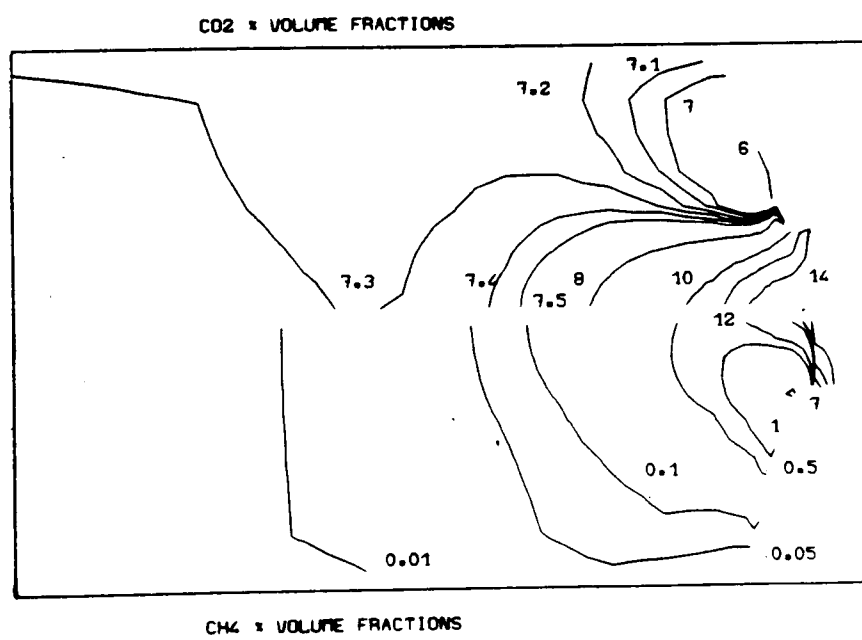
FIGURE 6.96: CH₄ AND CO₂ VOLUME FRACTIONS AT θ=11.25°

CO2 % VOLUME FRACTIONS

CH4 % VOLUME FRACTIONS
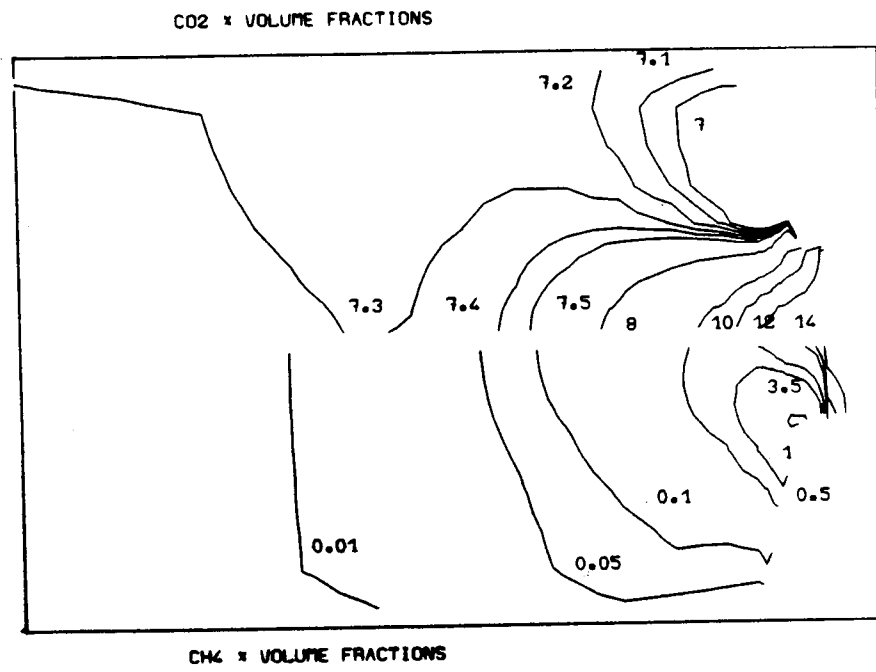
FIGURE 6.97: CH_4 AND CO_2 VOLUME FRACTIONS AT $\theta=18.75^\circ$

CO2 % VOLUME FRACTIONS

CH4 % VOLUME FRACTIONS
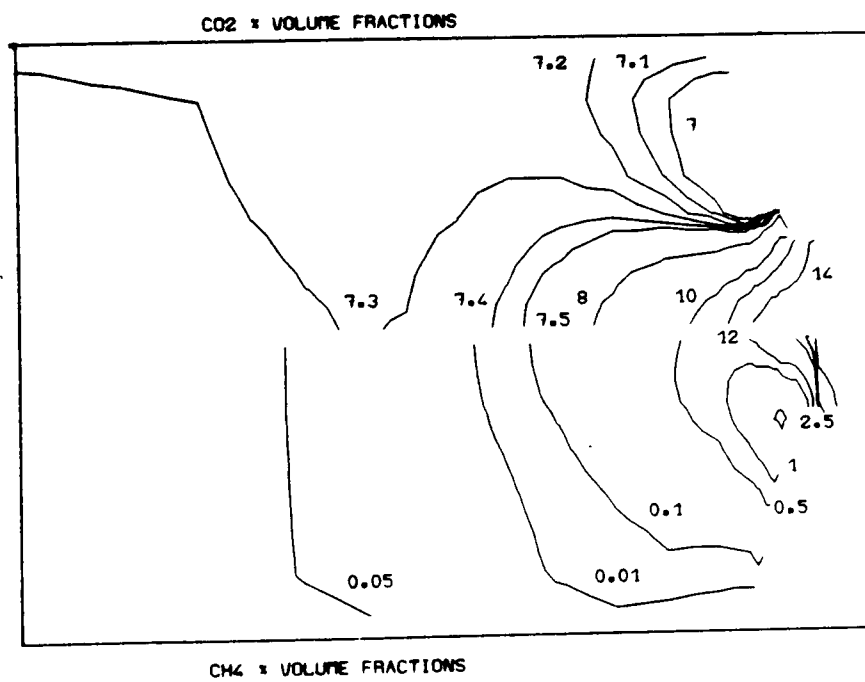
FIGURE 6.98: CH_4 AND CO_2 VOLUME FRACTIONS AT $\theta=26.25^\circ$

INJECTION PLANE
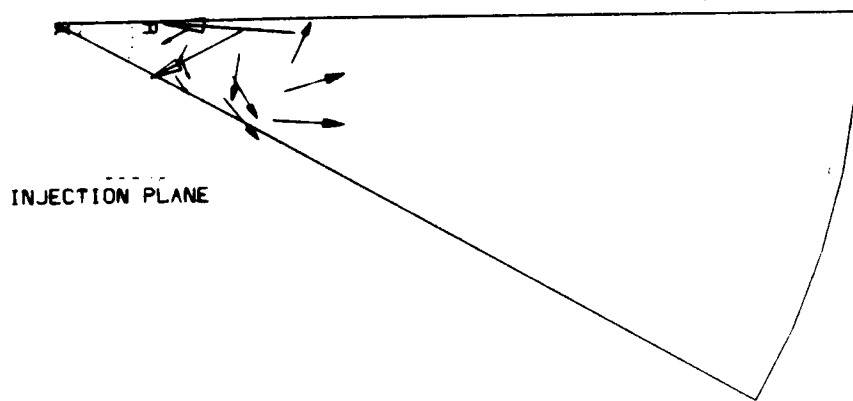
FIGURE 6.99: RADIAL VELOCITY VECTORS AT 0.875m
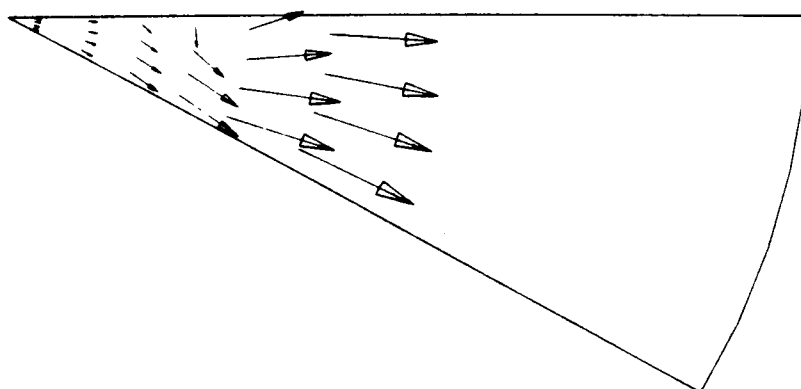
FIGURE 6.100: RADIAL VELOCITY VECTORS AT 1.05m
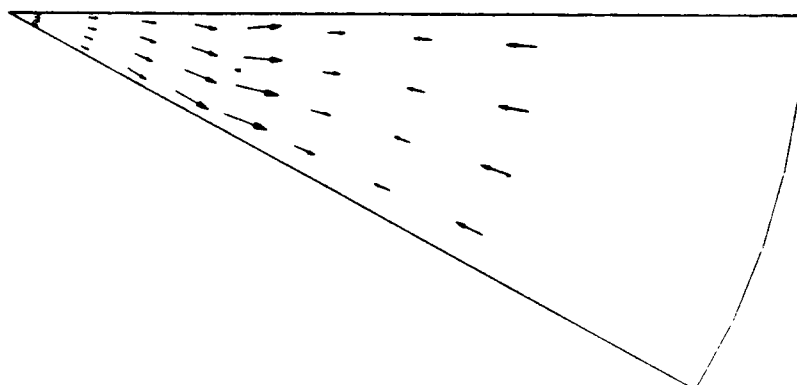
FIGURE 6.101: RADIAL VELOCITY VECTORS AT 1.25m
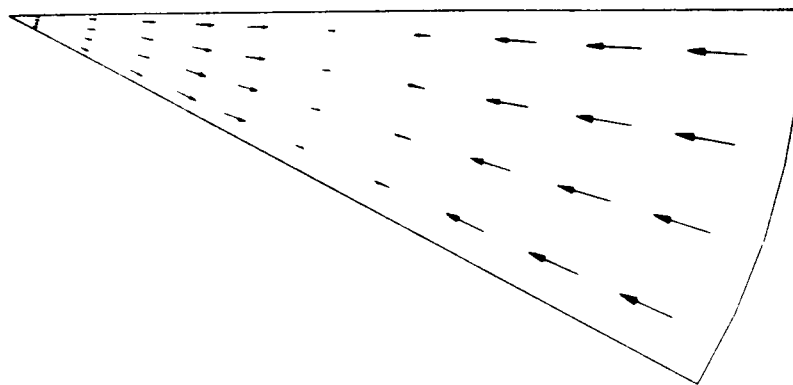
FIGURE 6.102: RADIAL VELOCITY VECTORS AT 1.45m

(a) side view

(b) plane view
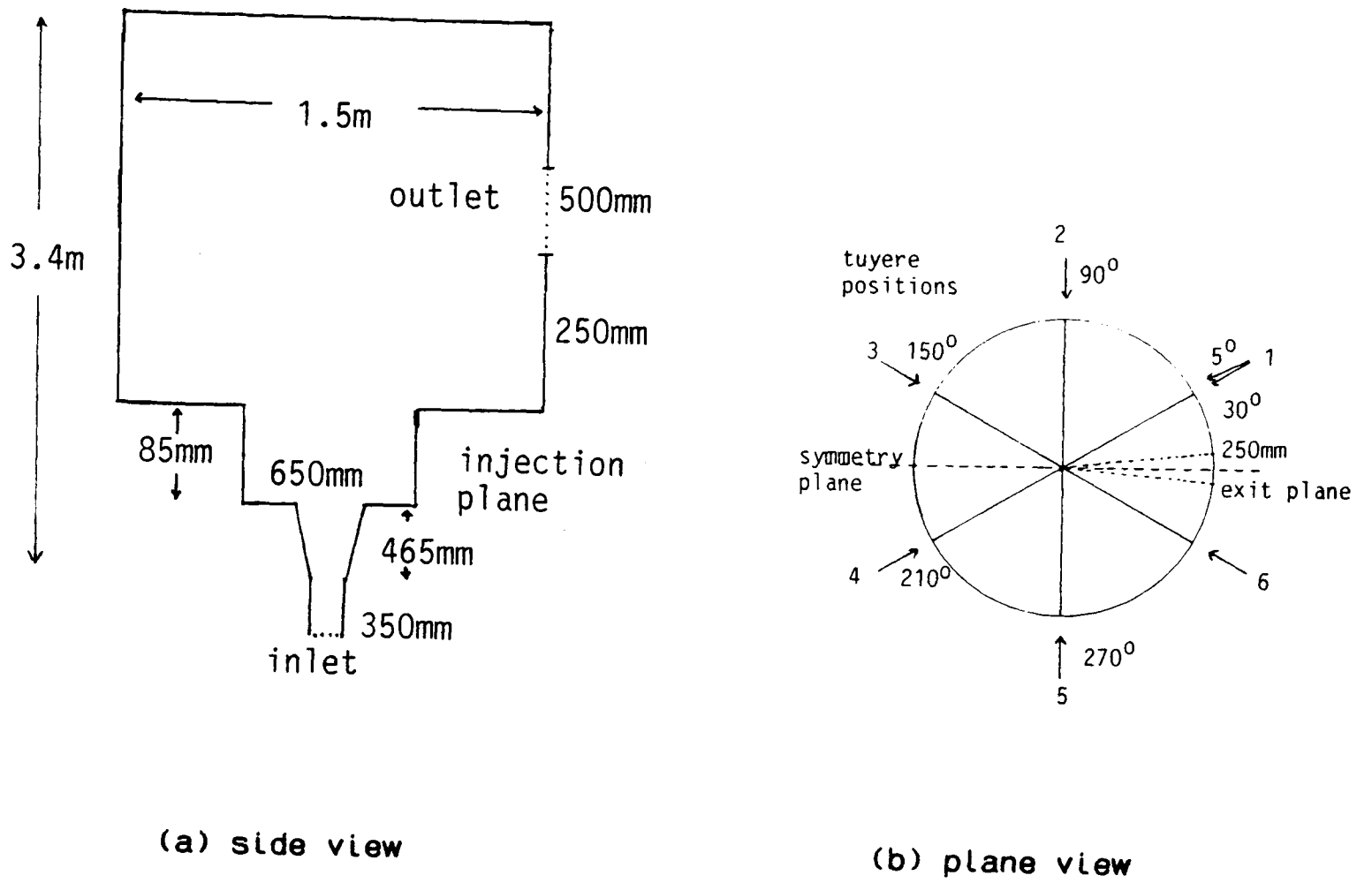
FIGURE 6.103:   RV1 GEOMETRY

TEMPERATURE CONTOURS (C)
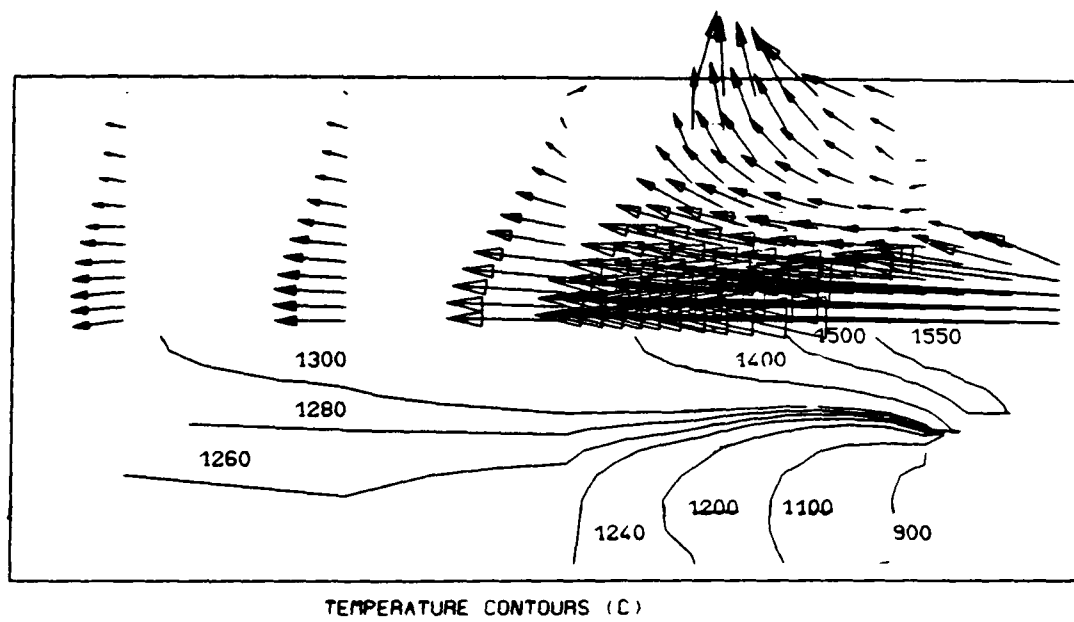
FIGURE 6.104:   VELOCITY VECTORS AND TEMPERATURES AT $\theta=10^\circ$

TEMPERATURE CONTOURS (C)
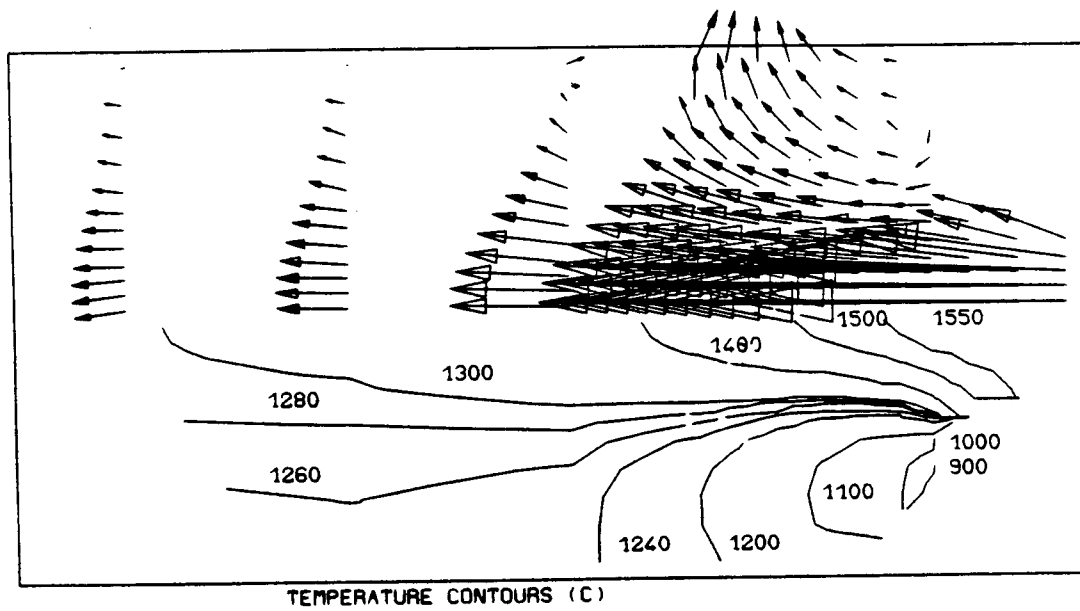
FIGURE 6.105:   VELOCITY VECTORS AND TEMPERATURES AT θ=20°

TEMPERATURE CONTOURS (C)
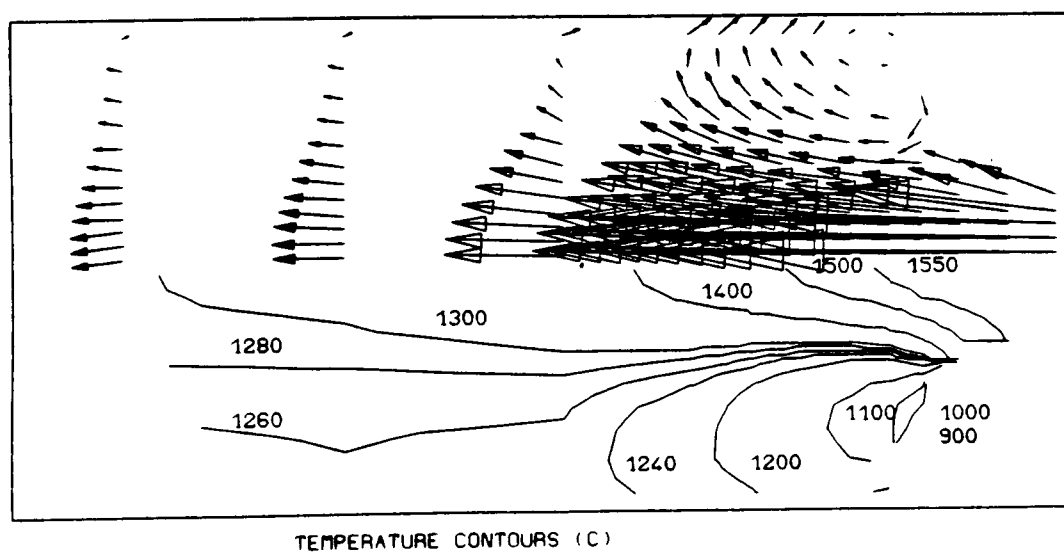
FIGURE 6.106:   VELOCITY VECTORS AND TEMPERATURES AT θ=30°
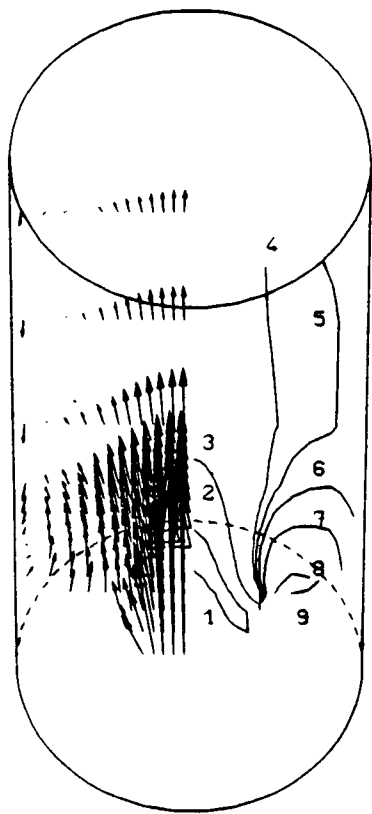
CONTOUR LEVELS

1	:	1550
2	:	1500
3	:	1400
4	:	1300
5	:	1280
6	:	1260
7	:	1240
8	:	1200
9	:	1100

FIGURE 6.107:   VELOCITY VECTORS AND TEMPERATURES AT θ=60°
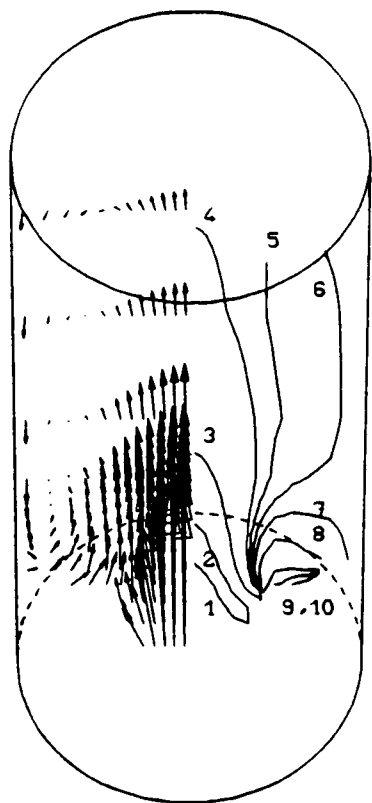
CONTOUR LEVELS

1	:	1550
2	:	1500
3	:	1400
4	:	1300
5	:	1280
6	:	1260
7	:	1240
8	:	1200
9	:	1100
10	:	1000

FIGURE 6.108:   VELOCITY VECTORS AND TEMPERATURES AT θ=90°
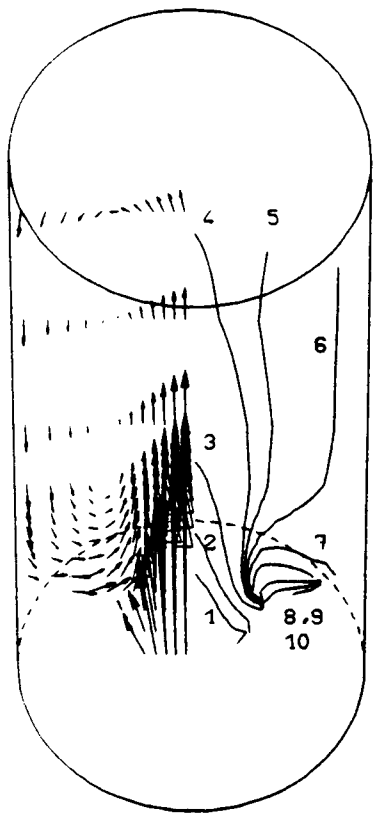
CONTOUR LEVELS		
1	:	1550
2	:	1500
3	:	1400
4	:	1300
5	:	1280
6	:	1260
7	:	1240
8	:	1200
9	:	1100
10	:	1000

FIGURE 6.109:   VELOCITY VECTORS AND TEMPERATURES AT $\theta=150^o$

CO2 x VOLUME FRACTIONS

CH4 x VOLUME FRACTIONS
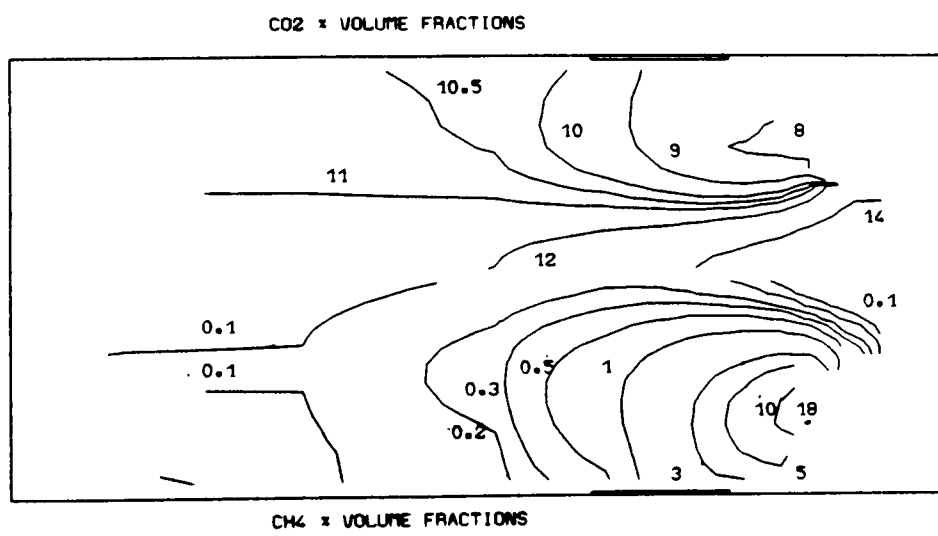
FIGURE 6.110: CH_4 AND CO_2 VOLUME FRACTIONS AT $\theta=10^o$

CO2 % VOLUME FRACTIONS

CH4 % VOLUME FRACTIONS
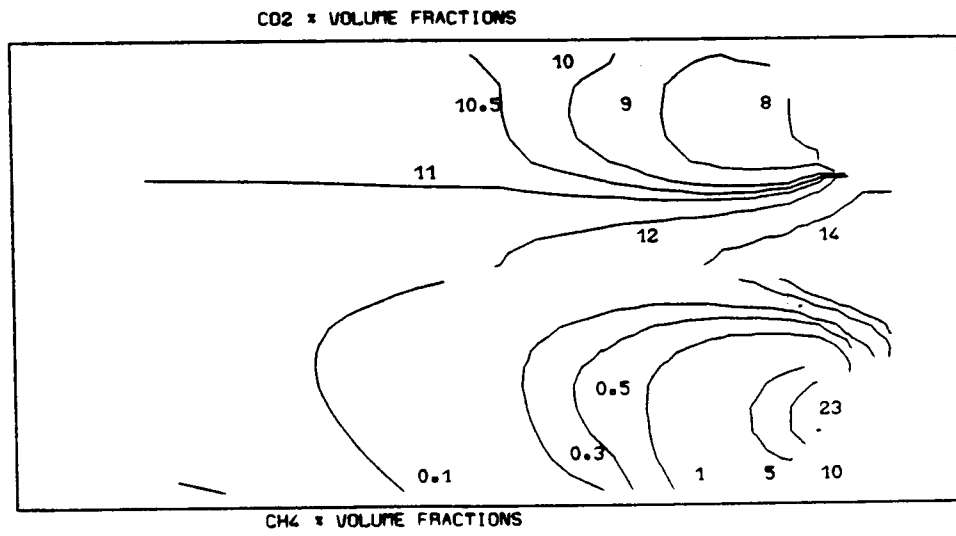
FIGURE 6.111:   CH$_4$ AND CO$_2$ VOLUME FRACTIONS AT θ=20°

CO2 % VOLUME FRACTIONS

CH4 % VOLUME FRACTIONS
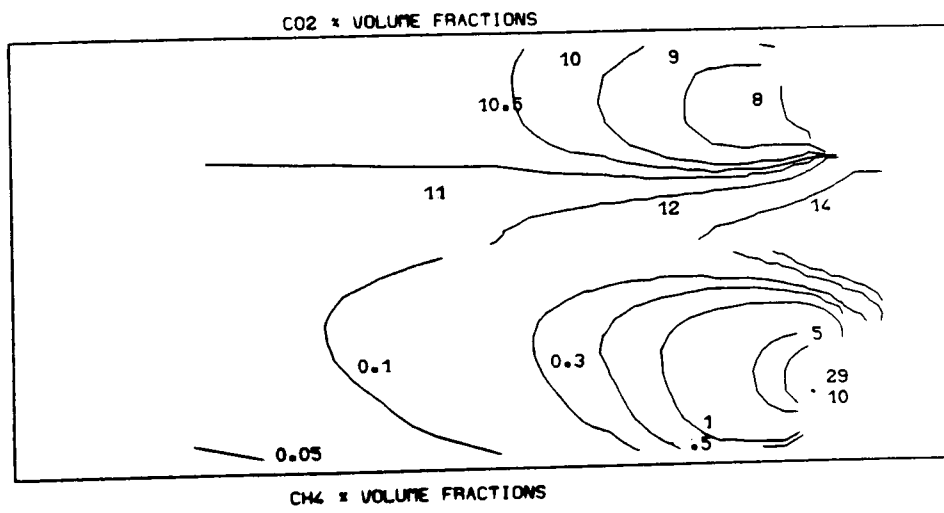
FIGURE 6.112:   CH$_4$ AND CO$_2$ VOLUME FRACTIONS AT θ=30°

CO₂ % VOLUME FRACTIONS
CONTOUR LEVELS

1	:	14
2	:	12
3	:	11
4	:	10.5
5	:	10
6	:	9
7	:	8

CH₄ % VOLUME FRACTIONS
CONTOUR LEVELS

1	:	12
2	:	5
3	:	1
4	:	0.5
5	:	0.1
6	:	0.05
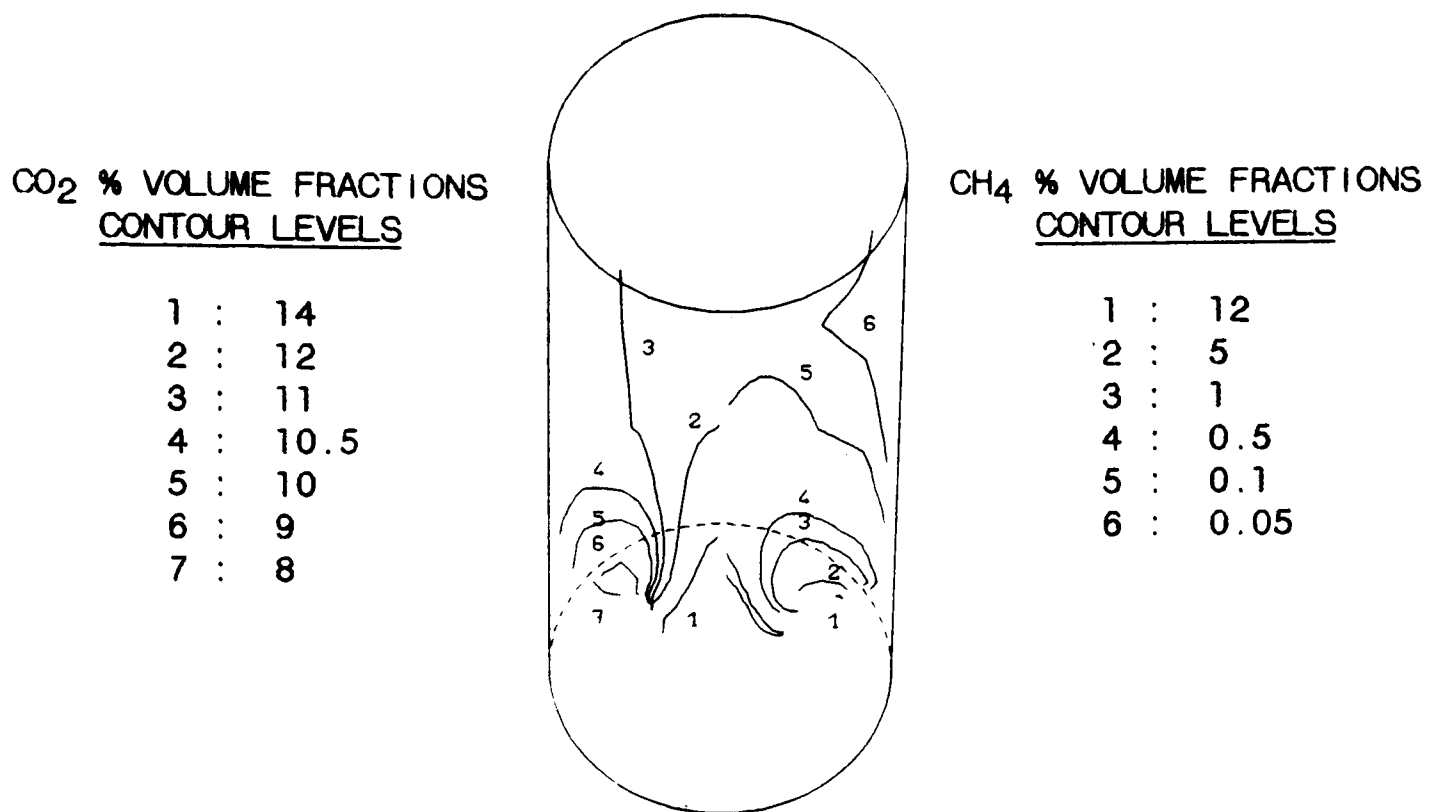
FIGURE 6.113:   CH$_4$ AND CO$_2$ VOLUME FRACTIONS AT $\theta=60^o$

CO₂ % VOLUME FRACTIONS
CONTOUR LEVELS

1	:	14
2	:	12
3	:	11
4	:	10.5
5	:	10
6	:	9
7	:	8

CH₄ % VOLUME FRACTIONS
CONTOUR LEVELS

1	:	26
2	:	10
3	:	5
4	:	1
5	:	0.5
6	:	0.1
7	:	0.05
8	:	0.01
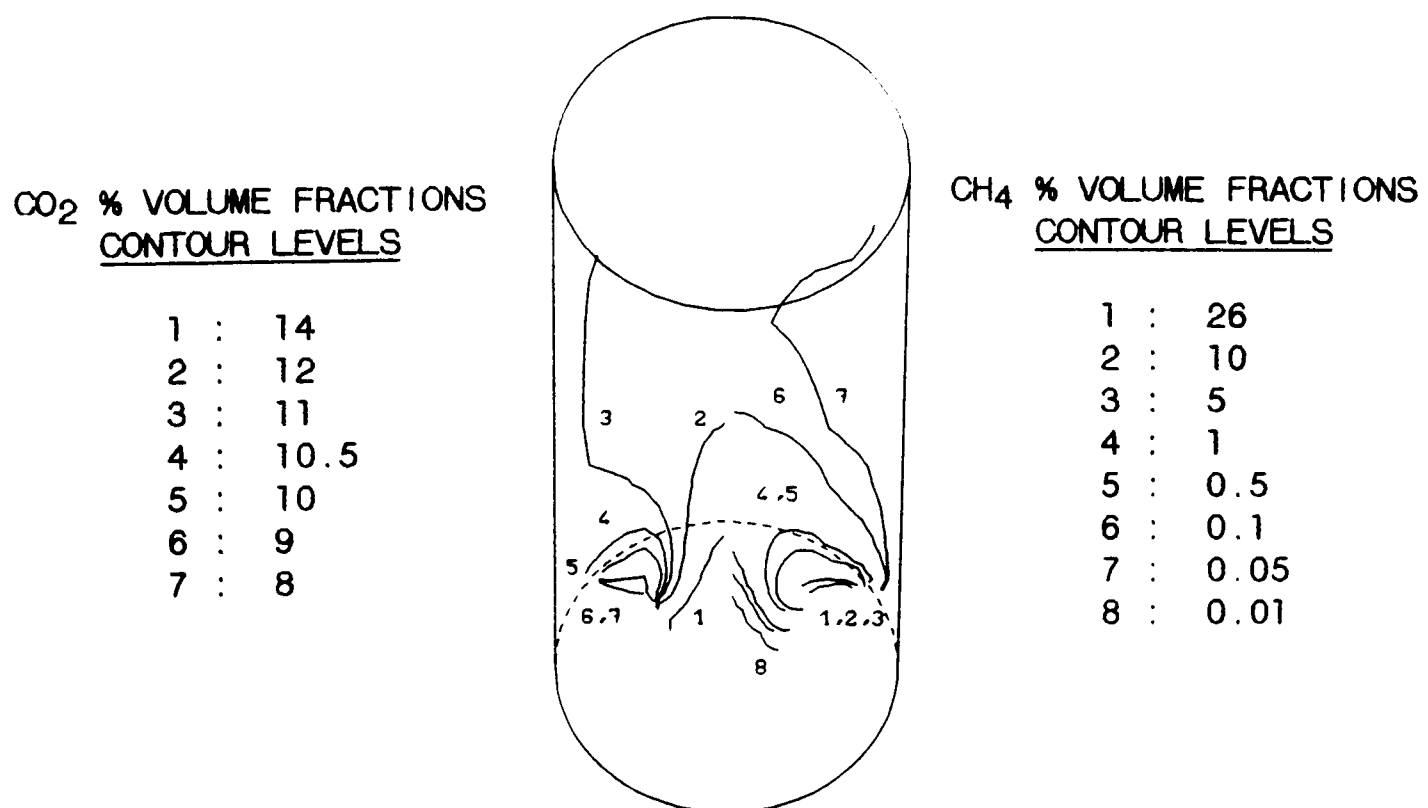
FIGURE 6.114:   CH$_4$ AND CO$_2$ VOLUME FRACTIONS AT $\theta=90^o$

CO_2 % VOLUME FRACTIONS
CONTOUR LEVELS

1 : 14
2 : 12
3 : 11.5
4 : 11.3
5 : 11
6 : 10.5
7 : 10
8 : 9
9 : 8
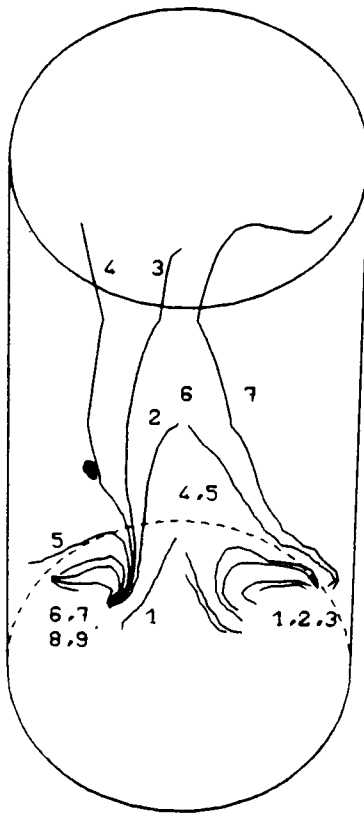
CH_4 % VOLUME FRACTIONS
CONTOUR LEVELS

1 : 25
2 : 10
3 : 5
4 : 1
5 : 0.5
6 : 0.1
7 : 0.05

FIGURE 6.115:   CH_4 AND CO_2 VOLUME FRACTIONS AT θ=150°
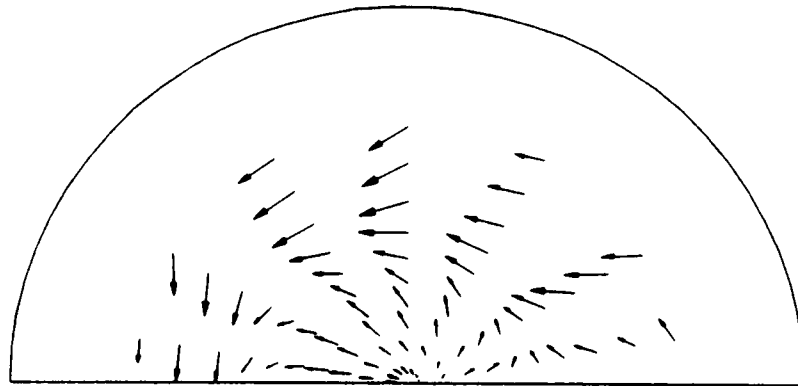

FIGURE 6.116:   RADIAL VELOCITY VECTORS AT 0.465m

INJECTION PLANE
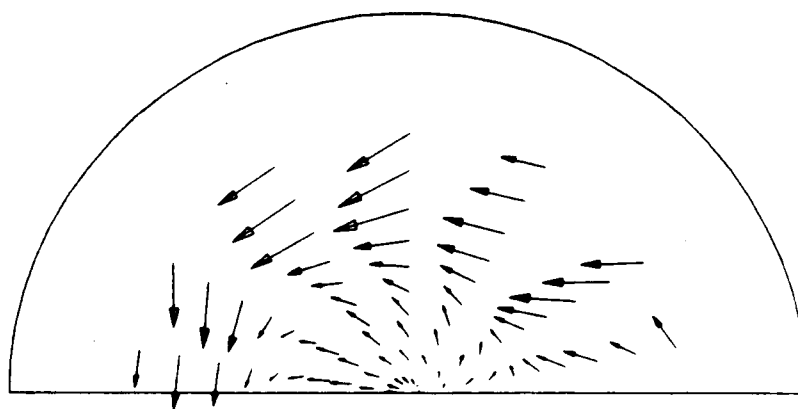
FIGURE 6.117:   RADIAL VELOCITY VECTORS AT 0.5075m
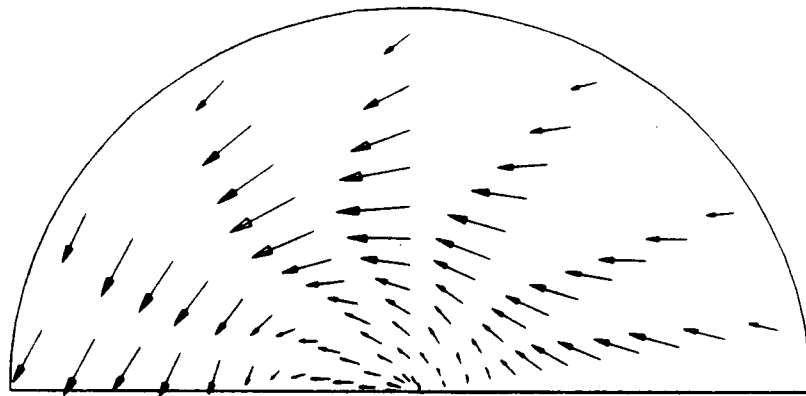
FIGURE 6.118:   RADIAL VELOCITY VECTORS AT 0.6125m
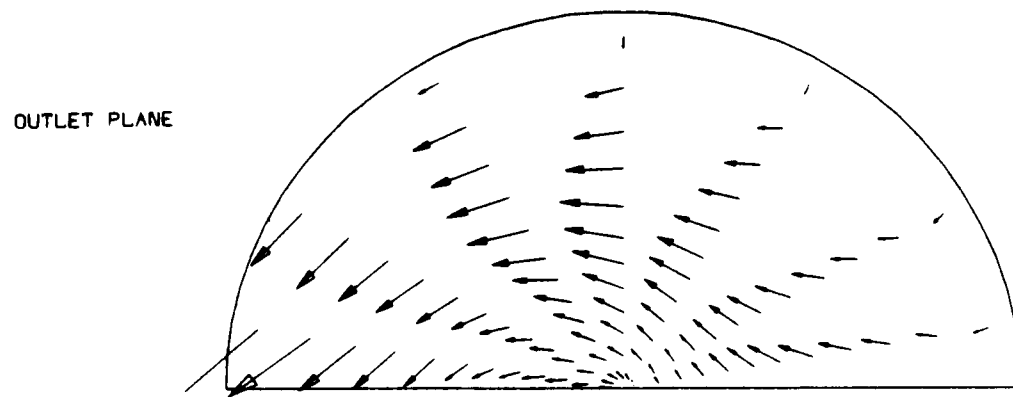
OUTLET PLANE

FIGURE 6.119:   RADIAL VELOCITY VECTORS AT 0.85m
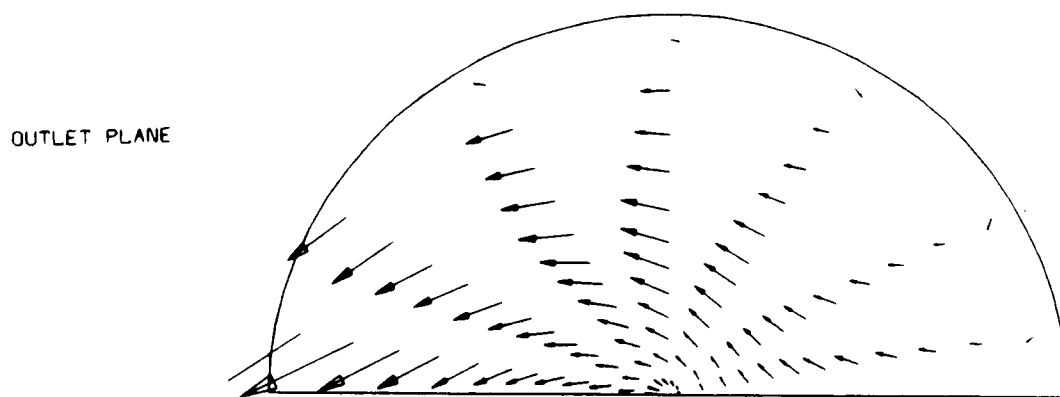
OUTLET PLANE

FIGURE 6.120:   RADIAL VELOCITY VECTORS AT 1.05m

OUTLET PLANE
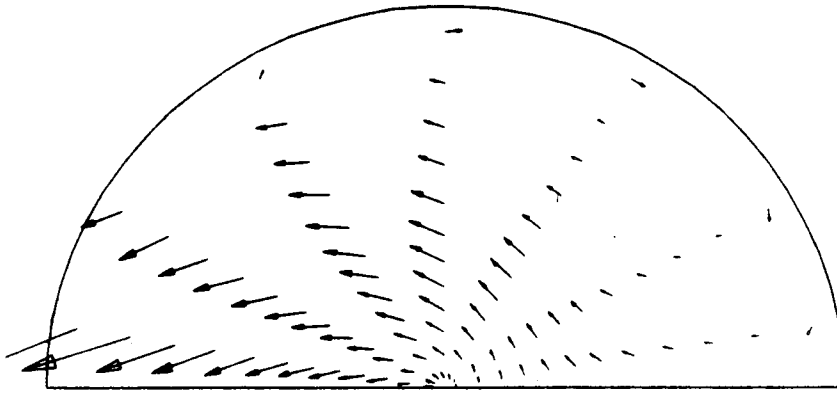
FIGURE 6.121:   RADIAL VELOCITY VECTORS AT 1.25m
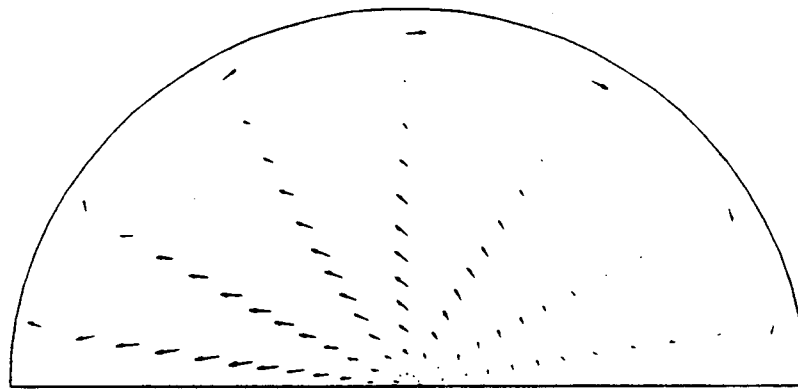
FIGURE 6.122:   RADIAL VELOCITY VECTORS AT 1.70m
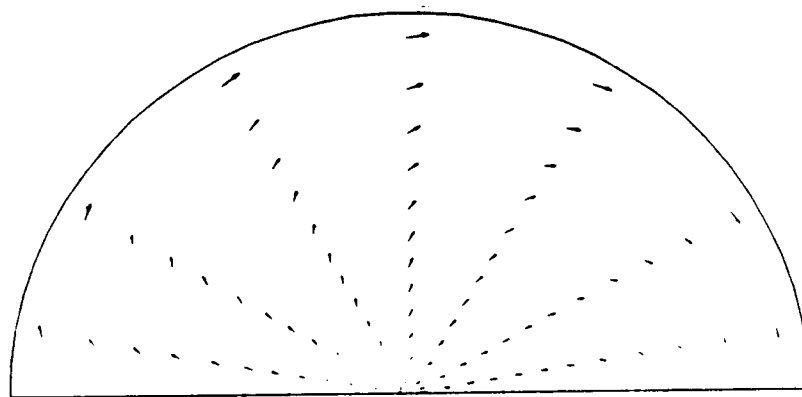
FIGURE 6.123:   RADIAL VELOCITY VECTORS AT 2.55m
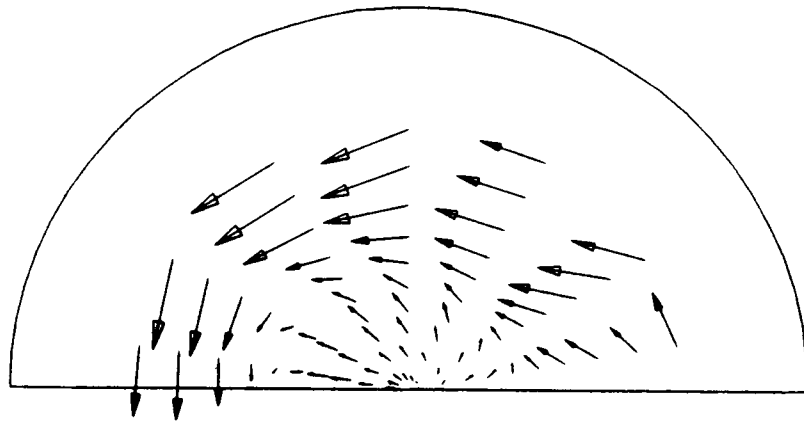
FIGURE 6.124:   RADIAL VELOCITY VECTORS AT 0.5075m
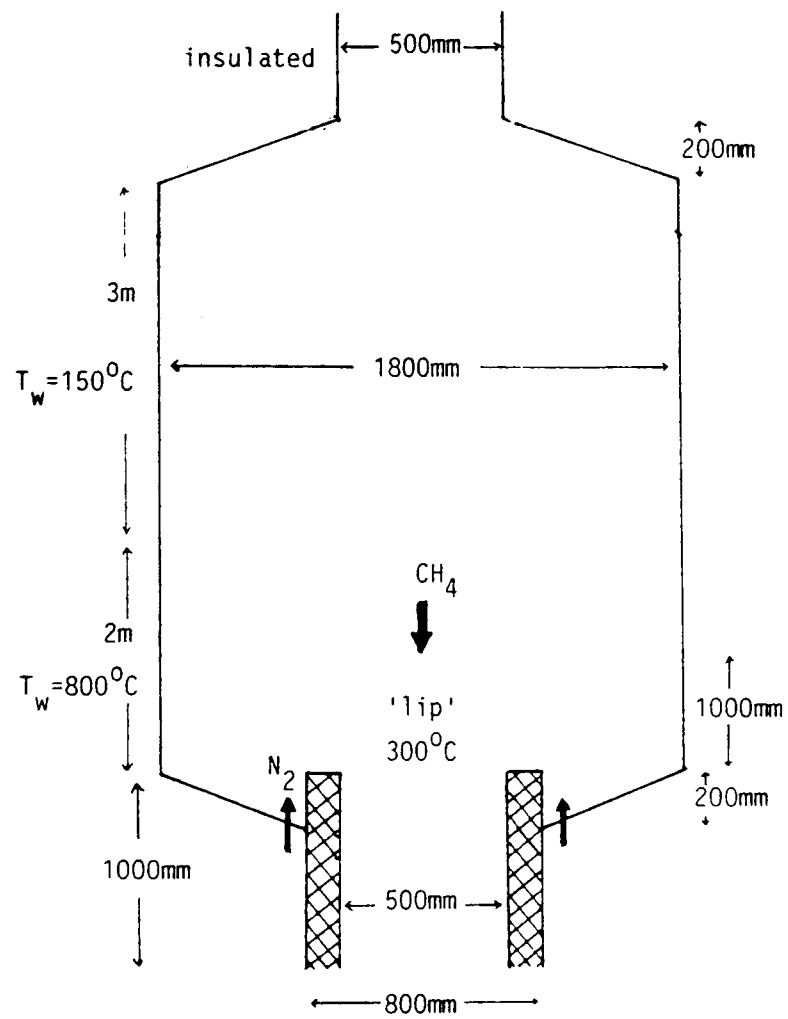
FIGURE 6.125:   OFF-GAS REACTION VESSEL II
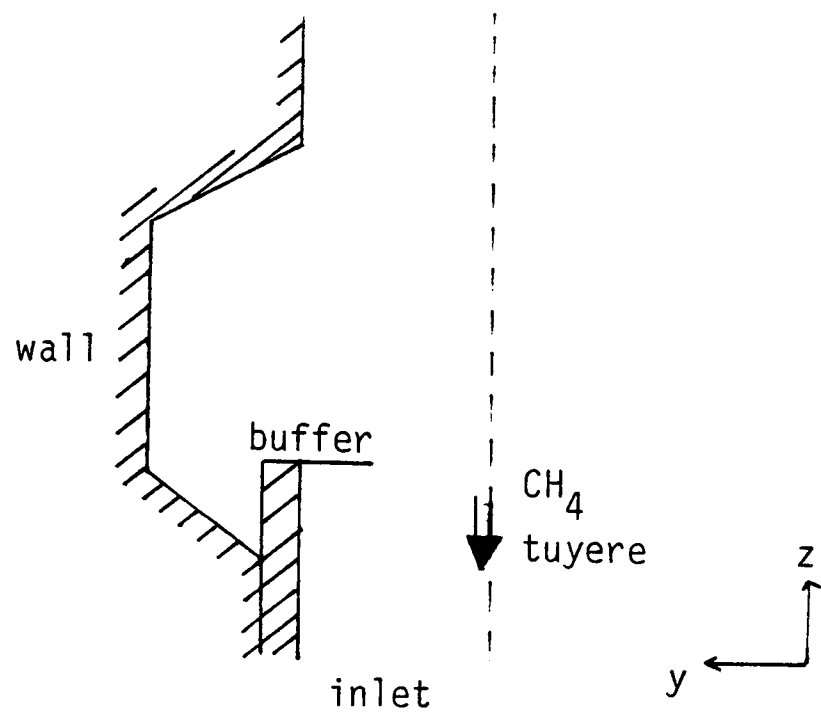
FIGURE 6.126:   BUFFER POSITION
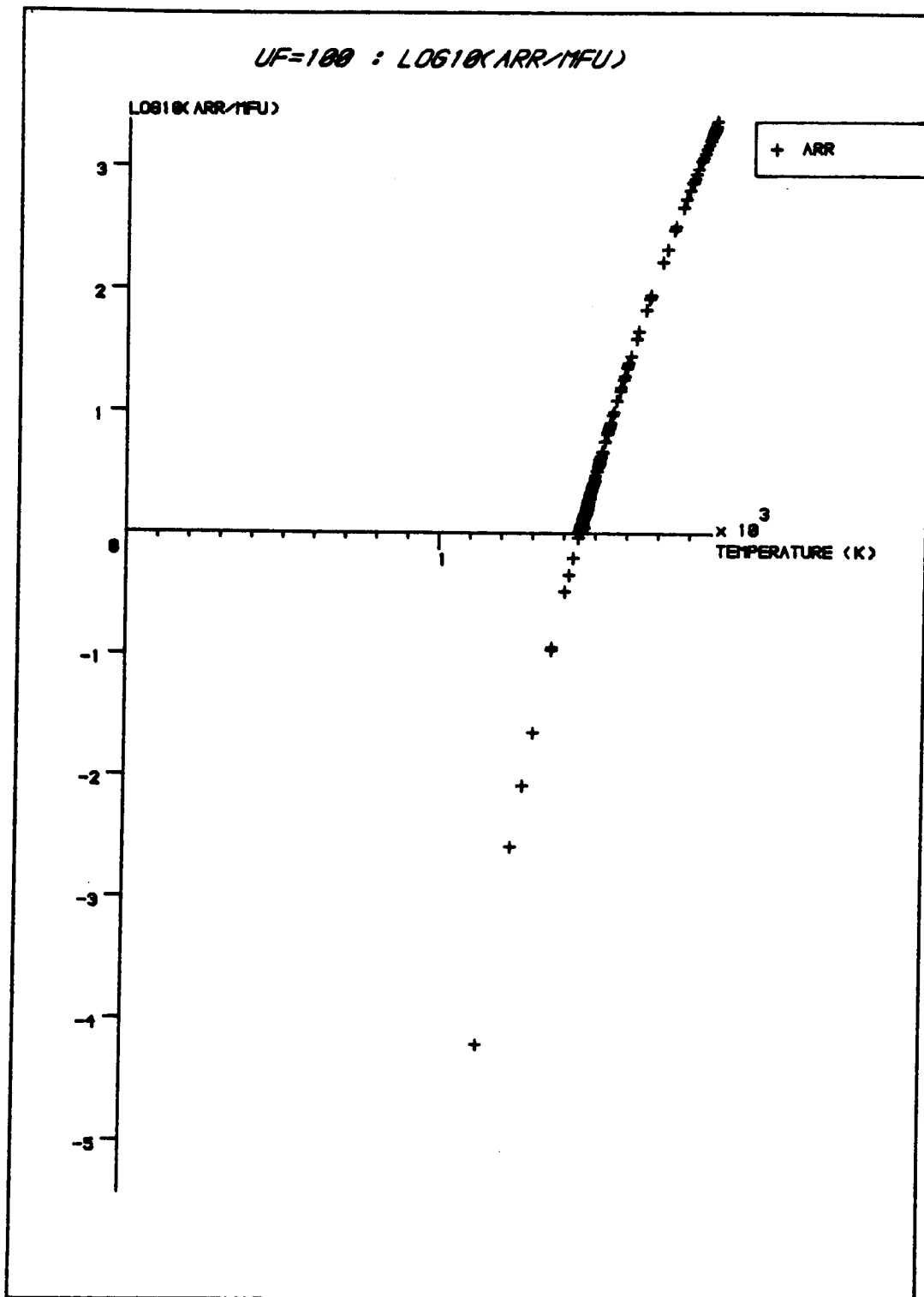
FIGURE 6.127:   ARRHENIUS RATE WITH UF=100

-270-
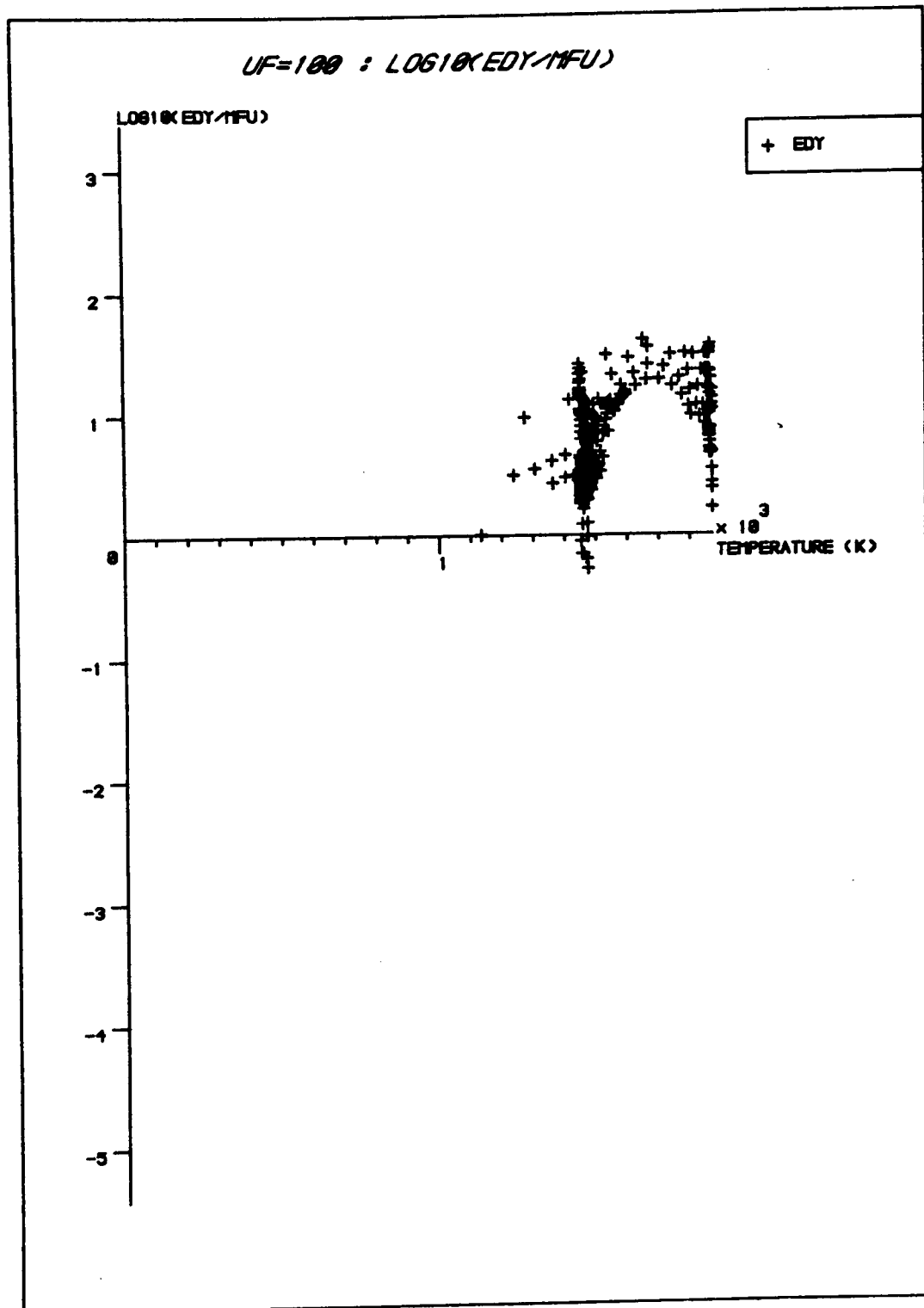
FIGURE 6.128:   EDDY-BREAKUP RATE WITH UF=100
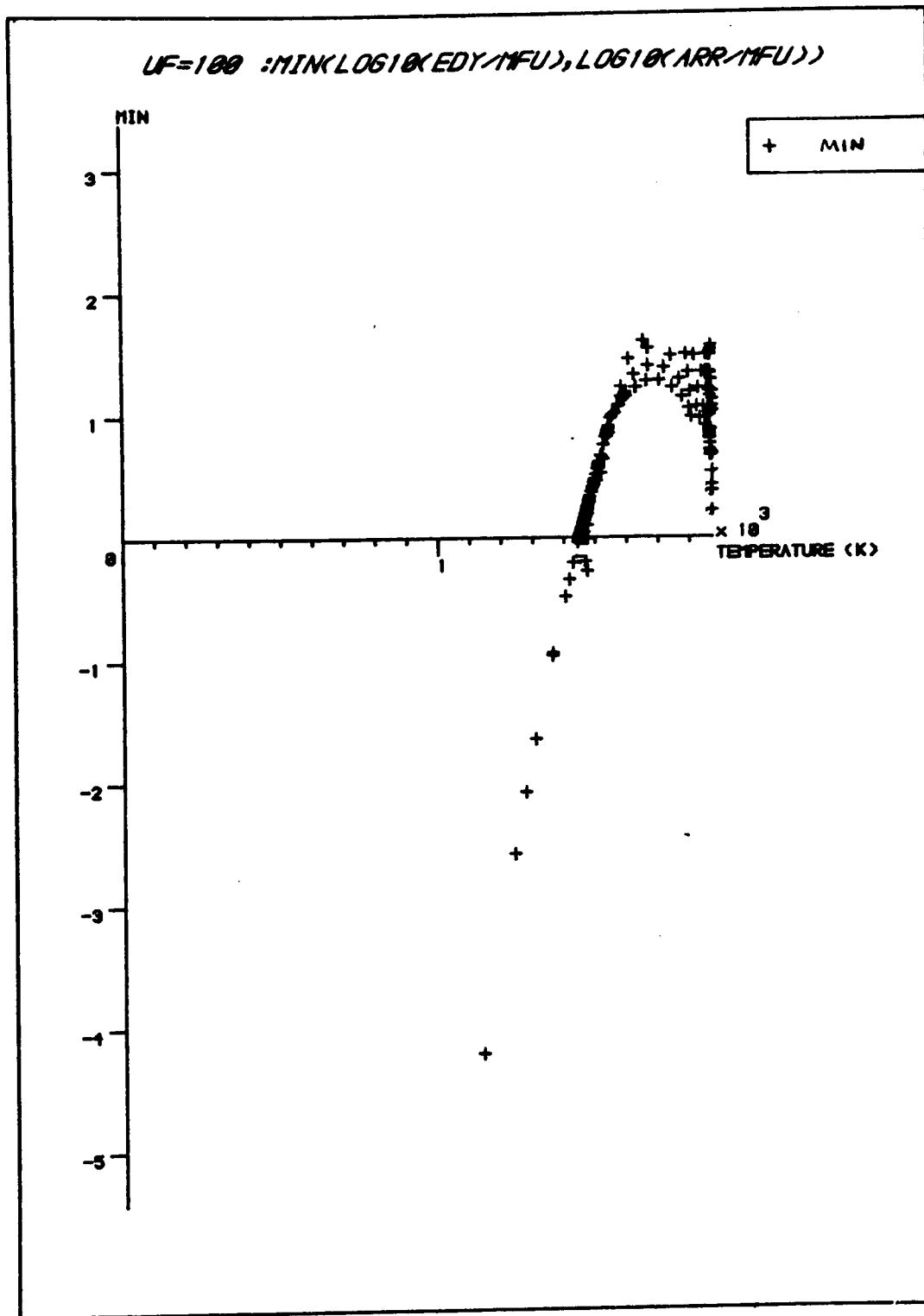
FIGURE 6.129:   MINIMUM REACTION RATE WITH UF=100
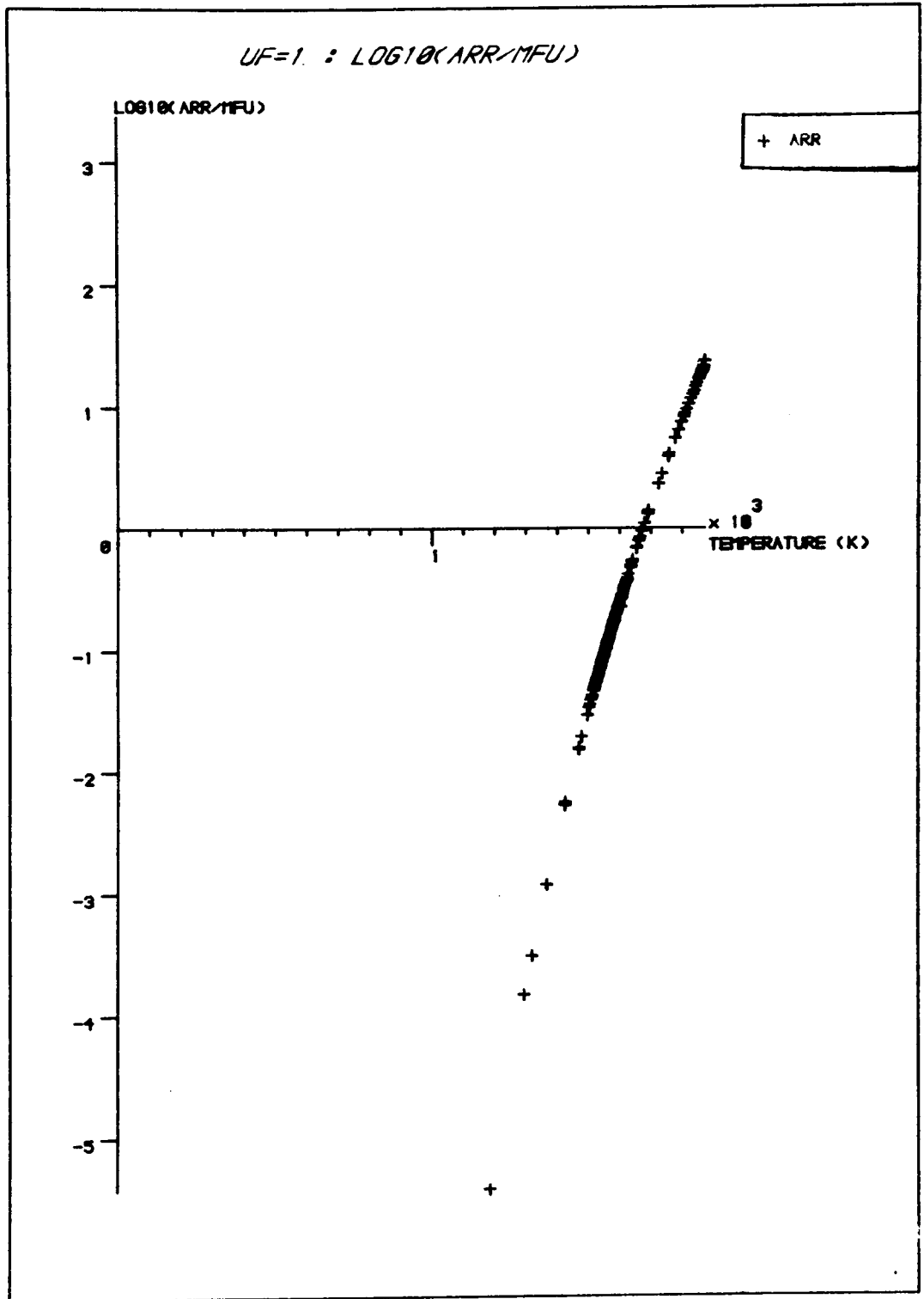
FIGURE 6.130:   ARRHENIUS RATE WITH UF=1

-273-
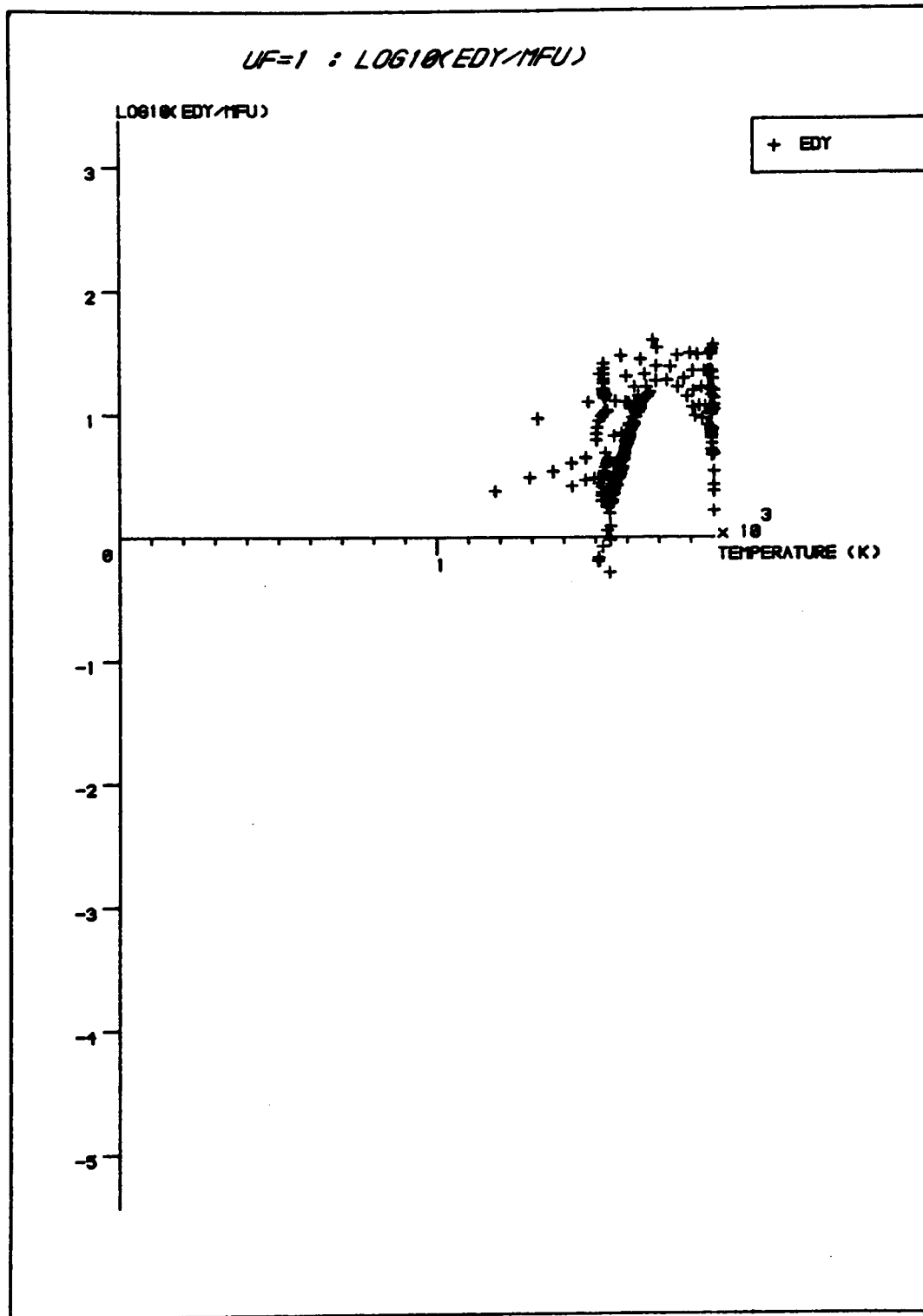
FIGURE 6.131:   EDDY-BREAKUP RATE WITH UF=1
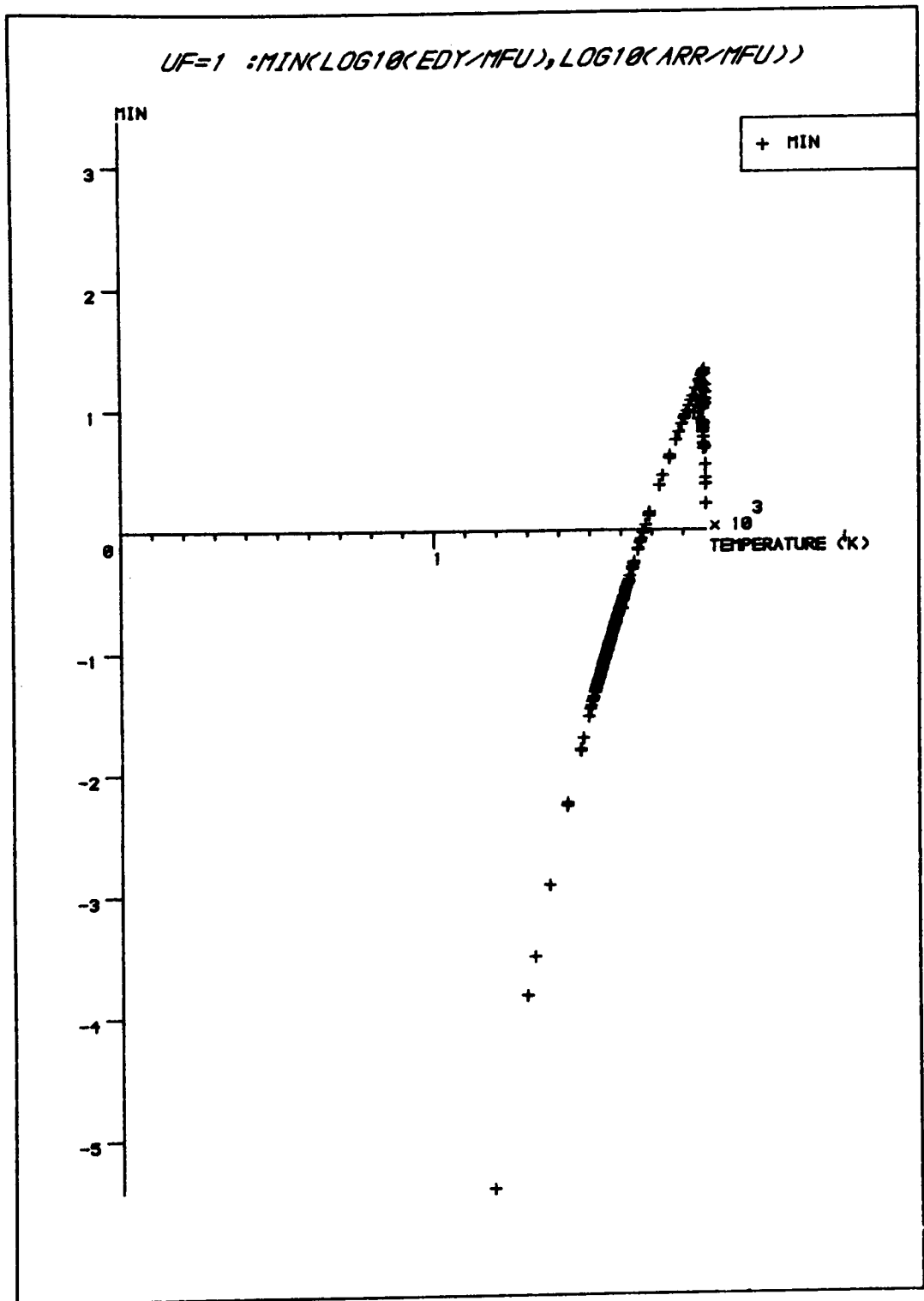
FIGURE 6.132:   MINIMUM REACTION RATE WITH UF=1
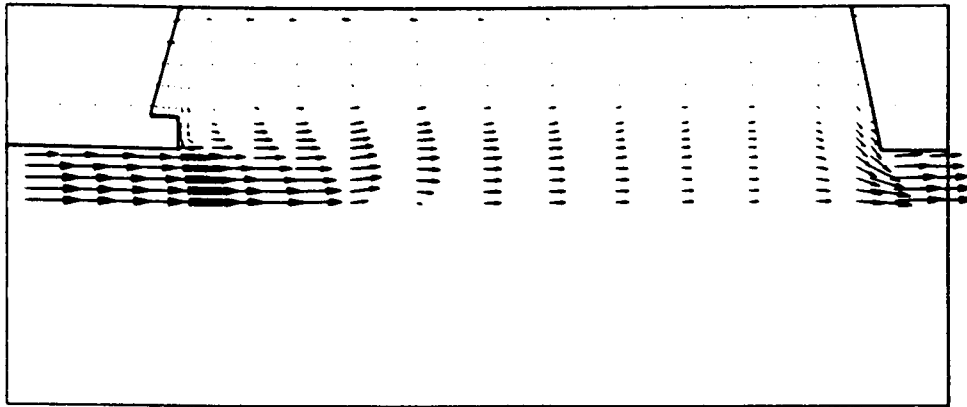
FIGURE 6.133:   VELOCITY VECTORS
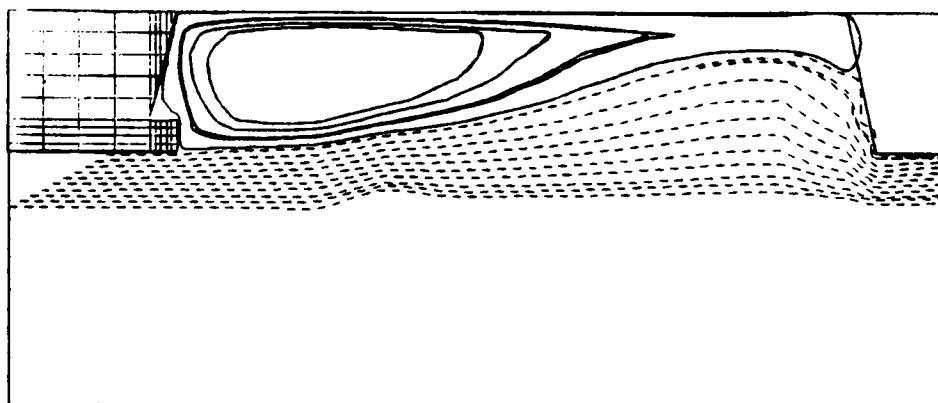
FIGURE 6.134:   STREAMLINES
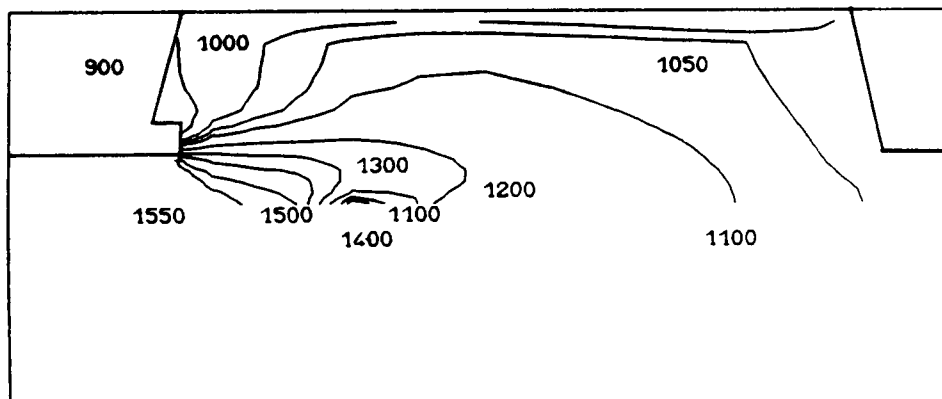
FIGURE 6.135:   TEMPERATURE CONTOURS (C)

-276-
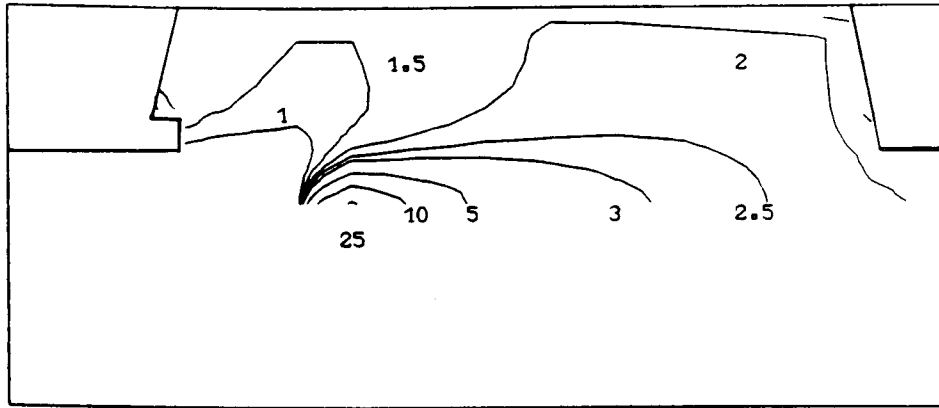
FIGURE 6.136:   CH₄ VOLUME FRACTIONS
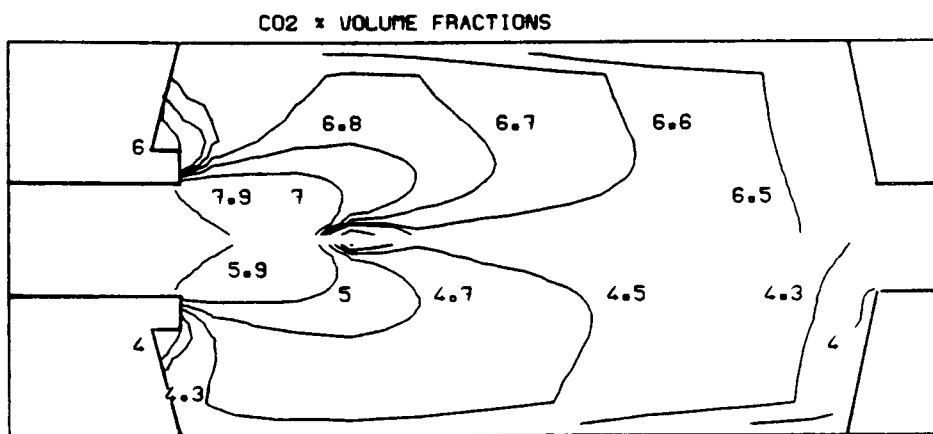
FIGURE 6.137:   CO₂ AND H₂O VOLUME FRACTIONS
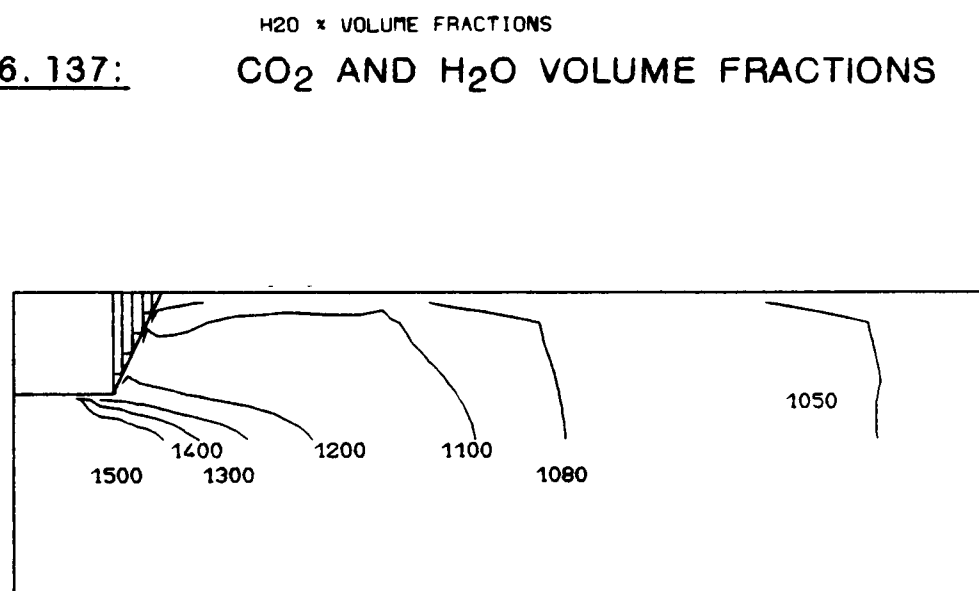
FIGURE 6.138:   TEMPERATURE CONTOURS (C)
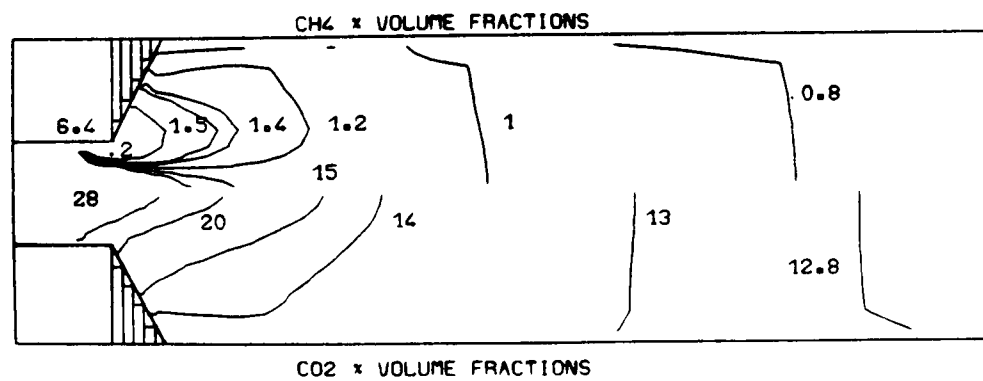
FIGURE 6.139:   CH₄ AND CO₂ VOLUME FRACTIONS

CHAPTER 7 - CONCLUSIONS

The objectives of the present work, as stated in Section 1.4, were the development and application of a complete mathematical model and computer simulation method for off-gas ducting systems. The aim was to provide both insight into the interaction between the major physicochemical factors and a tool for design and optimisation. The software should provide the design engineer with a general economical prediction procedure, enabling the performance of a proposed design to be determined with an acceptable engineering accuracy in the absence of a costly experimental programme The work reported in this thesis and its main conclusions are summarised below and the extent to which the objectives have been reached is discussed. Recommendations for future work are also given.

7.1   Recapitulation

In Chapter 2 the basic mathematical model was discussed along with the solution procedure, embodied in the general purpose software package PHOENICS. In order to make the model more realistic, the various auxiliary relations were introduced which included interphase heat transfer, particle solidification, interphase friction, wall functions and inlet/outlet boundary conditions. The two-equation, $k-\epsilon$ (energy-dissipation rate) turbulence model was used, because of its simplicity and computational economy.

Radiative heat transfer plays a dominant role in industrial furnaces and its relevance to the present work was discussed in Chapter 3. Thermal radiation is governed by integro-differential equations which are time consuming to solve, and hence require a computationally efficient model.

A novel six-flux, two-phase, radiation model was used that accounts for emission and absorption of radiation from both phases and scattering by the particulate phase. The model made possible the prescription of different radiation parameters for both phases. Previous models assume either a linear function for the absorption coefficient to account for the second-phase radiation contribution, or they disregard it completely, thus limiting the scope of the model. Results with radiation indicated that the particle size was the most important parameter in the calculation of the heat losses. The smaller the particle size, the bigger the heat losses.

Variation of the other radiation parameters indicated that the gas absorptivity coefficient was the most important of them. The particle scattering coefficient had a negligible effect on the heat losses and it was included only for completeness of the model. Wall temperature and wall emissivity were also found to be important parameters in the calculation of the heat losses.

When water-cooling was incorporated into the model, the increase in surface areas due to the cooling pipes was modelled by enhancing the heat transfer parameter by an appropriate factor.

Both phases enter the domain with the same temperature and their velocity profiles are assumed to be the same. The general characteristics of the flow were established for various inlet/wall-boundary conditions, particle sizes and particle-loading, with two-dimensional geometries. A secondary flow was also established, through a side-injection port and its prime effect was to push the particulate phase away from the walls. Water-cooling and radiation heat losses decreased

the temperatures of both phases and resulted in particle solidification. The model was found to be simple and economical to use, predicting realistic results.

Chemical reactions play an important role in the off-gas duct processes. This role is not well-understood and therefore there is a pressing need for better understanding. The complexity of the problem arises mainly from the difficulty of identifying the actual reaction control mechanisms, and secondly, from the lack of reliable experimental data. A number of new chemical reaction models have been used in this work in order to represent the process more realistically. These models vary from a simple, irreversible chemical reaction model, where the mixture fraction is a conserved quantity, to complex, two-simultaneous reaction models. All models are suitable for both exothermic and endothermic reactions and are able to cope with non-premixed gases of arbitrary composition. The reaction rate is controlled by the physical rate of mixing of the turbulent fluid and the temperature dependent chemical kinetics. For the reaction considered under the conditions prevailing in the off-gas ducts, the reaction rate is usually controlled by the eddy-breakup rate at higher temperatures and by the Arrhenius rate at lower temperatures. There is a small overlapping of the two rates for temperatures between $1500^{\circ}-1573^{\circ}K$, where either mechanism may control the rate, providing a smooth transition. Up to six chemical species have been accommodated in the models, yielding plausible results, which agreed with experimental measurements (when available) for two- or three-dimensional geometries.

Initially, air was injected from the side of the duct to react exothermically with CO. The diffusion and the simple kinetically-influenced models

were compared. It was concluded that the diffusion model is not suitable for serious studies because it overpredicts the temperatures at the reaction zone by as much as 500°C. (This is confirmed in the literature). Next, natural gas (CH_4) was injected into the system to react endothermically with CO_2. The kinetically-influenced model was employed. It predicts total consumption of CH_4 for all the inlet CH_4 concentrations employed. It was concluded that the theoretically predicted reaction cut-off temperature of 916°K was not suitable for the calculations. Experimental evidence suggested that (probably because of the high catalytic action of the iron particles) the cut-off temperature should be 1100°K. The new value was implemented yielding more accurate results, identical to the previous results in the lower part of the duct but with slightly higher temperatures, and slightly more CH_4 at the outlet. Introduction of the variable gas-specific that also improved the results. Originally, the specific heat was taken to be a constant value of 1552 J/Kg/K. This was too high and not consistent with the large temperature variations.

Next, the two-reaction model was employed, where it was assumed that CH_4 results with CO_2 and H_2O in the ratio 1:2. The model yielded good results.

The model was then developed by introducing sonic tuyeres, either co-current or counter-current, positioned in the centre of the duct and wall-tuyeres at various positions along the walls. It was concluded that the counter-current case induced a sudden drop in the gas temperature at the injection plane and a small temperature gradient above. For the co-current case there was no sudden drop and the temperature gradient

was smoother. This was because of the rapid mixing of the gases in the counter-current case and consequently the higher reaction rate. However, at the outlet, both gases gave approximately the same results. It was interesting to note that unlike the wall tuyeres, where the lowest temperatures were on the walls, for the centrally-positioned tuyeres, the lower temperatures were at the centre of the duct.

When the new geometries with restricted inlet and sloping wall were introduced, cooling effects resulted in particle solidification which accumulated on the sloping wall, below the recirculation zone. This created severe convergence problems. It was decided to withdraw the particles, and subsequent results consider only one phase.

The number of wall tuyeres were increased up to six, positioned at regular intervals. Various parametric cases were considered with respect to the CH_4 injected amounts and the position of the tuyeres (wall, throat). All cases exhibited similar characteristics. The major difference between wall and throat cases was the position of the recirculation reattachment point, which was lower for the wall case. The wall case also attained lower temperatures than the throat-case, especially inside the recirculation zone.

For the three-dimensional case of RV2 with side-outlet and six radial tuyeres it was predicted that significant amounts of CH_4 were escaping unreacted, confirming experimental measurements. Good agreement for exit temperatures and species concentrations were obtained with experimental measurements. Similar results were also obtained for tuyeres inclined at 5° to the radii.

Subsequent introduction of the Arrhenius rate minimum gave better agreement with experimental measurements. It was concluded that the uncertainty factor was vitally important and that the highest quoted value viz. 100 must be used. This is probably due to the high catalytic effect of the particles. This was also confirmed from the literature. The position of the tuyeres was also found to be a crucial factor in the efficiency of the reaction mechanism. It was established that tuyeres should be positioned in regions of high temperature, away from walls, otherwise CH_4 would not react in large amounts. This was because temperatures were dropping very rapidly and the reaction could not proceed. It was further concluded that temperatures above $1200^{\circ}C$ were needed for good reaction, but this proved to be impractical due to engineering limitations. For lower temperatures, the particulate phase was solidifying and accumulated on the walls with catastrophic consequences.

Introduction of the water-gas reaction into the system of two reactions, proved to be unrealistic for the supplied inlet compositions. It also had little effect on the exit results.

The findings of this thesis strongly suggest that the processes occurring in a off-gas duct, can be predicted to a good level of engineering accuracy at very low cost by numerical procedures.

The modelling of all relevant physical and chemical processes, in two- and three-dimensions, constitutes a major improvement to the previous treatment of the problem and more importantly, provides the engineer with good estimates of all related parameters.

Radiation from both phases and wall-heat losses can now be predicted more efficiently with better flexibility in the choice of parameters.

Chemical reaction rates are still not fully understood and quoted empirical relationships specify a wide band of uncertainty. The presence of the iron results in faster reaction of CH_4. It was found that the highest possible uncertainty factor must be used in such cases. With this value realistic results can be produced at low computational costs.

On the whole, the objective for providing a realistic tool for the design engineer has been achieved. Furthermore, the models developed are applicable, not only to off-gas ducts, but also to a wide variety of industrial plant.

7.2   Suggestions for Future Work

The greatest need is for reliable experimental data to validate more thoroughly, the chemical reaction models. It is unlikely that good experimental results will become available for a full-scale production plant, but results from small-scale apparatus, if available, would be valuable. This would enable much more detailed parametric tuning to be performed. Data on the catalytic mechanism of the iron particles on the gas reaction rates are also needed.

In many of the studies it was necessary to remove the particulate phase in order to get converged results. This is due to a well-known deficiency on the solvers for two-phase flow. Thus, if two phases enter a vertical duct under gravity, if the particulate gas comprises large particles and the duct is long, the particles cannot reach the top of the

duct and must fall back down. This will cause divergence. In such situations, which are modelled as steady-state, a single velocity or the particulate phase is inappropriate since in a single cell there will be particles moving in two completely different directions. The situation is further complicated by recirculating gas flow which traps particulate matter. These situations often lead to the deposit of this matter on adjacent walls. Study of these processes would be an interesting non-trivial exercise. Either the solvers used for two-phase flow would have to be improved or, to live with existing solvers, particulate matter moving in different directions would be stored separately and sources and sinks used to accommodate changes in direction. Trapping of particulate matter by walls, could be accomplished by specifying narrow cells adjacent to the walls and removing all or a fraction of the particulate matter entering this cell, by means of a sink term.

In the three-dimensional studies, the storage requirements pushed the available core storage to the limit and it was not always possible to perform grid refinement studies. This situation could be remedied by either superior algorithms or models requiring less core storage or use of bigger machines. Since the capacity of machines continues to grow at a phenomenal rate it is likely that the latter course will be the route to follow.

The radiation model introduced proved very successful but it is open to improvement in some respects. If more storage were available, a direct method of solving for radiation could be employed. Also the model could be improved to take account of the wavelengths of the radiation involved and their influence on parameters such as absorptivity, etc.

This would be particularly relevant in cases where H_2O and/or CO_2 predominate. In addition, extending the applicability of the model to smaller $(<0.1\mu m)$ particle diameter would be a worthy exercise. However, it may well be that such particulate matter is best treated by modifying the gas radiation parameters.

In real industrial plants, particulate matter may coalesce to form larger particles. This would be another field for research.

REFERENCES

Abou-Ellail M M M, Abou-Arab T W (1981)

Prediction of Turbulent Mixing in Confined Co-axial Reacting Jets.

Numerical Methods in Laminar and Turbulent Flow, Pineridge Press.

Abou-Ellail M M M, Gosman A D, Lockwood F C & Megahed I E A

(1977)

A Three-Dimensional Procedure for Combustion Chamber Flows.

AIAA 15th Aerospace Sciences Meeting, Los Angeles, California.

January 24-26, 1977, Paper 77-138.

Anderson D A, Tannehill T C & Pletches R H (1984)

Computational Fluid Mechanics and Heat Transfer.

Hemisphere Publishing Corporation, London.

Arbib H A, Goldman Y, Greenberg J B & Timnat Y M (1980)

A Numerical Model of High Intensity Confined Hydrocarbon Combustions.

Comb. Flame, 38.

Arrhenius S (1889)

Uber die Reaktions Geschwindigkeit bei der Inversion von Rohrzucken

durch Sauren.

Z. Phys. Chem., 4, 226.

Baulch D L, Drysdale D D, Horne D G & Lloyd A C (1972, 1973)

Evaluated Kinetic Data for High Temperature Reactions.

Vols 1 & 2, Butterworths, London.

Baulch D L, Drysdale D D, Duxbury J & Grant S (1976)

Evaluated Kinetic Data for High Temperature Reactions.

Vol 3, Butterworths, London.

Baum H R, Corlen D M & Rehm R G (1986)

Time-Dependent Simulation of Small-Scale Turbulent Mixing and Reaction.

21st Symposium (International) on Combustion.   The Combustion

Institute.

Barin I, Knacke O & Kubaschewsk O (1982)

Thermodynamic Properties of Inorganic Substances.

Springer-Verlag, New York.

Beer J M (1974)

Methods for Calculating Radiative Heat Transfer from Flames in

Combustors and Furnaces.

Heat Transfer in Flames, John Wiley, London.

Beer J M & Siddall R G (1973)

Radiative Heat Transfer in Furnaces and Combustors.

Italian Flame Day, 20-21 March 1973.   Italian Flame Res. Comm.,

Milano.

Bernasconi G F, Editor (1986)

Investigation of Rates and Mechanisms of Reactions.

Part I - Techniques in Chemistry, Volume VI.

J Wiley & Sons, 4th Edition, London.

Bilger R W (1977)

Reaction Rates in Diffusion Flames.

Comb. Flame, 30.

Borghi R (1973)

Etude Theorique de l'evolution Residuelle de Produits Pollutants dans les Jets de Turboreacteurs.

AGARD Meeting, CP125.

Boyd R K & Kent J H (1986)

Three-Dimensional Furnace Computer Modelling.

21st Symposium (International) on Combustion.   The Combustion Institute.

Bowman C J (1974)

Non-equilibrium Radical Concentrations in Shock-Initiated Methane Oxidation.

15th Symposium (International) on Combustion.   The Combustion Institute.

Bradshaw P, Cebeci T & Whitelaw J H (1981)

Engineering Calculation Methods for Turbulent Flows.

Academic Press, London.

Bray K N C (1974)

Kinetic Energy of Turbulence in Flames.

Dept of Aeronautics and Astronautics, Report No. 332, University of Southampton.

Bray K N C (1978)

The Interaction between Turbulence and Combustion.

17th Symposium (International) on Combustion. The Combustion Institute.

Carvalho M D G M D S (1983)

Computer Simulation of a Glass Furnace.

PhD Thesis, University of London.

Carvalho M D G M D S & Lockwood F C (1985)

Mathematical Simulation of an End-Point Regenerative Glass Furnace.

Proc. Instn. Mech. Engrs. Vol 199, No. C2.

Cebeci T & Bradshaw P (1984)

Physical and Computational Aspects of Convective Heat Transfer.

Springer-Verlag, New York.

Chung Y C & Yun C K (1985)

Detection of Two Moving Boundaries in a Burning Pellet of Coal.

Chem. Eng. Science, Vol 40, No. 7.

Clift R & Gauvin W H (1971)

Motion of Entrained Particles in Gas Streams.

The Canadian J. Chem. Eng., Vol 49, 339.

Creighton J R (1977)

Some General Principles obtained from Numerical Studies of Methane Combustion.

The Journal of Physical Chemistry, Vol 81, No. 25.

De Marco A G & Lockwood F C (1975)

A New Flux Model for Calculation of Radiation in Furnaces.

Italian Flame Day, La Rivista Dei Combustibili, No. 5-6, 29.

Devanpaul G, Ganesan V & Sitharama R T L (1983)

Numerical Prediction of Flow Characteristics of Confined Turbulent Premixed Flame.

Numerical Methods in Laminar and Turbulent Flow.   Pineridge Press.

Dixon-Lewis G & Islam S M (1982)

Flame Modelling and Burning Velocity Measurements.

19th Symposium (International) on Combustion.   The Combustion Institute.

Edelman R B & Harsha P T (1978)

Some Observations on Turbulent Mixing with Chemical Reactions.

Progress in Astronautics an Aeronautics, Vol 58.

Edwards D K (1981)

Radiation Heat Transfer Notes.

Hemisphere Publishing Corporation.

Elghobashi S E & Pun W M (1974)

A Theoretical and Experimental Study of Turbulent Diffusion Flames in Cylindrical Flames.

15th Symposium (International) on Combustion. The Combustion Institute.

Engleman V S (1976)

Survey and Evaluation of Kinetic Data on Reactions in Methane/Air Combustion.

Environmental Protection Agency, Report EPA-600/2-76-003.

Gardiner W C Jr, Editor (1984)

Combustion Chemistry.

Springer-Verlag.

Gardiner W C Jr, Owen J H, Clark T C et al (1974)

Rate and Mechanism of Methane Pyrolysis from 2000°K to 2700°K.

15th Symposium (International) on Combustion. The Combustion Institute.

Glasstone S (1960)

Thermodynamics for Chemists.

D van Nostrand Company Inc.

Gosman A D & Lockwood F C (1972)

Incorporation of a Flux Model for Radiation into a Finite-Difference

Procedure for Furnace Calculations.

14th Symposium (International) on Combustion.   The Combustion

Institute.

Gosman A D & Lockwood F C (1973)

Predictions of the Influence of Turbulent Fluctuations on Flow and Heat

Transfer in Furnaces.

Heat Transfer Section Report No. HTS/73/52, Dept of Mech. Eng.,

Imperial College, London.

Gosman A D, Lockwood F C & Salooja A P (1978)

The Prediction of Cylindrical Furnaces, Gaseous Fuelled with Premixed

and Diffusion Burners.

17th Symposium (International) on Combustion.   The Combustion

Institute.

Grosshandler W L & Nguyen H D (1985)

Application of the Total Transmittance Non-Homogeneous Radiation Model

to Methane Combustion.

J. Heat Transfer, Vol 107.

Gunton M C, Rosten H I & Spalding D B et al (1983)

PHOENICS: An Instruction Manual.

CHAM Report No. TR/75.

Gupta AK & Lilley D G (1985)

Flow Field Modelling and Diagnostics.

Abacus Press.

Hamaker H C (1947)

Radiation and Heat Conduction in Light-Scattering Material.

Phillips Res. Rep 2, 55, 103, 112, 420.

Hottel H C (1975)

First Estimates of Industrial Furnace Performance - The One Gas-Zone

Model Re-examined.

Heat Transfer in Flames. Scripta Book Company.

Hottel H C & Cohen E S (1958)

Radiant Heat Exchange in a Gas-Filled Enclosure: Allowance for

Non-Uniformity of Gas Temperature.

AIChE J, Vol 4, No. 1.

Hottel H C & Sarofim A F (1967)

Radiative Transfer

McGraw-Hill, New York.

Hutchinson P, Khalil E E & Whitelaw J (1976)

The Calculation of Wall Heat Transfer Rate and Pollutant Formation in

Axisymmetric Furnaces.

Proc. 4th Member Conference of the IFRF.

Jeng S M and Faeth G M (1984)

Radiative Heat Fluxes near Turbulent Buoyant Methane Diffusion Flames.

J. Heat Transfer, Vol 106.

Jensen D E & Jones G A (1978)

Reaction Rate Coefficient for Flame Calculations.

Comb. Flame, 32, 1-34.

Jones W P & Whitelaw J H (1982)

Calculation Methods for Reacting Turbulent Flows: A Review.

Comb. Flame, 48.

Kansa E J & Perlee H E (1980)

A Transient-Dust-Flame Model: Application to Coal Dust Flames.

Comb. Flame, 38.

Karman D & Steward F R (1984)

The Radiation Spectrum from a Test Furnace.

Int. J. Heat and Mass Transfer, Vol 27, No. 8.

Khalil E E (1979)

On the Modelling of Turbulent Reacting Flows in Furnaces and Combustion

Chambers.

Acta Astronautica, Vol 6, 449-465.

Khalil E E (1982)

Modelling of Furnaces and Combustors.

Abacus Press.

Khalil E E, Spalding D B & Whitelaw J H (1975)

The Calculation of Local Flow Properties in Two-Dimensional Furnaces.

Int. J. Heat and Mass Transfer, 18.

Khalil E E, Hutchinson P & Whitelaw J H (1981)

The Calculation of the Flow and Heat Transfer Characteristics of Gas-Fired Furnaces.

18th Symposium (International) on Combustion.   The Combustion Institute.

Kondrat'ev V N (1964)

Chemical Kinetics of Gas Reactions.

Pergamon Press.

Krivandin V & Markov B (1980)

Metallurgical Furnaces.

Mir Publishers, Moscow (English Translation).

Kurosaki Y & Spalding D B (1979)

One-Dimensional Unsteady Two-Phase Flow with Interphase Slip: A Numerical Study.

Presented at the 2nd Multiphase Flow and Heat Transfer Symposium Workshop, Miami Beach, April 1979.

Latimer B R & Pollard A (1985)

Comparison of Pressure-Velocity Coupling Solution Algorithms.

Numerical Heat Transfer, Vol 8.

Launder B E & Spalding D B (1974)

The Numerical Computations of Turbulent Flows.

Computer Methods in Applied Mechanics and Engineering, 3, 269-289.

Libby P A & Williams F A, Editors (1980)

Turbulent Reacting Flows.

Topics in Applied Physics, Springer-Verlag.

Lixing Z, Wenyi L, Jian Z & Zuolan W (1986)

Numerical Modelling of Three-Dimensional Flow Field and Two-Dimensional Coal Combustion in a Cylindrical Combustor of Co-Flow Jets with Large Velocity Difference.

21st Symposium (international) on Combustion.   The Combustion Institute.

Lockwood F C (1977)

The Modelling of Tubulent Premixed and Diffusion Combustion in the Computation of Engineering Flows.

Comb. Flame, 29.

Lockwood F C, Salooja A P & Syed S A (1980)

A Prediction Method for Coal-Fired Furnace.

Comb. Flame, 38.

Lockwood F C & Spalding D B (1971)

Prediction of a Turbulent Reacting Duct Flow with Significant Radiation.

Thermodynamic Sesion, Proc. Colleques d'Evian de la Societe Francaise de Physique, May 1971.

Lockwood F C & Shah N G (1978)

Evaluation of an Efficient Radiation Flux Model for Furnace Prediction Procedures.

Proc. 6th Int. Heat Transfer Conf. Paper No. EC6.

Lockwood F C & Shah N G (1980)

A New Radiation Solution Method for Incorporation in General Combustion Prediction Procedures.

18th Symposium (International) on Combustion. The Combustion Institute.

Lumley J L (1983)

Turbulence Modelling.

J. Applied Mechanics, Vol. 50.

Ma A S C, Spalding D B & Sun R L T (1982)

Application of 'ESCIMO' to the Turbulent Hydrogen-Air Diffusion Flame.

19th Symposium (International) on Combustion. The Combustion Institute.

Magnussen B F, Hjertager B H, Olsen J G & Bhaduri D (1978)

Effects of Turbulent Structure and Local Concentrations on Soot Formation and Combustion in C_2H_2 Diffusion Flames.

17th Symposium (International) on Combustion. The Combustion Institute.

Malin M R, Tatchell D G & Wang-Ving-Shi (1982)

Calculation of Steady-Three-Dimensional, Turbulent, Reacting Flow in a Combustion Chamber.

CHAM Report PDR/CHAM UK/19.

Markatos N C (1986)

The Mathematical Modelling of Turbulent Flows.

Appl. Math. Modelling, Vol 10.

Markatos N C & Kirkcaldy D (1983)

Analysis and Computation of the Three-Dimensional, Transient Flow and Combustion through Granulated Propellants.

Int. J. Heat and Mass Transfer, Vol. 26, No. 7, 1037-1053.

Markatos N C & Pericleous K A (1984)

An Investigation of Three-Dimensional Fires in Enclosures.

Rev. Gen. Therm. Fr. No. 266.

Markatos N C & Spalding D B (1983)

Computer Simulation of Fluid Flow and Heat/Mass Transfer Phenomena - The PHOENICS Code System: A Lecture Course.

School of Mathematics, Thames Polytechnic, London.

Mason H B & Spalding D B (1973)

Prediction of Reaction Rates in Turbulent Premixed Boundary-Layer Flows.

Proc. of the Combustion Institute, European Symposium. Academic Press.

Megahed I E A (1979)

The Prediction of Three-Dimensional Gas-Fired Combustion Chamber Flows.

PhD Thesis, University of London.

Moodie J (1984, 1985, 1986)

Private Communications.

Ng K H & Spalding D B (1972)

Turbulence Model for Boundary Layers near the Wall.

The Physics of Fluids, Vol. 15, N1.

Nguyen T V & Pope S B (1984)

Monte-Carlo Calculations of Turbulent Diffusion Flames.

Comb. Science. Tech, 42.

O'Brien E E (1986)

Recent Contributions to the Statistical Theory of Chemical Reactants in Turbulent Flows.

PCH. Vol 1.

Pai B R, Michelfelder S & Spalding D B (1978)

Prediction of Furnace Heat Transfer with a Three-Dimensional Mathematical Model.

Int. J. Heat and Mass Transfer, 21, 571-580.

Patankar S V (1980)

Numerical Heat Transfer and Fluid Flow.

Hemisphere Publishing Corporation.

Patankar S V (1981a)

Computer Analysis of Fluid Flow and Heat Transfer.

Recent Advances in Numerical Methods in Fluids.   Editors: C Taylor and

K Morgan, Vol 2, Pineridge Press.

Patankar S V (1981b)

A Calculation Procedure for Two-Dimensional Elliptic Situations.

Num. Heat Transfer, Vol 4, 409-425.

Patankar S V & Spalding D B (1972)

A Computer Model for Three-Dimensional Flow in Furnaces.

14th Symposium (International) on Combustion.   The Combustion

Institute.

Patankar S V & Spalding D B (1974)

Simultaneous Predictions of Flow Patterns and Radiation for

Three-Dimensional Flames.

Heat Transfer in Flames.   Editors: Afgan and Beer, John Wiley & Sons.

Pope S B (1976)

The Probability Approach to the Modelling of Turbulent Reacting Flows.

Comb. Flame, 27.

Pope S B (1985)

PDF Methods for Turbulent Reactive Flows.

Prog. Energy Combust. Sci., Vol 11.

Pope S B & Correa S M (1986)

Joint PDF Calculations of Non-Equilibrium Turbulent Diffusion Flame.

21st Symposium (International) on Combustion.   The Combustion

Institute.

Pun W M & Spalding D B (1967)

A Procedure for Predicting the Velocity and Temperature Distribution in a

Confined, Steady, Turbulent, Gaseous Diffusion Flame.

Proc. Int. Astronautical Federation Meeting, Belgrade.

Reynolds W C (1976)

Computation of Turbulent Flows.

Annual Review of Fluid Mechanics, Vol 8.

Rodi W (1980)

Turbulence Models and their Application in Hydraulics.

State-of-the-Art Paper presented by the IAHR-Section of Fundamentals of

Division II: Experiments and Mathematical Fluid Dynamics.

Serag-El-Din M A S (1977)

The Numerical Prediction of the Flow and Combustion Processes in a

Three-Dimensional Can Combustor.

PhD Thesis, University of London.

Shah N G (1979)

New Method of Computation of Radiation Heat Transfer in Combustion Chambers.

PhD Thesis, University of London.

Siddall R G S (1973)

Flux Methods for the Analysis of Radiant Heat Transfer.

4th Symposium on Flames and Industry, London.

Skinner G B, Lifshitz A, Scheller K and Burcat A (1972)

Kinetics of Methane Oxidation.

J. Chem. Physics, Vol 56, No 8.

Smith I W (1982)

The Combustion Rates of Coal Chars: A Review.

19th Symposium (International) on Combustion. The Combustion Institute.

Smith T F, Shen Z F & Alturki A M (1985)

Radiative and Convective Transfer in a Cylindrical Enclosure for a Real Gas.

J. Heat Transfer, Vol 107.

Spalding D B (1971)

Mixing and Chemical Reaction in Steady Confined Turbulent Flames.

13th Symposium (International) on Combustion. The Combustion Institute.

Spalding B (1972)

Mathematical Models of Continuous Combustions.

Emissions from Continuous Combustion Systems.   Plenum Press, 3-21.

Spalding D B (1974)

Numerical Computation of Practical Combustion Chamber Flows.

AGARD Meeting, No. 164.

Spalding D B (1977a)

A Simple Model for the Rate of Turbulent Combustion.

Progress in Astronautics and Aeronautics, Vol. 58.

Spalding D B (1977b)

A General Theory of Turbulent Combustion.

AIAA 15th Aerospace Science Meeting, Los Angeles, Paper 77-141.

Spalding D B (1978)

The Influence of Laminar Transport and Chemical Kinetics on the
Time-Mean Reaction Rate in a Turbulent Flame.

17th Symposium (International) on Combustion.   The Combustion
Institute.

Spalding D B (1979a)

Numerical Computation of Multiphase Fluid Flow and Heat Transfer.

Recent Advances in Numerical Methods in Fluids.   (Editor: C Taylor),

Vol 1, Pineridge Press.

Spalding D B (1979b)

Combustion and Mass Transfer.

Pergamon Press.

Spalding D B (1980a)

Mathematical Modelling of Fluid-Mechanics, Heat Transfer and Chemical_Reaction Processes.

A Lecture Course, Heat Transfer Section, Report HTS/80/1, Imperial College, London, January 1980.

Spalding D B (1980b)

Mathematical Methods in Nuclear-Reactor Thermal Hydraulics.

Paper presented at the American Nuclear Society meeting on Nuclear-Reactor Thermal Hydraulics, Saratoga, N.Y.

Spalding D B (1981)

A General Purpose Computer Program for Multi-dimensional One- or Two-Phase Flow.

Mathematics and Computers in Simulation, XIII, 267-276.

Spalding D B (1982a)

Turbulence Models - A Lecture Course.

Computational Fluid Dynamics Unit, Report CFD/82/4. Imperial College, London.

Spalding D B (1982b)

The 'Shadow' Method of Particle-Size Calculation in Two-Phase Combustion.

19th Symposium (International) on Combustion. The Combustion Institute.

Spalding D B (1983a)

Chemical Reactions in Turbulent Fluids.

PCH, Vol 4, No 4.

Spalding D B (1983b)

Turbulence Modelling – A State-of-the-Art: Review.

Computational Fluid Dynamics Unit, Report CFD/83/3, Imperial College, London.

Steward F R & Guruz K H (1974)

The Effect of Solid Particles on Radiative Transfer in a Cylindrical Test Furnace.

15th Symposium (International) on Combustion. The Combustion Institute.

Takenaka Y, Ashie T, Kaneko D et al (1981)

Effect of Catalytic Action of Reduced Iron on CH_4 Reforming Reaction.

Presented at the 101st ISIJ Meeting, April 1981, Lecture No. S57.

Truelove J S (1976a)

Differential Equation Models for Radiative Transfer.

Thermodynamics Division, AERE Harwell, April 1976, Report AERE R8364.

Truelove J S (1976b)

A Mixed Grey Gas Model for Flame Radiation.

Thermodynamics Division, AERE Harwell, December 1976, Report AERE R8494.

Truelove J S (1984)

Radiant Heat Transfer through the Cover Gas of a Sodium-Cooled Fast Reactor.

Int. J. Heat Mass Transfer, Vol 27, No 11.

Tsatsaronis G (1978)

Prediction of Propagating Laminar Flames in Methane, Oxygen, Nitrogen Mixtures.

Comb. Flame 33, 217-239.

Von Bogdandy L, Brotzmann K & Fabbinder H G (1984)

Post Combustion and Fuel Injection in the Converter Process.

Proc. of the 4th Process Technology Conference, Vol 4, Chicago.

Wall T F, Duong H T, Stewart M C & Truelove J S (1982)

Radiative Heat Transfer in Furnaces: Flame and Furnace Models of the IFRF M1- and M2-trials.

19th Symposium (International) on Combustion. The Combustion Institute.

Westbrook C K, Creighton J, Lund C & Dryer F L (1977)

A Numerical Model of Chemical Kinetics of Combustion in a Turbulent

Flow Reactor.

The Journal of Physical Chemistry, Vol 81, No. 25.

Westbrook C K & Dryer F L (1981)

Chemical Kinetics and Modelling of Combustion Processes.

18th Symposium (International) on Combustion.   The Combustion

Institute.

Whitacre R & McCaun R A (1975)

Comparison of Methods of Prediction of Radiant Heat Flux Distribution and

Temperature.

ASME Paper 75-HT-9.

Williams F A & Libby P A (1980)

Some Implications of Recent Theoretical Studies in Turbulent Combustion.

AIAA 18th Aerospace Sciences Meeting, California.   Also Paper

AIAA-80-0012.

Xu-Chang Xu (1981)

Mathematical Modelling of Three-Dimensional Heat Transfer from Flame in

Combustion Chambers.

18th Symposium (International) on Combustion.   The Combustion

Institute.